GAP WINDS IN A FJORD: HOWE SOUND, BRITISH COLUMBIA

By

Peter L. Jackson

B. Sc. (hons.) (Physical Geography focus Climatology/Meteorology)

A THESIS SUBMITTED IN PARTIAL FULFILLMENT OF

THE REQUIREMENTS FOR THE DEGREE OF

DOCTOR OF PHILOSOPHY

in

THE FACULTY OF GRADUATE STUDIES

GEOGRAPHY

We accept this thesis as conforming

to the required standard

THE UNIVERSITY OF BRITISH COLUMBIA

1993

In presenting this thesis in partial fulfilment of the requirements for an advanced degree at the University of British Columbia, I agree that the Library shall make it freely available for reference and study. I further agree that permission for extensive copying of this thesis for scholarly purposes may be granted by the head of my department or by his or her representatives. It is understood that copying or publication of this thesis for financial gain shall not be allowed without my written permission.

Geography

The University of British Columbia

2075 Wesbrook Place

Vancouver, Canada

V6T 1Z1

Date:

March 26 / 93

Abstract

Gap, outflow, or **Squamish** wind, is the cold low level seaward flow of air through fjords which dissect the coastal mountain barrier of northwestern North America. These flows, occurring mainly during winter, can be strong, threatening safety, economic activity and comfort.

Howe Sound gap winds were studied using a combination of observations and several types of models. Observations of winds in Howe Sound showed that gap wind strength varied considerably along the channel, across the channel and vertically. Generally, winds increase down the channel, are strongest along the eastern side, and are below 1000 m depth. Observations were unable to answer all questions about gap winds due to data sparseness, particularly in the vertical direction. Therefore, several modelling approaches were used.

The modelling began with a complete 3-dimensional quasi-Boussinesq model (CSU RAMS) and ended with the creation and testing of models which are conceptually simpler, and more easily interpreted and manipulated. A gap wind simulation made using RAMS was shown to be mostly successful by statistical evaluation compared to other mesoscale simulations, and by visual inspection of the fields. The RAMS output, which has very high temporal and spatial resolution, provided much additional information about the details of gap flow. In particular, RAMS results suggested a close analogy between gap wind and hydraulic channel flow, with hydraulic features such as supercritical flow and hydraulic jumps apparent. These findings imply gap wind flow could potentially be represented by much simpler models. The simplest possible models containing pressure gradient, advection and friction but not incorporating hydraulic effects, were created,

tested, and found lacking. A hydraulic model, which in addition incorporates varying gap wind height and channel geometry, was created and shown to successfully simulate gap winds.

Force balance analysis from RAMS and the hydraulic model showed that pressure gradient and advection are the most important forces, followed by friction which becomes an important force in fast supercritical flow. The sensitivity of gap wind speed to various parameters was found from sensitivity tests using the hydraulic model. Results indicated that gap wind speed increases with increasing boundary layer height and speed at the head of channel, and increasing synoptic pressure gradient. Gap wind speed decreases with increasing friction, and increasing boundary layer height at the seaward channel end. Increasing temperature differences between the cold gap wind air and the warmer air aloft was found to increase the variability of the flow – higher maximum but lower mean wind speeds.

Table of Contents

List of Tables

List of Figures

Acknowledgment

Chapter 1

Introduction

If the surface of Earth were smooth and homogeneous, climate (averaged weather) would vary by latitude only. It is apparent that the northwest coast of North America is neither flat (it is a mountain chain dissected by fjords) nor of homogeneous surface type (having both land of varying surface roughness, and water). Since the detailed expression of climate depends on the local configuration of surface types, it consequently displays a variety of climates. One of the most striking winter wind regimes affecting the fjords of western North America, is *gap*, *outflow* or, colloquially, *Squamish*[1] wind.

Outflow wind is the movement of cold, dry air at low levels from the interior of the continent to the coast. A major barrier to this motion, especially if the air is stable, is the Coast Mountain chain. Thus, low level air will preferentially flow through major valleys, and over lower mountain passes, to coastal inlets. This will generally occur whenever a pressure gradient is directed from the interior to the Coast. Under certain conditions outflow winds can be very strong and damaging. For example surface winds of 51 m s^{-1} with higher gusts were recorded near Portland Inlet in northern British Columbia [2] on January 10 1969 (Beal, 1985), while on January 14 1950, Abbotsford, in the lower Fraser valley, had seven hours of gap winds in excess of 26 m s^{-1} (Tyner, 1951b).

[1] All three terms: **gap, outflow,** and **Squamish wind** are closely related and will be used interchangeably in the thesis. The term **Squamish wind** seems to be come from the geographic place name "Squamish" which is the name of both a town at the head of Howe Sound, and of the native peoples whose ancestral lands cover the area. The term **Squamish wind** is generically applied to similar winds in other fjords along the British Columbia coast (Schaeffer, 1975)

[2] NOTE: place names used in the thesis can be found in figures 2.1, 3.1 and 3.2

1

In British Columbia, the conditions creating the most intense gap winds occur during winter when a strong arctic anticyclone builds over the interior of the province (Tyner, 1950; Tyner, 1951a; Tyner, 1951b). In this situation arctic air, which cools and deepens in the interior, is partially contained by the Coast Mountains which separate it from relatively warm, moist, air on the coast. The difference in temperature, humidity, and hence density, on either side of the mountain barrier results in a large pressure gradient, oriented perpendicular to the mountain barrier. As a result, and because cold dense air on a slope will accelerate under the influence of gravity, strong low level winds can develop through inlets and valleys. This is depicted schematically in figure 1.1 which is an oblique view of Howe Sound with the axes of strong outflowing air indicated by heavy arrows. Figure 1.1 is a composite from observations and numerical model output. The onset of strong outflow is often accompanied by passage of an arctic front onto the coast. Although air moving down slope is dynamically warmed due to adiabatic compression, it is still cold relative to the maritime air it is displacing. When this situation at the surface is combined with outflowing winds at mid levels, (which results in both a lee trough due to the mountains and a thermal trough due to the warm ocean) the pressure gradient and gap wind strength are further enhanced.

Strong outflow can also occur without an arctic outbreak - usually as the result of a deep cyclonic centre approaching the coast. While gap winds can occur whenever sea level pressure is greater inland than on the coast, the preceding paragraph describes a conceptual model of an intense outflow event. A goal for this research will be to validate and quantify the conceptual model of gap wind flow.
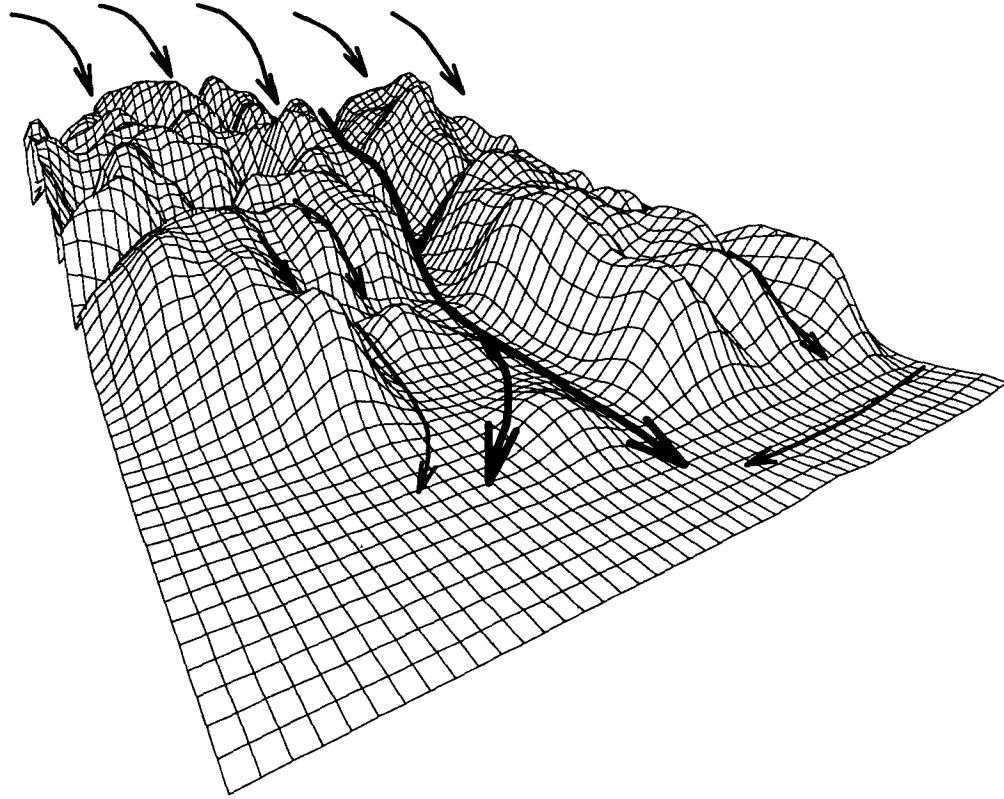
Figure 1.1: Visualization of gap wind flow superimposed on perspective view of topography in southern Howe Sound. View is from south, looking north-northeastwards. Vertical exaggeration is 10.

1.1 Motivation

The effects of strong outflow wind can be dramatic: extreme wind chill, storm to hurricane force winds, crop damage, and blizzard conditions with visibility near zero in blowing snow or dust. High winds are hazardous to aircraft because of severe low level turbulence, and to shipping because of potential severe icing and sea state (Atmospheric Research Incorporated, 1986). Strong outflow in winter results in "snow belts" on the east coasts of Vancouver Island and the Queen Charlotte Islands as the cold air acquires moisture, and becomes unstable from the warm ocean. The moist, unstable air when forced to

rise up the eastern slope, can form clouds and snow. Episodes of strong gap winds can result in widespread power outages due to wind-blown trees knocking down electric power lines (The Vancouver Sun, 1989a; The Vancouver Sun, 1989b). When these winds are associated with extreme cold, the result is large power consumption, and severe damage to transportation, property, domestic water supplies, etc. (North Shore News, 1989; The Vancouver Sun, 1989c).

While the effects of strong but relatively rare outflow events can be dramatic, it is also important to understand less dramatic more frequent outflow events of moderate intensity. In narrow valleys and fjords, such as those dissecting British Columbia's Coast Mountains, significant winds can only occur either as inflow (up-valley) or outflow (down-valley). Outflow is the dominant direction in winter (Jackson and Steyn, 1992; Steyn and Jackson, 1990), so that understanding its characteristics is an important part of understanding the wind climatology of fjords in the region.

Present forecast techniques employed by Atmospheric Environment Service (AES) meteorologists using surface pressure prognoses are able to provide some guidance on outflow onset and duration. If an observation exists with which to calibrate the forecast, the range of intensity at a point can also be estimated. However, very little is known about the detailed spatial and temporal variability of the flow, or about its intensity, with any accuracy. By studying outflow winds, improved analysis and forecasts of the onset, duration and intensity of the flows, as well as their spatial and temporal variability will be possible.

1.2 Objectives

Gap winds are an expression of the internal flow dynamics controlled by an interaction between external forcing parameters (synoptic weather conditions) and the internal

boundary conditions (terrain) within an inlet or valley. Questions to be studied concerning these winds are divided into two groups which are listed below. The first is a series of questions about the detailed nature and characteristics of gap winds. The second is questions concerned with external parameters which cause and control the wind flow.

Characteristics of gap winds

horizontal outflow structure:

- Where does the maximum wind speed occur?

- How do changes in internal boundary conditions (topography, valley slope, roughness and width) affect the flow?

- What are the effects of obstacles such as islands, on outflow winds?

- How does flow vary temporally / diurnally? Are there wave-like (periodic in space or time) fluctuations?

vertical outflow structure:

- What is the depth of outflowing air, and how does it vary along a fjord?

- Where is the vertical speed maximum? How does the height of the speed maximum vary along the fjord?

- What is the vertical temperature structure? Does an inversion mark the top of the outflowing air?

- Is it possible to extrapolate results from the study of one fjord to others? Is it possible to separate the phenomena from their internal boundary conditions?

Reaction of flow to external boundary conditions

Based on the conceptual model described previously, by analogy with downslope windstorms (see for example Clark and Peltier (1984), Durran and Klemp (1987), Klemp and Lilly (1975), Peltier and Clark (1983), Smith (1985)), from the work done on gap winds in Alaska (Lackmann and Overland, 1989; Macklin, Overland and Walker, 1984; Macklin, 1988; Macklin, Bond and Walker, 1990), from the work done on a closely related phenomenon called the Bora in Croatia (Klemp and Durran, 1987; Smith, 1987; Yoshino, 1976a) and from local studies of related wind flow patterns (Mass and Albright, 1985; Overland and Walter, 1981; Reed, 1981; Reed, 1931), it is possible to make several general statements about external parameters that are thought to affect gap winds. These are: direction and magnitude of horizontal surface pressure gradient; temperature contrast between the cold air inland and the warmer maritime air on the coast; geostrophic wind velocity at mountain top level; depth of cold air in interior (height of inversion); vertical wind profile – presence of critical layers and regions of wind reversal. These are outlined in more detail in the literature review presented in chapter 2.

The following questions provide a framework for assessing the importance of the above controls:

- Are these the important external parameters for gap winds?

- What is the relative importance of each?

- Are there other important external parameters?

- Are there threshold values which these parameters must exceed for the flow to begin or to be maintained?

- How do external forcing parameters affect flow characteristics?

- Which parameters are most important?

1.3 Approach

A three-pronged approach was employed to fulfill these objectives and answer the previous questions: field measurements, numerical modelling using a mesoscale model, and analytical / numerical modelling using simpler models. Field measurements and numerical model output provide answers to questions about the internal dynamics and structure. Numerical and analytical modelling provide answers to questions about the influence of external parameters.

1.3.1 Field measurements

To better understand gap wind characteristics in Howe Sound, a field measurement program was mounted. The program consisted of a network of surface stations and a series of vertical soundings. The surface stations continuously monitored and recorded wind, temperature, and pressure, providing information on the horizontal structure of outflow near the surface. The vertical soundings provided information about the vertical structure at one location during selected outflow events. The data obtained from the field were used to examine the synoptic setting and mesoscale structure of a gap wind event.

1.3.2 Numerical and analytical modelling

A numerical mesoscale model was used to simulate the detailed structure of the flow, and validated against observations. If the model simulates the flow adequately, then model output can be used to determine horizontal and vertical flow structure. The use of numerical models to examine detailed flow structure can be extremely informative, since the horizontal and vertical resolution is much greater than that of the observational

network. Numerical model output is used to suggest analytic and simpler numerical models representing simplifications of the equations of motion.

Once analytical, or a simple numerical model has been created and verified, it will be used to determine the sensitivity of the flow to external parameters. To do this, all external boundary conditions will be held constant at some typical value, except one which will be varied through a range of values for each computation. This will be done successively for the major forcing parameters which are included in the simple model. Thus it will be possible to judge the sensitivity of analytical model output (eg. wind speed) to external forcing parameters. Sensitivity analyses using a simple model is preferred to the "brute force" method of performing multiple computations with the full 3D model for several reasons:

- computational costs required to perform many simulations is prohibitive.

- simple models are much easier to manipulate.

- interpretation of primitive equation numerical model output is often very difficult, whereas interpretation of the results from a simpler set of equations is often clearer and more scientifically satisfying.

Chapter 2

Gap winds around the world — a review of the literature

2.1 Nomenclature and classification

Before reviewing the literature concerning gap winds and other similar local winds, nomenclature and terminology will be defined. Gap winds have been loosely defined as resulting from a balance between the horizontal pressure gradient, and inertia (acceleration). Overland and Walter (1981) have described gap winds as:

$$v\frac{dv}{dx} = -\frac{1}{\rho}\frac{dP}{dx} \tag{2.1}$$

where x is aligned along the channel, v is the down-channel wind speed, ρ is air density, and $\frac{dP}{dx}$ is the channel-parallel pressure gradient. This represents a balance between acceleration and horizontal pressure gradient.

Therefore, by applying the name "gap" to Squamish wind a statement is made about the process which accounts for it. In previous studies (Macklin, Lackmann and Gray, 1988; Macklin, Bond and Walker, 1990; Overland and Walter, 1981), the term "gap wind" has been applied to winds in horizontal channels in situations where the horizontal pressure gradient is oriented along the channel. While this is the case for Howe Sound Squamish winds, the effect of changing channel elevation may be important over land.

Gap winds are related to a class of downslope winds, typified by the "bora" of Croatia. Bora winds, unlike gap winds, are not constrained horizontally by channel walls. Changes in elevation, as cold air flows down steep slopes, is an important source of kinetic energy for bora winds. Several classification schemes have been developed to better

9

understand and describe bora winds. The first scheme, originally developed by Bénévant (1930), classified boras by synoptic type as follows: Anticyclonic — high pressure inland; Cyclonic — low pressure over the sea; and Mixed — a combination of the first two. The next classification scheme, proposed by Paradiž (1957) and Paradiž (1959), considered the relative importance of pressure gradient and temperature contrast across the Dinaric Alps. Yoshino (1976b) proposed a scheme with six different classifications based on the relative positions of anticyclonic and cyclonic centres.

Bora winds are closely related to föhn winds, like the Chinooks of Alberta. The main difference between the two, seems to be that föhn winds are relatively warm, whereas bora winds are relatively cold. Classification becomes difficult when the wind is relatively cold at one part of the slope and relatively warm at another (Jurčec, 1981). Bora and föhn winds in turn are related to "downslope windstorms", which occur when air flowing over a mountain barrier develops a large amplitude lee wave, resulting in very strong winds at the foot of the lee slope. Processes accounting for downslope windstorms are still under active research, although a consensus is developing (Atkinson (1981), Smith (1987)) which states that hydraulic theory, or some derivative of it, can explain all of these phenomena.

2.2 Observations and studies of gap winds in western North America

Some of the earliest studies of strong outflow in British Columbia were conducted by Tyner (1950, 1951a, 1951b), who first used the term "Squamish" in scientific literature to refer to gap winds in Howe Sound. He reported strong outflow through the inlets and valleys along British Columbia's coast frequently coincide with an arctic outbreak. This occurs during winter when an arctic anticyclone builds a cold stable airmass over the interior. The outbreak is often "triggered" by falling pressures on the coast due to the

passage of a cyclone to the south (Tyner, 1950) . In a study of outflow through Portland Inlet during the 1949-1950 winter, Tyner (1950) reported 46 percent of recorded winds were outflow, and 38 percent of these were gale force (greater than 34 knots). He also noted that outflow winds persisted up to 30 km offshore, and usually had a depth of 1000 m although depths as high as 2500 m had been observed (Tyner, 1951a). He reported small pressure ridges at the mouths of the inlets during outflow events and postulated the size of the ridges is related to outflow strength. However no mention is made of how the pressure field is resolved at that scale.

A study of several very intense arctic outbreaks was made by Tyner (1951b). It reported at Abottsford, on January 25 to 26 1950 there were 15 hours of 35 knot outflow winds with a peak gust of 61 knots, with 61 knot winds also observed in Howe Sound. During another outbreak, Abottsford had seven hours of wind in excess of 52 knots and 50 year record minimum temperatures were set all over southern British Columbia (many of which still stand).

A more recent report, Schaeffer (1975), studied wind records for Squamish from 1969 to 1972. It found that outflow winds occur mainly in December and January, often persisting for 3 to 5 days with speeds commonly reaching 35 knots gusting up to 60 knots. Outflow episodes occurred an average of twice a month during December and January.

Patrick (1980), while studying a gap wind event with uniform pressure gradient across the Coast Mountains, examined a visual satellite image which depicted low cloud and fog being pushed offshore by outflow winds. Using this, and a topographic map, he postulated that wide, low elevation valleys allowed easiest flow of air from the interior to the coast. Thus, outflow would occur first in Portland Inlet and Douglas Channel, followed by the Fraser Canyon. As the depth of cold air increased over the interior, Skeena valley, Dean Channel, Burke Channel, Knight Inlet, Bute Inlet, Howe Sound and

	Observed Northeasterly Winds	
	>35 knots	>50 knots
October	5.5%	.05%
November	11.5%	.11%
December	19.6%	1.6%
January	15.1%	2.9%
February	13.1%	.81%
March	4.3%	.20%

Table 2.1: Green Island relative outflow percentages (Beal, 1985)

Harrison Lake would also record strong outflow (see figure 2.1 for locations).

A climatological study of outflow winds (Beal, 1985) at Green Island (located at the mouth of Portland Inlet – figure 2.1) using data from 1909 to 1983 found outflow wind speeds were distributed as shown in table 2.1. Outflow occurs most frequently in December and January, and gale force outflow at these times is common. Peak outflow was measured at 99 knots with higher gusts on January 10 1969. During December 1977 and January 1978, 32 consecutive days of outflow had winds greater than 35 knots.

A mesoscale study of an outflow event through the Fraser Valley, on February 13 1980 (Overland and Walter, 1981), used an instrumented aircraft, 8 meteorological buoys, and four upper air sounding stations in addition to the existing meteorological network, to study gap wind in southern Strait of Georgia and in Juan de Fuca Strait. A core of 30 to 35 knot winds whose border was sharply defined by wind shear and by large temperature and moisture gradients was observed. This was arctic air pouring out of the Fraser River valley. By plotting the arrival time of cold air, it was shown that a narrow core of air moved rapidly from the Fraser River valley through Bellingham to Victoria. The air then spread into the Juan de Fuca Strait and the central Strait of Georgia. The wind velocity in the core of cold air remained constant while the core spread horizontally and vertically

as arctic air "filled up" the southern Strait of Georgia. Winds below 2000 m came from northeast with a maximum speed at 700 m elevation. The outflowing air had a large cross isobaric component, with the pressure gradient acting to increase momentum in the core of strong winds (the jet). Overland and Walter (1981) postulated that an eddy feature at the mouth of Juan de Fuca Strait may have been caused by a hydraulic jump. Another study using the same data (Faulkner, 1980), reported a dry adiabatic lapse rate up to 800 m indicating strong mechanical mixing, and a maximum observed speed of 40 knots.

There have been several cases of outflow winds examined in the Northwestern United States (Cameron (1931), Cameron and Carpenter (1936), Reed (1981), and Mass and Albright (1985)). Reed (1981) examined a strong "bora like" outflow event with wind speeds over 50 knots in Western Washington. The strongest winds flowed through the Stampede Pass and Columbia Gorge which are the least obstructed passages through the Cascade Mountains. He found the strong winds resulted from a large pressure gradient (12 mb per 100 km, or .012 Pa m^{-1}) which existed between a strong anticyclone inland and a deep cyclone offshore. This large pressure gradient was sustained because the mountain barrier separated cold air inland from warm air on the coast. The mountain chain also acted to restrict low level subsidence warming inland, which further increased the temperature contrast. The measured wind speeds were consistent with analytic theory (the Bernoulli equation, discussed later). Reed (1981) calculated that air flowing over higher passes would have lower speeds and would not be cold enough to penetrate the coastal inversion. Although the cause of acceleration was the large pressure gradient, it was enhanced by kinetic energy resulting from the loss of potential energy as the air moved down the slope.

A Central American example of strong outflow winds has been observed in southern Mexico - near the Gulf of Tehuantapec. Hurd (1929) reported observations of strong

northerly winds in a polar outbreak through a topographic gap in the Sierra Madre Mountains. Other examples of the blocking effect of mountains on low level winds occur in Alaska (Schwerdtfeger (1975), Mitchell (1956)).

Macklin, Lackmann and Gray (1988) describe the wind field and force balance outside the topographic gap for two gap wind events in Alaska, using low-level aircraft data as well as routine observations. Gap winds were 750 – 1100 m in depth, and no hydraulic effects were observed. The flow was ageostrophic (down the pressure gradient) in the "jet" but tended toward geotriptic balance (a balance between pressure gradient force, Coriolis force, and friction) beyond one Rossby radius of deformation from the coast. The Rossby radius of deformation gives the e-folding distance for geostrophic adjustment in the vicinity of a barrier (Mass, Albright and Brees (1986), Bannon (1981)), and in the case of flow within a neutrally stratified boundary layer surmounted by an inversion, is defined as:

$$R = \frac{(g'h)^{\frac{1}{2}}}{f} \tag{2.2}$$

where

$$g' = \frac{(\theta_{TOP} - \theta_{BOT})}{\theta_{BOT}} \times g \tag{2.3}$$

is the effective or reduced gravity; h is boundary layer depth; f is the Coriolis parameter; θ_{TOP} is the potential temperature above the inversion; and θ_{BOT} is the potential temperature in the neutral layer below the inversion.

Lackmann and Overland (1989) discuss a gap wind event through the relatively wide Shelikof Strait, Alaska, also using low-level aircraft data. Momentum and equivalent potential temperature budgets found the following:

- temperature and inversion height differences accounted for cross strait pressure gradients.

- along strait winds diverged, however the inversion height increased due to entrainment of air from aloft.

- pressure ridging occurred along the right side of the flow at the end of the strait due to geostrophic adjustment in which the Coriolis force turns wind to the right, resulting in convergence along the right side of the channel. This increases the inversion height and therefore the surface pressure. It can occur if the duration of the flow exceeds the time scale for geostrophic adjustment (10^4 seconds $\sim$ 3 hours).

- a sharp transition occurs at the channel exit when the channel width is less than the Rossby radius.

- pressure gradient force is the largest component of the along channel momentum budget, accounting for 180% of the observed acceleration. Vertical entrainment and surface friction are the retarding forces that equally account for the difference.

- events with large potential temperature changes across the inversion and less shear, show the most acceleration because the effect of entrainment in decelerating the flow is reduced.

- along channel winds were generally in geostrophic balance, which was favoured by the large width of the channel, and its northerly location.

Macklin, Bond and Walker (1990) analysed a gap wind event near Prince William Sound, Alaska, in which the gap wind "jet" flowed over open ocean after it had left the constraining fjord. A 0.2 KPa ridge of high pressure was observed slightly to the right of the jet. The gap wind was relatively constant at 500 m in depth. A momentum budget analysis corroborated previous findings that the pressure gradient force was most important, being opposed by surface friction, and to a lesser extent by entrainment.

These Alaskan aircraft case studies, while very informative, were concerned with the structure and dynamics of gap winds over open ocean, or through the wide Shelikof Strait, which parallels the coast. They did not examine the structure of gap winds within the topographic gap itself. They found that wind acceleration could be explained as a balance between pressure gradient, surface drag, and entrainment, and that geostrophic adjustment of the wind and mass field occurred when the duration of the flow approached 10^4 seconds ($\sim$ 3 hours).
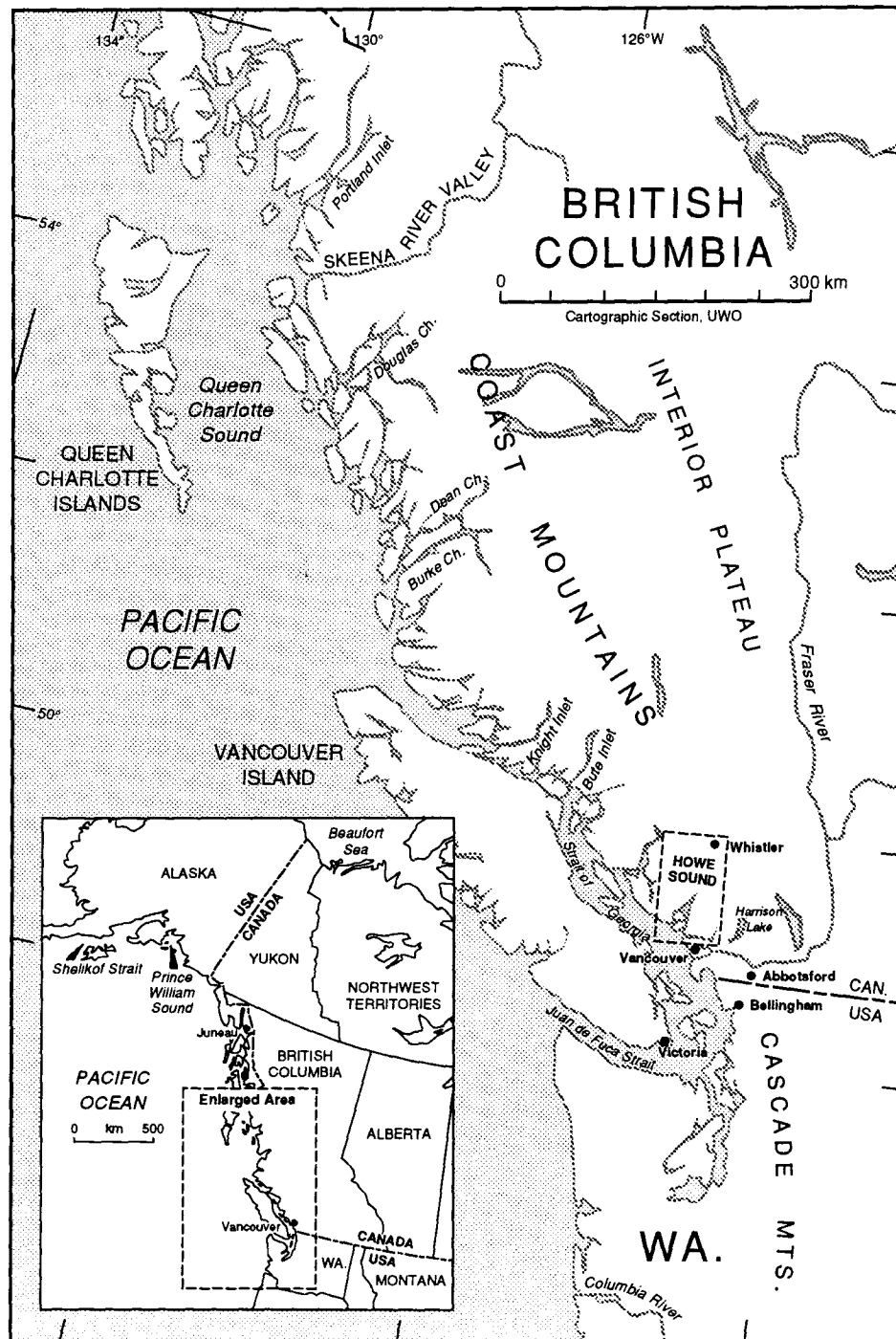
Figure 2.1: Location map of northwestern North America.
Howe Sound region box is enlarged in figure 3.2

2.3 Bora winds

Bora winds have been documented frequently in European scientific literature since the mid-nineteenth century (Yoshino, 1976b). The name "bora" was originally given to the downslope winds of the northeastern Adriatic coast from Croatia to Trieste, Italy. Other downslope winds which have been studied are the bora near Novorossiysk on the Black Sea's northeastern coast, the "mistral" of Mediterranean France (Pettre, 1982), bora-like winds at Novaya Zemlya in the Russian Arctic, and outflow winds in the Salt and Bols fjords of northern Norway; as well as bora-like winds reported near Lake Baykal, Crimean Peninsula, coast of Sea of Okhotsk, Central Sardinia, and Bulgaria (Jurčec (1981), Yoshino (1976b)).

The most intensely observed and studied wind of this type is the bora on the northeastern Adriatic coast. This coastline is topographically somewhat similar to the British Columbian coastline, as a mountain range (the Dinaric Alps) near the coast separates the coastal zone from an elevated inland plateau. One significant difference is the Adriatic coast lacks long, narrow, steep sided fjords which dissect British Columbia's coastline. Bora winds can occur at any time of the year but, as in British Columbia, they are strongest in winter when they are associated with an arctic outbreak (Jurčec, 1981). This occurs when a strong anticyclone lies over eastern Europe, often in conjunction with a cyclonic circulation in the Mediterranean. In this situation, a pressure gradient is directed across the Dinaric Alps and allows arctic air to move across Hungary where the Dinaric Alps partially block the flow. Arctic air then deepens and eventually spills through passes onto the coast (Jurčec (1981), Yoshino (1976b), Smith (1985)).

Of the studies conducted by the Yugoslav and Japanese researchers, only one was based on a specially collected data set (Yoshimura, Nakamura and Yoshino, 1976). The rest of the studies relied on routinely collected data or non- meteorological indicators

such as wind shaped trees (Yoshino et al., 1976).

The following summarizes salient features of bora winds in Croatia:

- strongest winds occur during winter and at night (Jurčec, 1981)

- generally 10 "bora days" occur per month each winter (Yoshino, 1972)

- most bora winds last 12 to 20 hours but can last as long as 10 days (Yoshino, 1969)

- anticyclonic bora winds affect a localized area, but a cyclonic bora has widespread strong winds (Jurčec, 1981)

- bora winds are strongest at coastal stations except for the very highest mountain stations (Yoshimura, 1976)

- wind velocities greater than 30 knots are frequent in winter (Yoshino, 1969)

- the strongest bora wind reported was a gust to 95 knots in February 1929 at Trieste (Yoshino, 1975)

- a stable layer usually exists at mountain top level — 1500 to 2000 m above sea level (Yoshino, 1976a)

- bora wind velocity increases as the stability of the air increases (Yoshimura, Nakamura and Yoshino, 1976)

- maximum bora depths are 2000 to 3000 m (Jurčec, 1981)

- at the onset of strong bora winds, temperatures often rise and then fall (Yoshimura, Nakamura and Yoshino, 1976)

- bora winds are usually cold (Yoshino, 1976a)

- there have been frequent observations of föhn wall clouds, lee wave and rotor clouds over the mountain tops during bora events

Novorssiysk on the Black Sea (Yoshino, 1975), averages 54 bora days per year with winds often reaching 45 knots and occasionally 60 knots. At Salt Fjord Norway, similar winds have been observed, with Mook (1962) noting the wind speed was directly proportional to the pressure gradient. Many known features of British Columbia's outflow winds are similar to those observed in bora-like winds in other parts of the world. Bora-like winds are possible where a mountain range separates two contrasting airmasses. Although bora-like winds are commonly observed, there has been no detailed study of the flow structure or its temporal and spatial variability – in any environment which remotely resembles a British Columbian fjord.

2.4 Theoretical work on severe downslope winds

Theoretical work related to gap winds has studied periodically occurring windstorms in the lee of the Colorado Front Range Mountains. Although a concensus is forming in the literature (Atkinson (1981), Smith (1987)) that various winds which occur downstream from major mountain barriers are all members of the mountain lee wave family and can be described by hydraulic shallow water theory, there are significant differences between gap winds and lee slope windstorms:

- Most observations of lee slope windstorms indicate strong, uniform flow aloft which result in large amplitude stationary lee waves. These lee waves have horizontal wavelengths of 50 to 100 km and propagate vertically until reaching a critical level where breaking occurs. Conversely, outflow wind, is essentially a low level flow. It is forced by large low level horizontal pressure gradients created when a mountain barrier partially blocks cold inland arctic air from reaching the coast. The presence

of large amplitude lee waves accompanying gap wind has not been observed (Mass and Albright, 1985).

- Previous North American west coast gap wind studies, (Overland and Walter (1981), Mass and Albright (1985), and Macklin, Lackmann and Gray (1988)) indicate strong winds persist over relatively long horizontal distances. Strong lee winds observed in Colorado however, have small horizontal length scales which is related to their lee wave forcing.

- Previous lee slope wind studies have considered the flow to be 2-dimensional — the flow of air over an infinitely wide mountain barrier. Conversely, outflow wind is fundamentally 3-dimensional as it originates through mesoscale gaps in mountain barriers and is modulated and controlled by valleys and inlets through which the air flows.

Despite these differences, many controlling factors considered important for lee slope winds are also felt important for outflow. These are: large scale sea level pressure gradients across the mountain barrier, moderate flow normal to the barrier at mountain crest level, and a stable layer near mountain crest level upstream of the barrier. Noting these similarities and differences, a brief review of previous downslope wind studies will be made.

Three mechanisms have been proposed to account for strong lee slope wind development. The first mechanism, based on hydraulic theory, was first proposed by Long (1954), and used by Houghton and Kasahara (1968), Houghton and Isaacson (1968), and Arakawa (1968,1969). The theory proposed by Smith (1985) is similar, except the atmosphere is presumed to have constant stratification rather than layers separated by a density interface. The Smith (1985) work was extended by Smith and Sun (1987) to

incorporate Long's model. The flow of air over a mountain is modelled by fluid flow-
ing over a barrier using shallow water equations. Strong winds occur on the lee slope
when the fluid (air) goes from subcritical flow upstream, to supercritical flow over the
mountain, becoming subcritical again downstream as kinetic energy dissipates in a tur-
bulent hydraulic jump. When applied to the atmosphere, the main weaknesses of this
theory are that it doesn't allow continuous stratification, or vertical propagation of en-
ergy above either the free surface or rigid lid upper boundary condition. However this
theory is attractive because of its simplicity, and its apparent inclusion of important fea-
tures observed in downslope windstorms. Work by Durran (1986), suggests that vertical
propagation of energy plays only a minor role in strong lee slope wind development which
appears to be the case for gap wind, but is a departure from other lee slope wind theories.
A strong inversion typically present over arctic air in an outflow event, resembles the step
change in density represented by water in the shallow water equations, indicating that
this theory may be applicable to gap winds.

The second mechanism thought to account for Colorado downslope windstorms (Klemp
and Lilly, 1975) is the amplification of linear vertically propagating gravity waves, by
waves reflected off the tropopause (or some other layer where the Scorer parameter,
(Scorer, 1949) changes rapidly). The wave amplitude is determined by the superposition
of these upward and downward propagating modes and will depend upon whether or
not the atmosphere is "tuned" to constructive interference. As this theory is linear, its
applicability to large amplitude waves has not been determined (Durran, 1986).

The third mechanism proposed (Clark and Peltier (1977,1984), Peltier and Clark
(1979, 1983)), suggests large amplitude waves and downslope winds occur after a devel-
oping wave breaks. The area of wave breaking creates a critical layer with strong mixing
and wind reversal. This self-induced critical layer traps and reflects upward propagat-
ing waves resulting in resonance and strong surface winds. A comprehensive review of

downslope winds can be found in Durran (1990).

Due to the differences between gap winds produced on the West Coast of North America and lee slope windstorms in Colorado, the applicability of lee slope wind storm theories to outflow wind phenomenon is unknown. In particular, the presence of large amplitude lee waves during outflow events has not been observed. Rather, previous studies, (Overland and Walter (1981), Mass and Albright (1985), and Reed (1981)), have found an approximate ageostrophic balance between pressure gradient and inertia.

2.5 Numerical modelling studies

Most numerical model work has been involved in simulating lee slope windstorms in the Colorado Front Range Mountains, (Clark and Peltier (1977,1984), Peltier and Clark (1979, 1983), Klemp and Lilly (1975, 1978), Lilly and Klemp (1979), Durran (1986), Klemp and Durran (1987), Durran and Klemp (1983, 1987), and others). The subset concerned with modelling outflow-like winds is fairly small.

2.5.1 Numerical modelling of the bora

Klemp and Durran (1987), performed a series of 2-dimensional numerical simulations of the Croatian bora using idealized topography and initial and boundary conditions. They performed a number of sensitivity analyses to determine how well shallow water theory could represent the bora, finding that wave overturning within the cold air was responsible for strong lee slope flow, and that it resembled hydraulic flow produced both by shallow water theory and by their simulations in which wave overturning was suppressed. Klemp and Durran (1987) also found strong lee slope response even when the flow was not initially forced. In one simulation, the model was initialized with cold air on the inland side of the mountains and no wind. Thus, horizontal thermal inhomogeneity created

the pressure gradients which generated the flow. Their results agreed quite well with observations. By comparing the assumed fundamental mechanisms behind severe lee slope winds in the Croatian bora and the Colorado lee slope windstorms, Klemp and Durran (1987) postulate that despite flow differences, the mechanisms producing the strong wind are fundamentally the same. This supports the notion that the essentials, if not the details of severe lee slope winds may be embodied in simple hydraulic theory (despite its simplifications and limitations).

Chapter 3

Observational program

3.1 Introduction

To better understand outflow characteristics in Howe Sound, a field measurement program was mounted from October 1987 until April 1988. Nine surface-based stations were installed. The location of these stations, and those of other agencies, are shown in figure 3.1. Each station recorded hourly values of wind speed and direction and temperature; some stations also recorded surface pressure. Additionally, a series of 18 upper air soundings were made during several outflow events.

The station locations were chosen with the following goals in mind:

- to maximize horizontal flow structure information.

- to sample the entire Howe Sound region, from the mountain pass at Whistler, to the mouth of the fjord.

- to sample the wind across and along the fjord.

- to locate anemometers where they were exposed to outflow winds, and where their measurements were representative of winds in the area.

This last goal was often difficult to attain, given the nature of the terrain. Islands, while being useful anemometer sites, also pose problems by perturbing the flow.

The data averaging time was another factor considered in planning the observational program. If data are averaged over too long a time interval, details of temporal variation

25

will be lost. On the other hand, if data are averaged over a very short time interval practical problems arise: data must be downloaded more frequently and will be voluminous. More frequent data retrieval was not feasible as several of the sites (RAG, DEF, FIN) were inaccessible except by boat, hovercraft or air. As a compromise, an averaging time of one hour was chosen which also matched the observation frequency of other agencies. Since the time scale of a typical gap wind event is a few days, this observing frequency was felt sufficient to resolve important temporal variations. The standard deviation of speed and direction were retained so that not all of the higher frequency wind information was lost.

3.1.1 Geographic Setting

Outflowing air originates on British Columbia's interior plateau northeast of the Coast Mountains. During its path to the coast, relatively dense cold air spills over lower mountain passes and is channelled by valleys. Thus, the topographic setting – width, depth, and roughness of valleys, and elevation of passes – is important in determining outflow characteristics.

Twenty kilometres northwest of Vancouver British Columbia, is a glacial valley which dissects the Coast Mountains (figure 3.1 and 3.2). The "wet" part of the valley is a fjord named Howe Sound. Shaped like a twisted 2-dimensional funnel, the fjord's "cone" (20 km across) opens south-southwestwards onto the Strait of Georgia, and its "tube" (5 km wide) points north-northeast, ending at the town of Squamish. Coast mountains on either side of Howe Sound, rise steeply to 1200 - 2000 m above sea level, over horizontal distances of about 5 km. The funnel "cone" contains many small islands. A perspective representation of Howe Sound's topography underlies the schematic illustration of gap winds in figure 1.1.

Entering the head ("tube") of Howe Sound at the town of Squamish, is the Squamish

River which divides 10 km north of the town. The western fork retains the name "Squamish River", and is in a comparatively broad, low elevation valley. The valley ends abruptly 50 km to the north-northwest without becoming a mountain pass. A tributary of the Squamish River, the Elaho, continues on to the northwest and eventually crosses the Coast Mountains, but at a high elevation of 900 m. The eastern fork, the Cheakamus River, has a valley which is more rugged and at higher elevation in its lower reaches than the Squamish River valley. The Cheakamus valley gradually rises to a significant mountain pass (Whistler) at 640 m elevation, about 50 km north-northeast of the fork. On either side of each of these valleys, mountains of the Coast range rise sharply to elevations in excess of 2200 m.

George Vancouver, who became the first European to visit Howe Sound during his explorations in June 1792 (Vancouver, 1798), described it as follows:

> "Quitting point Atkinson and proceeding up the sound ... we made a rapid progress, by the assistance of a fresh southerly gale, attended with dark gloomy weather that greatly added to the dreary prospect of the surrounding country. The low fertile shores we had been accustomed to see, though lately with some interruption, here no longer existed: their place was now occupied by the base of the stupendous snowy barrier, thinly wooded and rising from the sea abruptly to the clouds; from whose frigid summit, the dissolving snow in foaming torrents rushed down the sides and chasms of its rugged surface, exhibiting altogether a sublime, though gloomy spectacle, which animated nature seemed to have deserted ...

> ...We had scarcely finished our examinations when the wind became excessively boisterous from the southward attended with heavy squalls and torrents of rain.

> ... About nine o'clock (we) landed for the night near the west point of entrance
>
> into the sound, which I distinguished by the name of Howe's Sound in honor
>
> of Admiral Earl Howe."

The Howe Sound/Squamish/Whistler area (hereafter referred to as the Howe Sound region) is the most populated and heavily used fjord in British Columbia. The town of Squamish is a major transportation centre where containers are unloaded from ships for railway transport eastwards. There are two major pulp and paper mills on the western shores of Howe Sound, one at Wood Fibre 7 km southwest of Squamish, and the other at Port Mellon further south (figure 3.2). As a consequence, tugboats towing log booms are common. The waters of Howe Sound are used extensively for recreation, by boaters, windsurfers, scuba divers, and commercial and recreational fishermen. The mountains, especially along eastern Howe Sound and near the Cheakamus valley, contain many parks and recreational areas used extensively all year by hikers and campers from nearby Vancouver. Whistler and Blackcomb mountains at the town of Whistler (figure 3.2), are world renowned ski facilities.

Although outflow winds occur through most valleys dissecting the coastal mountain chain of western North America, the Howe Sound region was chosen for this detailed study because:

- gap winds occur with a fairly high frequency and strength.

- anemometers can be placed where they are well exposed and fairly representative of wind in the surrounding area.

- it is accessible for instrument deployment and maintenance, and downloading of data as well as for vertical profile sampling.

- Howe Sound is relatively heavily used and populated, increasing the usefulness of this study.

- it is fairly typical of other British Columbia fjords facilitating possible extrapolation of results.

- several surface weather stations are already in place and supplement data from those deployed for this study.

The main disadvantage in using the Howe Sound region is that the frequency and strength of outflow events are reduced in comparison to northern fjords.
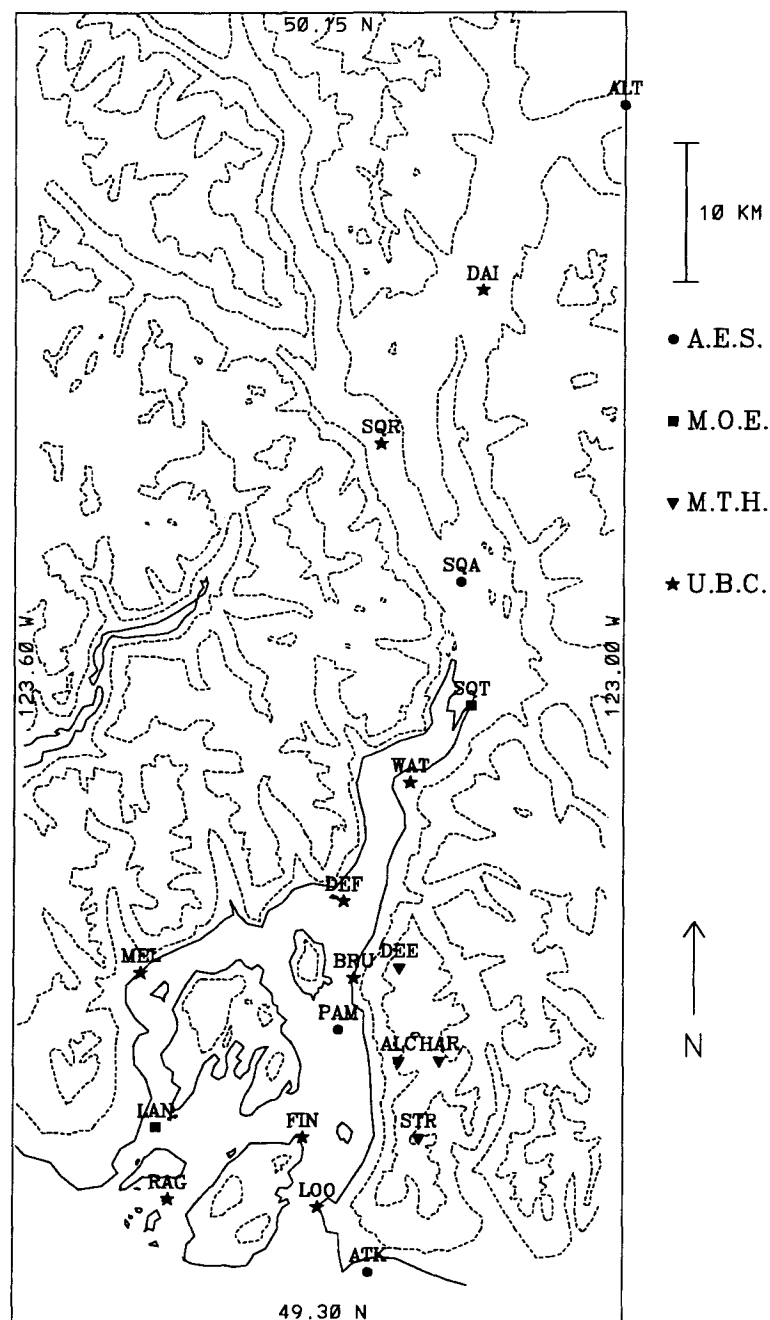
Figure 3.1: Topography of Howe-Sound region, showing meteorological stations used in the study. Solid contour is the coastline. Dashed contours are at 300, 900 and 1800 m elevation. Abbreviations can be found in the Glossary.
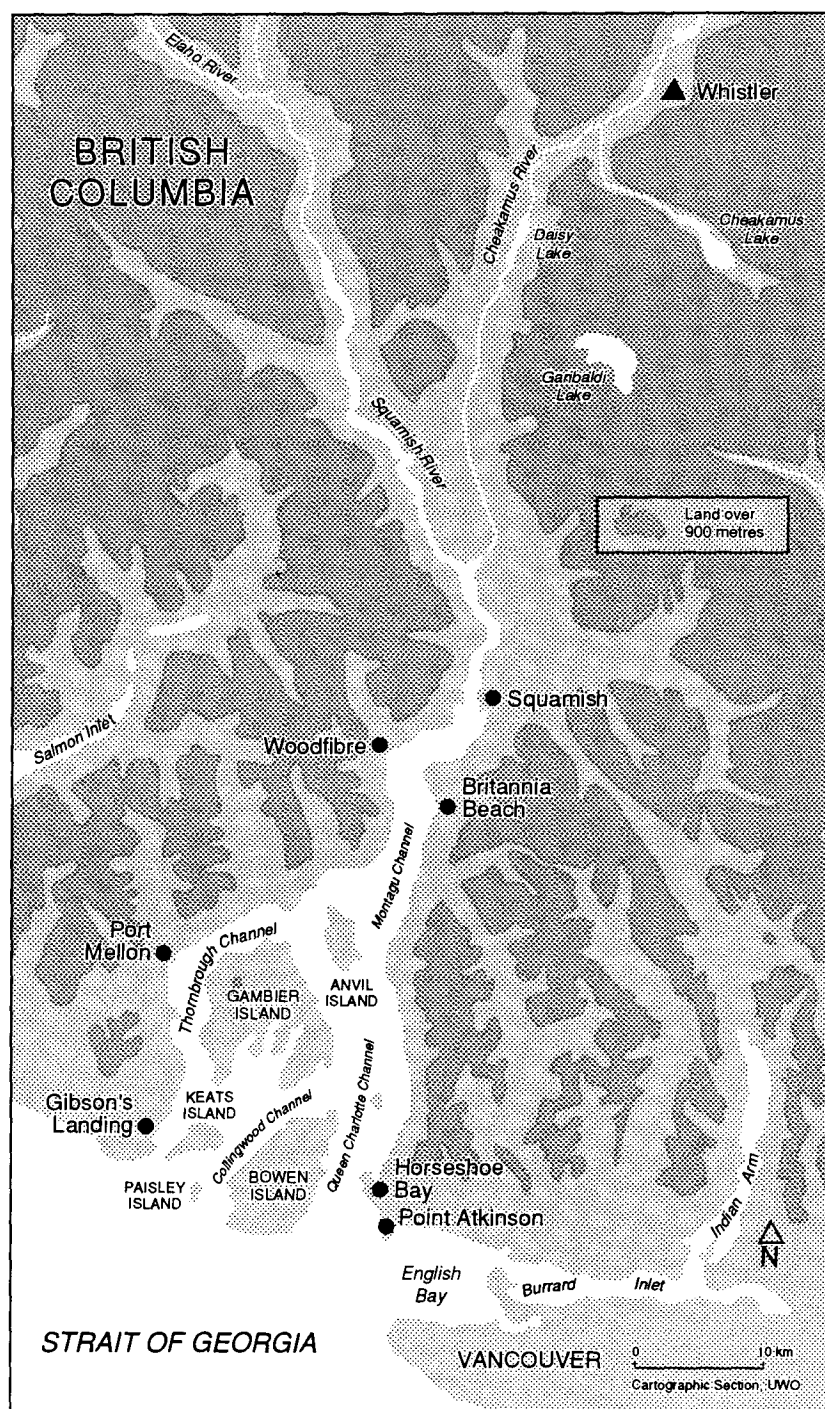
Figure 3.2: Location map of Howe-Sound region.

3.2 Surface observations

Surface observations were made at the stations shown in figure 3.1 during the course of the field program. Table 3.2 lists the types of measurements recorded at each station. University of British Columbia (UBC) and B. C. Ministry of the Environment (MOE) data were one hour averages (except pressure which was instantaneous). Atmospheric Environment Service (AES) and B. C. Ministry of Transportation and Highways (MTH) data were recorded each hour, but averaged over a shorter time. Wind measurements at most stations were made at 10 m above ground level, except where indicated below. To obtain representative wind measurements, sites were selected where the influence of near field surface roughness elements (trees, rocks, hills etc.) was minimized. However, this was not always possible.

The surface data were from four agencies:

- AES — provided data from Alta Lake (ALT), Squamish Airport (SQA), Pam Rocks (PAM) and Point Atkinson (ATK). ALT and SQA are staffed 13 hours daily. PAM is an automatic buoy transmitting 24 hourly observations daily. During this field program, PAM data were intermittent. ALT, SQA and PAM gave hourly observations of wind, temperature, dew-point temperature, surface pressure, visibility, cloud and weather. ATK, a Canadian Coast Guard manned lighthouse, provided wind observations every three hours. It is closed for the 01:00 PST observation time (09:00 UTC). Wind sensors at ALT, SQA and ATK are mounted at 10 m above ground level. PAM's wind sensor is about 1.5 m above sea level. The wind data from these stations are a two minute average ending at the observation time. The largest wind speed variation greater than 5 knots above the average, for the period ten minutes prior to the observation time, is reported as a gust speed.

station		agency	elevation	W	T	T_D	P	comments
				\# obs. / day				
Alta L.	(ALT)	AES	658 m	13	13	13	24	closed at night
Squamish A.	(SQA)	AES	52 m	13	13	13	13	heavy trees
Pam Rocks	(PAM)	AES	0 m	24	24	24	24	buoy
Pt. Atkinson	(ATK)	AES	9 m	7	—	—	—	3 hourly
Squamish Town	(SQT)	MOE	3 m	24	24	—	24	roof of bldg.
Langdale	(LAN)	MOE	12 m	24	24	—	24	Ferry gantry
Deeks Peak	(DEE)	MTH	1280 m	24	24	—	—	
Mt. Harvey	(HAR)	MTH	1560 m	24	24	—	—	
Mt. Strachan	(STR)	MTH	1420 m	24	24	—	—	
Alberta Cr.	(ALB)	MTH	670 m	24	24	—	—	
Daisy L.	(DAI)	UBC	380 m	24	24	—	—	on dam
Squamish R.	(SQR)	UBC	34 m	24	24	—	24	in swamp
Watts Pt.	(WAT)	UBC	260 m	24	24	—	—	on μwave tower
Defence I.	(DEF)	UBC	3 m	24	24	—	—	
Brunswick Pt.	(BRU)	UBC	18 m	24	24	—	—	side of slope
Port Mellon	(MEL)	UBC	3 m	24	24	—	24	
Finisterre I.	(FIN)	UBC	21 m	24	24	—	—	
Lookout Pt.	(LOO)	UBC	4.6 m	24	24	—	24	
Ragged I.	(RAG)	UBC	12 m	24	24	—	—	

Table 3.1: Summary of surface station data during field season, October 1987 to April 1988. See glossary for abbreviations.

- MOE — provided Hourly averaged wind and temperature data for automatic stations at Squamish townsite (SQT) and Langdale (LAN). The SQT wind observations are taken from a 5 m mast mounted on a 2 story provincial government building in the town of Squamish. The anemometer height is about 15 m above ground. The LAN wind observations are from a 13.7 m mast mounted on top of a 12 m gantry at the B.C. Ferry terminal, for a total instrument height of 25.7 m ASL. The wind data are one hour averages.

- MTH — provided data for Deeks Peak (DEE), Mount Harvey (HAR), Mount Strachan (STR) and Alberta Creek (ALB), located on ridges along the east shore of Howe Sound. All are automatic stations with hourly averaged observations of wind and temperature at 10 m AGL.

- UBC — installed nine stations for the purposes of this study: Daisy Lake (DAI), Squamish River (SQR), Watts Point (WAT), Defence Island (DEF), Brunswick Point (BRU), Port Mellon (MEL), Finisterre Island (FIN), Lookout Point (LOO), and Ragged Island (RAG). All wind measurements, except LOO and WAT were at 10 m AGL. The LOO station used a 6 m mast. The WAT wind sensor was mounted at 15 m AGL on a pole extending 1.8 m from the side of a B.C. Telephone Company Microwave tower. The DAI 10 m mast was mounted at the base of the Daisy Lake Dam. Thus the total instrument elevation above the dam was 6.75 m. All wind data are one hour averages.

3.2.1 Summary of surface wind data

The wind data for the period of the field program are summarized by wind rose diagrams, in figure 3.3. These diagrams are representations of the frequency of wind occurrence by direction, in various wind speed classes. Frequency is the radial coordinate in 10% increments. The "arms" of the rose point in the direction from which the wind is coming. The speed class is indicated by the thickness of the "arm" — increasing thickness means higher speed. Speed classes are in increments of 2 m s^{-1} from 0 to 20 m s^{-1}. It should be emphasized these are not long-term wind roses, but the results of just one winter season. The exception is Mount Strachan which is a summary of wind data from the winters of 1985/86 and 1986/87, and does not include the field season.

Several interesting features can be noted from the wind roses. In Squamish and

Cheakamus river valleys, north of Howe Sound, surface winds are frequently light and mostly bidirectional. This bidirectionality is a consequence of topographic channelling. Light winds are partially a consequence of greater surface roughness when compared with surface roughness over the sea to the south. Near Squamish, topographically induced bidirectionality is again apparent. Here, the frequency of stronger winds, particularly from the northern to eastern quadrants, is much greater. This indicates the importance of gap wind events in the winter time wind climatology (at least for this year). Bidirectionality is less apparent at Defence Island, as the fjord widens so that topographic channelling is decreased. The wind roses from stations in western Howe Sound, Port Mellon and Langdale, show bidirectionality and a high frequency of northerly light winds. Both of these wind roses also show a large frequency of light northwesterly winds, due to katabatic drainage flow down the western slopes of Howe Sound. The Pam Rocks and Finisterre Island wind roses, show bidirectionality and a high frequency of strong northerly winds indicating the relative importance of gap winds here. The wind rose for Ragged Island, in the less topographically constrained southern end (mouth) of Howe Sound, is not bidirectional, but shows a high frequency of northeasterly winds. Mount Strachan on a mountain ridge along the eastern side of Howe Sound and above the topographic channelling, has a wind rose showing frequent strong easterly winds, as does Point Atkinson which is "around the corner" from the mouth of Howe Sound.
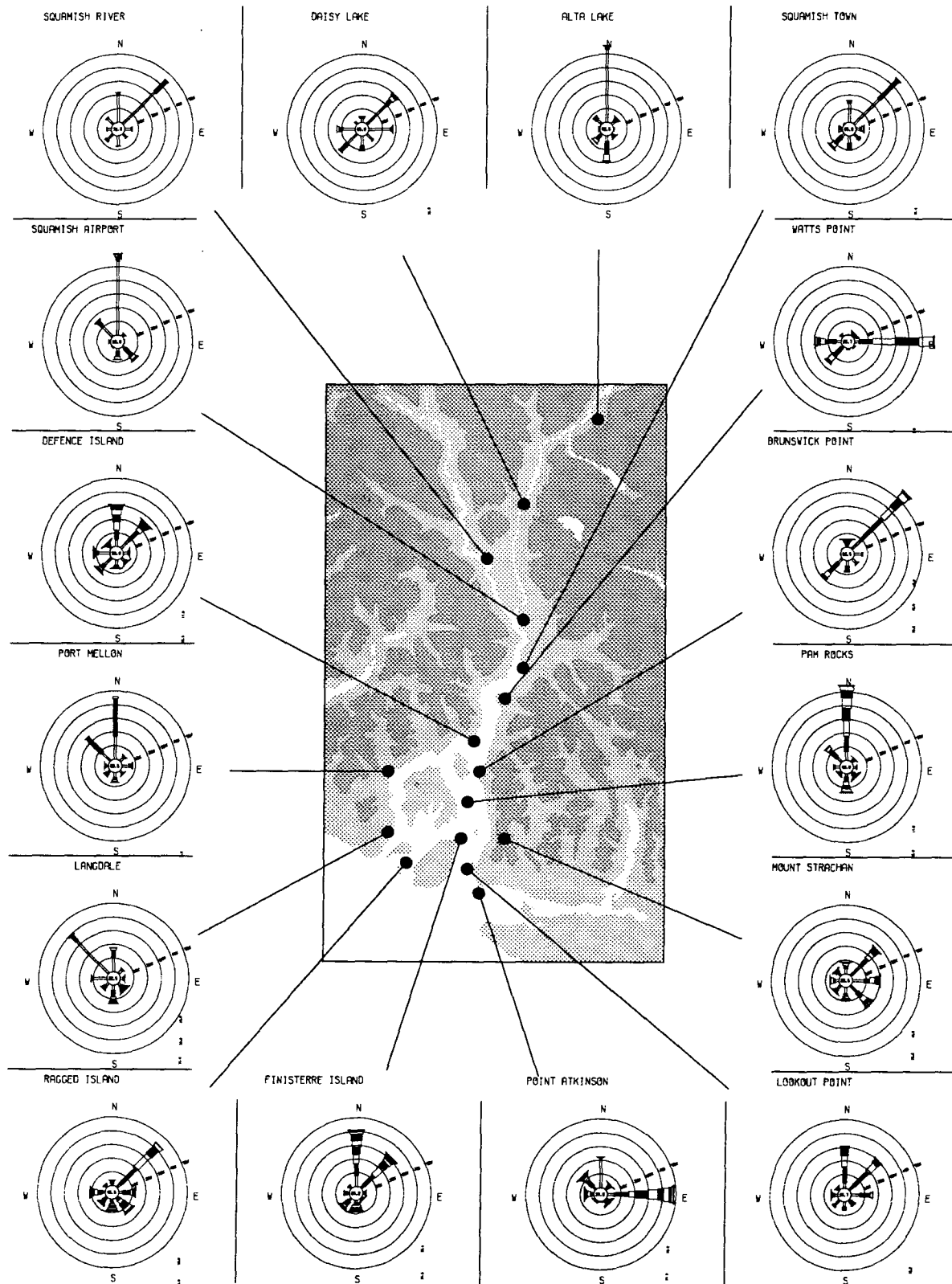
Figure 3.3: Wind rose diagrams for October 1987 until April 1988. Concentric rings are frequency in 10 % increments.

3.3 Vertical profiles

While the surface network described in the previous chapter gave a reasonable picture of the horizontal details of surface wind flow, it said nothing about the vertical structure of wind and temperature. Consequently, during gap wind events, vertical soundings of wind, temperature and moisture were made from the Squamish River delta at the head of Howe Sound, just south of the town of Squamish (figure 3.2). This was accomplished using an AIRsonde™ system which consisted of the following components:

- a helium balloon which carried the instrument package aloft.

- an AIRsonde™ instrument package which included: an electronic aneroid barometer, a "dry" thermistor, a "wet" thermistor (for dry- and wet- bulb temperature), and a radio transmitter to send this information to the ground station. These instruments were contained in a styrofoam case shaped like a propeller. The whole package rotated as it ascended, ventilating the temperature sensors located at the ends of the propeller "blades".

- the AIRsonde™ ground station which received and decoded the radio signal from the AIRsonde™, placing the data on cassette tape.

- the meteorological theodolite used to visually track the balloon and instrument package.

In total, eighteen AIRsonde™ flights were made during four gap wind events. The date of each flight superimposed on a plot of the down-channel component of the maximum daily wind at Watts Point (WAT) shown in figure 3.4, indicates that most of the significant gap wind events were sampled.

The altitude of AIRsonde™ observations was determined by converting the pressure measured by the barometer, to a height using the hydrostatic equation. The mean

horizontal wind between two levels was found by locating the balloon at two times, subtracting the two horizontal locations to find a distance, and then dividing by the time interval to find the velocity. The balloon location was found by combining the elevation and azimuth angles from a theodolite with the balloon elevation from the on-board barometer. The expected accuracy of theodolite derived wind velocity, ΔU, is equal to the square root of 2 times the error in horizontal location divided by the observing time interval:

$$\Delta U = \sqrt{2}\frac{\Delta X}{\Delta T} \tag{3.1}$$

ΔX can be found as a function of the balloon elevation angle, θ, the balloon altitude, H, and the error in estimating the balloon elevation angle, $\Delta\theta$, by simple trignometry as:

$$\Delta X = \frac{H\tan\Delta\theta}{\sin^2\theta} \tag{3.2}$$

This results in the following expression for the expected error in theodolite / barometer derived wind speed measurements:

$$\Delta U = \frac{\sqrt{2}}{\Delta T}\frac{H\tan\Delta\theta}{\sin^2\theta} \tag{3.3}$$

Since the balloon is carried downwind from the theodolite location, errors in theodolite azimuth angle do not contribute significantly to computed wind velocity errors and were left out of the error analysis. For values of H below 2000 m, using typical values of θ (30°) and a pessimistic $\Delta\theta$ of .5° (the smallest resolvable angle increment on the theodolite used was .1°) the maximum estimated wind velocity error is 2.5 m s^{-1}. If a more optimistic $\Delta\theta$ value of .2° is used, the maximum wind velocity error below 2000 m is 1.0 m s^{-1}.

3.3.1 Summary of vertical profile data

Composite vertical profiles of wind and potential temperature (θ) from the three cases represented by groups of solid triangles in figure 3.4 are shown in figures 3.5, 3.6, and
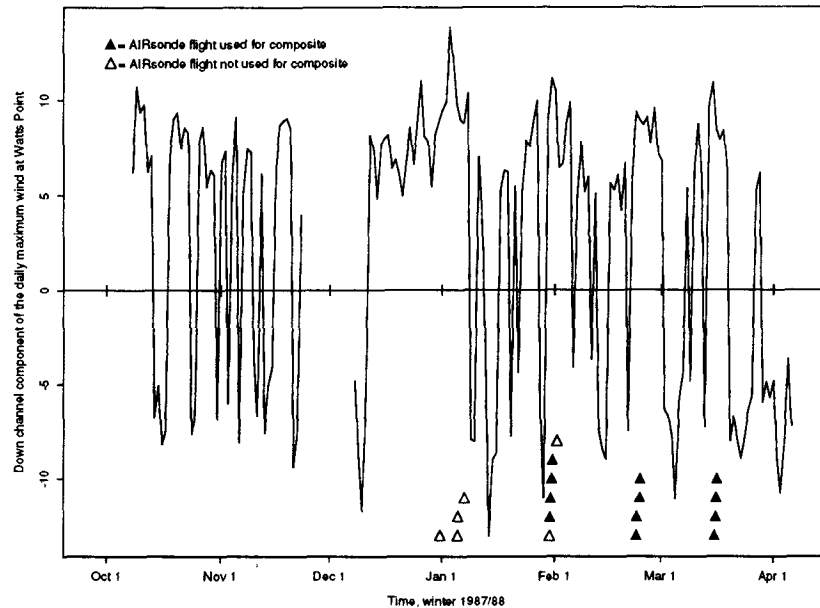
Figure 3.4: Down channel component of the Daily maximum wind at Watts Point (WAT) and AIRsonde flights during the field season. Times of AIRsonde flights are indicated by triangles. AIRsonde flights represented by solid triangles are included in composite profiles.

3.7. In each of these figures, four profiles of θ are plotted, and 500 m layer mean u and v wind components averaged over all four flights are shown. The dashed crosses indicate $\pm$ 1 standard deviation from the mean wind. The wind representation is a hodograph: the wind at the indicated level "blows" from the centre of the hodograph to the plotted point.

All three composite hodographs show a northeasterly wind maximum below 1250 m, winds decreasing above this level, and usually increasing again above 2250 m but from another direction. Case 1, January 30-31, (figure 3.5) is examined in more detail through the rest of the thesis. This hodograph shows peak northeasterly winds in the 500 – 1000 m layer (labelled 750 in figure 3.5a) which decrease to near zero, and then increase and become northwesterly above 2250 m. A similar pattern is shown in the

hodograph for case 2, February 23 – 24 (figure 3.6a), except that winds above 1750 m become light southeasterly. The case 3, March 15 – 16 (figure 3.7), hodograph also shows relatively strong northeasterly winds below 1750 m which increase above 2250 m, from a northeasterly direction.

The composite potential temperature profiles all show evidence of a neutral or less stable layer below 1000 m, and indicate another neutral or less stable layer between about 1200 and 2200 m. The neutral layer below 1000 m is mechanically well mixed, whereas the top of the elevated less stable layer indicates the upper boundary of the outflowing cold air from the interior. This is confirmed by the hodographs. The strongest outflowing winds in each case are located below about 1000 m, and the winds below about 2200 m are distinct from those above, having different directions and speeds. The separation of the two near neutral or less stable layers seems to be due to nocturnal radiational cooling of the surface, the effects of which are mixed by mechanical turbulence only into the lowest 1000 m. This separation is much less distinct in the afternoon soundings (see figures 3.5b and 3.7b), where surface radiational cooling is offset by solar radiation which heats the surface resulting in thermal / mechanical mixing penetrating the full depth of the outflowing air.

The potential temperature profile for case 1 (figure 3.5b) shows a lower, nearly neutrally stratified layer (below about 1000 m) which cools with time. This diurnal cooling is due to nocturnal radiant energy losses at the surface, but could also be attributed to increased advection of cold air from the interior source region, or katabatic drainage down the fjord sides (which is also driven by nocturnal radiational cooling of the surface). The lower layer is surmounted by a stable layer which underlies another less stable layer extending to about 2500 m. The upper and lower near neutral layers are almost indistinct in the late afternoon sounding. The vertical profiles of potential temperature for case 2 (figure 3.6b), show very little change over time. Since all soundings were made

in the early morning (eliminating diurnal effects), little change in cold air advection is indicated. The potential temperature profiles indicate a layer of relatively low stability below 800 m, and another between 1200 and 2000 m. These would be connected by convective thermal mixing in the afternoon to form one deep layer. The case 3 potential temperature profiles (figure 3.7b) show an initially neutral layer below 2600 m in the late afternoon. Overnight the bottom of this layer cools while the upper part warms, and it decreases in height to about 2000 m, with a distinct layer below 1000 m forming. The diurnal behaviour is similar to that observed in the case 1 vertical profiles (figure 3.5). This confirms the hypothesis that two less stable layers observed on most profiles become one during daytime due to convective mixing from instability caused by solar radiation absorbed by the surface, and are separated again at night due to surface radiant energy losses which cool the layer below 1000 m.

a)
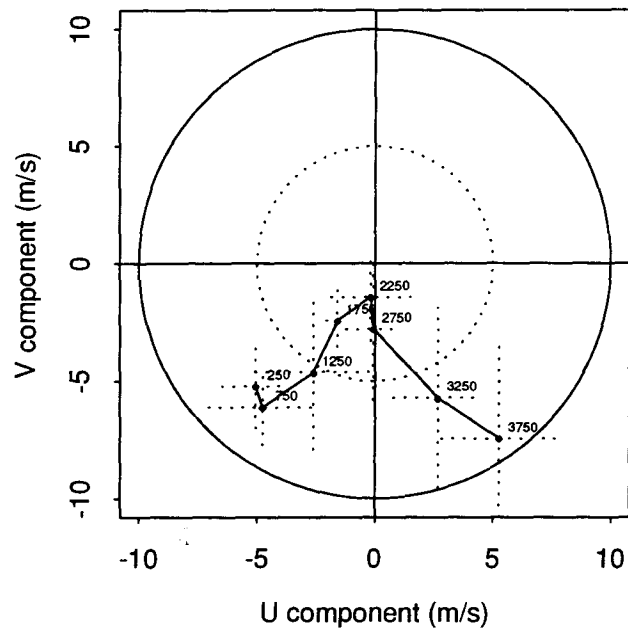
b)
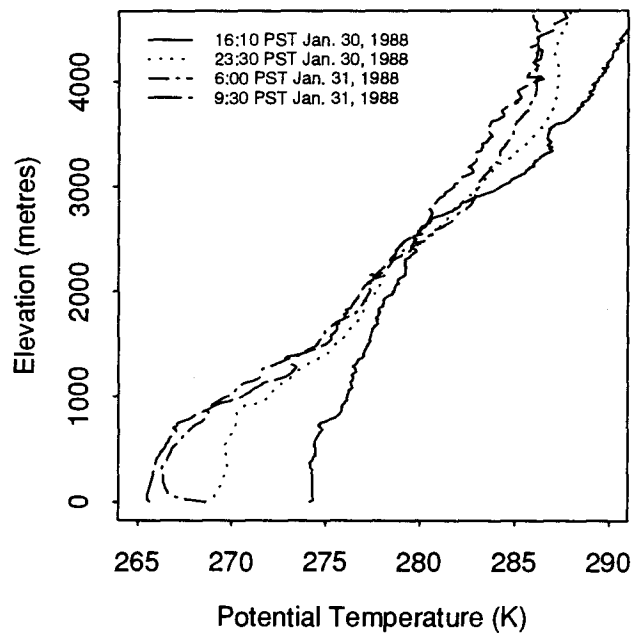
Figure 3.5: Composite of AIRsonde observed profiles of a) wind, and b) potential temperature at Squamish town for case 1 (January). Winds are 500 m averages. Flight times are: January 30 1988 16:10 and 23:30 PST; and January 31 1988 6:00 and 9:30 PST. The dashed crosses indicate ±1 standard deviation from the mean wind.

a)
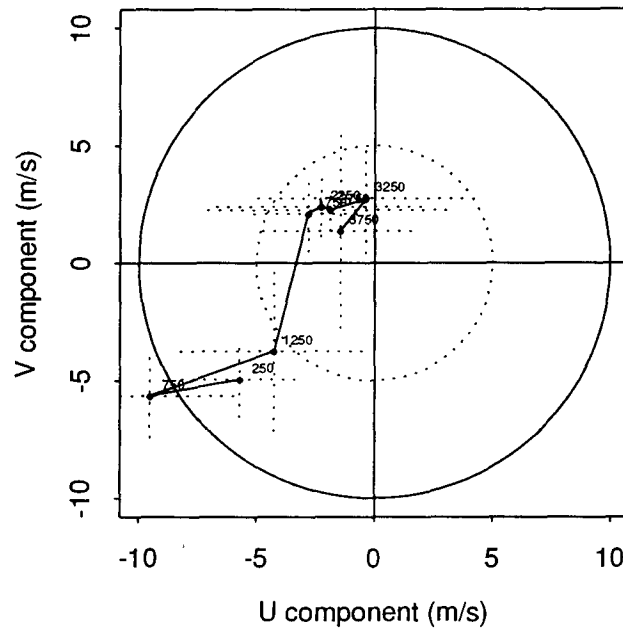
b)
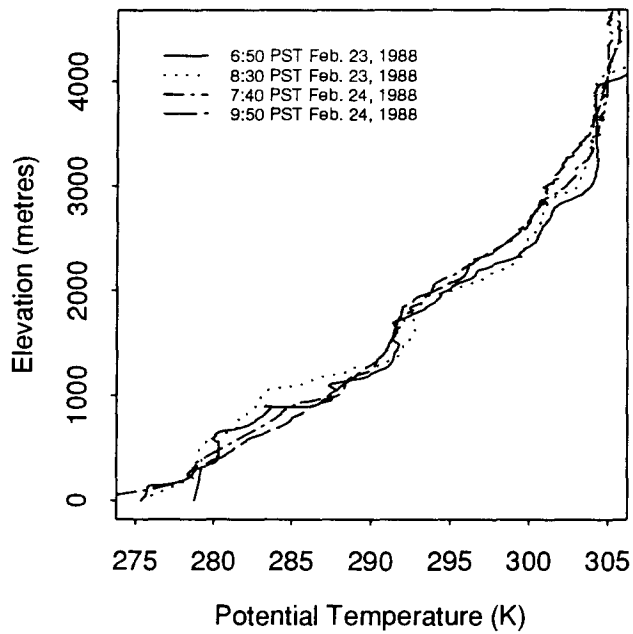
Figure 3.6: Composite of AIRsonde observed profiles of a) wind, and b) potential temperature at Squamish town for case 2 (February). Winds are 500 m averages. Flight times are: February 23 1988 6:50 and 8:30 PST; and February 24 1988 7:40 and 9:50 PST. The dashed crosses indicate ±1 standard deviation from the mean wind.

a)
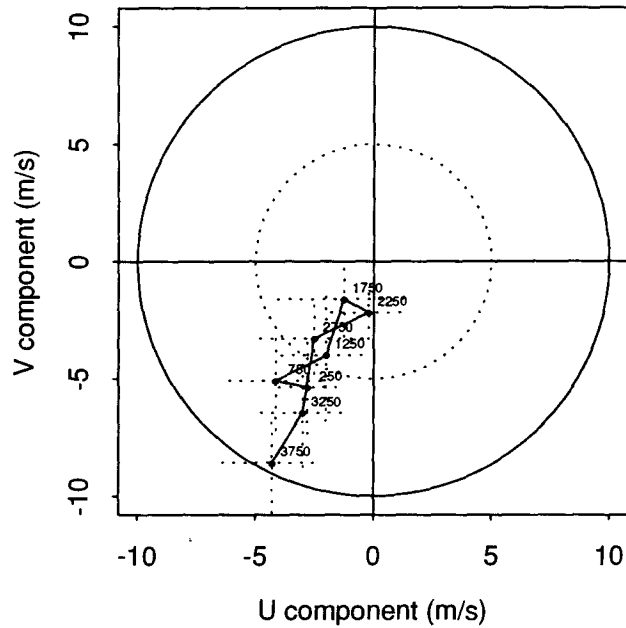
b)
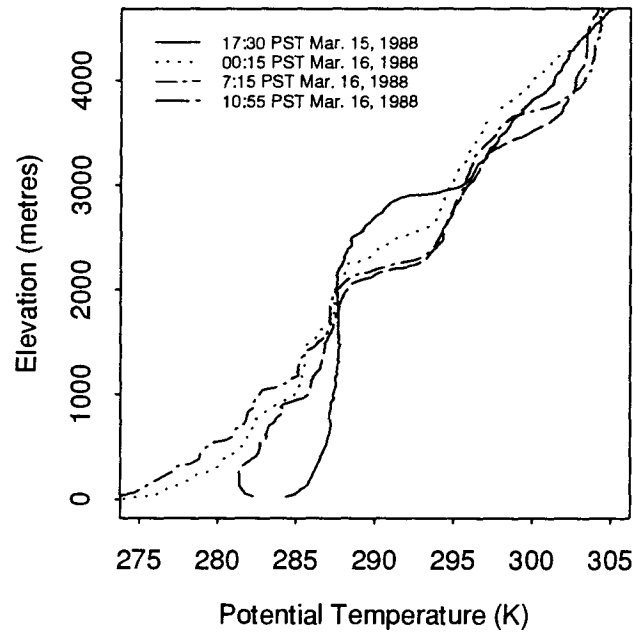
Figure 3.7: Composite of AIRsonde observed profiles of a) wind, and b) potential temperature at Squamish town for case 3 (March). Winds are 500 m averages. Flight times are: March 15 1988 17:30 PST; and March 31 1988 0:15, 7:15 and 10:55 PST. The dashed crosses indicate ±1 standard deviation from the mean wind.

3.4 Synoptic observations for the case studied

The two previous sections described and summarized mesoscale surface and AIRsonde™ observations made during the course of the field program. Synoptic scale features form the meteorological backdrop in which mesoscale outflow winds develop. This section will describe the synoptic scale observations for the event studied in detail in the rest of the thesis — January 30 to February 2, 1988. Detailed mesoscale observations for this event are described in chapter 5 where they are compared to numerical model results.

3.4.1 Synoptic scale features

The synoptic setting for January 30 to February 2 is typical of moderate gap wind events along the west coast of North America. A ridge at 50 kPa (figures 3.8a – 3.10a) builds offshore, increasing its amplitude, while a deep 50 kPa trough in the interior intensifies. This configuration aloft results in north to northeasterly airflow and cold air advection over the coastal zone. Associated with this pattern aloft, a large area of surface high pressure forms to the east of the upper level ridge over Alaska, Yukon and Northern British Columbia (figure 3.8b). Surface radiational cooling in this high pressure zone helps to further decrease the temperature, increasing the air density and surface pressure. As the upper level ridge (figures 3.8a to 3.10a) increases in amplitude to the north and moves eastward, the surface high pressure zone moves southward in the interior of British Columbia (figures 3.8b to 3.10b). Cold low level air associated with the surface high pressure area is partially trapped over the interior plateau by the Coast Mountains, allowing the large surface pressure gradient (figure 3.10b) to form across the Coast Mountains. An arctic front located in a surface trough of low pressure separates the leading edge of cold arctic air associated with the area of high surface pressure, from the warmer air which it is displacing. The passage of this front marks the onset of outflow

wind through the fjords dissecting the Coast Mountains.

In a study of a much stronger outflow wind episode, Jackson (1993) found an initially similar synoptic scale setting. However in that case, a 50 kPa low like that seen in figure 3.8a, continued to deepen and move south of Vancouver Island, placing the region in northeasterly flow aloft, resulting in much stronger gap winds. In the present case, the upper level low propagated to the east (rather than southwards down the coast), hence significant northeasterly flow aloft never developed over the coastal zone, and the gap wind strength through the fjords was less.

a)
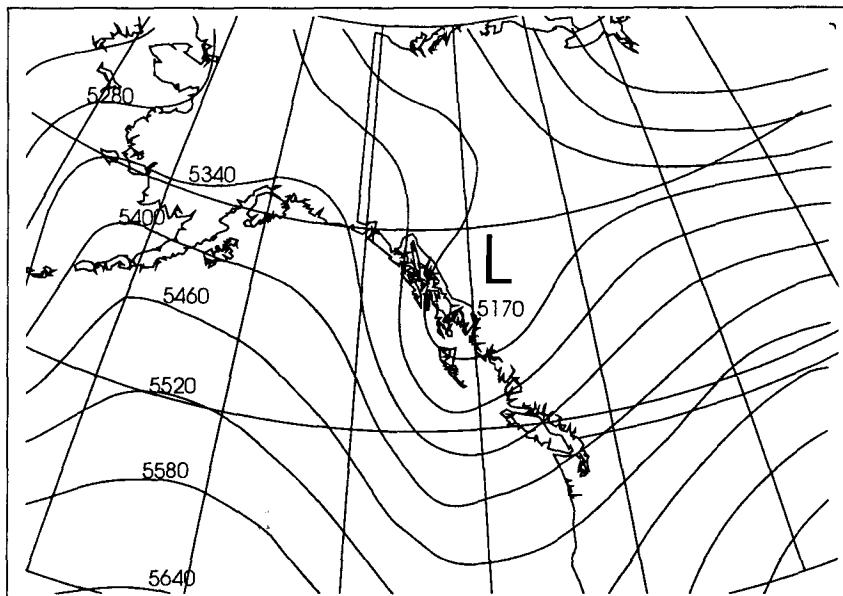
b)
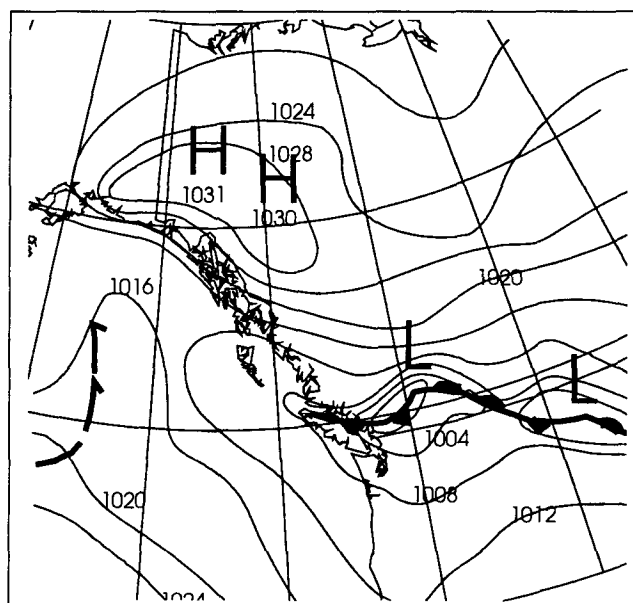
Figure 3.8: a) 50 kPa chart for January 29, 1988 04:00 PST. b) Sea level pressure chart for January 29, 1988 10:00 PST. For a), heights are in metres. For b) pressure is in millibars (1 mb = .1 kPa).

a)
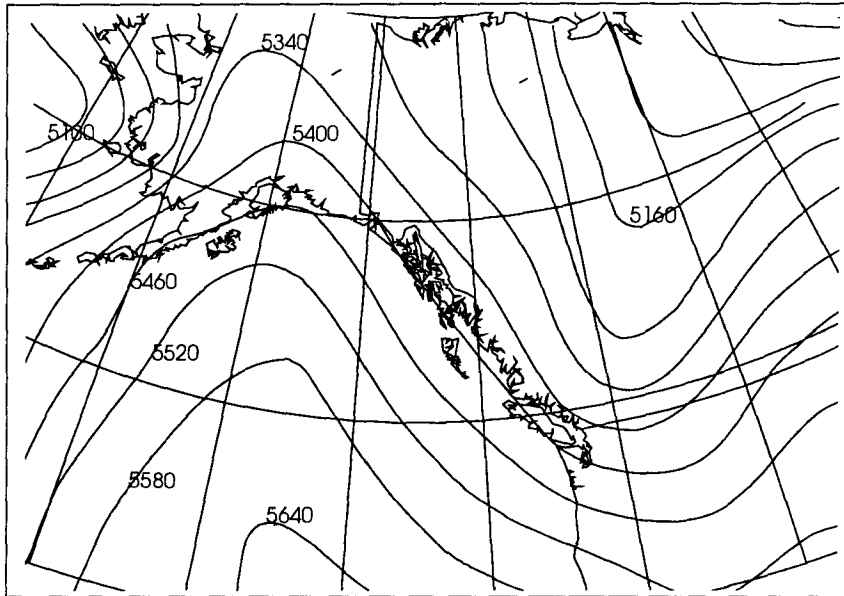
b)
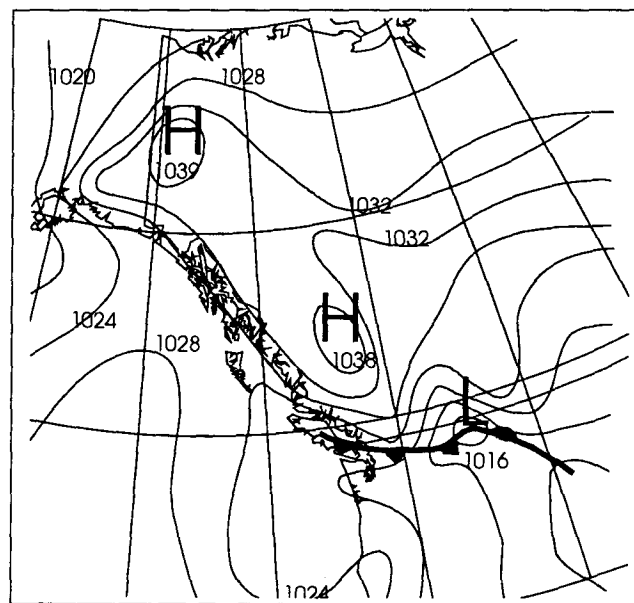
Figure 3.9: a) 50 kPa chart for January 30, 1988 04:00 PST. b) Sea level pressure chart for January 30, 1988 10:00 PST. For a), heights are in metres. For b) pressure is in millibars (1 mb = .1 kPa).

a)
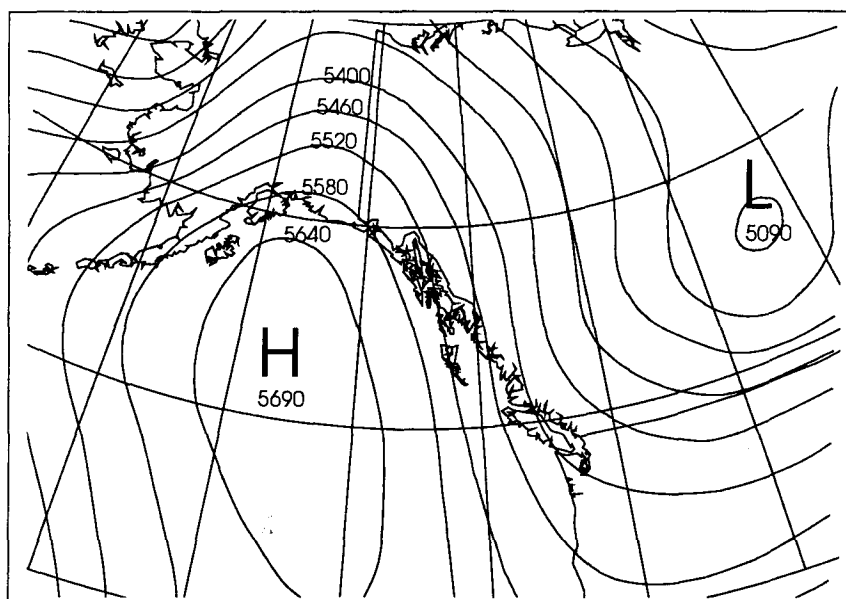
b)
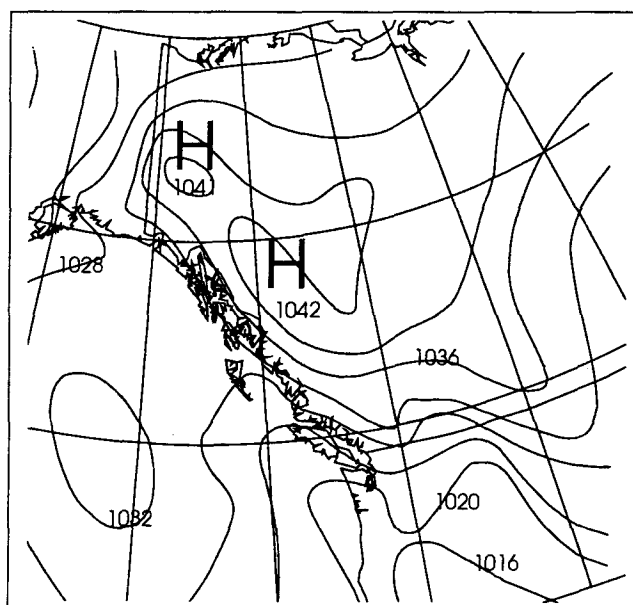
Figure 3.10: a) 50 kPa chart for January 31, 1988 04:00 PST. b) Sea level pressure chart for January 31, 1988 10:00 PST. For a), heights are in metres. For b) pressure is in millibars (1 mb = .1 kPa).

3.5 Summary of observational program

The observational program, comprising continuously recorded hourly surface observations at several stations, and vertical profiles at select times during gap wind events, was able to help answer only some of the important questions about gap winds sought in this work. This is discussed further in chapter 5 in relation to model validation. The field program itself however was a qualified success. There were very little data lost from the surface network, and nearly all of the gap wind events during the program were sampled with AIRsondes™. The wind and temperature data seemed reliable, however the barometric data from the stations with electronic aneroid barometers appeared unreliable. AIRsonde™ wind measurements made by visually tracking the balloon were prone to error, and difficult to make at night.

There were no strong gap wind events during the field season, so that a moderate event was chosen for analysis and modelling. The spatial resolution of data, as well as the temporal resolution of vertical data made analysis of detailed flow structure (for example hydraulic effects discussed later) impossible. There were not enough gap wind events sampled to be able to use observations to answer questions about interactions between the flow and external boundary conditions. However, despite these difficulties, the observations provide the most detailed analysis to date of gap winds in Howe Sound, and are very useful for model validation.

Chapter 4

Numerical modelling: RAMS strategy and configuration

4.1 Introduction

Environmental fluid dynamics are inherently non-linear. As such the only way of re-
alistically modelling detailed environmental flows (except in a few idealized cases), is
with a numerical model (or possibly a physical scale model). Such a model consists of
a set of differential equations – the Navier Stokes equations (or close approximations to
them), which due to their non-linearity, must be solved numerically. This can be done by
defining variables on a rectangular grid (in one, two or three dimensions), using variables
at neighbouring space locations to give spatial derivatives, and using variables at neigh-
bouring time locations to give temporal derivatives allowing the system to be stepped
forward in time.

Using a 3-dimensional numerical model to examine detailed flow structure can be
extremely informative, since vertical and horizontal model resolution is typically much
greater than that of an observational network. In this study, the application of a 3-
dimensional mesoscale numerical model provides detailed information about gap wind.
This information would otherwise be impossible to obtain without the prohibitively ex-
pensive use of aircraft. Model output, because it represents a dynamically balanced
realization of the flow in which all the important terms of the primitive equations are
defined, allows important forces to be diagnosed by reconstructing terms in the primi-
tive equations. Because a numerical model represents nature by a computer code, it is

possible to perform numerical "experiments" with it, which cannot be done in nature. These experiments, or sensitivity tests, can be performed by varying initial and boundary conditions and noting changes in the flow which ensue. Because of computational constraints, this was not done with the full 3-dimensional numerical model in the present study. Rather, a simpler model was used for sensitivity experiments, which are described in chapter 7.

Models can give useful information, but they must first be validated by comparison with observations, or possibly with an analytic solution to an ideal linearized case. Conclusions based on poor modelling results are dubious. A model may not produce a realistic simulation for several reasons:

- incomplete or inaccurate parameterization of sub grid scale effects

- errors or inadequacies in the numerical schemes used in the model to solve the spatial and temporal differential equations

- coding errors in the model

- user errors resulting from incorrect application of the model

- incorrectly specified boundary or initial conditions

- non-optimal choices of model parameters and options

To validate the model, the episode (described in section 3.4) for which surface and AIRsonde™ observations are available was chosen for simulation. This is the first time a mesoscale numerical model, incorporating actual topography and observations as initial and boundary conditions, has been applied to this class of atmospheric flow. Technical obstacles, stemming from the large range of atmospheric and topographic horizontal length scales which are important for gap winds, make realistic simulations difficult.

Gap winds are mesoscale phenomena since they occur through, and are enclosed by, narrow gaps in mountain barriers. Evidence from numerical and analytical modelling (chapters 5 and 7) indicates that internal structure of gap flow is governed by small scale hydraulics which are intimately linked to small scale topography. However, gap winds occur because the fjords are relatively long, providing a path for air to flow through a much larger scale mountain range. The atmospheric precursors (boundary conditions) to a gap wind event, occur at synoptic scales in the atmosphere – scales of hundreds to thousands of kilometres. Thus there are three horizontal scales of importance:

- valley width of order 1-10 km

- valley length (mountain width) of order 100 km

- synoptic scale atmospheric boundary conditions of order 1000 km

This range of scales presents a problem for a numerical model. To resolve small scale features of the flow, grid spacing (distance between adjacent nodes in the model grid) must be small. To contain and model the atmospheric, and to a lesser extent topographic, boundary conditions of the flow, the horizontal domain must be large. This implies a large number of grid points and a small time-step which is computationally expensive. These technical difficulties are surmounted by using a nested model – one which has grids with fine resolution (small horizontal grid spacing, domain size, and consequently time step) nested within coarse resolution grids (larger horizontal grid spacing, domain size and time step). For this study, a model with four nested grids is used. Another way these difficulties are overcome, is by effectively "nesting" the largest model grid into a much larger scale (hemispheric) forecast model (Canadian Meteorological Centre Finite Element Model — CMC FEM), and allowing the time dependent lateral boundary conditions of the mesoscale model to be "nudged" to match those of the larger scale model.

The 3-dimensional, mesoscale numerical model capable of gap wind simulations, and chosen for this study is the Colorado State University Regional Atmospheric Modelling System (CSU RAMS). RAMS was applied to the case described in section 3.4 for which observational data from the field program were available. For a description of RAMS refer to appendix A.

4.1.1 Modelling strategy

RAMS was used to simulate a moderate gap wind event for which surface and AIRsonde™ data are available because:

- the data can be used to validate the model and assess its applicability for this class of wind flow by comparing model output with observations

- once validated, the model output can be used to describe detailed features of gap wind flow

- validated model output can be used to find the forces important in gap wind flow

- model output can suggest simpler models (analytic or numerical) which would be easier to interpret and apply to forecast and analyse gap wind events

Implicit in the above progression is the assumption that successful model validation at the scale of the observing network (stations are 10's of kilometres apart) leads to realistic results on the smaller scales contained in the model (1.25 km horizontal spacing on grid 4). Because the atmosphere is a non-linear system, it could be argued that this would not be the case for simplistic, linear models. However, RAMS is not a simple, linear model. RAMS is a 3D quasi-Boussinesq model incorporating the important non-linearities of atmospheric flows, so that validation at a slightly larger scale should indicate a degree of realism at the scale of the model resolution.

The event chosen for simulation had the strongest surface winds of any during the field program for which AIRsonde™ vertical soundings were available. It is a moderate gap wind event – there were no strong events during the course of the field program. In the years following the field program, there have been a few extreme events, which could have been chosen for simulation (Jackson, 1993). However in those events, the surface network and AIRsonde™ data were not available for model verification, so the present case, for which verification data were available, was chosen. In future studies, it would be worthwhile to simulate an extreme event.

The simulation was started several hours before the onset of outflow, and continued for a total of 40 hours, which was less than the life span of the outflow event. It was able to contain the onset of the event, but not the termination, which is a more gradual feature. This was due primarily to a limitation in the computer resources available.

4.2 RAMS configuration

RAMS is a very versatile mesoscale model. It is capable of operating in two or three dimensions; in one or several nested grids; in hydrostatic or non-hydrostatic mode; and with or without topography, to mention just a few of the possible options. In this chapter the RAMS configuration used for this study will be described. A more detailed description of the model, and of the parameters used in this simulation is provided in appendix A.

4.2.1 Model parameters

The important parameters and options of RAMS used in these simulations are listed below:

non-hydrostatic; horizontally variable initial conditions and time dependent lateral boundary conditions; moisture as a passive tracer (no clouds, cloud forming or precipitation processes – gap winds are dry); rigid lid upper boundary condition (no other choice possible with horizontally variable fields and non-hydrostatic equations); solar and terrestrial radiation permitted on all grids (computed every 540 seconds); semi-implicit acoustic model; second order leapfrog (horizontal) advection and second order forward (vertical) advection; five grid levels in the soil ranging down to 1 m below the surface; surface roughness length of 1 m over land (dominant vegetation type is coniferous forest with rocky terrain giving high form drag)and computed from wind speed over water.

4.2.2 Grids and nesting

All grids in the model use the Arakawa type C grid stagger. Four grids were nested to bring the grid spacing from 60 km (required to efficiently resolve the synoptic scale) to 1.25 km (required to effectively resolve the fjord topography). Four are necessary because grid size ratios between neighboring grids greater than 4:1 can result in problems with wave and energy reflection at the grid boundaries (Walko, 1988).

The RAMS nesting scheme implements two-way interaction as described by Clark and Farley (1984). Briefly, at the boundaries of a fine grid, values are interpolated from the coarse grid in which it is nested, whereas in the grid interior, fine mesh values are averaged to replace the coarse mesh value which they surround. The grid spacing, number of grid points, total size, and time step of each of the four grids used in this simulation are shown in table 4.1. The location and horizontal extent of each grid is shown in figure 4.1.

Grid 1, with a horizontal extent of 1440 by 1740 km is just large enough to contain the synoptic atmospheric boundary conditions to gap wind flow. The grid spacing of 60 km is able to resolve ocean, Coast Mountains, Interior Plateau and Rocky Mountains (see

grid	ΔX (km)	N_X	Size W-E (km)	N_Y	Size N-S (km)	ΔT sec
1	60	25	1440	30	1740	90
2	20	26	500	35	680	45
3	5	42	205	46	225	15
4	1.25	38	46.25	58	71.25	5

Table 4.1: Grid structure of RAMS

figure 4.2). Topographically, the valleys dissecting the Coast Mountains are unresolved, so that gap winds are not modelled.

Grid 2, encompasses an area of 500 by 680 km, and is not large enough to contain the synoptic scale atmospheric forcing. At 20 km grid spacing, it can only crudely resolve major valleys dissecting the Coast Mountains. Gap winds are not adequately represented on this grid (see figure 4.3)

Grid 3, extends 205 by 225 km horizontally. The 5 km grid spacing can resolve the larger scale features of major valleys - see figure 4.4. Gap winds can be resolved on grid 3, although not in great detail.

Grid 4, with a horizontal extent of 46.25 by 71.25 km, must rely on intergrid communication from coarser grids at its lateral boundaries for synoptic scale information. The 1.25 km grid spacing (see figure 4.5) is sufficient to resolve the major terrain features of Howe Sound, and can represent gap winds in some detail.

Vertically, all grids had the same 30 levels, with vertical grid spacing starting at 100 m at the surface, and stretching by a factor of 1.15 for each successive level above the surface to a maximum separation of 1000 m. This results in vertical levels at the following elevations (in metres) for thermodynamic points (where variables other than velocity are defined) in the grid stagger:

0,	100,	215,	347.25,	499.338,	674.238,
875.373,	1106.679,	1372.680,	1678.581,	2030.367,	2434.921,
2900.159,	3435.183,	4050.460,	4758.029,	5571.733,	6507.493,
7507.493,	8507.493,	9507.493,	10507.493,	11507.493,	12507.493,
13507.493,	14507.493,	15507.493,	16507.493,	17507.493,	18507.493.

These levels are for grid points with a surface elevation of 0 m, for other grid points, the terrain following or "sigma-Z" coordinate scheme (Gal-Chen and Somerville, 1975) transforms the vertical elevation according to the following formula:

$$z^* = H\left(\frac{(z - z_s)}{(H - z_s)}\right) \tag{4.1}$$

where z^* is the height of a particular grid point in the terrain following coordinate system; z_s is terrain elevation at that grid point; z is the untransformed vertical coordinate; and H is the height of the model top at which the z^* coordinate surface becomes horizontal (ie. 18507.493 m in this case).

4.2.3 Initial data and boundary conditions

RAMS initial fields are horizontally variable (as opposed to horizontally homogeneous). Thus initial gradients are allowed to vary horizontally across the domain. This is an important feature of RAMS, allowing it to provide realistic pre-gap wind initial conditions. The data used to initialize (and provide lateral boundary conditions for) RAMS grid 1 were interpolated from the 0 hour prognosis of the CMC FEM. This dataset incorporates real data (surface data, aircraft observations, radiosonde profiles, satellite data, etc.) with previous CMC FEM runs to produce a dynamically balanced dataset. This is preferred over straight interpolation of real data, as there is less likelihood of the initial and boundary data producing errors (spurious waves for example) in the simulation.

As well as allowing horizontally variable initial conditions, RAMS permits time-dependent lateral boundary conditions. This means that fields on the lateral boundary of grid 1 are nudged (Davies, 1976) toward the time interpolated values obtained from CMC FEM output. The CMC FEM data used for this purpose were at 6 hour intervals. The nudging procedure is weighted so that a weight of 1.0 means at that grid point, the CMC FEM data are matched; a weight of 0.0 means the CMC FEM data are ignored and the RAMS modelled field is accepted completely; and a weight between 0.0 and 1.0 means there is some balance between the CMC FEM data and the RAMS modelled field. The nudging was applied 12 grid points from the edges of grid 1 with the following weights:

$$0.8, \quad 0.8, \quad 0.8, \quad 0.8, \quad 0.8, \quad 0.7, \quad 0.7, \quad 0.6, \quad 0.5, \quad 0.5, \quad 0.3, \quad 0.2.$$

The number and value of weights used was large. It was found in test runs with small weights that RAMS had difficulty accurately simulating the large scale features on grid 1 — there were spurious gradients (in perturbation pressure and vertical velocity) created in areas where nudging ended. Because of the grid communication scheme (where fine mesh values overwrite the corresponding coarse mesh values, except at the edge of the fine mesh), the use of large weights across grid 1 results in the direct effects of the nudging being felt on the lateral boundaries of grid 2, and not at all directly on grid 4.

Interpolation of CMC FEM data to RAMS initial fields

The CMC FEM data were obtained at 2° latitude by 2° longitude spacing at the following 11 pressure levels (kPa):

$$100, \quad 85, \quad 70, \quad 50, \quad 40, \quad 30, \quad 25, \quad 20, \quad 15, \quad 10, \quad 5.$$

The following were specified at each of these levels on the horizontal grid: U wind component, V wind component, potential temperature, geopotential height, and mixing ratio.

Additionally, over the ocean, sea surface temperature was provided.

To create a RAMS initial field, CMC FEM data were first vertically interpolated onto 40 isentropic levels with the horizontal spacing still the original 2° latitude by 2° longitude. The terrain elevation was found for each horizontal location by interpolation from a 0.5° latitude by 0.5° longitude terrain dataset obtained from NCAR. The final step was to horizontally interpolate all of the fields (including terrain) to model grid 1, creating RAMS initial fields.

4.2.4 Terrain

Due to the importance of interaction between small scale topography and the atmosphere for gap wind flows, representation of topography in the model which resolves the important small scale topographic features was critical. One problem with the data interpolation procedure described above is the terrain goes from a resolution of .5° to 2° (matching the CMC FEM data spacing). It is then *interpolated* to the 60 km resolution of grid 1. Usually in the RAMS initialization procedure, terrain for other grids is then interpolated from grid 1 terrain. This results in terrain on all grids having an effective accuracy of 2°. In order to circumvent this problem, and achieve the best possible terrain representation on all grids, high resolution terrain data were inserted at run time for grids 2, 3, and 4. Grid interaction meant that special care had to be taken to adjust terrain elevations on all grids. On the boundaries of a fine grid, the meteorological fields are interpolated from the next coarser grid. This means the terrain on the boundaries of a fine grid must also be interpolated from the coarse grid. The fields in the interior of a coarse grid which overlays a fine grid are replaced by averages of the surrounding fine grid field values. This means the terrain in a coarse grid interior which overlays a fine grid must be the average of the terrain elevations of the surrounding fine grid points. If these adjustments are not made, dynamic imbalances in the model result, causing

spurious results and model "blow-up". To avoid this, a terrain adjustment procedure was followed to adjust the prepared terrain data files making them acceptable to RAMS' nesting scheme.

Terrain preparation

The terrain for grid 1 of the model was obtained as previously described, from a .5° dataset interpolated to 2° and then to 60 km (the spacing on grid 1). The terrain data for the other grids were obtained from an Energy Mines and Resources 1 km dataset. These data were interpolated (using a 2D cubic spline) to 1.25 km, and averaged using a 25 point (5 X 5) binomial filter to 5 km, and 20 km. The raw 1.25 km, 5 km, and 20 km, terrain files were then filtered using a 2D fast Fourier transform to place the data in wavelength domain where all wavelengths less than 4 ΔX (5 km for grid 4) were removed using a ramp filter. An inverse fast Fourier transform then placed the data back in the space domain. These files were then adjusted according to the procedure outlined in the previous section to allow the grid nest interaction to function properly. The resulting contoured model terrain can be seen in figures 4.2 to 4.5 for grids 1 to 4 respectively.

Tests using other averaging / smoothing / filtering schemes were made, however the model was quite sensitive to the way in which the terrain is smoothed. In particular, if there is much variation at wavelengths less that 2ΔX, then numerical errors grow, ruining the simulation.
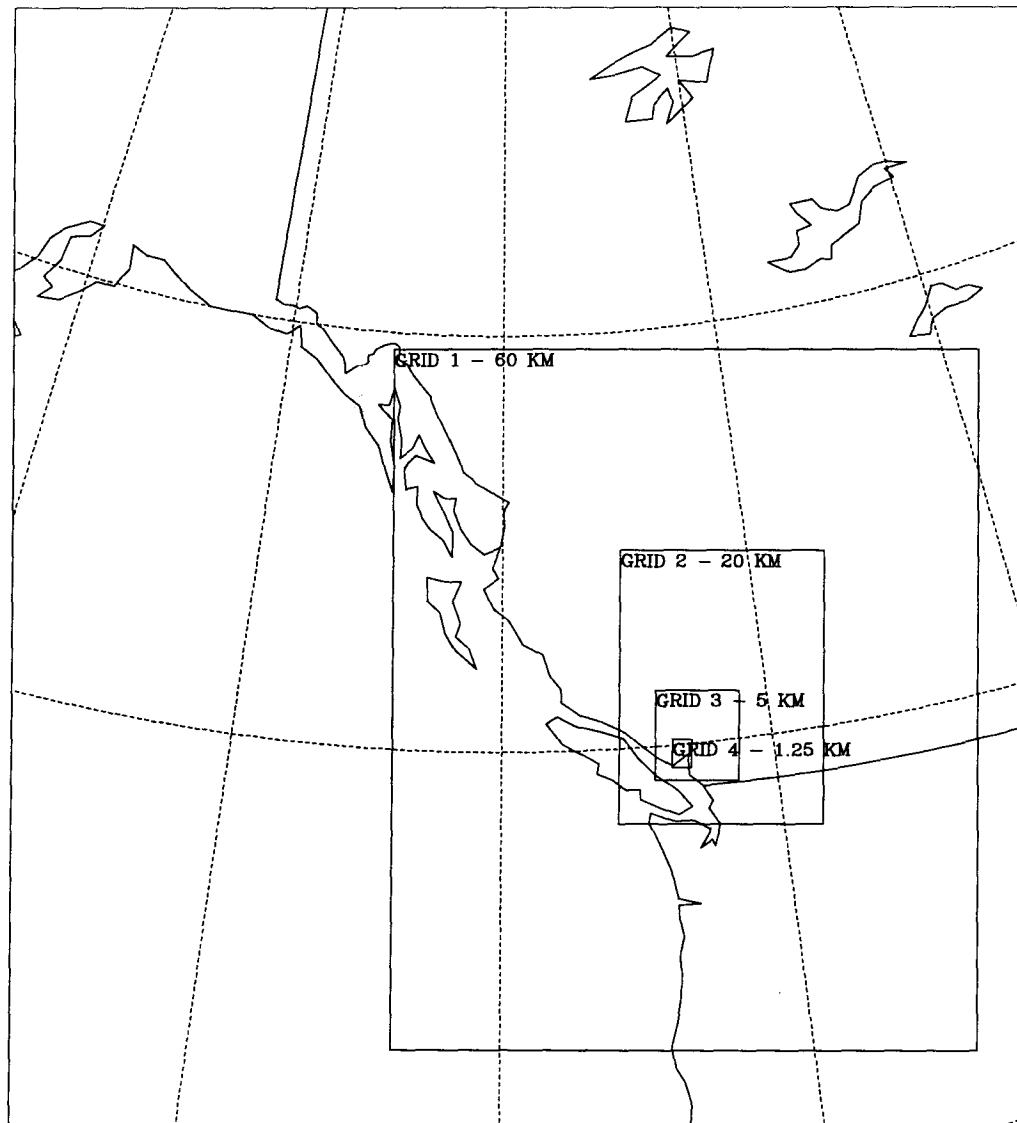
Figure 4.1: Location and grid spacing of the four RAMS grids used.
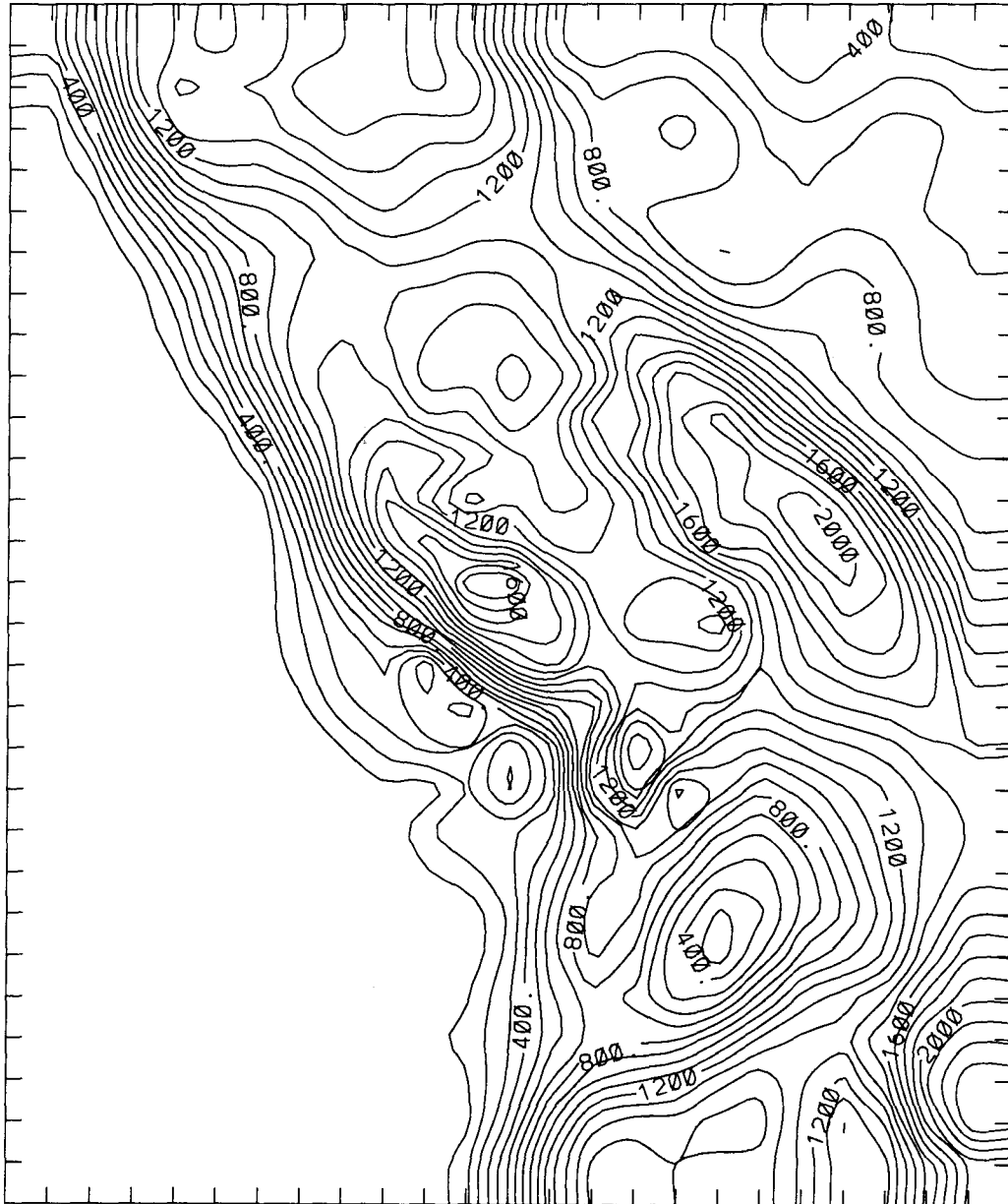
Figure 4.2: RAMS grid 1 after smoothing and adjustment. Contour interval is 100 m.
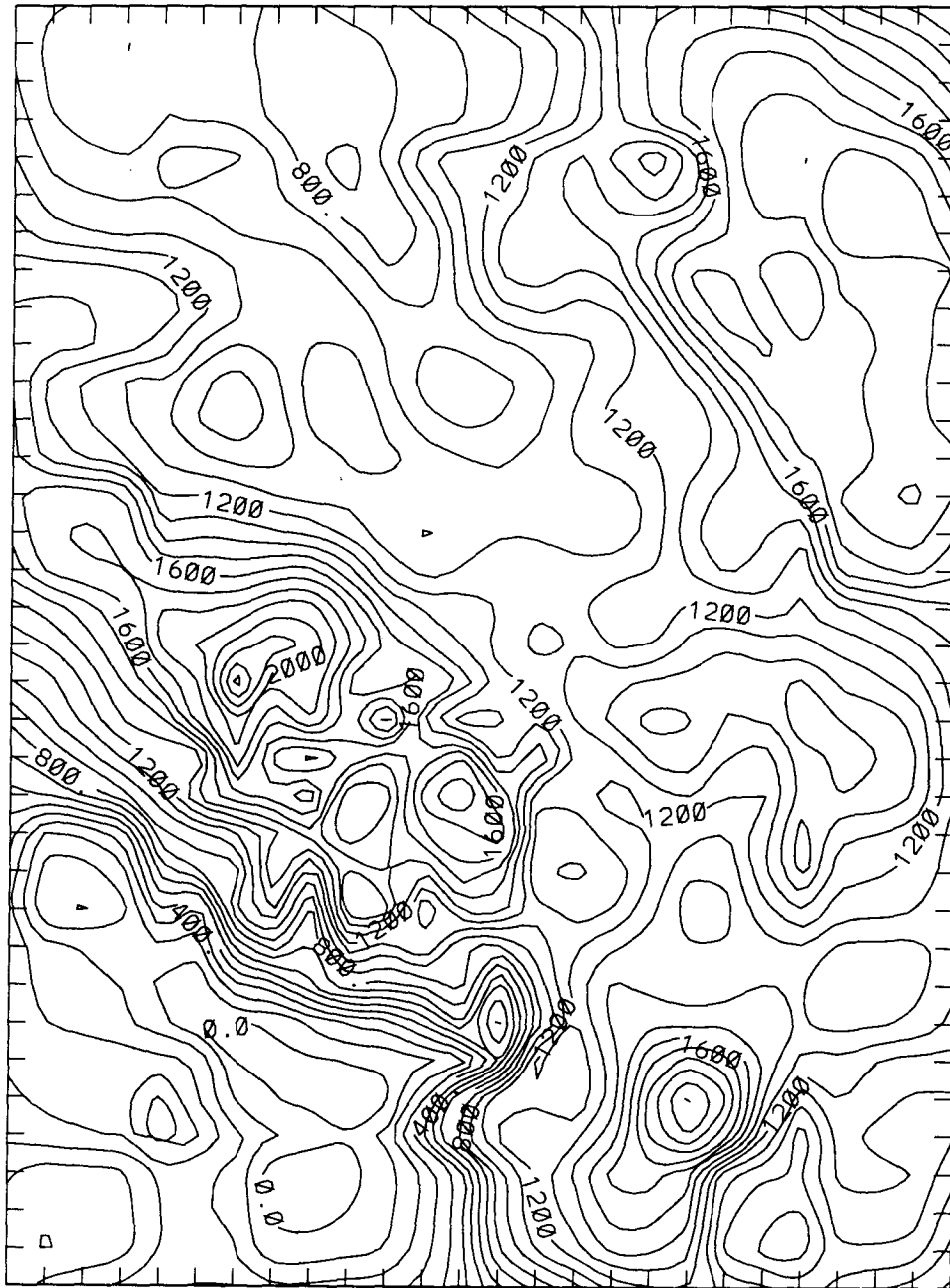
Figure 4.3: RAMS grid 2 after smoothing and adjustment. Contour interval is 100 m.
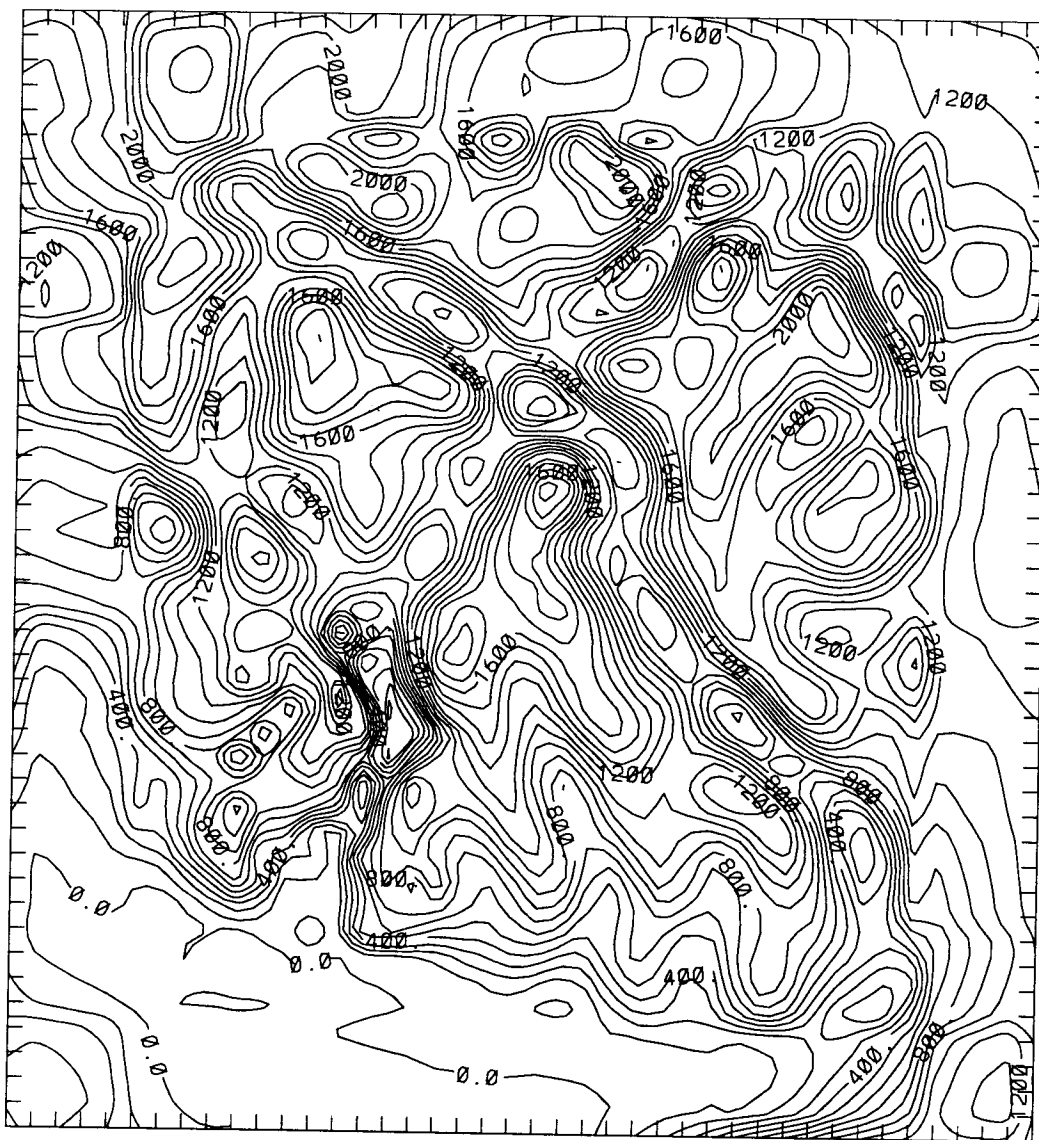
Figure 4.4: RAMS grid 3 after smoothing and adjustment. Contour interval is 100 m.
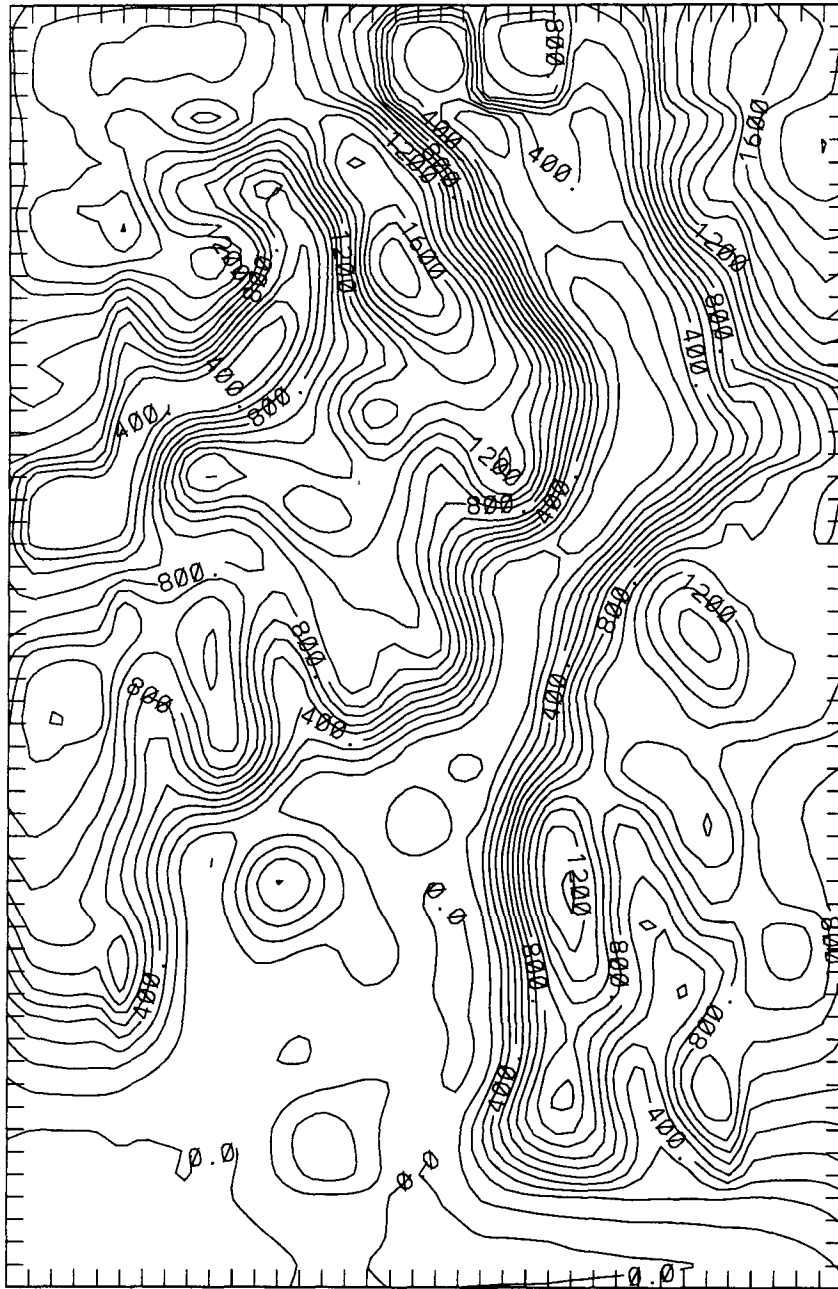
Figure 4.5: RAMS grid 4 after smoothing and adjustment. Contour interval is 100 m.

Chapter 5

Numerical modelling: RAMS results

The synoptic context of the case chosen for simulation using RAMS was described in section 3.4. This chapter provides a mesoscale description of the event while comparing observed data with RAMS output.

Several test runs were made (starting from run A), prior to the run presented here. It was found that modelled flow evolution was sensitive to the way in which the terrain was averaged, the amount of nudging applied to the time varying lateral boundary conditions on grid 1, and the time of day at which the run was initialized. The model runs from A to Y were incremental improvements in the simulation as errors were eliminated, better methods of terrain averaging and smoothing were developed, and different ways of applying lateral boundary conditions were tried. Most of the earlier runs were of short duration.

The run described here, (run X), was initialized on grids 1 and 2 starting at 04:00 PST January 30, 1988. After one hour of simulation, grid 3 was added. After a further hour of simulation, grid 4 was added. The model output presented is from hour 10 to hour 40 of the simulation (January 30, 14:00 PST to February 1, 20:00 PST). The simulation ended at hour 40. The model output were saved at 15 minute intervals, however results are shown at 3 hour intervals.

Most earlier runs were initialized 12 hours later than the initialization of run X (ie. at 16:00 PST January 30, 1988 rather than at 04:00 PST). The runs initialized at this later time in some cases had better flow representation, especially in the southern part of Howe

Sound, but were unable to simulate the flow reasonably for more than 10 hours. This is thought to be related to initialization of fields on fine grids in complex terrain. In the process of initializing fine grids, fields are interpolated from the next coarser grid onto the fine grid. This may result in small errors in the fine grid initial fields (due to differences in terrain elevation between grids) which can subsequently grow and contaminate the simulation. By starting a simulation at the beginning of nightfall (in the earlier runs for example), the model is in a cooling mode with a trend towards increasing atmospheric stability. Any errors near the ground would therefore be unable to dissipate by turbulent mixing and possibly grow during the simulation. There was evidence in support of this hypothesis from several earlier runs, which showed a tendency to pool unrealistically cold air in topographic bowls, especially on grid 3. This resulted in pockets of very stable air which continued cooling and could not be penetrated by the ambient airflow. This problem did not occur when the model was initialized at 0400 PST. By starting the simulation in the early morning hours, it is expected that errors of this type, arising from the interpolation of fields onto finer grids will be "mixed out" by turbulence as parameterized solar radiation heats the model ground.

Comparisons of modelled versus actual data are both qualitative and quantitative, encompassing visual comparisons of time-series, vertical profiles, and horizontal plots as well as statistical analyses of surface wind and temperature means, standard deviations, root mean square deviations and an index of agreement. The purpose of comparison is to show whether or not RAMS is able to produce a reasonable simulation of a gap wind case, and to validate the use of model output for more in depth analysis of gap wind flow. In depth analysis of RAMS output includes the presentation and discussion of vertical cross sections of wind and potential temperature, and horizontal Froude number plots.

5.1 Comparison of RAMS output with observations

Output from RAMS is compared with surface and AIRsonde™ observations for the January 30, to February 2, 1988 event. Directly comparing actual data with model output must be carefully considered, since they represent two different kinds of data. Surface observations are hourly averages of wind and temperature at a point 10 m above ground. Near-field local influences on the wind in particular are critically important (although site selection criteria tried to minimize this). RAMS wind (to which the surface observations are compared) is the instantaneous wind in a box which is 100 m high by 1.25 km on each side. Thus the terrain resolution is only 1.25 km (it has been filtered so that actual resolution is even coarser). Consequently, near-field local influences on the wind are not incorporated.

AIRsonde™ observations are a vertically tilted atmospheric profile since the helium balloon is advected downwind as it lifts the instrument package. With an average ascent rate of 1000 m in 300 seconds, this corresponds to a downwind shift of about 1 to 3 horizontal grid points (depending on the wind speed) per 1000 m of ascent. AIRsonde™ observed temperatures are instantaneous, and winds are layer averages. The RAMS output to which this is compared is layer averages of wind and temperature in one vertical column near the balloon release point. This horizontal shift in the AIRsonde™ profile is likely to make little difference, especially since largest displacements will occur at highest elevations where the wind is relatively constant and uninfluenced by terrain.

5.1.1 Quantitative evaluation of model performance

RAMS surface wind and temperature fields are compared with observed data using statistical measures recommended by Willmott (Willmott, 1981; Willmott, 1982; Willmott et al., 1985), and applied by Steyn and McKendry (1988) and Ulrickson and Mass (1990).

Willmott suggests the following parameters be used for quantitative evaluation of model performance:

- Observed and modelled means and standard deviations;

- Total, systematic, and unsystematic root mean squared differences (RMSD, RMSD$_S$, RMSD$_U$) between observed and modelled fields. These are defined as (Willmott et al., 1985):

$$\mathrm{RMSD} = \left[\sum_{i=1}^{N} w_i |P_i - O_i|^2 / \sum_{i=1}^{N} w_i\right]^{.5} \tag{5.1}$$

$$\mathrm{RMSD}_S = \left[\sum_{i=1}^{N} w_i |\hat{P}_i - O_i|^2 / \sum_{i=1}^{N} w_i\right]^{.5} \tag{5.2}$$

$$\mathrm{RMSD}_U = \left[\sum_{i=1}^{N} w_i |\hat{P}_i - P_i|^2 / \sum_{i=1}^{N} w_i\right]^{.5} \tag{5.3}$$

where P_i is the predicted and O_i is the observed value; N is the number of stations; $\hat{P}_i$ is the ordinary least squares estimate of P ($\hat{P}_i = a + bO_i$ where a, b are the intercept and slope); w_i represents the areal weight for each station, and is proportional to the fraction of the total area that station represents.

- The Index of Agreement, d, (d$_2$ in Willmott et al. (1985)) which is defined as:

$$d = 1 - \mathrm{RMSD}^2 / \left[\sum_{i=1}^{N} w_i (|P_i - \bar{O}| + |O_i - \bar{O}|)^2\right] \tag{5.4}$$

where $\bar{O}$ is the weighted mean of the elements contained in O:

$$\bar{O} = \sum_{i=1}^{N} w_i O_i / \sum_{i=1}^{N} w_i \tag{5.5}$$

in the application of these statistics to wind, O and P are considered as vectors, and the appropriate vector arithmetic is used.

Areal weights for each station are found using the Thiessen polygon technique (Thiessen, 1911). Only 12 stations with continuous hourly records in the southern 3/4 of the domain

ALC	BRU	DEE	DEF	FIN	HAR	LAN	LOO	MEL	RAG	SQT	WAT
8	12	8	22	15	10	19	22	30	16	25	20

Table 5.1: Stations and areal weights used in statistical evaluation of RAMS simulation.

were used for statistical evaluations. Stations in the northern part of the domain either didn't have continuous records (SQA) or were not well enough situated for representative wind measurements (SQR), so were not included. The stations and their weights are shown in table 5.1, and the locations can be found in figure 3.1.

According to the interpretations of Willmott, total RMSD represents the total difference between model and observations. The systematic component (RMSD$_S$) represents model linear bias, whereas the unsystematic component (RMSD$_U$) represents model precision. The Index of Agreement, d (a dimensionless number), is a measure of the relative error of the model, with a range of 0.0 (for no agreement) to 1.0 (for perfect agreement).

Figures 5.1a-c show observed and modelled direction, speed, and standard deviation of wind for 31 hours of simulation, averaged over the twelve stations listed in table 5.1. Simulated directions are slightly more easterly than observed in the first part of the simulation. Average simulated wind speeds show an increasing trend which is not seen in the observations. Modelled winds are less than observed until 11:00, January 31, when they become similar to observed speeds. They become greater than observed wind speeds near the simulation end. The observed standard deviation of wind velocity is greater than modelled by about 2 m s^{-1} during most of the simulation. This is likely due to sub-grid scale effects upon the observed wind unresolved in the model. Figures 5.2a and b show wind RMSD and Index of Agreement. Until about 11:00 January 31, the RMSD is near 6 m s^{-1}, most of which is systematic, due to the difference between observed and modelled means shown in figure 5.1b. The Index of Agreement lies between 0.5 and 0.6 during this

	Direction (°N)	Speed (m s^{-1})	Std. Dev. (m s^{-1})	RMSD (m s^{-1})	RMSD$_S$ (m s^{-1})	RMSD$_U$ (m s^{-1})	d (-)
observed	42.3	6.1	3.7	6.3	5.2	3.5	.59
modelled	60.8	4.9	2.3				

Table 5.2: RAMS modelled and observed wind evaluation statistics spatially averaged over all stations and over the 31 hours of simulation.

time. Between 11:00 and 13:00 on January 31, when observed and modelled mean wind speeds are similar, the systematic RMSD becomes small with the total RMSD mainly comprised of the unsystematic component. The Index of Agreement at this time peaks at 0.83. The RMSD becomes larger again after this time, as the systematic component again becomes large when average modelled winds become greater than observed. The averages of wind, standard deviation, RMSD, and Index of Agreement over the entire simulation are shown in table 5.2. The RMSD's are large compared to the mean wind speed, partly because they are found using observed and modelled wind as *vectors* (not just as speed values).

Similarly, the modelled and observed temperatures averaged over twelve stations, are compared for the 31 hours of simulation. Averages and standard deviations of observed and modelled temperature are shown in figures 5.3a-b. Modelled temperatures start and end somewhat cooler than observed, but show a similar trend. Observed and modelled standard deviations are virtually identical. Figure 5.4a presents the total, with the systematic and unsystematic components of Root Mean Squared Deviation (RMSD) for temperature. The total RMSD, comprised mostly of the unsystematic part, representing random deviations, is fairly constant at between 1.5 and 3 K. However, between 11:00 and 13:00, January 31, (the times when the wind field simulation is most accurate) the systematic RMSD becomes very small and the total RMSD also decreases. The Index of Agreement for temperature during the course of the simulation, remains high (greater

a)
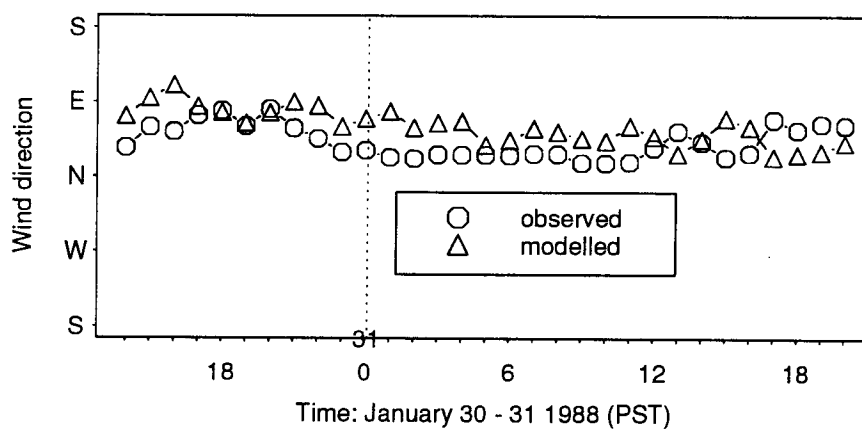
b)
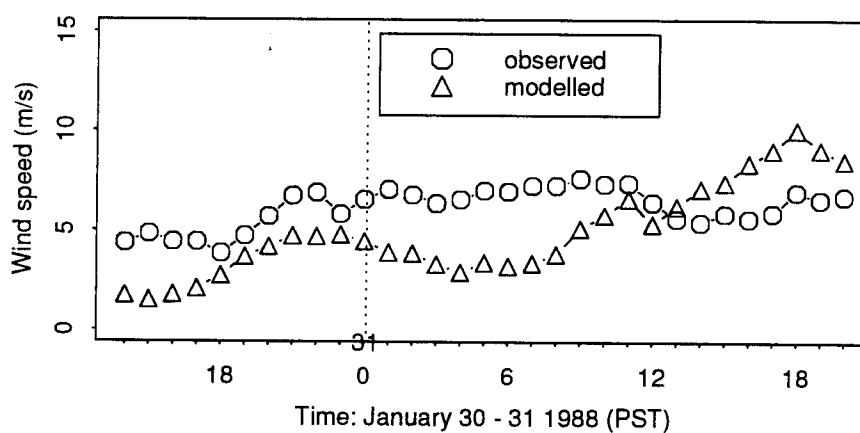
c)
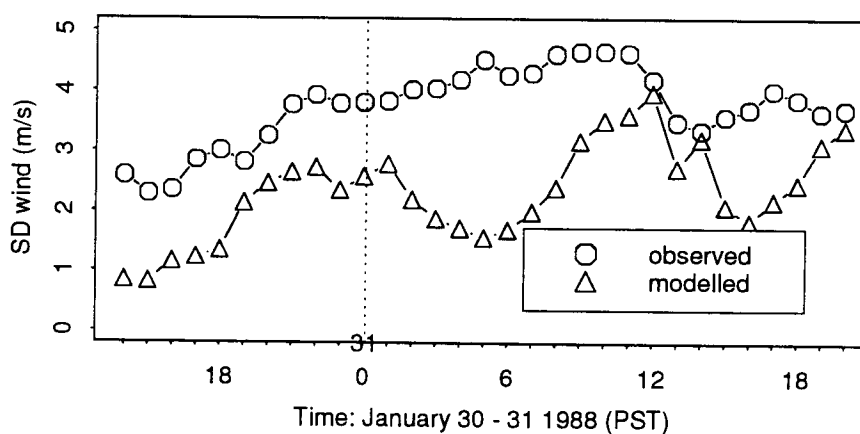
Figure 5.1: Time series of observed and modelled: a) wind direction, b) wind speed, and c) standard deviation of wind speed; averaged over 12 stations at each time during the simulation.

a)
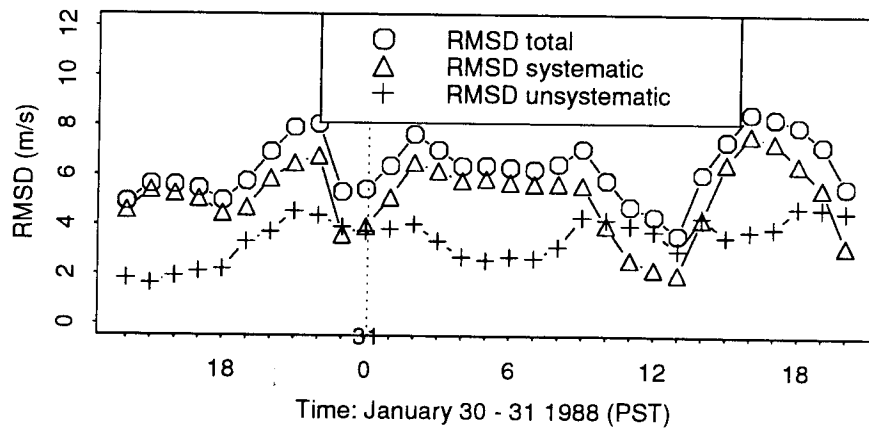
b)
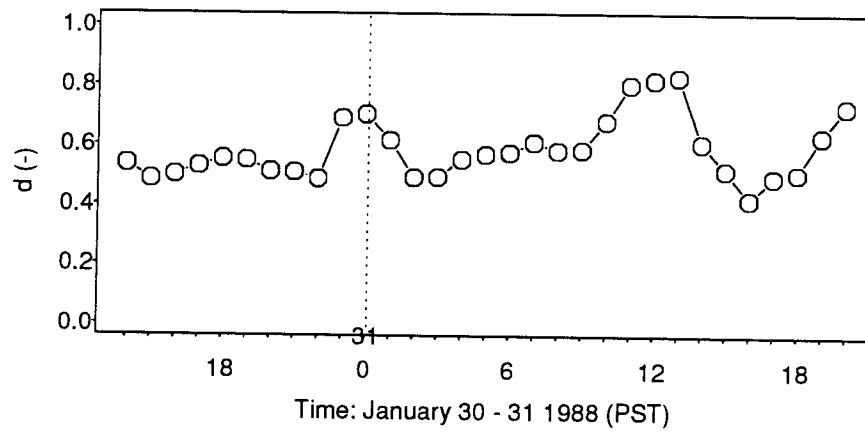
Figure 5.2: Comparison of observed and modelled wind as time series of a) total, systematic, and unsystematic components of the Root Mean Squared Differences; and b) the Index of Agreement.

than 0.8). Averages of temperature, standard deviation, RMSD and index of agreement over all stations for the whole 31 hours of simulation are shown in table 5.3.

As Willmott provides little guidance on values of d which represent "good" or "poor" simulations, the above statistics are compared to those found in other mesoscale simulations — Steyn and McKendry (1988) (hereafter SM88) and Ulrickson and Mass (1990) (hereafter UM90). Both SM88 and UM90 applied a hydrostatic predecessor to RAMS (described in Mahrer and Pielke (1977a), Mahrer and Pielke (1977b), Mahrer and Pielke (1978), McNider and Pielke (1981)), to simulate summertime seabreeze circulations in the complex terrain of Vancouver (SM88), and Los Angeles (UM90). While thermally forced seabreezes occurring under light synoptic conditions are considerably different from gap winds, there were no more similar simulations with appropriate evaluation statistics, available for comparison. While the SM88 and UM90 simulations are in complex terrain, the winds are not as severely constrained by topography as gap winds in Howe Sound. Given these considerations, statements about the relative veracity of the different models are not valid. However, at least the RAMS evaluation results can be placed in some context.

SM88 used identical statistics to evaluate wind and temperature fields, except they did not apply different spatial weights to the observations, and used data from 24 stations, as opposed to 12 stations used here. Their domain was about twice as large as the portion of the RAMS grid 4 terrain validated here however. SM88 had a wind field Index of Agreement, d which ranged between .41 and .61, with a mean value of .51 over 24 hours of simulation. RAMS run X, over 31 hours of simulation had d for wind ranging between .42 and .83, with a mean of .59. The SM88 temperature field Index of Agreement, d, ranged between .11 and .74, with a mean of .34. RAMS run X had a mean d for temperature of .88, with a range of .75 to .96. UM90 also used the Willmott recommended statistics to evaluate the simulated windfield. They found d ranging between .4 and .75 (but did not

report a mean value). They did not evaluate temperature in their simulation.

Despite difficulties in making direct comparisons, the RAMS gap wind simulation performs statistically better than SM88 and UM90 mesoscale seabreeze simulations. There are problems with the RAMS simulation, especially in the southern part of the domain for much of the time which will be discussed subsequently, however the relatively good statistical evaluation lends confidence to further interpretations of model output.

a)
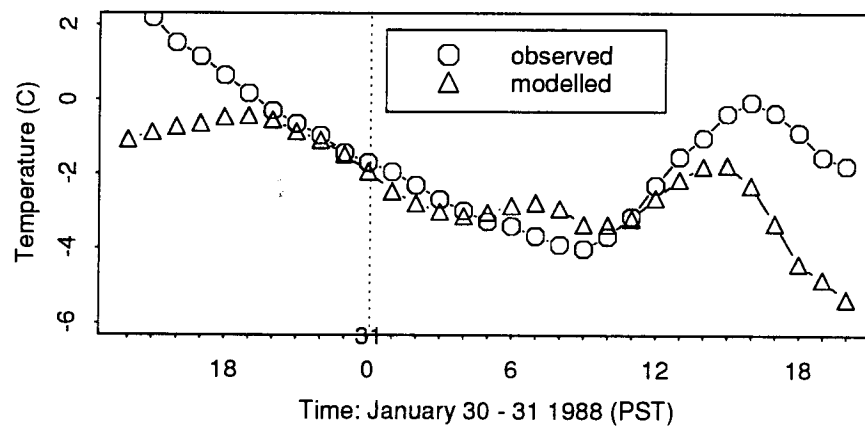
b)
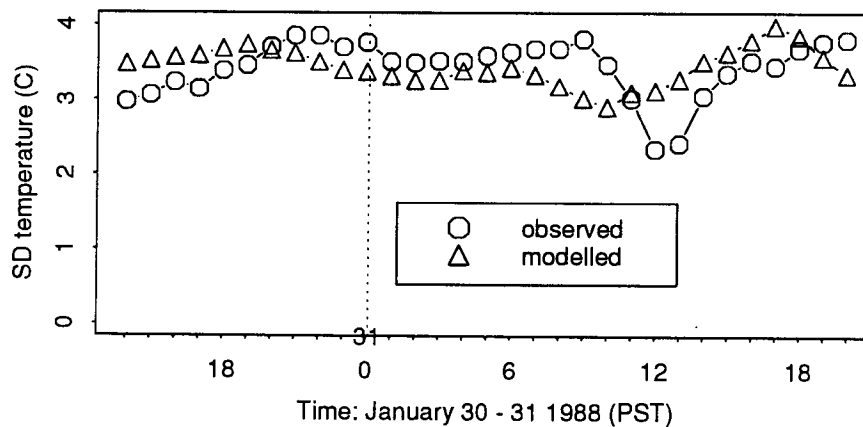
Figure 5.3: Time series of observed and modelled: a) temperature, b) standard deviation of temperature; averaged over 12 stations at each time during the simulation.

a)
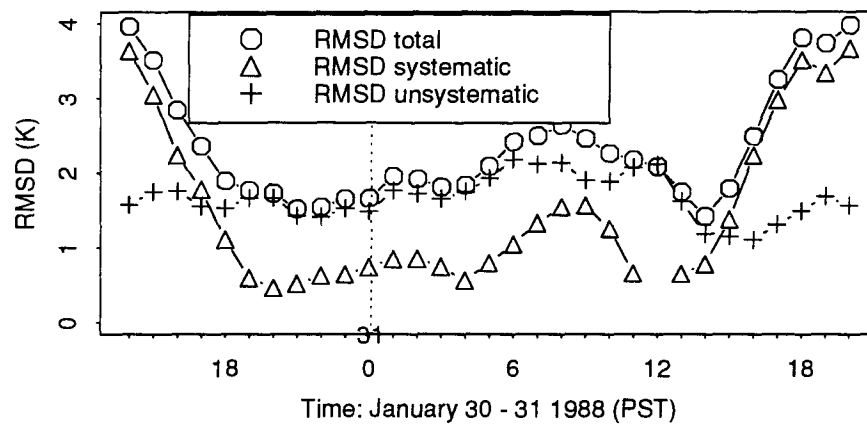
b)
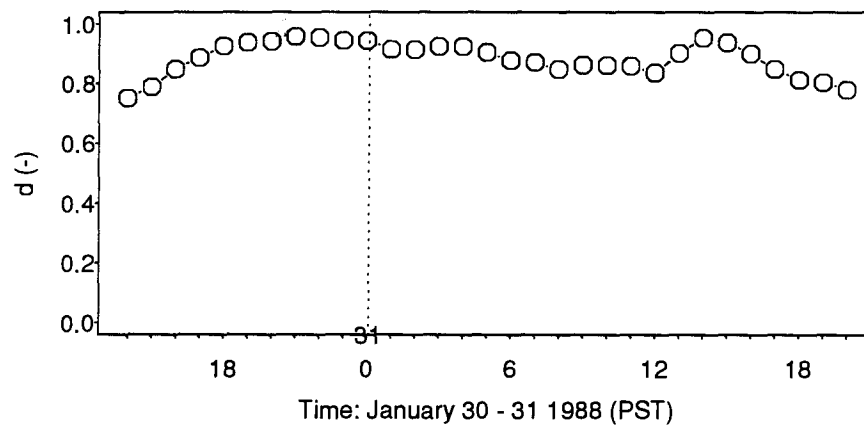
Figure 5.4: Comparison of observed and modelled temperature as time series of a) total, systematic, and unsystematic components of the Root Mean Squared Differences; and b) the Index of Agreement.

	Temperature (°C)	Std. Dev. (°C)	RMSD (°C)	RMSD$_S$ (°C)	RMSD$_U$ (°C)	d (-)
observed	-1.3	3.4	2.3	1.5	1.7	.88
modelled	-2.3	3.4				

Table 5.3: RAMS modelled and observed temperature evaluation statistics spatially averaged over all stations and over the 31 hours of simulation.

5.1.2 Qualitative evaluation – time series

Time series of temperature and down-channel wind components were constructed from the actual surface observations, and from RAMS model output. These are shown from figure 5.5 to figure 5.10. The general conclusion to be drawn from these comparisons is that RAMS seems to simulate the flow (and temperature) best, both in magnitude and time response, in the northern and middle part of the region (figures 5.5, 5.6, 5.7a), however the simulation is not nearly as good in the south (figures 5.7b and 5.8a).

In the northern and middle parts of the domain, observations and model output show down-channel winds increasing and temperatures dropping in the afternoon and evening of January 30. This trend continues until the afternoon of January 31 when winds begin decreasing and temperatures begin increasing at most stations. RAMS, in most places doesn't simulate the decrease in wind speed at the end of the simulation particularly well, tending to maintain the same speed or increase it slightly. Timing of the gap wind onset, especially in middle of the domain is quite good (see figures 5.6b and 5.7a). The ten hours of simulation prior to those shown in figures 5.5 to 5.10, had light winds.

Observations in the southern part of the domain do not compare favourably with RAMS model output (see figures figure 5.7b and 5.8a). Observed winds here are strongest, whereas modelled winds are weak. Reasons for this are discussed in more detail subsequently.

a)
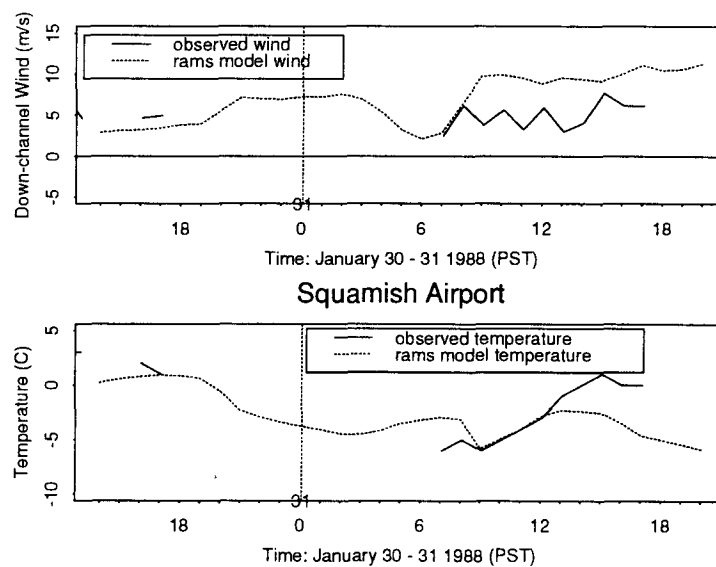
b)
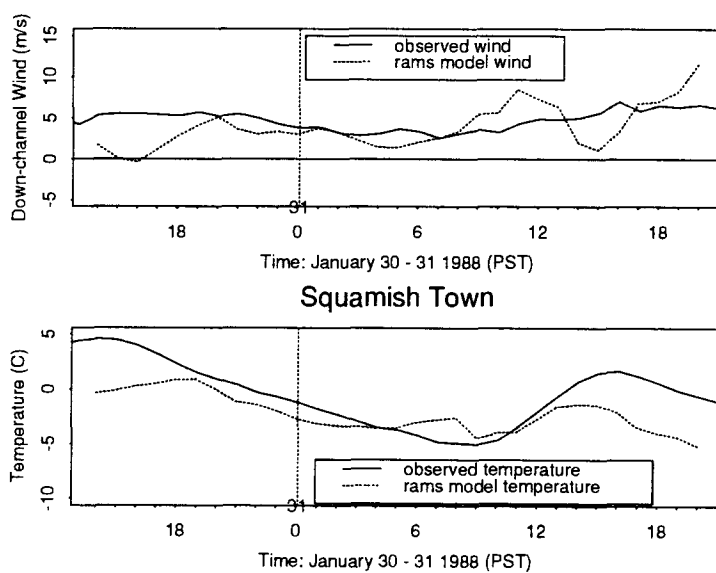
Figure 5.5: Time series of surface observations and RAMS model output for Squamish Airport (SQA) and Squamish Town (SQT)

a)

Watts Point

b)
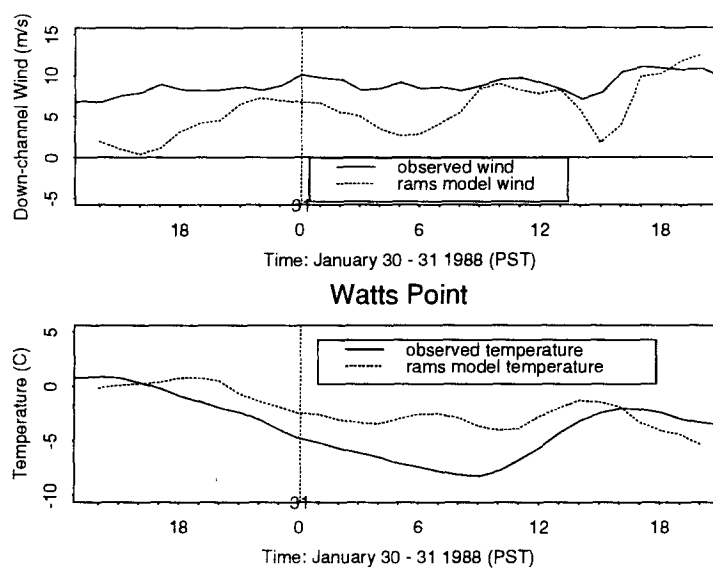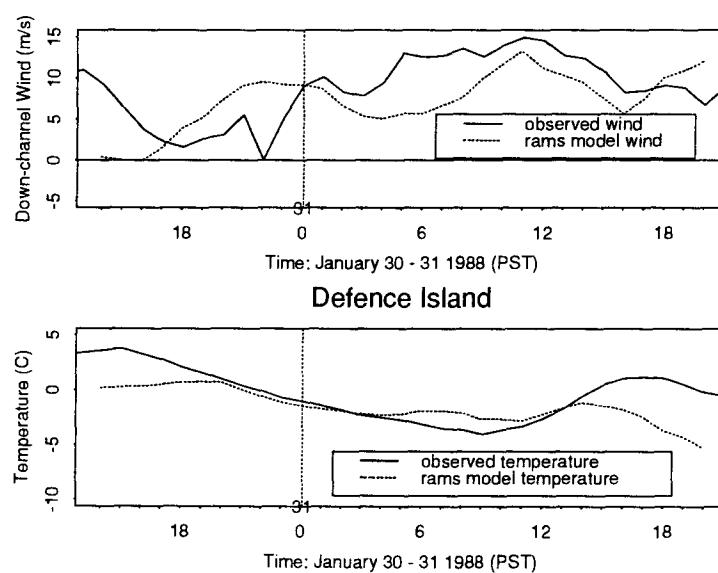
Defence Island

Figure 5.6: Time series of surface observations and RAMS model output for Watts Point (WAT) and Defence Island (DEF)

a)

Brunswick Point

b)
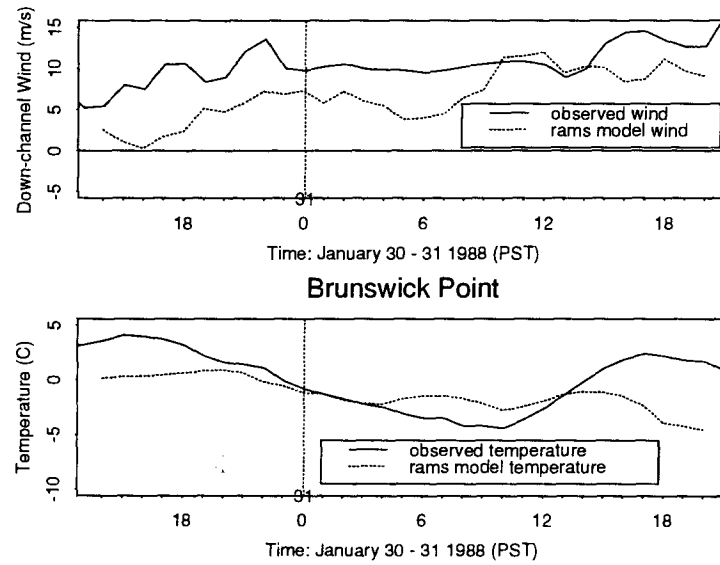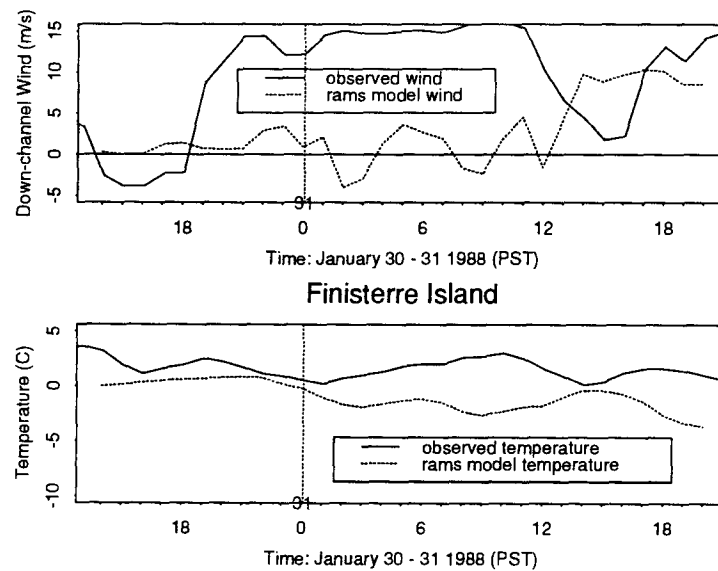
Finisterre Island

Figure 5.7: Time series of surface observations and RAMS model output for Brunswick Point (BRU) and Finisterre Island (FIN)

a)
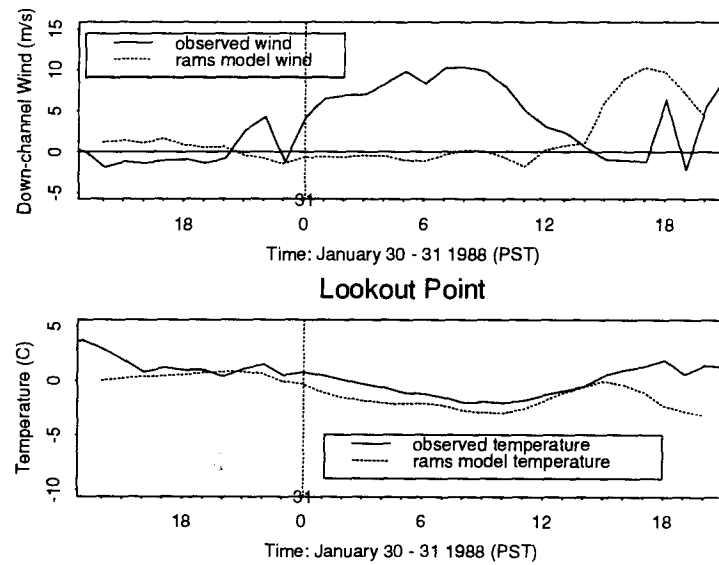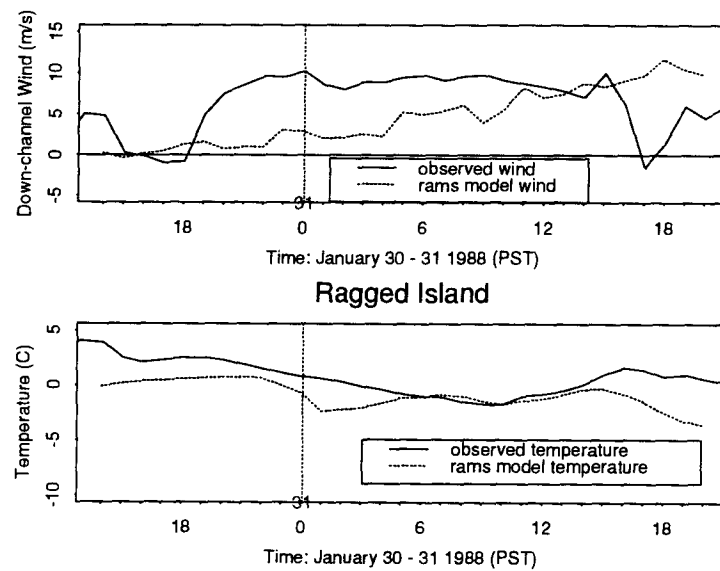
Figure 5.8: Time series of surface observations and RAMS model output for Lookout Point (LOO) and Ragged Island (RAG)

a)

Port Mellon

b)
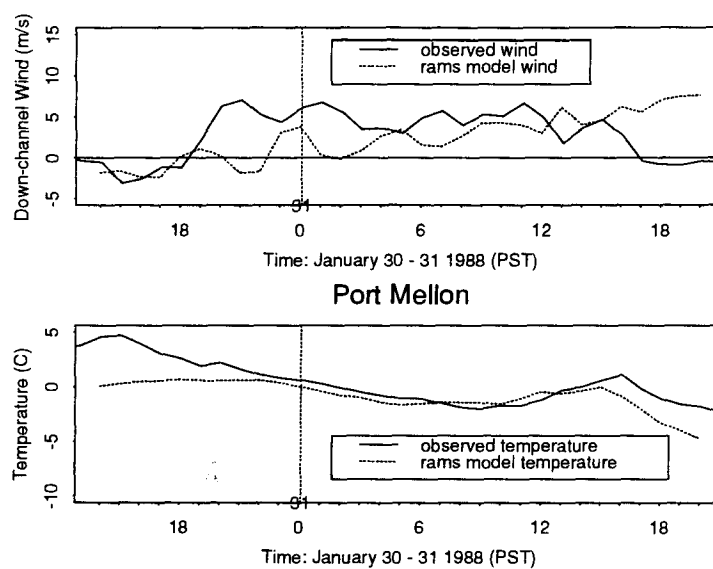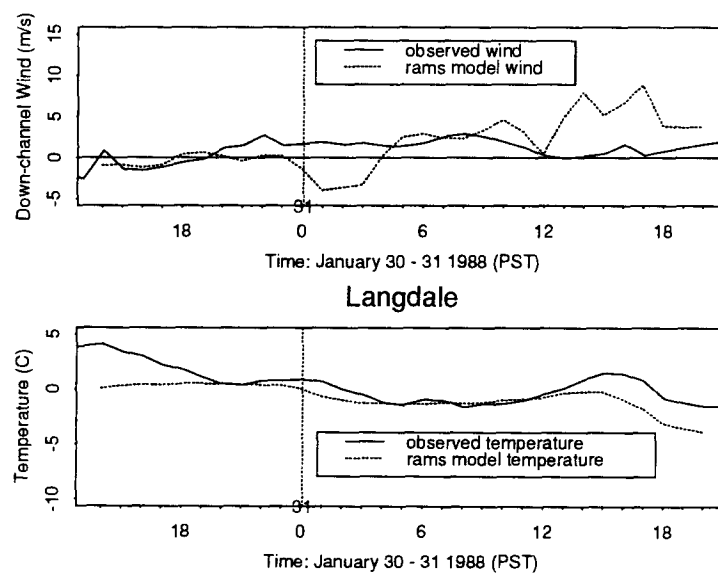
Langdale

Figure 5.9: Time series of surface observations and RAMS model output for Port Mellon (MEL) and Langdale (LAN)

a)
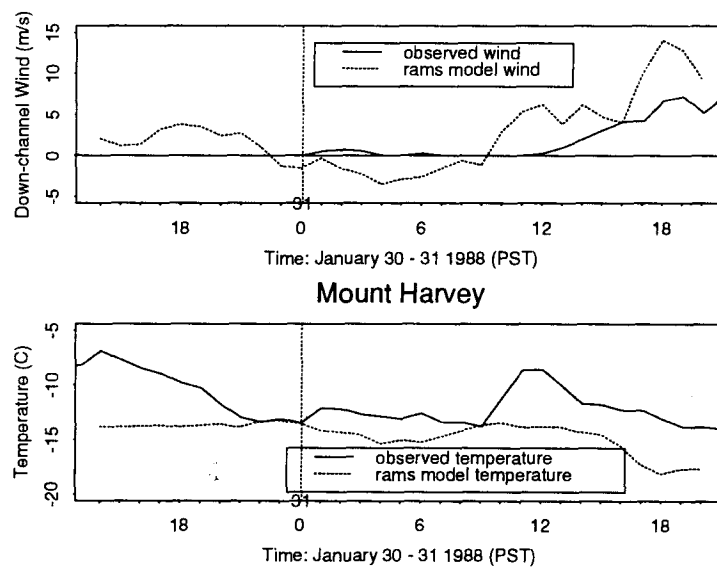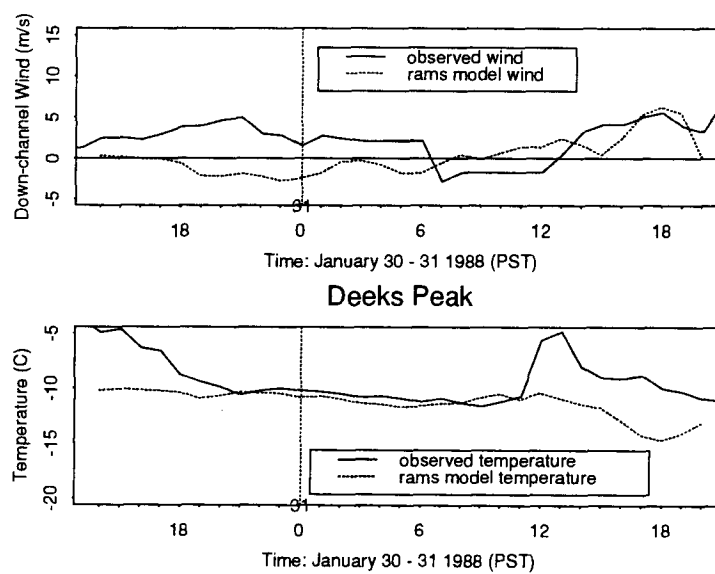
Figure 5.10: Time series of surface observations and RAMS model output for Mount Harvey (HAR) and Deeks Peak (DEE)

5.1.3 Qualitative evaluation – vertical profiles

Figures 5.11 to 5.14 show observed and modelled hodographs and vertical profiles of potential temperature at Squamish. The potential temperature profiles are quite close to those observed, both in value and shape. An elevated stable layer below about 2800 m above ground marks the top of outflowing air. A lower, mechanically mixed neutral layer near the surface about 1000 m deep is the region of strongest flow. Both observed and modelled hodographs show different speeds and directions below the stable layer than above it. Winds are stronger and more northeasterly in the outflowing layer. In the last vertical sounding shown, figure 5.14, the vertical profile shape is similar, however observed temperatures are several degrees cooler near the surface.

a)
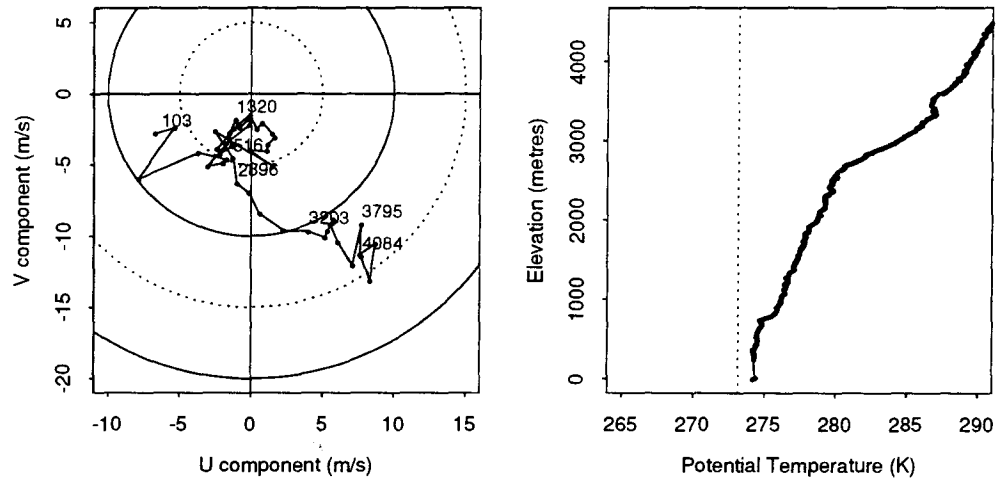
b)
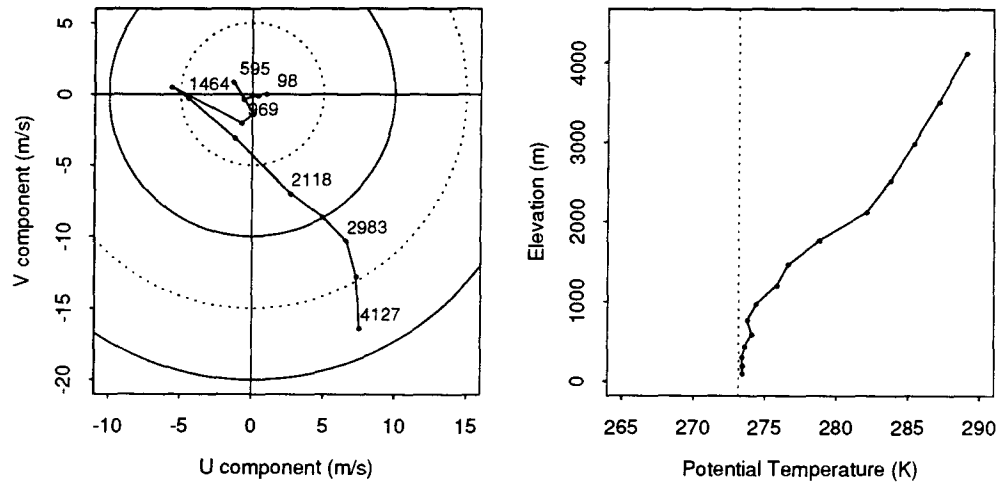
Figure 5.11: a) AIRsonde observed profile at Squamish town, 16:00 PST January 30 1988; b) RAMS generated vertical profile at same time and location as a)

a)
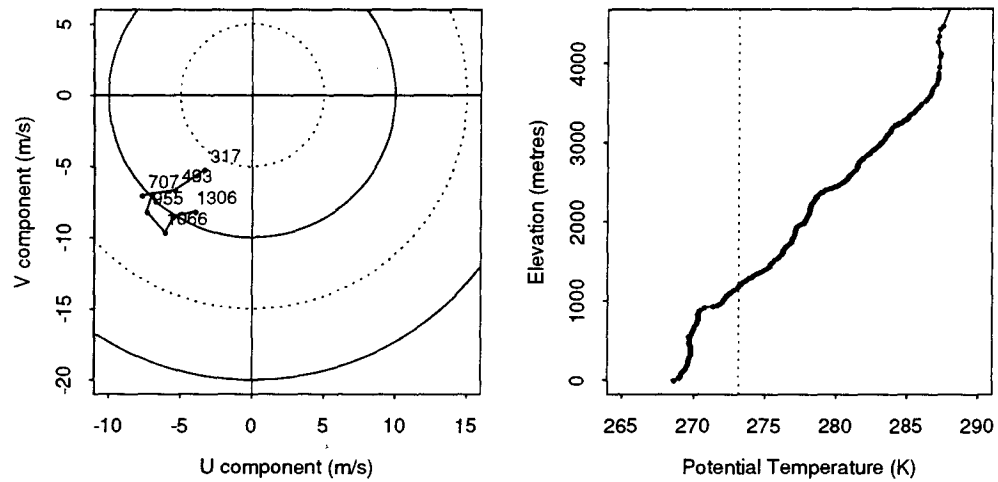
b)
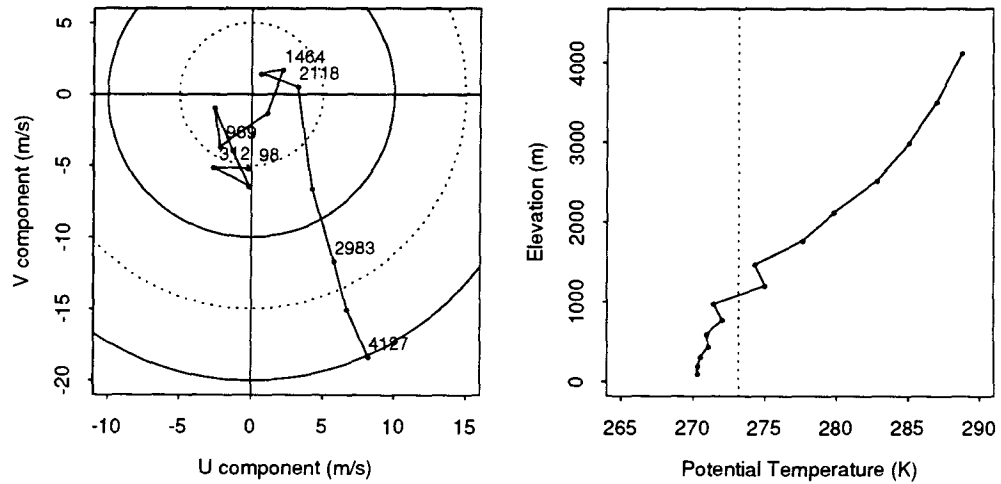
Figure 5.12: a) AIRsonde observed profile at Squamish town, 23:30 PST January 30 1988; b) RAMS generated vertical profile at same time and location as a)

a)
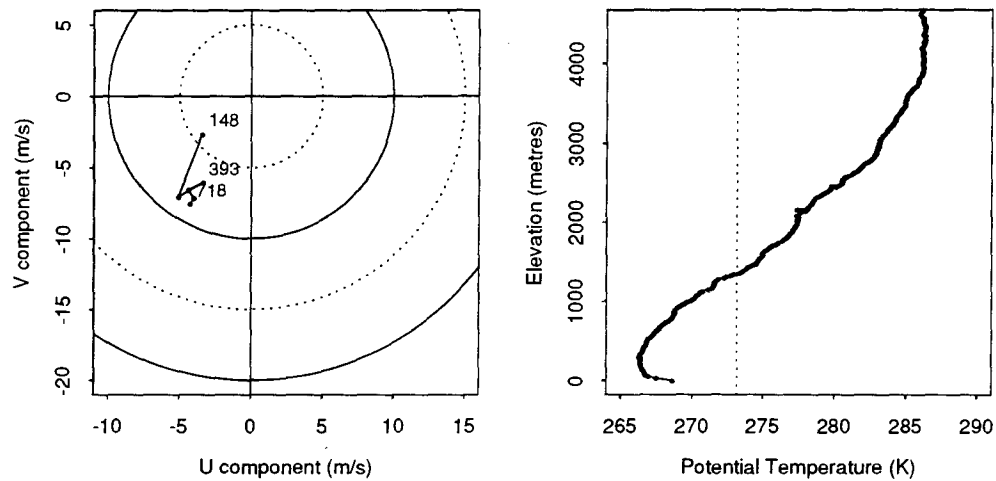
b)
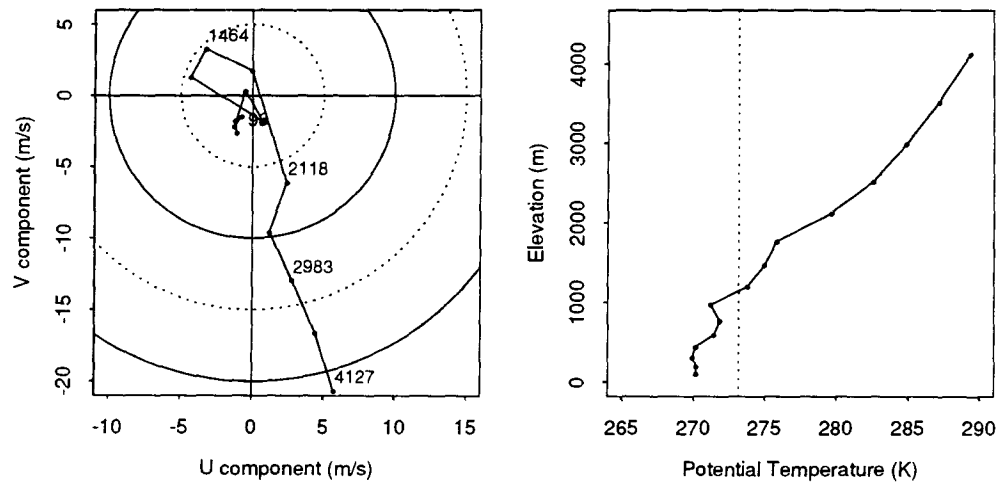
Figure 5.13: a) AIRsonde observed profile at Squamish town, 6:00 PST January 31 1988; b) RAMS generated vertical profile at same time and location as a)

a)
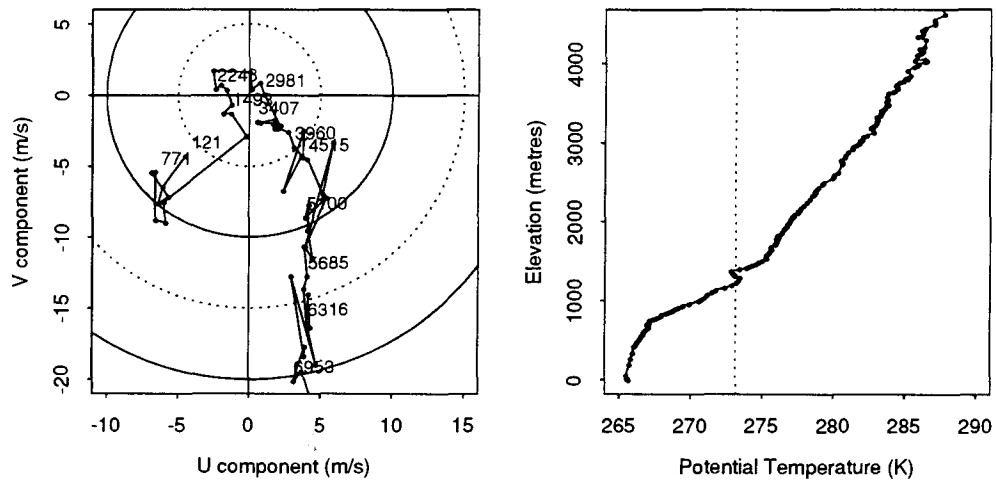
b)
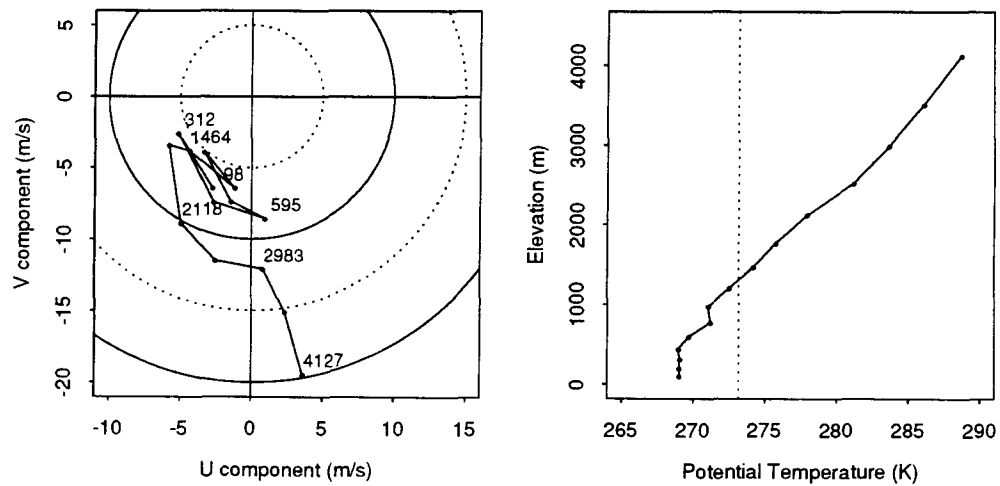
Figure 5.14: a) AIRsonde observed profile at Squamish town, 10:00 PST January 31 1988; b) RAMS generated vertical profile at same time and location as a)

5.1.4 Qualitative evaluation – surface winds

Figures 5.15 to figure 5.17 show modelled winds as vectors from the second model level at 3 hour intervals during the course of the simulation. These can be interpreted as averages over the 1.25 km by 1.25 km by 100 m high first grid in the model. Only one quarter of the model grid points are shown so that vector tails are 2.5 km apart. Observed surface winds are superimposed in bold with the vector heads terminating in a •, on the vector plots of modelled winds.

The modelled winds in 5.15a, show light flow everywhere before the onset of gap winds. As time progresses, down-channel wind speeds increase until the flow becomes fully developed through the fjord (figures 5.16 and 5.17). Observations suggest the flow is somewhat lighter than simulated in the north, and considerably stronger than simulated in the south. This can only partially be explained by near-field influences of surrounding topographic and roughness elements on the observations.

The general horizontal pattern of gap flow increasing down the fjord from north to south matches observations and the conceptual model of gap winds in Howe Sound. Acceleration along the channel observed near the simulation end, is also verified by observation and theory. The simulation's horizontal wind field, while not exactly matching observations (especially in the south early in the simulation), seems to capture the main flow features of the gap wind event. RAMS shows an initial pulse of gap wind developing by January 31, 23:00 PST (figure 5.15d), decreasing slightly after that, and then increasing and becoming fully developed after January 31, 11:00 PST (figure 5.16d).

As made apparent by the time series comparison, the simulation was quite successful in northern and central parts of Howe Sound, but there were simulation problems in the south. The vector plots give a clearer picture of the possible reasons for the differences. Initially, easterly flow across the southern part of the domain in the model was much

stronger than indicated by observations. The core of strong modelled northeasterly winds in southern Howe Sound in figures 5.15 and 5.16 is more northeasterly than observed, with the axis cutting diagonally across Gambier Island to the western side of Bowen Island, rather than being confined to the main channel between Bowen Island and the eastern wall as observations, particularly from Finisterre Island (FIN), suggest (see figure 3.2 for locations). This is likely due to stronger than observed modelled easterly winds south of Howe Sound, and at elevation over Howe Sound. This would result in enhanced transfer of easterly momentum downward into the outflowing air in Howe Sound, deflecting the core of strong winds into a northeasterly rather than a northerly orientation. Grid 3 (the 5 km grid in which grid 4 is nested), level 3 (layer between 100 and 215 m) winds, (not shown) clearly show the strong modelled winds across the south of the domain originating in the Fraser valley. In figure 5.17 the model's easterly winds across the south have decreased and modelled gap wind flow in the south more closely resembles flow observed 12 to 18 hours before (see figures figure 5.7b and 5.8a for example). Enhanced modelled easterly outflow from the Fraser River valley would also lead to an increased cold air height at the mouth of Howe Sound. According to hydraulic theory, which will be discussed in more detail in chapter 7, this also would result in decreased gap winds near and upstream of the mouth of Howe Sound.

It appears the reason modelled flow is stronger and more easterly than observed across the south is related to terrain resolution, particularly of the Fraser valley in its path through the coast mountain barrier (referred to as the Fraser Canyon). The Fraser Canyon is resolved but not fully contained on grid 3 (figure 4.4), but is partially resolved on grid 2 (figure 4.3) where it is the **only** passage through the Coast Mountain barrier that is resolved. This means low level air on grid 2 can only flow out the Fraser valley. Since grid 2 provides boundary conditions to grid 3 and grid 3 provides boundary conditions to grid 4 via the grid interaction scheme, this would result in a spuriously large amount of air

flowing out of the Fraser Valley. Attempts were made to solve this problem by increasing the horizontal extent of grid 3, both northwards (so the Howe Sound – Cheakamus valley could be fully resolved from the coast to the interior plateau), and eastwards (so the Fraser valley could be better resolved). Although this did result in an improved simulation compared to earlier runs where grid 3 was of a smaller horizontal extent, the problem was not completely solved. To eliminate this problem entirely, grid 3 would likely need a horizontal extent the size of grid 2, resulting in prohibitively large computer memory and cpu time requirements. Since this problem only appears after several hours of simulation, it is difficult (ie. computationally expensive) to find the minimum size of grid 3 required by making tests using successively larger grid 3 sizes.

5.1.5 Summary of simulation problems

As discussed previously, there were two major problems thought to contribute to simulation errors.

- The first was related to the simulation start time and initialization of fine grids in complex terrain. When the simulation was started at 16:00 PST, the model was in a cooling and stabilizing phase, and initially small, near surface temperature errors due to the initialization of fine grids grew with time. This problem disappeared when the model was initialized at 4:00 PST instead.

- The second problem, which wasn't satisfactorily resolved, is the lighter and more easterly than observed gap wind across the south of the domain. This seems to be related to terrain representation and resolution in the model. The Fraser Canyon is the only cross mountain channel resolved on grid 2 resulting in too much gap flow from the Fraser valley. Grid 3 was enlarged to better resolve other valleys as

a)   b)

c)   d)
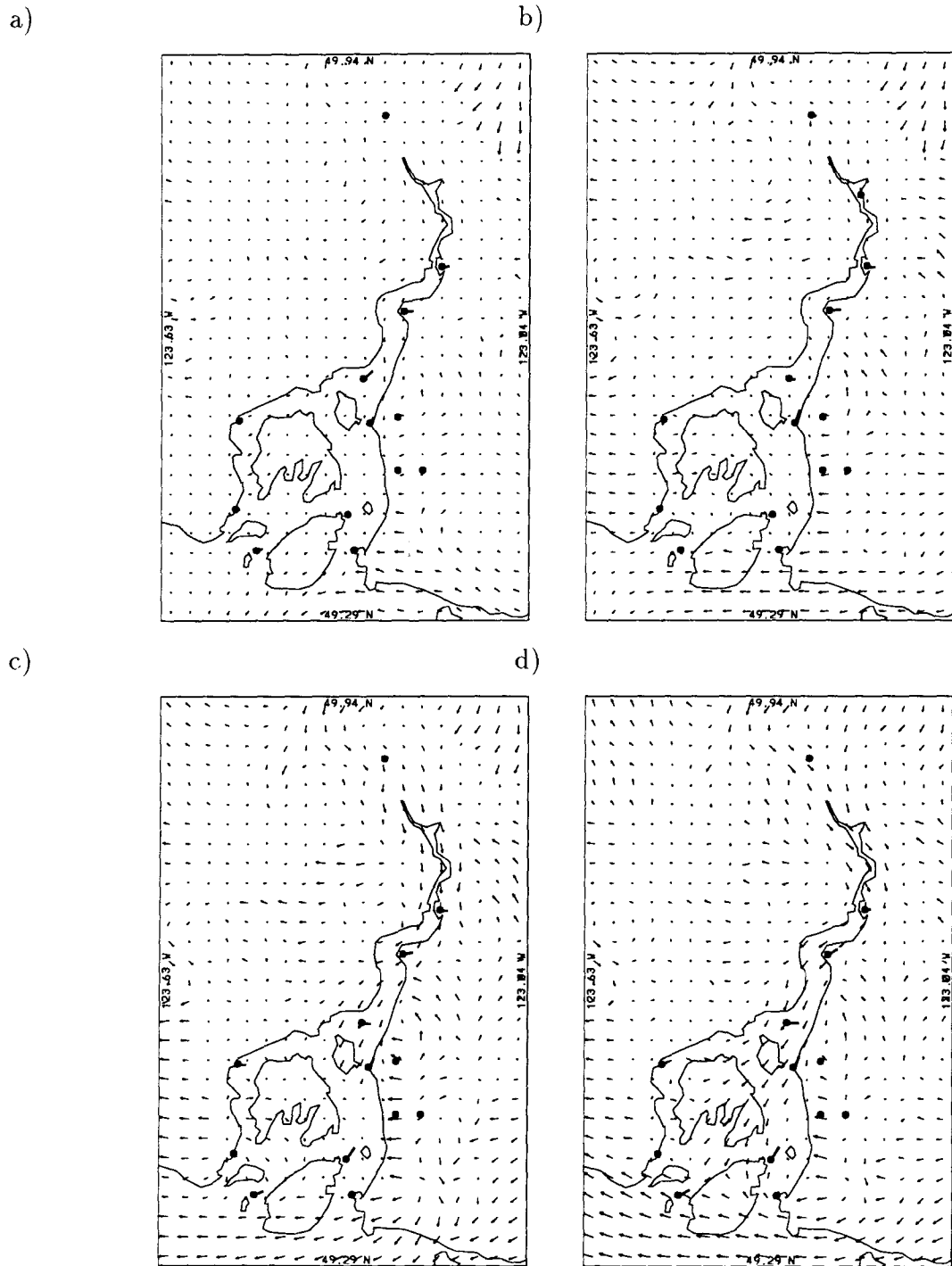
Figure 5.15: Surface winds at 3 hour intervals: a) January 30 14:00 PST; b) January 30 17:00 PST; c) January 30 20:00 PST; d) January 30 23:00 PST. Observed winds are indicated in bold with vectors that terminate in a ●. The spacing between vector tails represents 16 m s⁻¹.

a)

b)

c)

d)
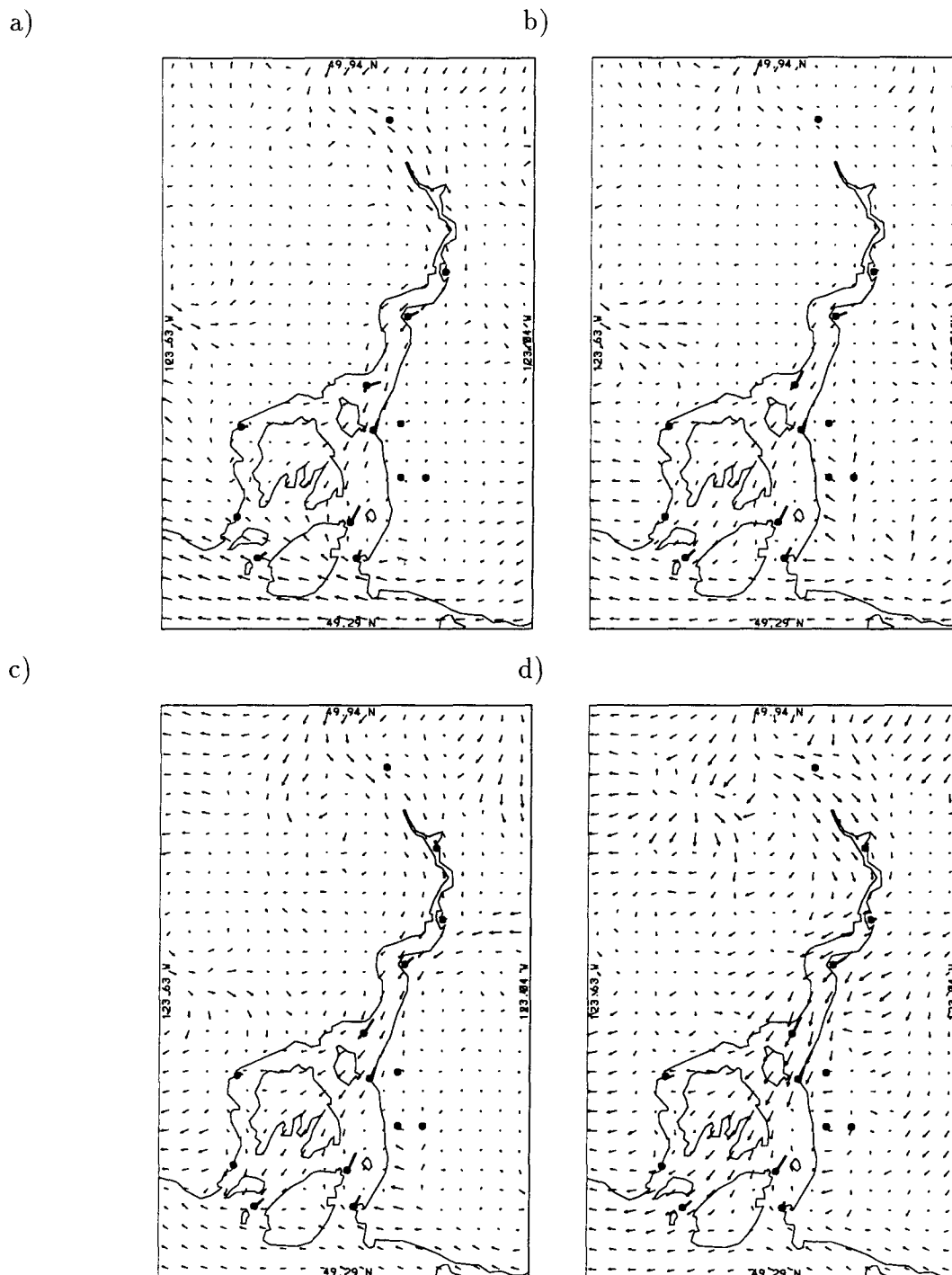
Figure 5.16: Surface winds at 3 hour intervals: a) January 31 02:00 PST; b) January 31 05:00 PST; c) January 31 08:00 PST; d) January 31 11:00 PST. Observed winds are indicated in bold with vectors that terminate in a •. The spacing between vector tails represents 16 m s^{-1}.

a)   b)

c)
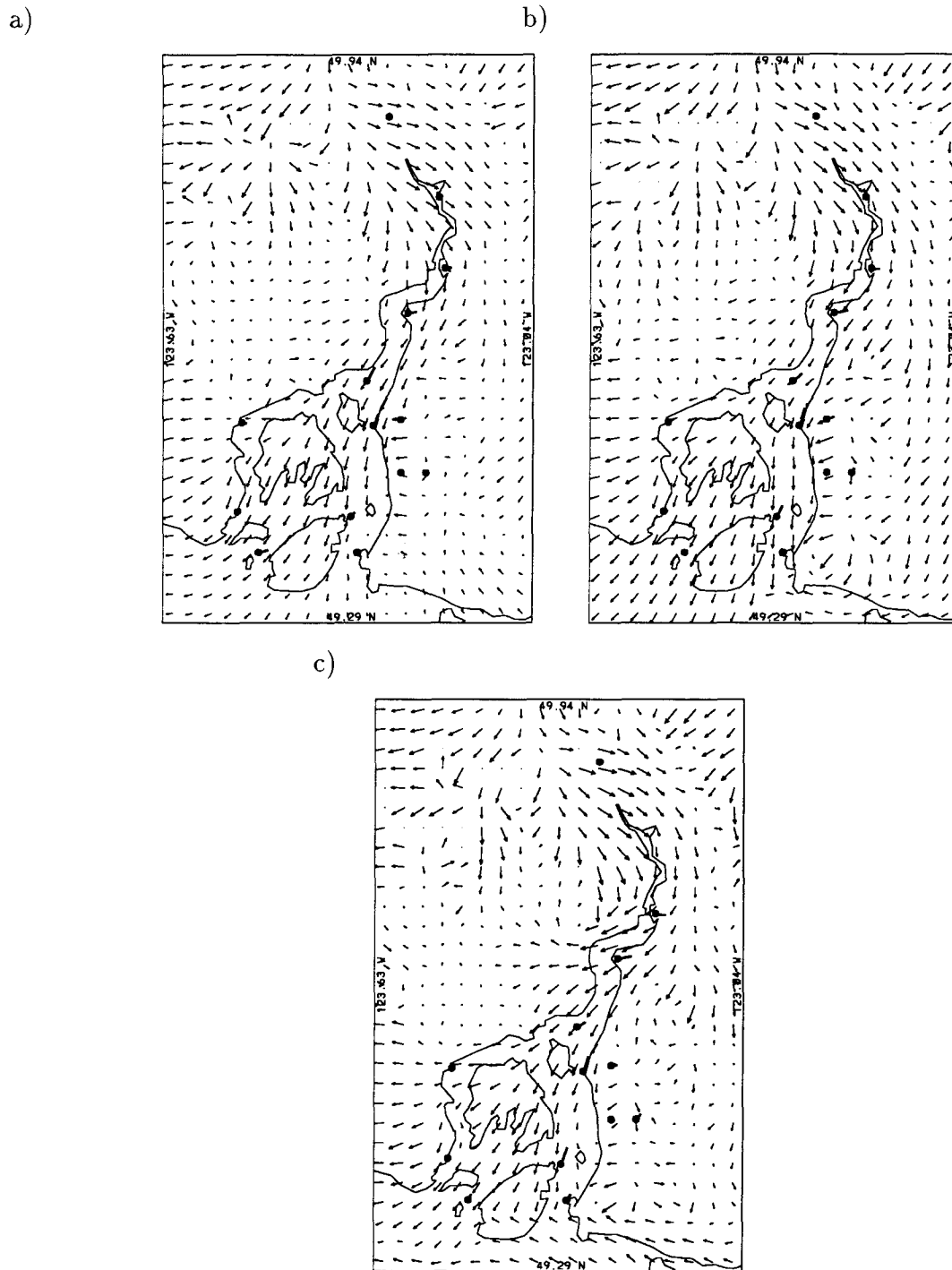
Figure 5.17: Surface winds at 3 hour intervals: a) January 31 14:00 PST; b) January 31 17:00 PST; c) January 31 20:00 PST. Observed winds are indicated in bold with vectors that terminate in a •. The spacing between vector tails represents 16 m s⁻¹.

well as the Fraser Canyon, but this was only partially successful, and limited by computing resources available.

Some features of an earlier run (run R, not shown), in which these errors had not yet developed, are worth mentioning. Run R, was initialized at 16:00, January 31 1988, 12 hours after run X. Consequently, the first problem described in the preceding paragraph, led to serious simulation errors after about 10 hours of simulation. These errors (too cold near the ground) however occurred on grid 3, quite a distance from the region of interest and did not seem to influence the simulation on grid 4 before this time. The second problem (too much airflow through the Fraser Canyon), which occurred after 6 to 8 hours of simulation, had not yet developed. Consequently, there is a period of time from hour 3 (after the model had properly initialized on all grids) to hour 7 (before the errors had time to develop) in the run R simulation, when simulated flow is closer to observed in the domain south near a time of maximum outflow. At this time, run X which was started 12 hours before, showed weak winds in the south due to the second problem, above. Despite an improved flow representation in the domain south, the overall wind verification for the entire domain did not show improvement over run X.

Despite these problems with flow representation in the south for part of the simulation, RAMS produced a gap wind simulation which qualitatively resembled observations over the rest of the domain. A statistical assessment of model performance showed that the RAMS gap wind simulation was as good or better than other mesoscale wind simulations which were available for comparison.

5.2 Analysis of model output

A very useful application of numerical model output, especially in situations where (generally expensive or impossible to obtain) complete data coverage is unavailable, is to use

model output to provide a detailed analysis. In this study, while a reasonably dense surface observation network was in place, the density and frequency of vertical sounding information was sparse. To extend observations and gain further insight into flow details, horizontal and vertical cross sections will next be presented and discussed.

5.2.1 Horizontal cross sections

Figures 5.18 to 5.20 are vector representations of run X winds from grid 4 in vertical level 4, at 3 hour intervals from January 30 1400 PST to January 31 17:00 PST. Level 4 of the model represents the layer between 215 and 347 m AGL, in terrain following coordinates. Superimposed on four of these plots are winds from the nearest AIRsonde™ time and elevation. These figures can be compared with figures 5.15 to 5.17 which show winds in the first hundred metres of the atmosphere. One should note however, that vector size is scaled differently in the two sets of figures – the lower layer wind has a maximum vector size (equal to the distance between the starting points of two adjacent vectors) of 16 m s^{-1}, while level 4 winds have a maximum vector size of 20 m s^{-1}. The two sets of figures are similar, with initially light flow on January 30 14:00 developing into a pulse of stronger gap flow by 23:00 (figure 5.15d and 5.18d), decreasing slightly after that, and then increasing again and becoming fully developed after January 31 11:00 PST. The winds on level 3 are also strong and easterly across the south, which seems to inhibit strong wind development there and divert it diagonally across Gambier and Bowen Island rather than down the main channel on the east side of the Sound.

a) b)

c) d)
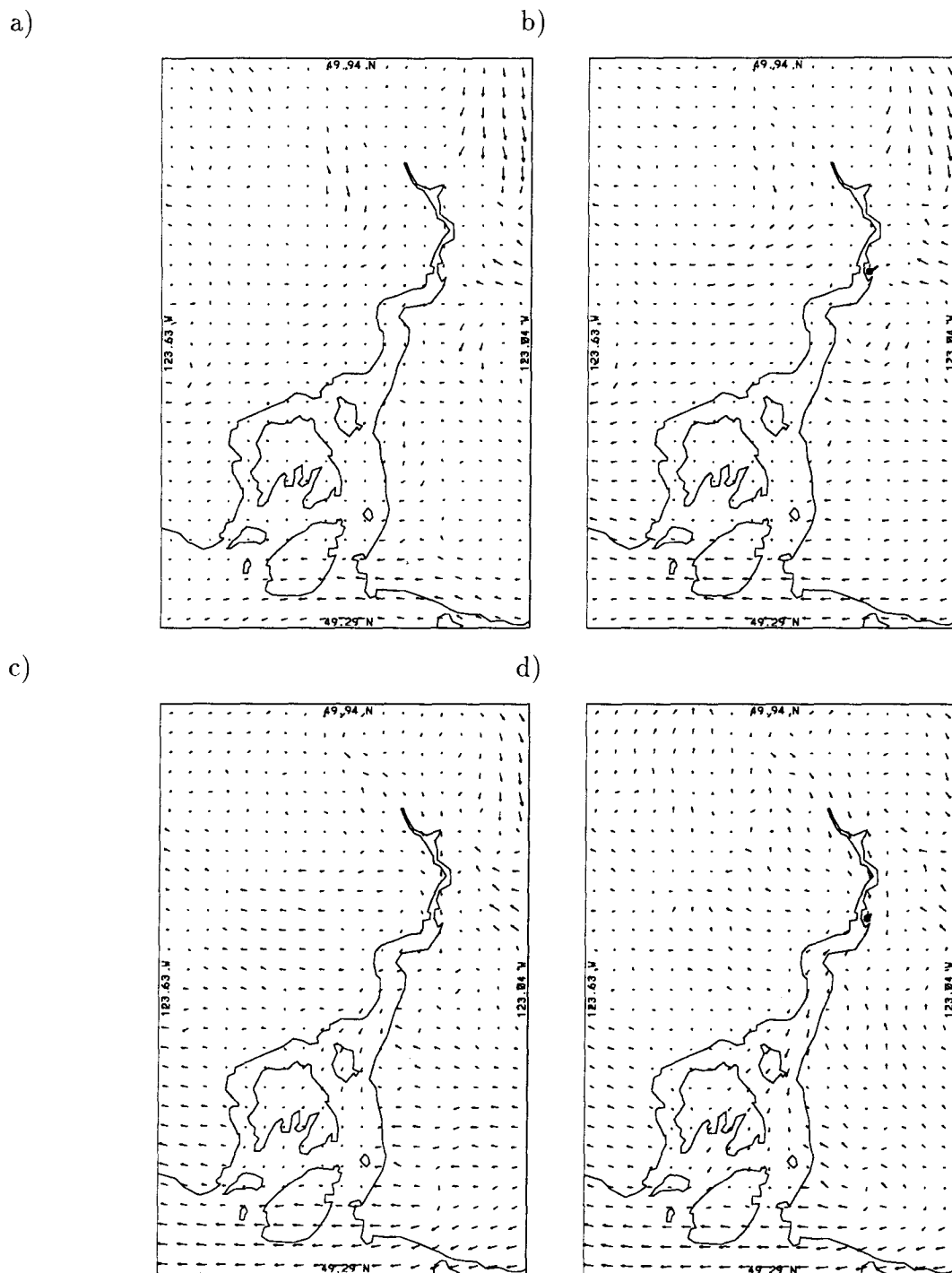
Figure 5.18: RAMS level 4 (279 m) winds at 3 hour intervals: a) January 30 14:00 PST; b) January 30 17:00 PST; c) January 30 20:00 PST; d) January 30 23:00 PST. The spacing between grid points indicates 20 m s^{-1}.

a) b)

c) d)
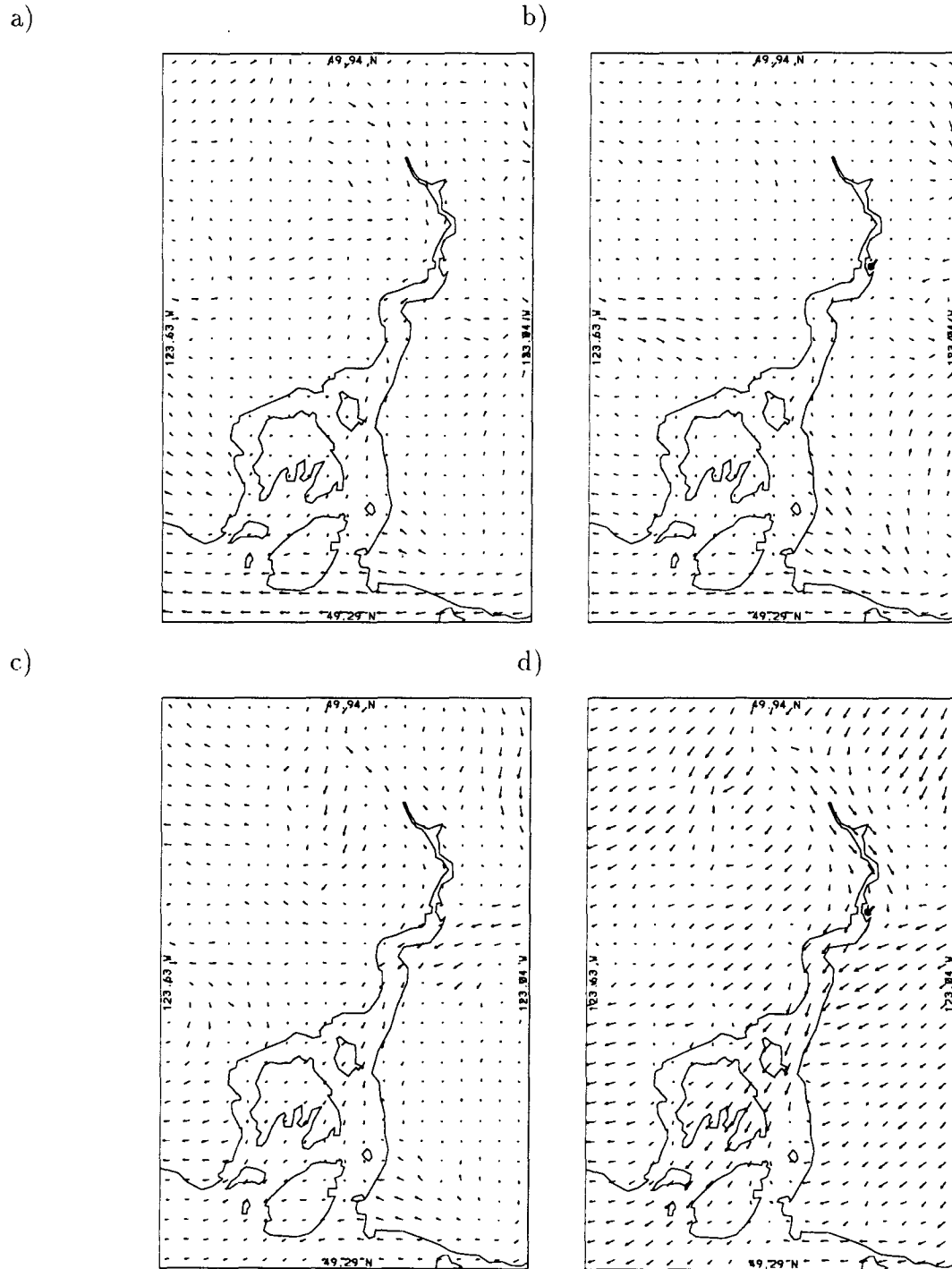
Figure 5.19: RAMS level 4 (279 m) winds at 3 hour intervals: a) January 31 02:00 PST; b) January 31 05:00 PST; c) January 31 08:00 PST; d) January 31 11:00 PST. The spacing between grid points indicates 20 m s^{-1}.

a)   b)

c)
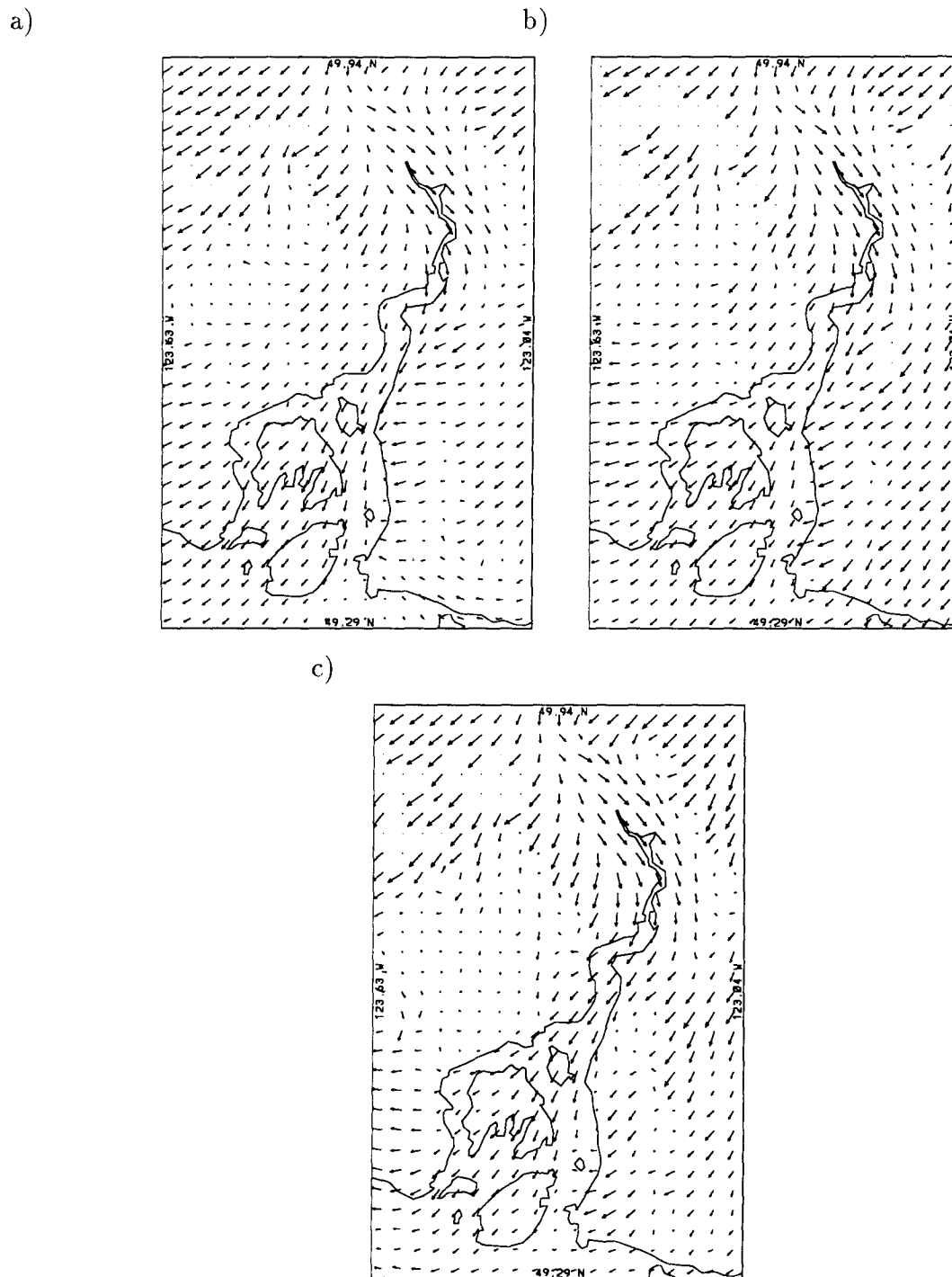
Figure 5.20: RAMS level 4 (279 m) winds at 3 hour intervals: a) January 31 14:00 PST;
b) January 31 17:00 PST; c) January 31 20:00 PST. The spacing between grid points
indicates 20 m s^{-1}.

5.2.2 Vertical cross sections

Vertical cross sections of potential temperature and down-channel component of wind have been prepared in *valley-following coordinates*. The valley-following coordinate system follows the main channel centre along the eastern side of Howe Sound. The model data used are from grid points which lie closest to the main channel axis. Interpolation of data between grid points to more closely follow the channel centre line seemed unnecessary given the density of model data points on grid 4. The exact path chosen for the main channel is indicated by the heavy solid line in figure 5.21. In the along channel vs. z (elevation) plane, wind nearly parallels isentropes (contours of potential temperature). This gives important flow information — whether it is descending or ascending, and whether layers are becoming thinner or thicker. The isentropes also give atmospheric vertical stratification and stability information.

Figures 5.22 to 5.32 show vertical cross sections of the down-channel and vertical components of wind as vectors, superimposed on contours of potential temperature at three hour intervals, for the lowest 2.6 km of the model domain (the first 13 levels of the model). The wind vector angle from the horizontal (but not the vector magnitude) is scaled to match the vertical exaggeration of the plots. Below the vertical cross sections are line plots of Froude number along the down-channel axis. The Froude number is calculated from RAMS output, and will be described later. At most times one can note a clearly marked layer below 1.5 km elevation where air is less stable, and down-channel wind component is larger than above this elevation. As the simulation progresses, structure in the layer below 1.2 km elevation becomes more distinct, and a core of outflowing air begins to form (figure 5.24). By January 30 23:00 PST (figure 5.25), a distinct jet of outflowing air bounded by the descending 273 K isentrope with maximum down-channel speeds of more than 10 m s^{-1} has formed below 1 km elevation. At this time, layers of
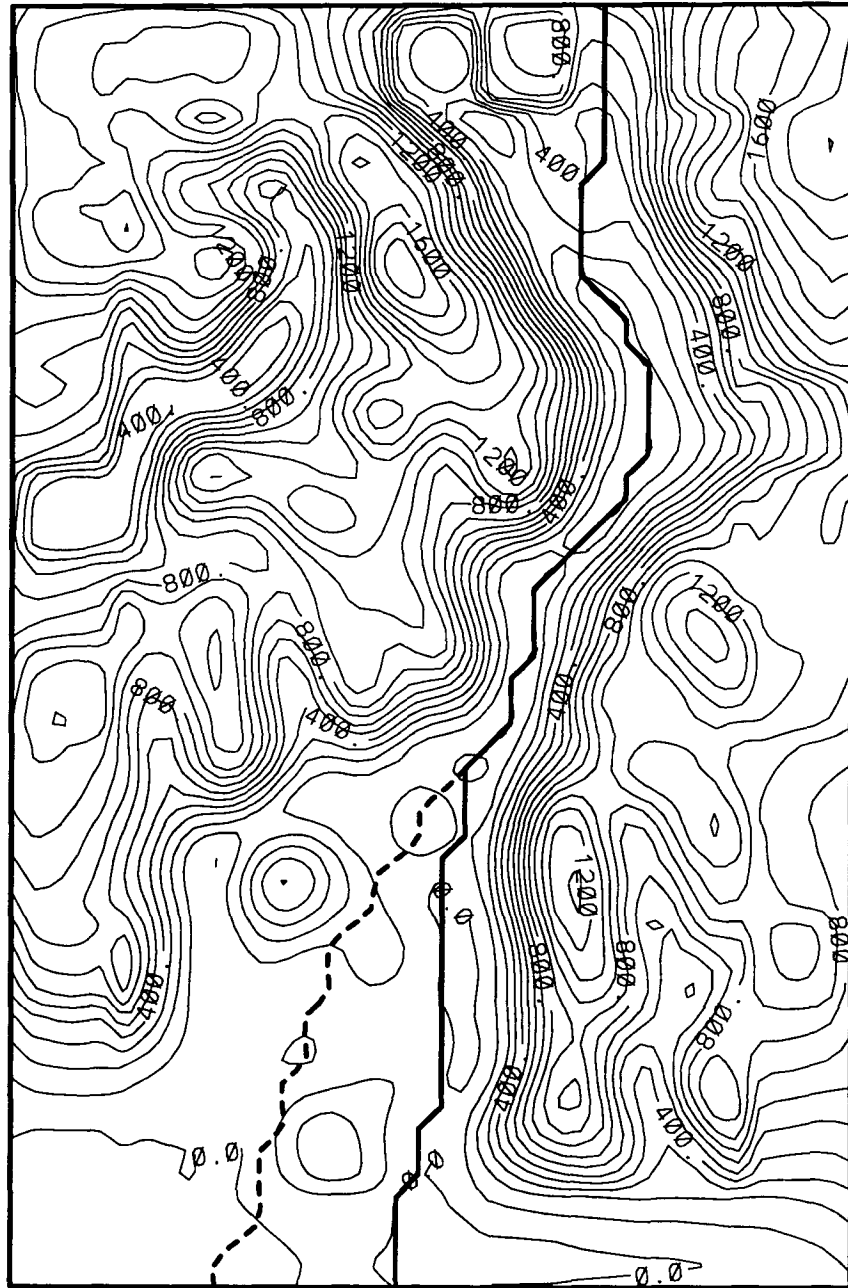
Figure 5.21: Rams grid 4 contoured terrain with heavy solid line indicating the channel centre line used in *down-channel* vertical profiles. The dashed line indicates the *down core* direction used in some vertical profiles.

increased stability also observed in the vertical profile (figure 5.12) are apparent above 1 km elevation. At the termination of this jet (near the down-channel (y) coordinate of between -150 and -160 km in figure 5.25), a zone of rapid deceleration and wind reversal is co-located with ascending isentropes. This resembles a hydraulic transition from subcritical to supercritical flow (in the zone of descending isentropes), which becomes subcritical again at a hydraulic jump (in the zone of ascending isentropes). While hydraulic theory is most commonly applied to two layer flow problems involving liquids such as water in a channel, enough apparent similarity exists between numerical model output and the flow of water in a channel, to suggest than application of hydraulic theory to this class of phenomenon would yield useful results. In fact hydraulic theory which has been previously used to account for related severe downslope windstorms (Long, 1954), is presently enjoying a resurgence in popularity (Durran, 1986). This will be discussed in more detail in the following section describing the Froude number analysis, and in chapter 7.

After January 30 23:00 PST, the flow intensity becomes somewhat less, and then increases once again reaching a maximum by January 31 11:00 PST (figure 5.29), with a core speed of more than 15 m s^{-1} at about 200 m elevation. At this time, there is a second descending layer which has formed to the north with down-channel winds of more than 11 m s^{-1}. This feature continues to develop at 14:00 PST (figure 5.30), becoming the dominant feature by 17:00 PST (figure 5.31), and apparently propagating across the entire domain by the end of the simulation at 20:00 PST as shown in figure 5.32.

Above 1.5 km elevation, the winds are no longer strongly channelled by topography, so that the valley following coordinate system is not an appropriate frame of reference. Because of this, small changes in the wind direction can result in changes in the down channel wind component which are not representative of wind speed changes. This accounts, at least in part, for the large variation in the down channel wind component
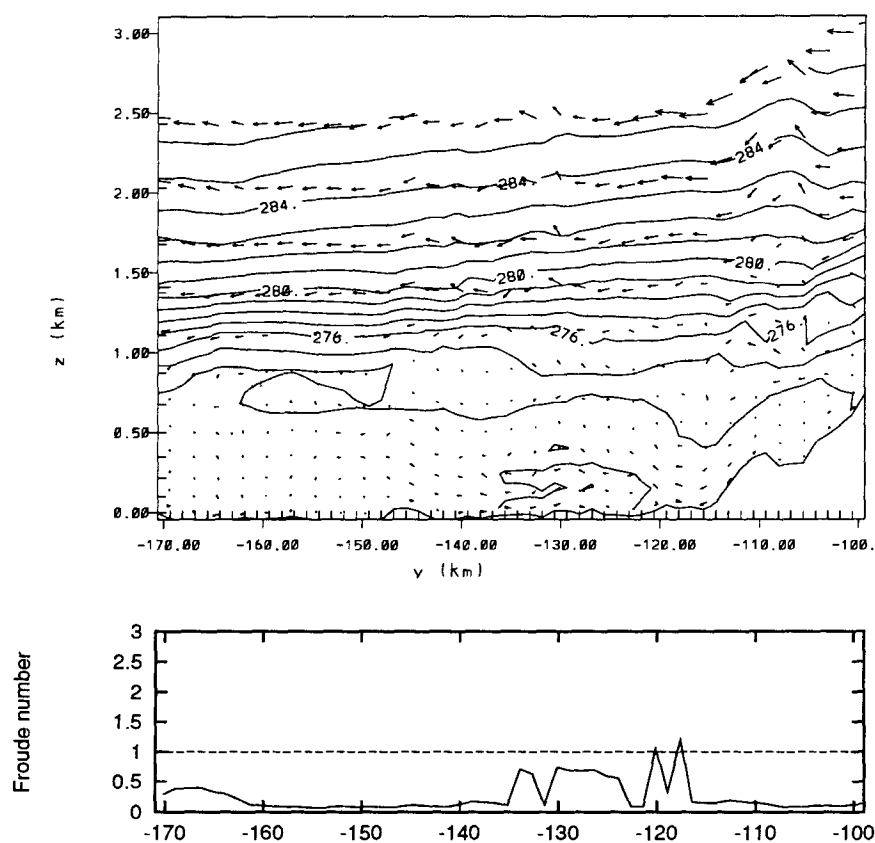
Figure 5.22: Vertical Cross section oriented along the main channel of Howe Sound for January 30 14:00 PST. The down-channel wind component as a vector superimposed on contours of potential temperature, is above a plot of the Froude number.

The horizontal spacing between vector tails represents 11 m s^{-1}. Vertical exaggeration is 10X.
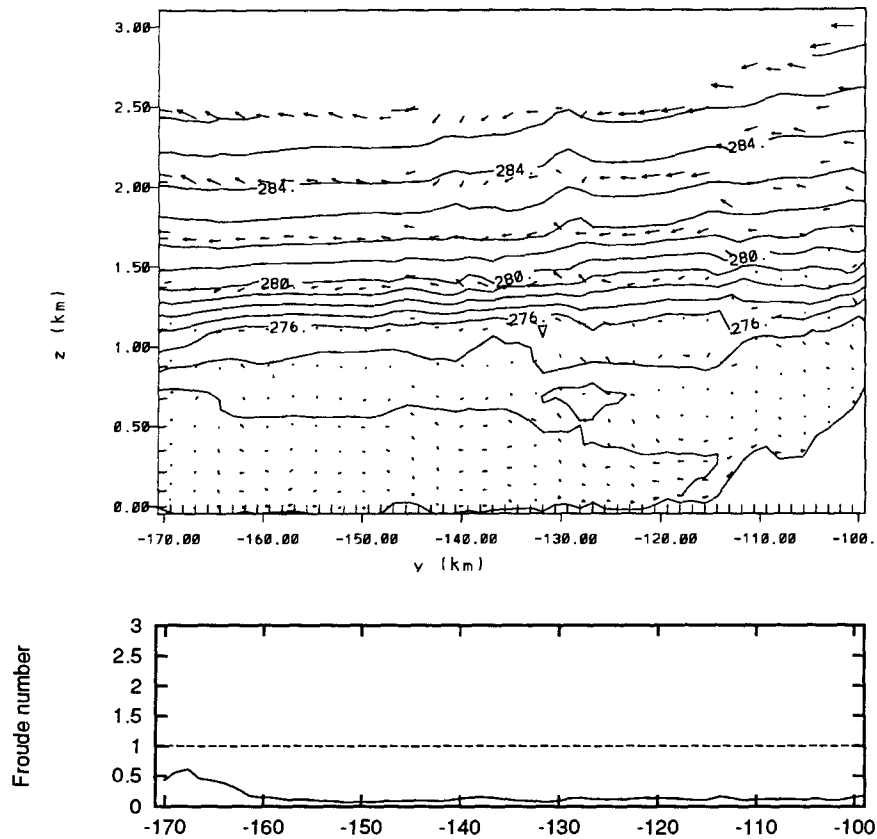
Figure 5.23: Vertical Cross section oriented along the main channel of Howe Sound for January 30 17:00 PST. The down-channel wind component as a vector superimposed on contours of potential temperature, is above a plot of the Froude number.

The horizontal spacing between vector tails represents 11 m s^{-1}. Vertical exaggeration is 10X.
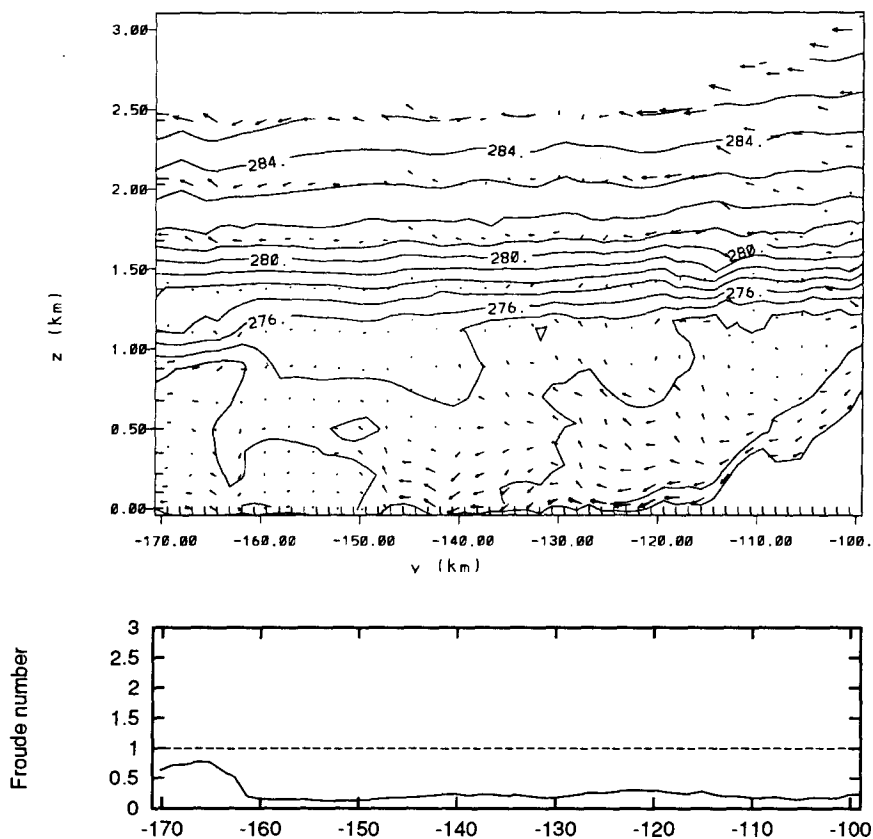
Figure 5.24: Vertical Cross section oriented along the main channel of Howe Sound for January 30 20:00 PST. The down-channel wind component as a vector superimposed on contours of potential temperature, is above a plot of the Froude number. The horizontal spacing between vector tails represents 11 m s^{-1}. Vertical exaggeration is 10X.
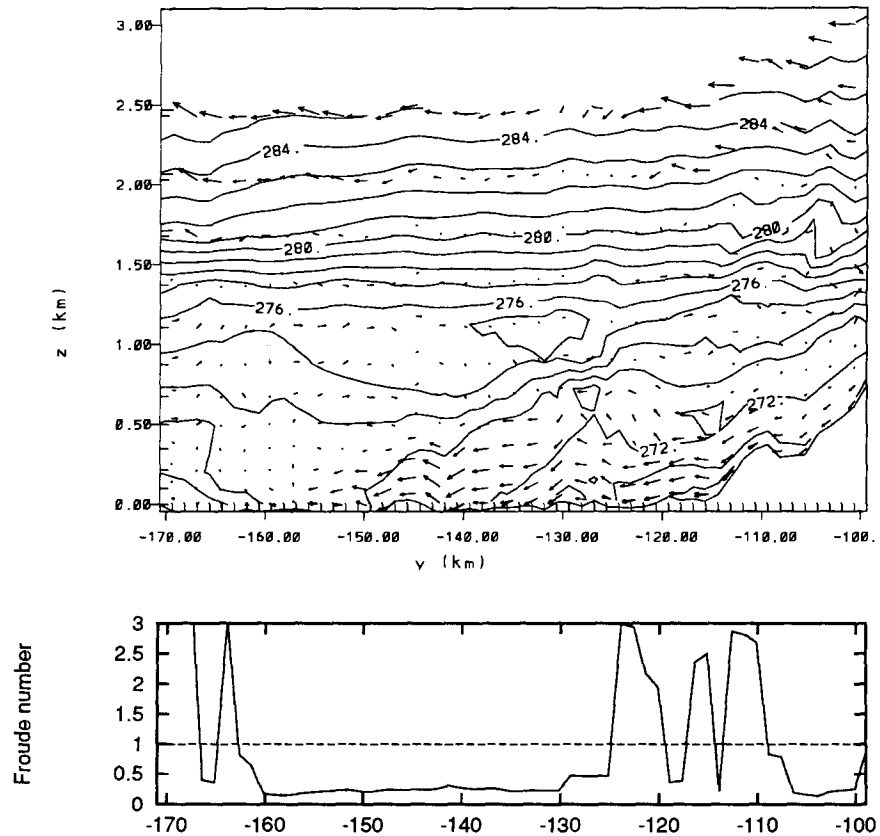
Figure 5.25: Vertical Cross section oriented along the main channel of Howe Sound for January 30 23:00 PST. The down-channel wind component as a vector superimposed on contours of potential temperature, is above a plot of the Froude number. The horizontal spacing between vector tails represents 11 m s^{-1}. Vertical exaggeration is 10X.
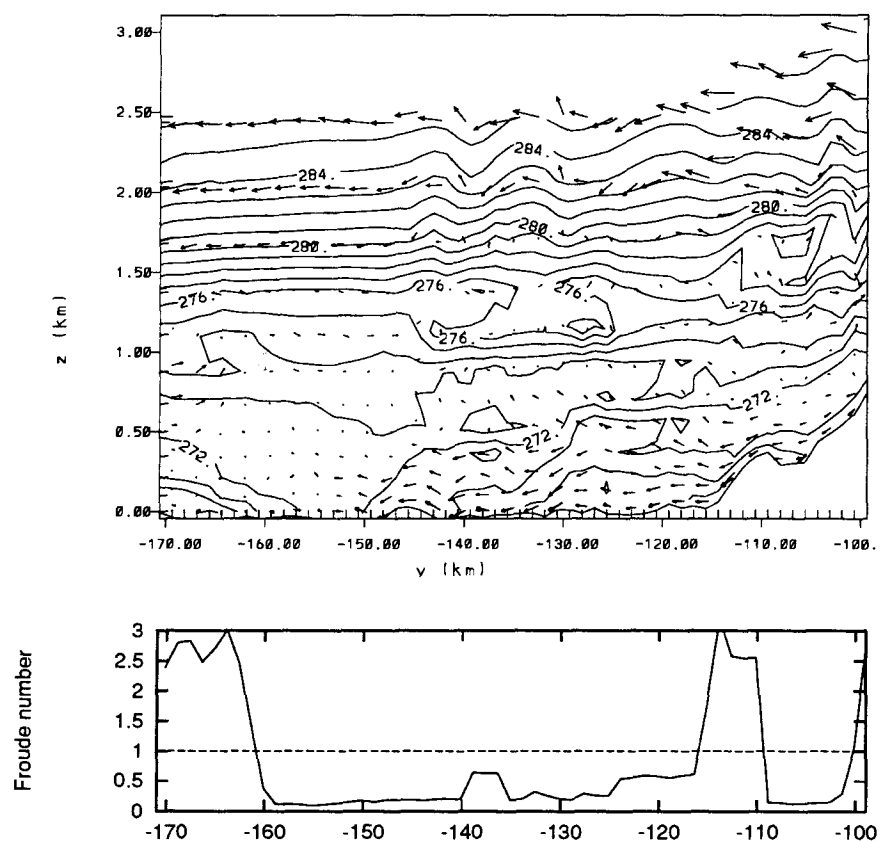
Figure 5.26: Vertical Cross section oriented along the main channel of Howe Sound for January 31 02:00 PST. The down-channel wind component as a vector superimposed on contours of potential temperature, is above a plot of the Froude number. The horizontal spacing between vector tails represents 11 m s^{-1}. Vertical exaggeration is 10X.
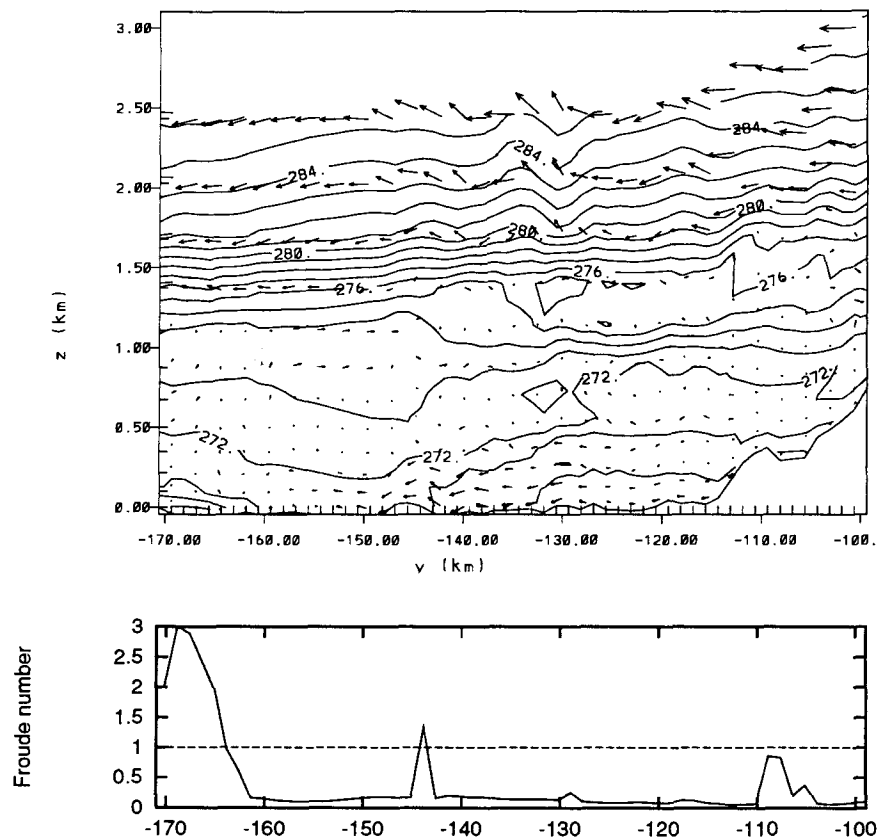
Figure 5.27: Vertical Cross section oriented along the main channel of Howe Sound for January 31 05:00 PST. The down-channel wind component as a vector superimposed on contours of potential temperature, is above a plot of the Froude number. The horizontal spacing between vector tails represents 11 m s^{-1}. Vertical exaggeration is 10X.
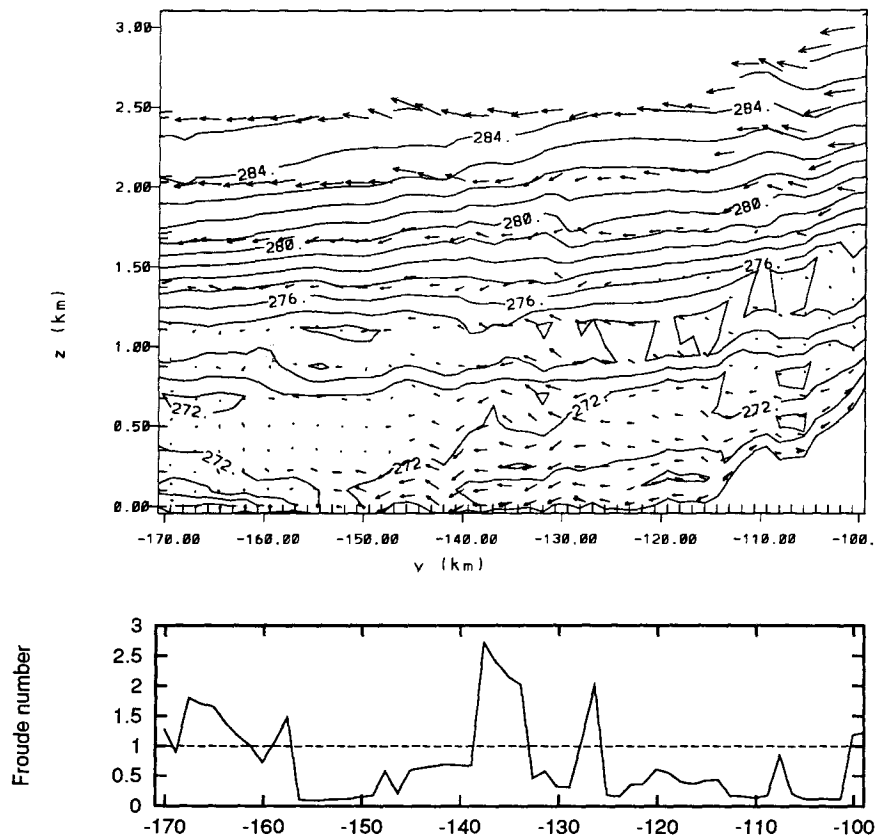
Figure 5.28: Vertical Cross section oriented along the main channel of Howe Sound for January 31 08:00 PST. The down-channel wind component as a vector superimposed on contours of potential temperature, is above a plot of the Froude number. The horizontal spacing between vector tails represents 11 m s^{-1}. Vertical exaggeration is 10X.
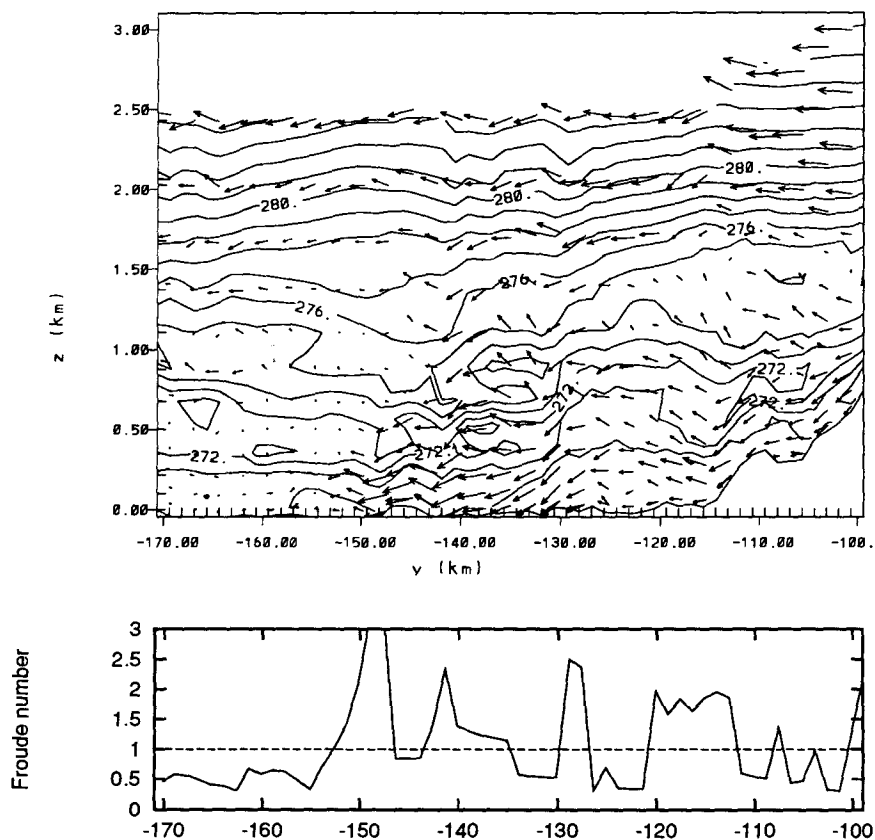
Figure 5.29: Vertical Cross section oriented along the main channel of Howe Sound for January 31 11:00 PST. The down-channel wind component as a vector superimposed on contours of potential temperature, is above a plot of the Froude number. The horizontal spacing between vector tails represents 11 m s^{-1}. Vertical exaggeration is 10X.
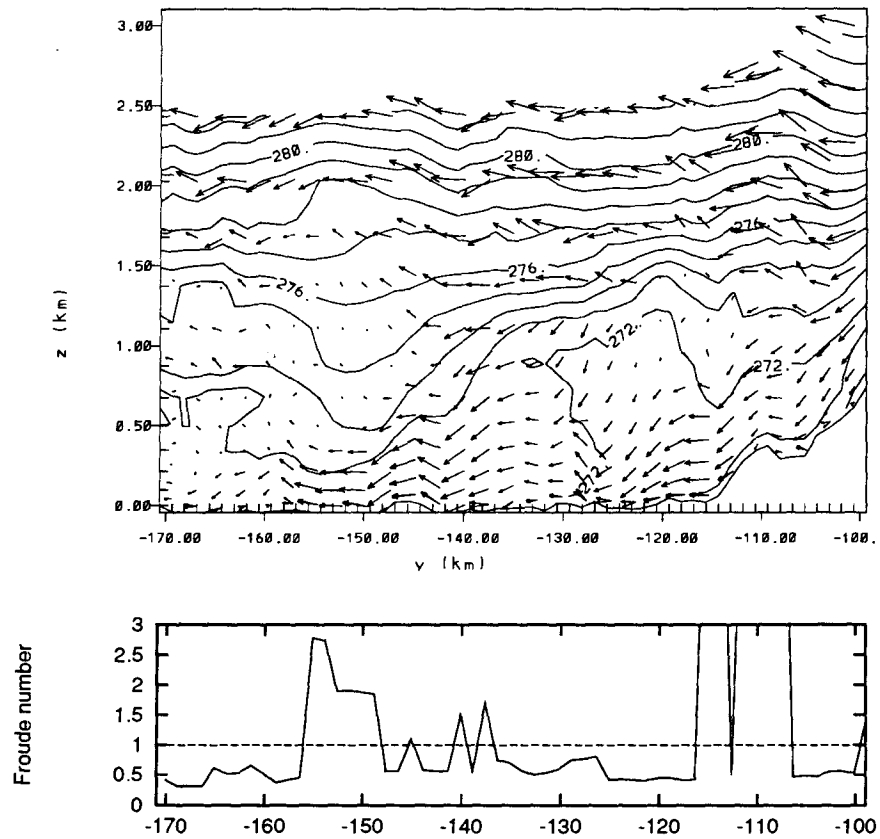
Figure 5.30: Vertical Cross section oriented along the main channel of Howe Sound for January 31 14:00 PST. The down-channel wind component as a vector superimposed on contours of potential temperature, is above a plot of the Froude number. The horizontal spacing between vector tails represents 11 m s^{-1}. Vertical exaggeration is 10X.
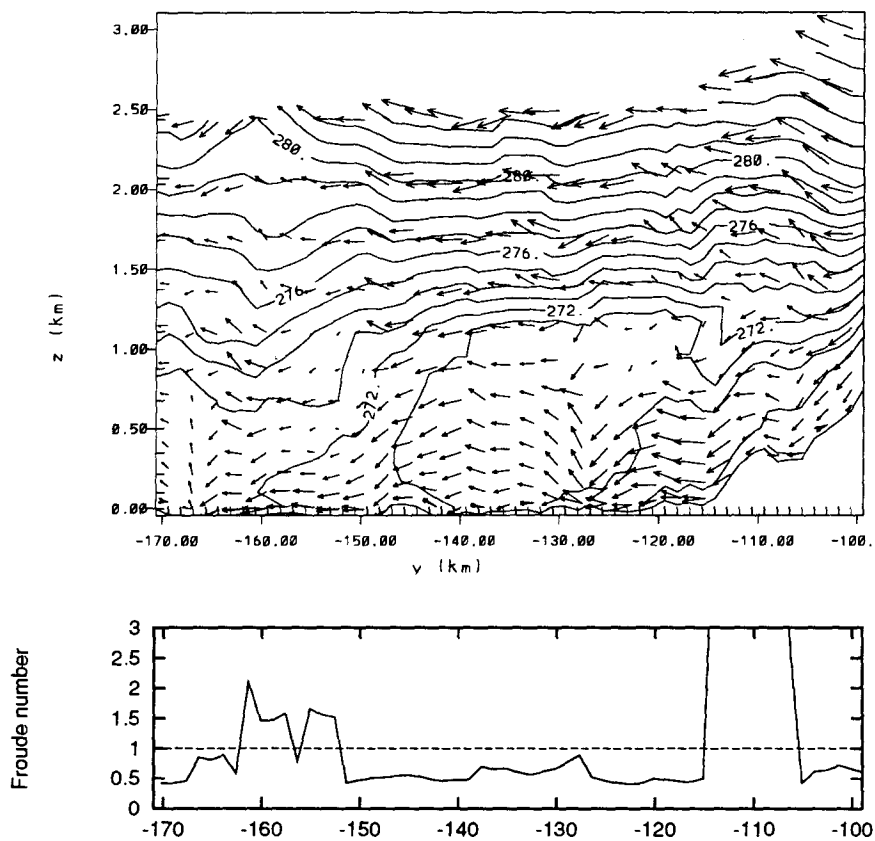
Figure 5.31: Vertical Cross section oriented along the main channel of Howe Sound for January 31 17:00 PST. The down-channel wind component as a vector superimposed on contours of potential temperature, is above a plot of the Froude number. The horizontal spacing between vector tails represents 11 m s^{-1}. Vertical exaggeration is 10X.
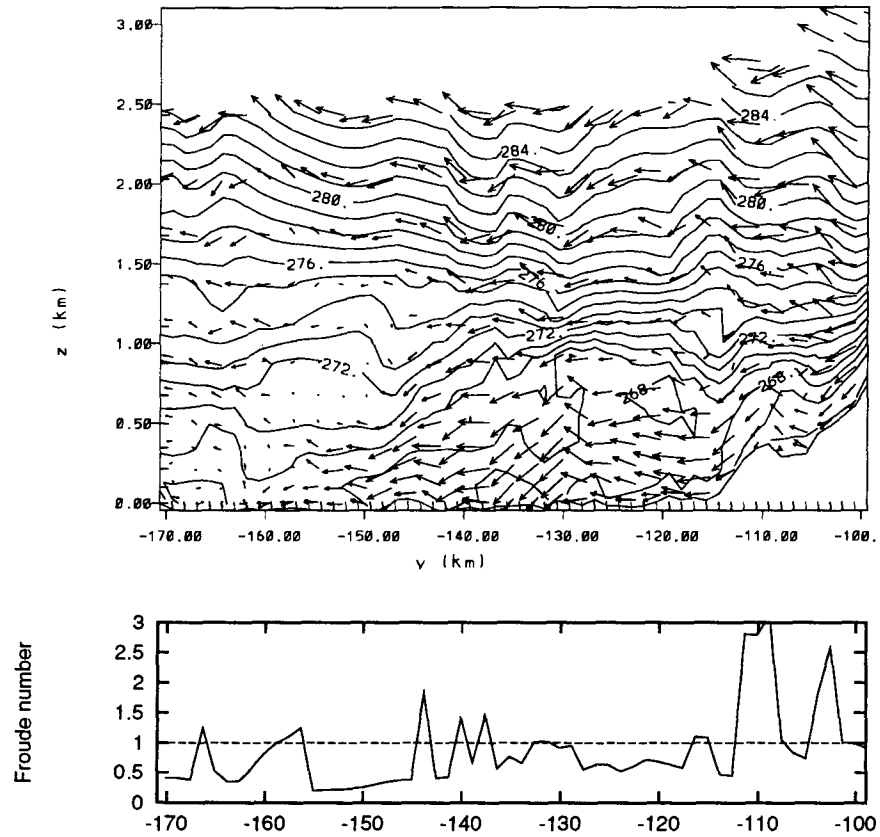
Figure 5.32: Vertical Cross section oriented along the main channel of Howe Sound for January 31 20:00 PST. The down-channel wind component as a vector superimposed on contours of potential temperature, is above a plot of the Froude number. The horizontal spacing between vector tails represents 11 m s^{-1}. Vertical exaggeration is 10X.

above this elevation, which can be seen in the vertical cross sections

Since the core of strong winds, in this simulation, is not directly along the main channel in the southern part of the domain, vertical profiles of potential temperature and *down core wind component* were computed and contoured for January 30, 23:00 PST (figure 5.33) and January 31, 11:00 PST (figure 5.34). In this case "down core" is the same as down-channel except in the south where the core cuts diagonally across Gambier and Bowen Islands. The "down core" path is shown by the heavy dashed line in figure 5.21. The figures showing the "down core" wind and temperature profiles are very similar to "down channel" plots of the same time, except as expected the zone of strong winds extends further south.
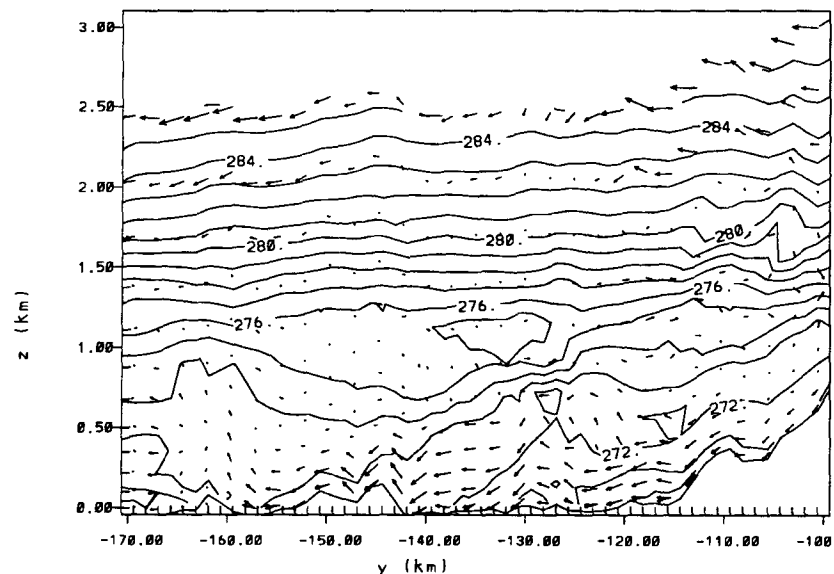
Figure 5.33: Vertical Cross section oriented along the core of strongest winds for January 30 23:00 PST. Down-channel wind component as a vector superimposed on contours of potential temperature. The horizontal spacing between vector tails represents 11 m s^{-1}. Vertical exaggeration is 10X.

Another interesting feature which can be seen in the vertical cross sections is a marked
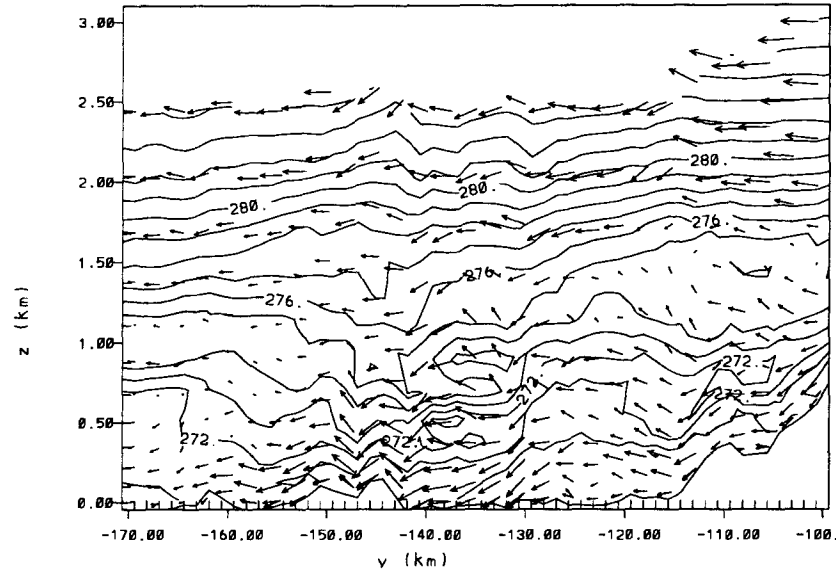
Figure 5.34: Vertical Cross section oriented along the core of strongest winds for January 31 11:00 PST. Down-channel wind component as a vector superimposed on contours of potential temperature. The horizontal spacing between vector tails represents 11 m s^{-1}. Vertical exaggeration is 10X.

diurnal change in the structure and character of outflowing air. During the night, nocturnal surface cooling and consequent atmospheric stabilization near the ground, possibly combined with hydraulic effects discussed in the following section, results in a decrease in the depth of the mechanically mixed surface-based neutral layer to about 800 m elevation (see figures 5.24 to 5.29). As solar radiation heats the ground during the day, convection mixes the low level momentum to a greater depth increasing the depth of the surface based neutral layer to about 1200 m (figures 5.30 to 5.31).

5.2.3 Froude number analysis

Because there are indications that gap wind flow in Howe Sound is similar to the hydraulic flow of water in a channel, Froude numbers from RAMS output were computed and plotted. The Froude number is dimensionless and defined as the ratio of fluid speed to

the speed of a gravity wave traveling on the fluid interface. In the water analogy, the fluid speed is the current, and the gravity wave speed is that of a long surface water wave. In gap winds, the fluid speed is the mean wind speed in the layer of outflowing air, and the gravity wave speed is that of a gravity wave traveling along the "interface" defined by the stable layer which surmounts the outflowing air. An assumption is made that this stable layer can be approximated by a step change in temperature, which is the simplest way of treating the problem. By referring to figures 5.24 to 5.29 a distinct stable layer can be seen. A more complete treatment would consider the air as a continuously stratified fluid (Smith, 1985; Smith and Sun, 1987) rather than a fluid of two distinct layers.

The Froude number is defined as:

$$F = \frac{U}{\sqrt{g'h}} \tag{5.6}$$

where: F is the Froude number; U is the mean speed of outflowing air; g' is the effective or reduced gravity defined by:

$$g' = \frac{\theta_{TOP} - \theta_{BOT}}{\theta_{BOT}} \times g \tag{5.7}$$

g is gravitational acceleration, 9.8 m s^{-2}; θ_{TOP} is the potential temperature at the top of the stable layer; θ_{BOT} is the average potential temperature in the lower (outflowing) layer; h is the height of the outflowing layer and is the layer over which U is averaged.

To compute h from RAMS output, it is found as the height from the ground to the inflection point in the θ vs. Z profile (ie. maximum in $\frac{d^2\theta}{dZ^2}$ – which is where the slope of θ vs. z changes most rapidly) where potential temperature begins increasing with height. This leads to an arbitrary definition of Froude number which forces a two layer structure on a continuously stratified fluid. This definition of Froude number is used in hydraulic modelling discussed in chapter 7. It is expected that there will be error in these automatically computed Froude numbers, so that they should be interpreted and used as an index only.

Flows with Froude number less than 1.0 have gravity wave speed greater than the fluid speed and are termed *subcritical*. In this case information (disturbances in the flow) can propagate both up and downstream as gravity waves. Flows with Froude number greater than 1.0 have fluid speed greater than gravity wave speed and are *supercritical*. In this case information can only propagate downstream. Flows with Froude numbers equal to 1.0 are *critical*. In this case the gravity wave speed equals the fluid speed. The flow has markedly different characteristics depending upon whether it is sub- super- or critical. In particular, according to hydraulic theory discussed in more detail in chapter 7, strongest gap winds will be associated with a supercritical flow regime. Plots of Froude number are shown below the vertical cross sections in figures 5.22 - 5.32. Horizontal plots of Froude numbers are computed and displayed at three hour intervals in figures 5.35 to 5.37. In these figures, areas with Froude number greater than .5 are enclosed by a dashed line, whereas areas which are supercritical are shaded. Light cross-hatched areas have Froude numbers between 1.0 and 2.0, whereas heavy cross-hatched areas have Froude numbers greater than 2.0.

Initially (figure 5.35a-c) only some areas over high terrain are supercritical. However as the gap flow develops (figure 5.35d) patches of supercritical flow, north of Squamish, and downstream of Gambier and Bowen Island begin to form. There is then a decrease in the extent of supercritical flow in Howe Sound around January 31, 2:00 to 5:00 PST except for the flow across the southern part of the Sound which is due to the too-strong easterly flow from the Fraser valley. Corresponding to the increase in gap wind flow apparent in figures 5.16d — 5.17 and figures 5.29 — 5.32, there is an increase in the supercritical area oriented along the main channel and diagonally across Gambier and Bowen Islands after January 30, 23:00 PST (shown in figures 5.36d and 5.37). This corresponds to the area of strong gap wind flow shown in figure 5.16d and 5.17. In comparing Froude number plots with the vertical cross section plots in shown in figures 5.22 to 5.32 it can

a) b)

Froude number from RAMS - January 30, 1400 PST

Froude number from RAMS - January 30, 1700 PST

c) d)

Froude number from RAMS - January 30, 2000 PST

Froude number from RAMS - January 30, 2300 PST
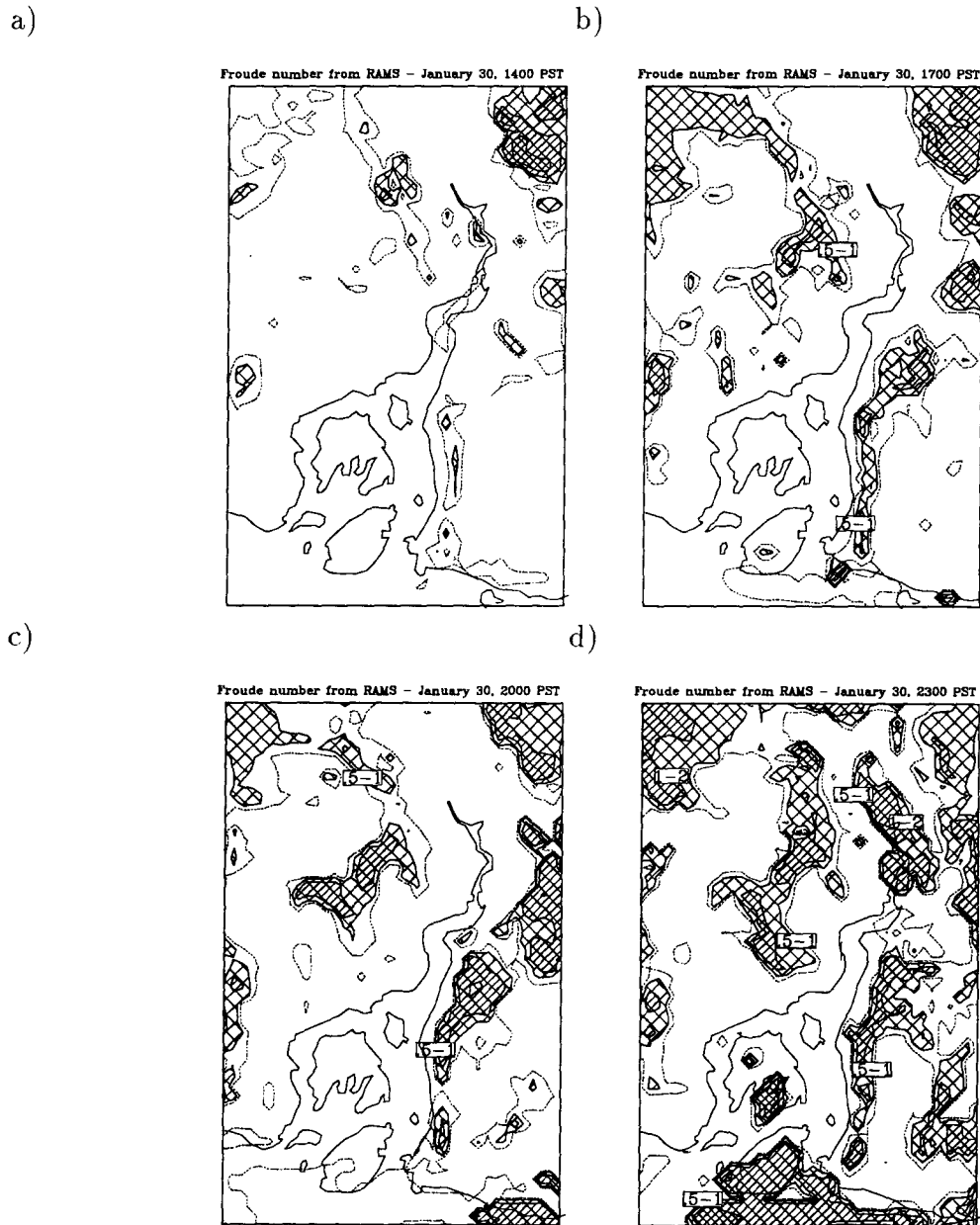
Figure 5.35: Froude number at 3 hour intervals: a) January 30 14:00 PST; b) January 30 17:00 PST c) January 30 20:00 PST; d) January 30 23:00 PST.
Dashed line encloses regions with Froude number greater than .5. Light cross hatched areas have Froude numbers between 1.0 and 2.0. Heavy cross hatched areas have Froude numbers greater than 2.0.

a)

b)

c)

d)
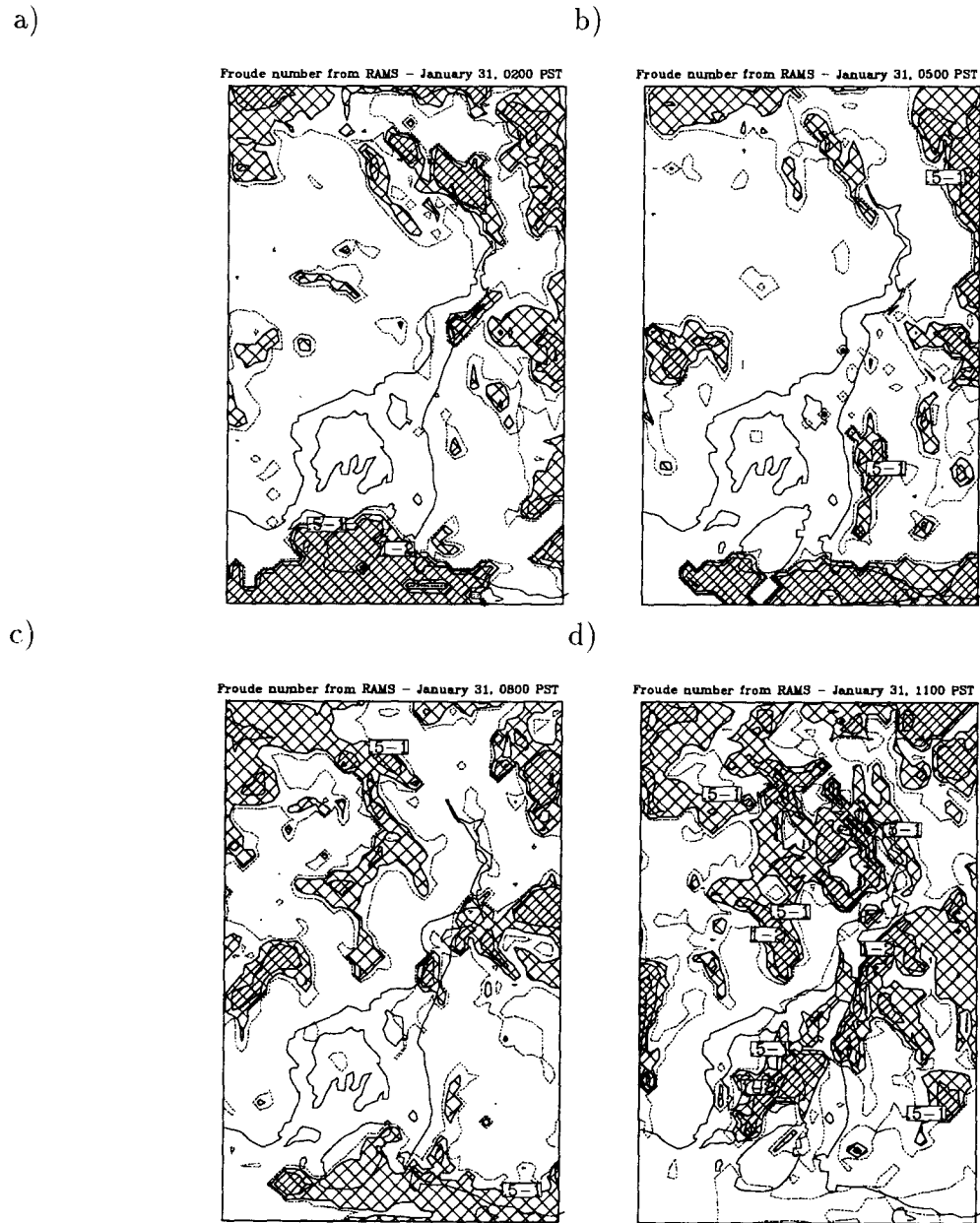
Figure 5.36: Froude number at 3 hour intervals: a) January 31 2:00 PST; b) January 31 5:00 PST; c) January 31 8:00 PST; d) January 31 11:00 PST. Shading as in figure 5.35.

a)   b)

c)
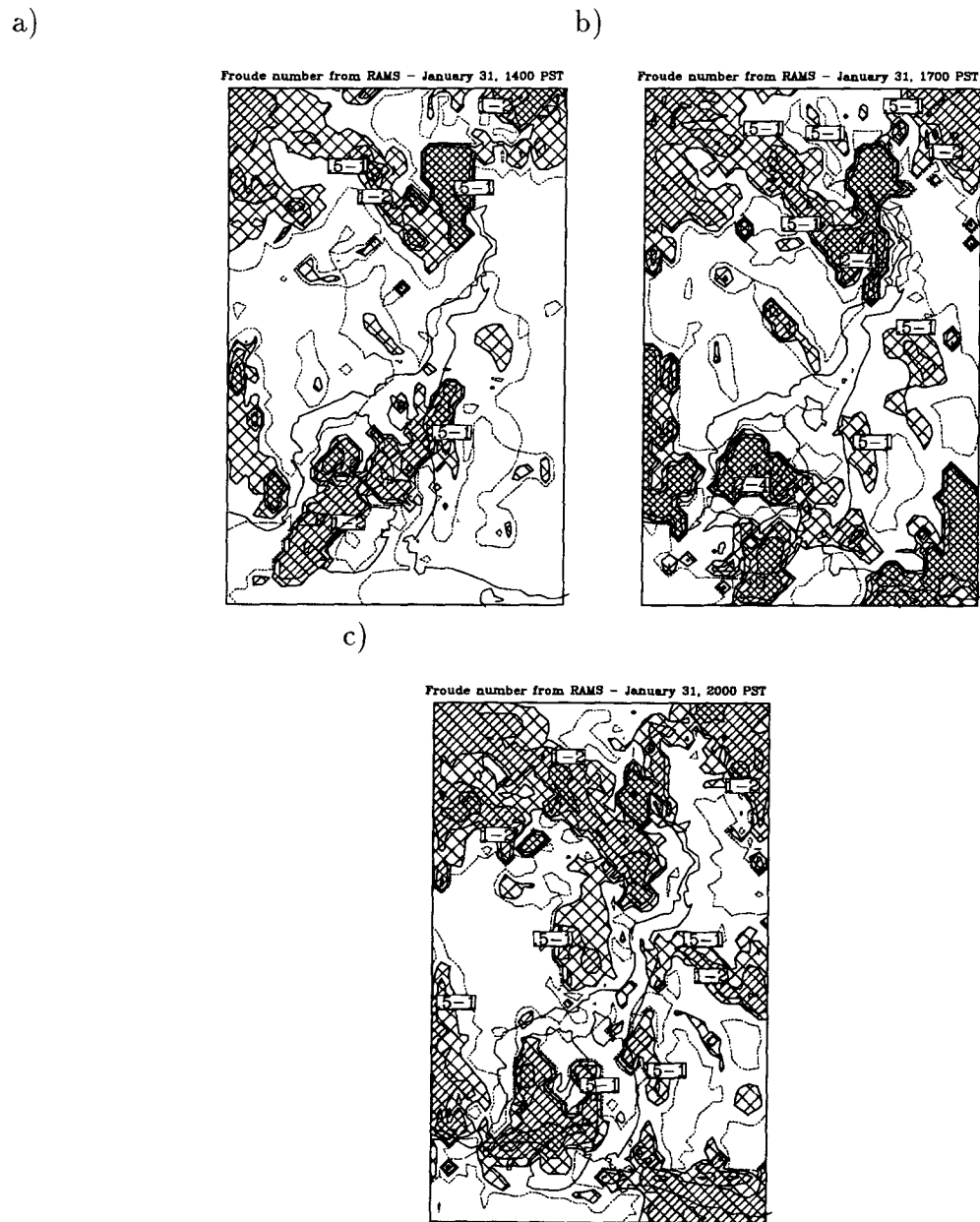
Figure 5.37: Froude number at 3 hour intervals: a) January 31 14:00 PST; b) January 31 17:00 PST; c) January 31 20:00 PST.
Shading as in figure 5.35.

be seen that zones of supercritical flow correspond to regions of descending isentropes and accelerating flow in the vertical cross sections. This is expected from the definition of Froude number. High Froude numbers across the south of many of these figures are from strong easterly flow originating in the Fraser valley, and not related to Howe Sound gap wind.

The Froude number analysis of RAMS output shown in figures 5.35 to 5.37 and discussed above, indicates a close relationship between gap wind intensity and the Froude number. This lends support to the notion that the essence of gap winds may be contained in hydraulic theory, which is a great simplification to the 3D quasi-Boussinesq system modelled by RAMS.

5.3 Summary of numerical modelling results

This chapter has quantitatively and qualitatively compared observations with RAMS model output for the case under consideration. The results show that RAMS is capable of producing a plausible gap wind simulation which matches conceptual theory and to a somewhat lesser extent, observations. Modelled surface temperature over the entire domain, and wind in the northern and central part of the domain are most similar to observations both in magnitude and temporal trend. Modelled vertical profiles of potential temperature and wind at Squamish, were very close to observations. Problems with simulated wind in the south were thought to be due to inadequate resolution of major valleys and fjords (except the Fraser valley) on grid 2. This resulted in a concentration of outflow through the grid 2 Fraser valley and consequently via the grid interaction scheme, stronger than observed modelled easterly wind across the southern grid 4 domain. This gave modelled winds a larger than observed easterly component and accounts for the poor comparison with observations for part of the simulation in this region. The increased modelled gap wind depth which would result from enhanced cold air flow through the Fraser valley, could also account (from hydraulic theory) for lighter than observed winds near the mouth of Howe Sound.

Following the evaluation of performance, further analysis of RAMS output was carried out to extend observations particularly in the vertical, to improve understanding of gap winds. Vertical cross sections of wind and potential temperature showed three clearly marked layers: the first, a zone of strongest gap wind flow below about 1 km with neutral stability due to mechanical mixing; the second, a zone of less strong gap wind and increased stability from about 1 to 2.5 km ; and the third, ambient air above 2.5 km, a stable zone uninfluenced by the gap flow below. Vertical cross sections indicated a possible analogy between gap winds, and the hydraulic flow of water in a channel. This

led to discussion of horizontal contours of Froude number computed from RAMS output. Froude numbers showed areas of supercritical flow located in zones of strongest gap winds which develop downwind of major obstacles (such as Gambier Island) and channel constrictions. This agrees well with hydraulic theory and will be discussed more in chapter 7. The RAMS modelling has also illustrated the technical difficulties in simulating a real flow of this kind which spans several topographic and atmospheric scales — all of which must be resolved. For this kind of simulation, accurate (but appropriately smoothed) representation of the fine scale topography, including all fjords and passes is critical.

5.4 RAMS momentum balance

Numerical models such as RAMS which solve a major subset of the full Navier-Stokes equations (ie. the quasi-Boussinesq equations), produce dynamically balanced synthetic "data" at very high spatial and temporal resolution. If a model produces credible simulations of a phenomenon, the synthetic data can be used in lieu of real data to provide a more complete analysis and understanding of the phenomenon, as has been done with RAMS model output. In addition, the model can be used to extract the forces which make up the individual components of the momentum equation. It is these forces which act to accelerate or decelerate wind, and hence account for its spatial and temporal variation. This chapter will describe and discuss the down- and cross-channel components of the momentum tendency in a valley-following vertical slice. A partial motivation for this is to aid creation and justification of simpler models, by indicating the relative importance of the various forces and by providing an indication of which of them can therefore be ignored.

5.4.1 Results

The RAMS momentum equation (equation A.8) which is described in more detail in appendix A, is reproduced here,

$$
\overbrace{\frac{\partial \rho_0 u_i}{\partial t}}^{1} + \overbrace{\frac{\rho_0 \theta_0}{a} \frac{\partial a b^{ij} \pi'}{\partial x_i^*}}^{2} =
$$

$$
\overbrace{ADV(\rho_0 u_i)}^{3} + \overbrace{\rho_0 TURB(u_i)}^{4} +
$$

$$
\underbrace{g(\frac{\theta'}{\theta_0} + 1.61 r_v - r_T)\delta_{i3}}_{5} + \underbrace{\varepsilon_{ij3} f u_i}_{6}
$$

This equation gives the momentum tendency, as found in the model, and has six components. The components are the:

1. total momentum tendency, (the acceleration) which is a consequence of the other tendencies or forces.

2. tendency due to pressure gradient force.

3. tendency due to advection of momentum.

4. tendency due to parameterized sub-grid scale turbulent diffusion.

5. tendency of vertical velocity due to buoyancy.

6. tendency due to Coriolis acceleration.

The horizontal down- and cross- channel components of the above tendencies (except 5, which is for vertical velocity), were found in a vertical slice which followed the axis of the main channel in Howe Sound. This was done by transforming the horizontal components from Cartesian (east, north) components to down- and cross-channel components. The location of this valley-following slice is shown in figure 5.21, and was the same used to display vertical cross sections of other RAMS fields in section 5.2.2. The down-channel direction is defined as tangent to the valley-following vertical slice, while the cross-channel direction is perpendicular. The time selected was January 31 at 11:00 PST, which is near the time when RAMS surface wind field was found to agree best with observations (see figure 5.2). Thirty-six time steps of the model were made (for a total of 180 seconds), at each of which the five tendencies were extracted. The tendencies shown are averages of these thirty-six values. The use of average values was not strictly required as the tendencies changed little over time, so that use of any one set of the thirty-six would have given a similar result.

Figure 5.38 is a vertical plot of the down-channel wind and momentum tendency components at the horizontal location of -143.875 km. Total velocity tendency which

is relatively small, is the sum of the other tendencies. The most important term is pressure gradient force which is balanced primarily by advection, and at low levels also by diffusion (friction). These three terms were found to be dominant in other vertical tendency profiles as well (not shown). Figure 5.39 is a vertical plot of down-channel wind
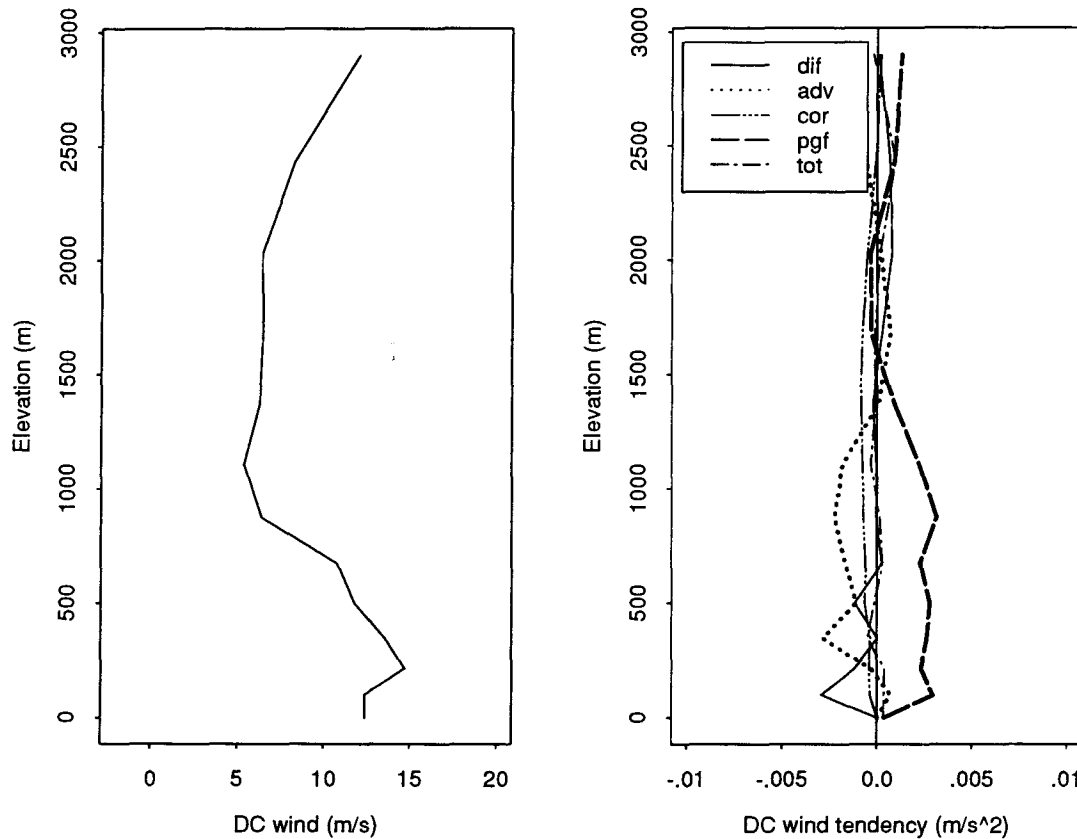
Figure 5.38: Vertical plot of down-channel (DC) wind speed and momentum tendencies for January 31 11:00 PST, at the horizontal location -143.875 km.
pgf – tendency due to pressure gradient force; adv – tendency due to advection; dif – tendency due to parameterized turbulent diffusion; tot – the actual total tendency due to all of the others; cor – tendency due to Coriolis effect.

and absolute value of the down-channel momentum tendencies, horizontally averaged over the slice. Because some tendencies, most notably pressure gradient force and advection, fluctuate greatly on either side of zero in the horizontal, averaging the actual values

results in partial cancellation which under represent their relative importance. This is corrected by looking at average absolute values of tendencies in order to get a picture of the relative importance of each. The dominant terms, especially near the surface are pressure gradient, advection and diffusion. The importance of diffusion decreases above 1000 m, becoming first similar in magnitude to, and eventually smaller than, the Coriolis and acceleration term. Figure 5.40, showing the cross-channel wind and absolute value of the cross-channel momentum tendencies, gives a similar picture. Pressure gradient, advection and diffusion are the dominant forces in the gap wind below about 1000 m elevation. The Coriolis force becomes equal in magnitude to advection and pressure gradient above 2500 m, while diffusion tends to zero. This is expected since the frictional drag exerted by the surface (the dominant source of diffusion in the model) decreases away from it.

Figure 5.41 is a horizontal plot of down-channel wind and tendencies, vertically averaged below 679 m and not including the first level. The first level is excluded, as it is set equal to level 2 in the model formulation. Clearly pressure gradient force, balanced by advection and to a lesser extent diffusion, are most important. Coriolis force and the total tendency are much smaller by comparison. There are large horizontal fluctuations in pressure gradient force and advection tendencies, with one being a mirror image of the other. Areas where the wind speed is increasing down the channel are marked by positive pressure gradient force tendencies, and by negative advection tendencies. The pressure gradient force is acting to increase the speed down the channel, explicitly resulting in a negative advection tendency. Figure 5.42 which is a horizontal plot of cross-channel wind and tendencies vertically averaged below 679 m, gives a similar picture. Diffusion becomes an important force when the winds are strong. The large fluctuations in pressure gradient force indicate that this force is not solely the result of a steady synoptic pressure gradient, but that hydraulic pressure gradients due to fluctuating gap wind depth are
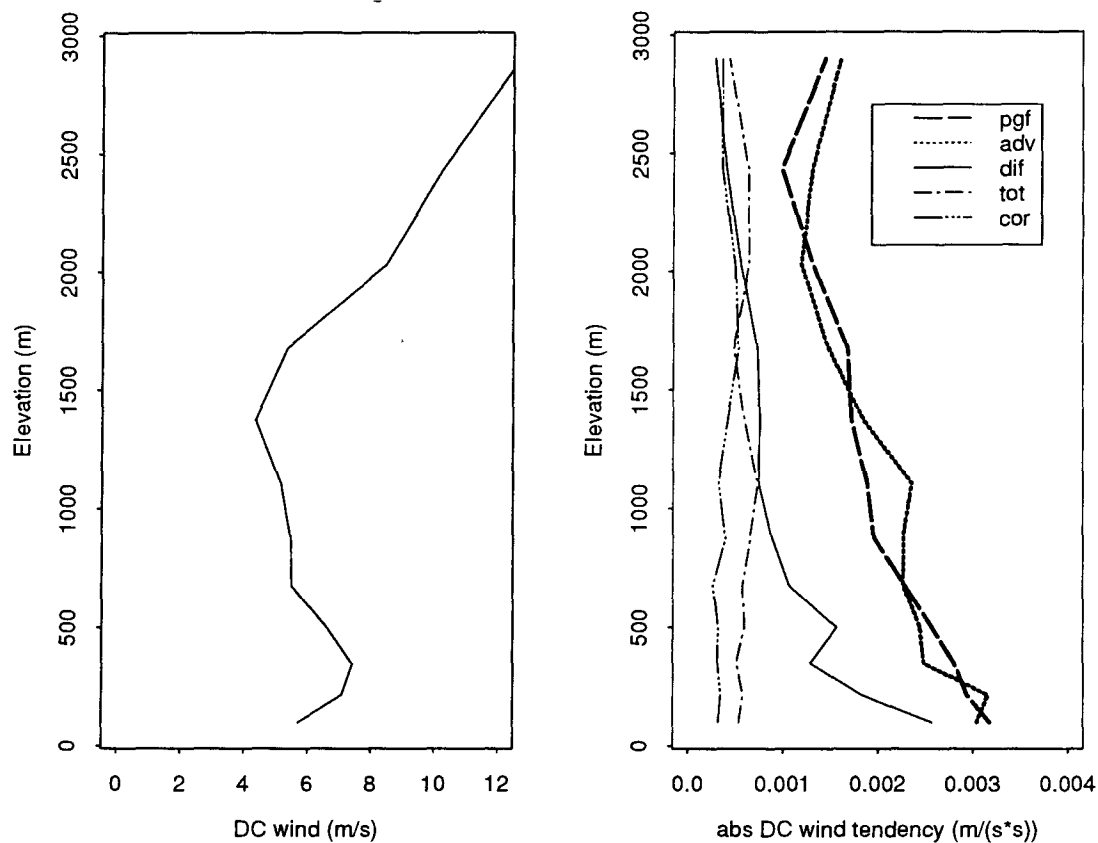
Figure 5.39: Vertical plot of horizontally averaged down-channel (DC) wind speed and absolute value of down-channel momentum tendencies for January 31 11:00 PST. Legend is the same as in figure 5.38.
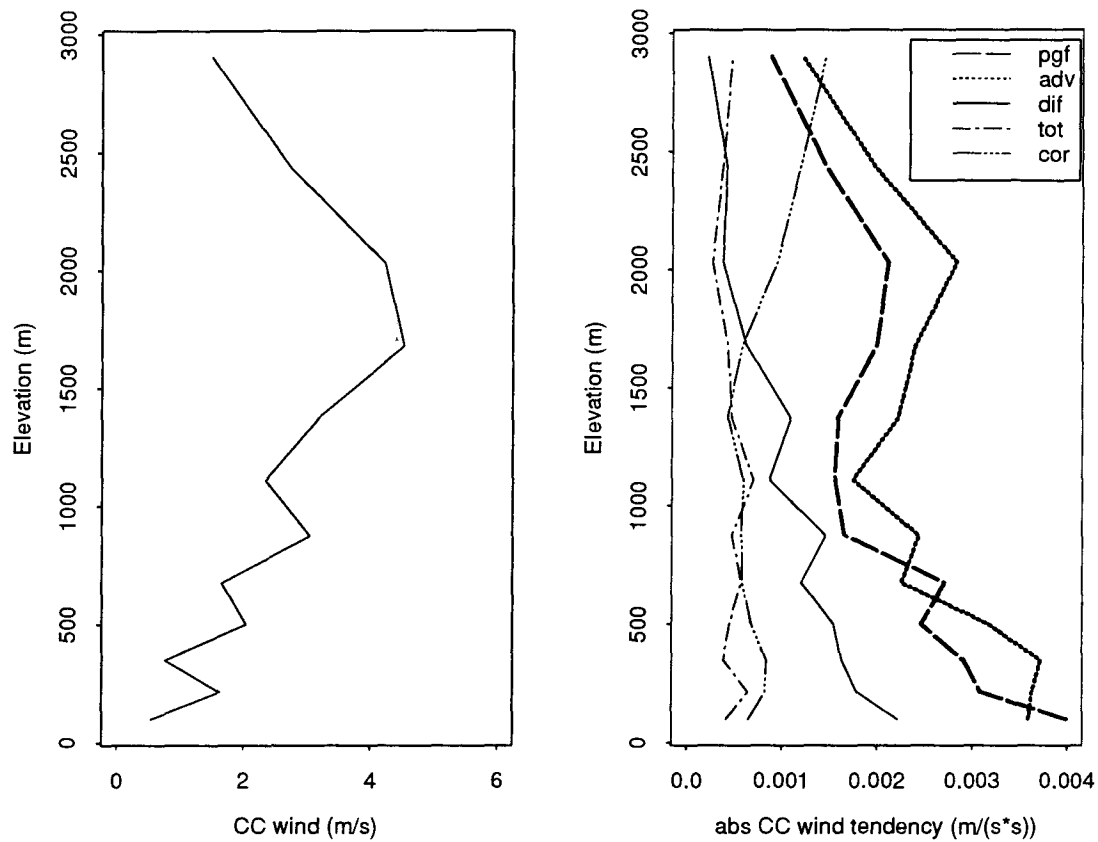
Figure 5.40: Vertical plot of horizontally averaged cross-channel (CC) wind speed and absolute value of cross-channel momentum tendencies for January 31 11:00 PST. Legend is the same as in figure 5.38.

important. In summary, pressure gradient force, balanced by advection, and to a lesser

extent, by diffusion, are the dominant forces in this gap wind simulation.
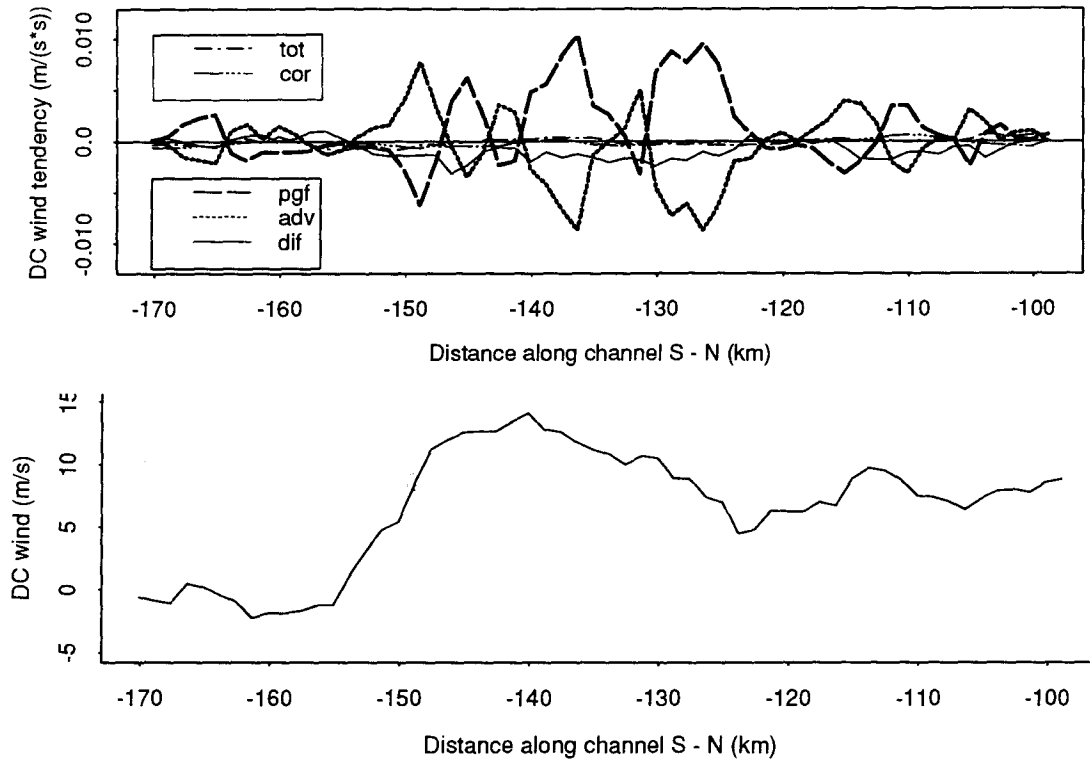
Figure 5.41: Horizontal plot of down-channel velocity and down-channel momentum tendency, vertically averaged below 679 m for January 31 11:00 PST.
Legend is the same as in figure 5.38.

5.4.2 Implications

The important forces for gap winds simulated by RAMS, are pressure gradient, advection, and to a lesser extent, parameterized turbulent diffusion. The influence of Coriolis force on down-channel momentum tendency is, as expected, small. The flow was in near steady state, so the total tendency also was small.

These findings can be used to aid creation of simpler models. Such models should, at a minimum, contain the pressure gradient force, and advection. Turbulent diffusion or
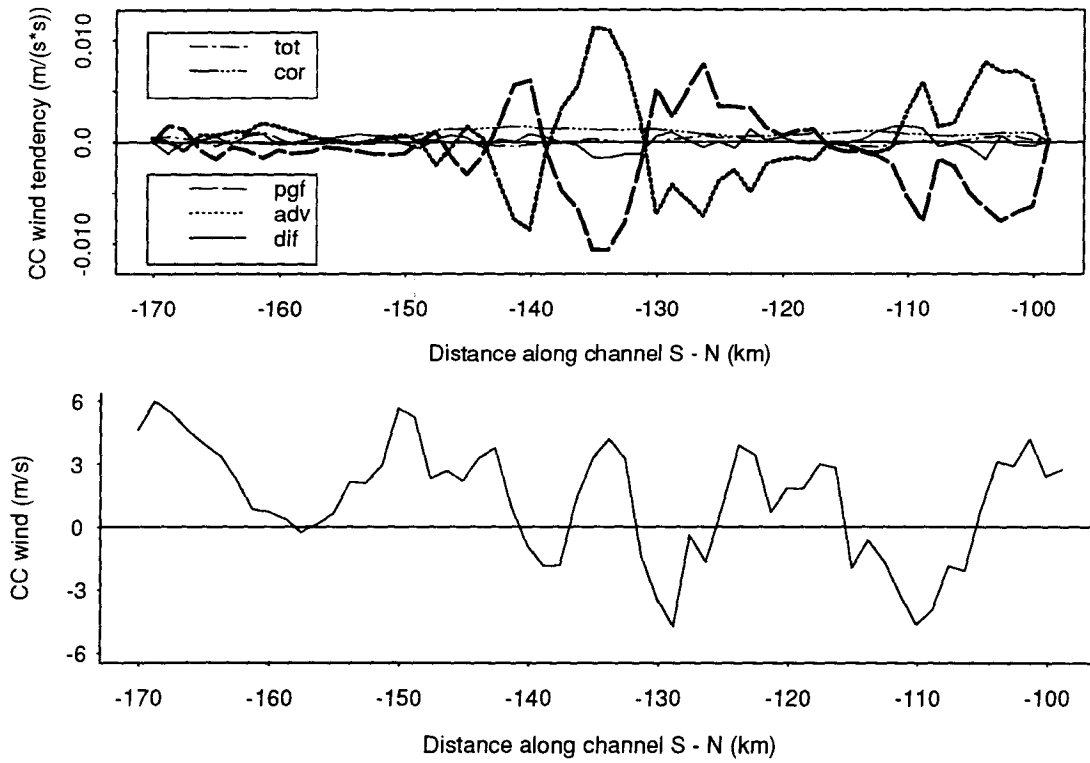
Figure 5.42: Horizontal plot of cross-channel velocity and cross-channel momentum tendency, vertically averaged below 679 m for January 31 11:00 PST.
Legend is the same as in figure 5.38.

friction, while of lesser importance, could also be included. Pressure gradients are due to horizontal variation in pressure at a constant elevation. Pressure varies horizontally because the weight of the atmosphere above a horizontal plane changes. This is due to horizontal variations in air density, caused mainly by temperature variations. In searching for simpler models of gap wind flow, two approaches will be taken. The first, expanded upon in chapter 6, is to consider gap wind flow of constant depth, so that horizontal pressure gradient at the surface is due to different atmospheric weights above the gap wind (ie. the pressure gradients are synoptically imposed). The second, and more realistic, described in chapter 7 is to allow synoptically imposed pressure gradients, but also to permit the depth of gap wind flow to vary, which also results in horizontal pressure gradients, and is analogous to hydraulic channel flow.

Chapter 6

Simple analytic models

The use of a full 3-dimensional mesoscale model for diagnosis and forecasting gap winds routinely is not practical. This is because a 3D mesoscale model capable of realistically simulating such an event, would take too long to execute on even the fastest computers presently available. In addition, the technical expertise required to use such a model would make implementation in a forecast office difficult. Thus it would be useful to find simpler models to simulate the flow. While simple models will not be capable of producing detailed comprehensive simulations, they may be able to provide enough information to be useful. Overland and Walter (1981), Reed (1981), and Mass and Albright (1985) made successful use of the Bernoulli equation to explain strong gap, and downslope-like winds.

Toward this, the first step is the elucidation and testing of the simplest analytic models possible. When considering the flow of air in a channel such as Howe Sound, it is possible to derive very simple analytic relations to describe the wind, by eliminating "small" terms from the momentum equation and either ignoring or finding a suitable parameterization for surface friction. In this chapter, two such models are developed and compared to observations and RAMS simulation output. The usefulness and applicability of these models are discussed. This provides impetus to the development of a more comprehensive model in chapter 7.

6.1 Theory

This section presents the momentum equation and make several simplifications to it in order to apply it to wind flow in a channel of constant elevation. The derivation follows that of Jones (1985), except that here an analytic solution for the wind speed is found, whereas Jones used numerical methods. The momentum equation in vector notation is:

$$\underbrace{\frac{d\vec{V}}{dt}}_{1} = \underbrace{-\frac{\nabla P}{\rho}}_{2} - \underbrace{f\hat{k} \times \vec{V}}_{3} + \underbrace{\frac{1}{\rho}\frac{d\tau}{dz}}_{4} \qquad (6.1)$$

where: $\vec{V}$ is the vector wind, t is time, ρ is air density, P is pressure, f is the Coriolis parameter, $\hat{k}$ is a unit vector directed upwards, and τ is the eddy stress. In this equation: term 1 is the Lagrangian acceleration (ie. the acceleration following the flow); term 2 is the pressure gradient force, term 3 is the Coriolis force, and term 4 is friction. In order to simplify this equation the following assumptions will be made:

- The channel is straight, and aligned along the x direction.

- Term 3, the Coriolis term can be ignored. As the wind is topographically constrained by the channel, geostrophic adjustment is inhibited. This is supported by the fact that velocity tendency due to the Coriolis effect was found to be small in the chapter 5.4 force balance analysis (see figures 5.38 – 5.42).

- The friction term (4) can be parameterized using a drag coefficient parameterization after Deardorff (1972).

The surface stress, $\tau_s = \rho u_*^2$ can be set equal to $C_D u^2$, where C_D is a drag coefficient and u is the 10 m wind speed. According to Deardorff (1972), if h is the height of the Planetary Boundary Layer (in this case the neutral layer of gap wind flow), and $\tau = 0$

at $z = h$, then the friction term, 4, can be approximated:

$$\frac{1}{\rho}\frac{d\tau}{dz} \simeq \frac{-1}{\rho}\frac{\tau_s}{h} = \frac{-C_D u^2}{h} \tag{6.2}$$

which assumes the drag is exerted throughout the boundary layer. Under neutral and stable conditions, 6.2 is a poor approximation because the stress doesn't increase linearly with height. Deardorff (1972) modified this equation to incorporate stability:

$$\frac{1}{\rho}\frac{d\tau}{dz} \simeq \frac{-C u^2}{h} \tag{6.3}$$

$$C = c C_D \quad c \quad = 1 \text{ for unstable conditions}$$

$$c \quad = 2.8 \text{ for neutral and stable conditions}$$

Therefore equation 6.1 can be simplified to:

$$\frac{du}{dt} = \frac{d}{dx}(\frac{u^2}{2}) = \eta - \frac{C u^2}{h} \tag{6.4}$$

$$\text{where } \eta = \frac{-1}{\rho}\frac{dP}{dx}$$

The balance between pressure gradient, friction and acceleration represents a *geotriptic* wind. Implicit in the formulation is that u in the friction term, which is meant to be a 10 m wind, is the same as u in the acceleration term, which is an average speed over depth h. If friction is neglected altogether, the result is a form of the Bernoulli equation:

$$\frac{du}{dt} = \frac{d}{dx}\left(\frac{u^2}{2}\right) = \frac{-1}{\rho}\frac{dP}{dx} \tag{6.5}$$

which can be integrated to give:

$$\frac{u^2}{2} = \frac{u_0^2}{2} - \frac{\Delta P}{\rho} \tag{6.6}$$

where u_0 is the initial speed, ΔP is the pressure difference between the end point and the initial point, and u is the Lagrangian velocity. For $u_0 = 0$ this reduces to:

$$u = \sqrt{\frac{-2\Delta P}{\rho}} \tag{6.7}$$

This result describes the flow neglecting rotation, friction and changes in elevation and will be called the "Bernoulli" model. Incorporating friction, equation 6.4 can be solved analytically. This is done by substituting $\phi = \frac{u^2}{2}$ into 6.4 which results in:

$$\frac{d\phi}{dx} + \frac{2C}{h}\phi = \eta \tag{6.8}$$

which has a solution:

$$\phi = \frac{u^2}{2} = \frac{\eta h}{2C} + \mathcal{A}e^{\frac{-2Cx}{h}} \tag{6.9}$$

One can find $\mathcal{A}$, by letting $u = u_0$ at $x = 0$, resulting in:

$$u = \sqrt{\frac{\eta h}{C} + (u_0^2 - \frac{\eta h}{C})e^{\frac{-2Cx}{h}}} \tag{6.10}$$

which is the "Friction" model. For $u_0 = 0$ this simplifies to:

$$u = \sqrt{\frac{\eta h}{C}}\sqrt{1 - e^{\frac{-2Cx}{h}}} \tag{6.11}$$

after a long time in a long channel, this reduces to:

$$u = \sqrt{\frac{\eta h}{C}} \tag{6.12}$$

which represents the upper boundary of steady state speed.

To see that the above solution reduces to the Bernoulli equation in the limit as $C \rightarrow 0$, one can rewrite the Bernoulli equation (equation 6.7) in terms of the horizontal pressure gradient as:

$$u = \sqrt{2\eta x} \tag{6.13}$$

The Friction model (equation 6.11)is:

$$u = \frac{\sqrt{1 - e^{\frac{-2Cx}{h}}}}{\sqrt{\frac{C}{\eta h}}} \tag{6.14}$$

which in the limit as $C \to 0$ is indeterminate $(= \frac{0}{0})$. To resolve this, L'hospital's rule is applied:

$$u^2 = h\eta \frac{1 - e^{\frac{-2Cx}{h}}}{C} \tag{6.15}$$

$$\lim_{C \to 0} u^2 = h\eta \frac{\lim_{C \to 0} \frac{d}{dC}(1 - e^{\frac{-2Cx}{h}})}{\lim_{C \to 0} \frac{dC}{dC}} \tag{6.16}$$

$$u^2 = h\eta \frac{2x}{h} \tag{6.17}$$

$$u = \sqrt{2\eta x} \tag{6.18}$$

which is the same as the Bernoulli result.

The Friction model (equations 6.10 and 6.11) is visually depicted in figure 6.1 showing wind speed as a function of distance down-channel and boundary layer height over drag coefficient, h/C, for a pressure gradient of .005 Pa m^{-1}. The Friction model neglects Earth's rotation, pressure gradients resulting from channel elevation changes, and changes in outflow depth. The effects of varying channel cross section – width constrictions and expansions – are also not included in the formulation. This model represents a balance between friction, an externally imposed pressure gradient, and acceleration.

6.2 Results – comparison with observations and RAMS output

In order to assess the two simple analytic models – Bernoulli and Friction – comparisons with observations and RAMS output will be made for four times during the episode. The times chosen span the RAMS simulation at six hour intervals. They are (PST): January 30, 23:00; January 31, 05:00; January 31, 11:00; and January 31, 17:00. The stations used for comparison from north to south are: Squamish Airport (SQA), Squamish townsite (SQT), Watts Point (WAT), Defence Island (DEF), Brunswick Point (BRU), Finisterre Island (FIN), and Lookout Point (LOO).

The Friction and Bernoulli models have modest input data requirements. The Bernoulli
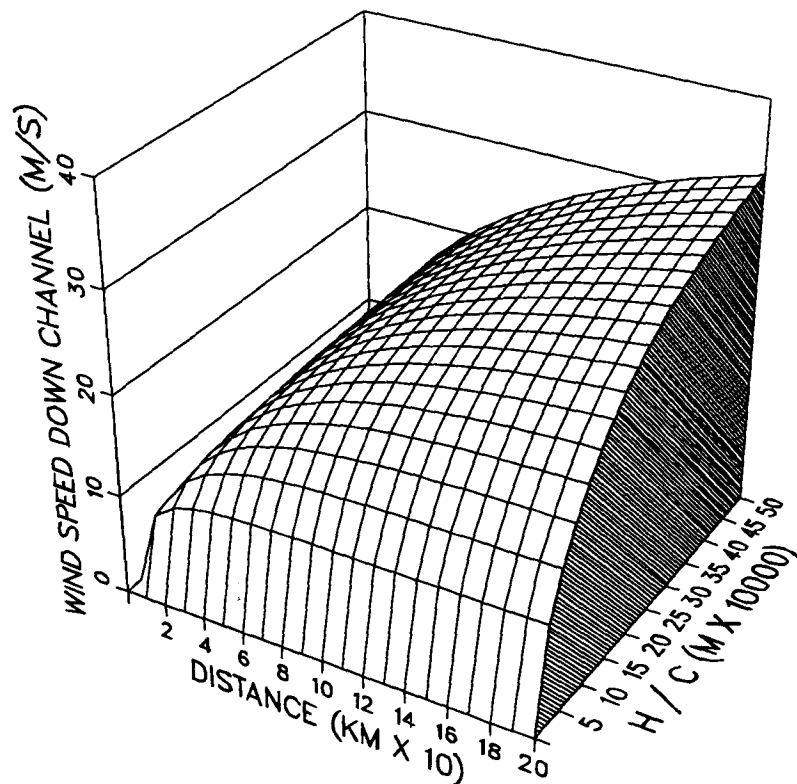
Figure 6.1: Visualization of Friction model. Wind speed along channel is represented on the vertical axis as a function of distance down channel and boundary layer height divided by drag coefficient (h / C). A pressure gradient of .005 Pa m^{-1} (5 mb / 100 km) is used.

model only needs a horizontal pressure gradient (change in pressure between two points), and a down-channel wind speed at the channel head. In addition to these, the Friction model needs an estimate of boundary layer height (h), and drag coefficient (C).

There was some difficulty in estimating the horizontal pressure gradient at specific times. A mean pressure gradient found from a synoptic weather map central to all four times gave a value of .004 Pa m^{-1}. The pressure gradient found by using the reduced sea level pressure at SQR and LOO, was between .002 and .003 Pa m^{-1}, while that found using SQT and LOO gave values between .0083 and .0092 Pa m^{-1}. The higher pressures

observed at SQT could be due in part to the presence of a deeper layer of cold air over SQT than SQR. A simple hydrostatic calculation indicates that a 4 ° temperature difference over a depth of 1000 m could account for this, however the surface temperatures are slightly colder at SQR. It was found that the calibration of the electronic barometers used at these stations changed between the beginning and end of the field season. The pressure data were subsequently found using a linearly variable calibration, which assumes the barometer calibration changed gradually and at a constant rate over the field season. This may not be the case, and could at least account in part for the difference. Because of this uncertainty, results using both values of horizontal pressure gradient at each time are shown. The starting down-channel wind speeds were found from the average of winds at Squamish Airport and Daisy Lake. The initial velocity and pressure gradients used are shown in table 7.3.

The boundary layer height, h, was found by inspecting the vertical profiles in figure 3.5 and lie between 500 and 900 m. A mean value of 800 m was chosen as appropriate. The drag coefficient, C, is more difficult to estimate, in part because it is smaller over water than over land. Garratt (1977) in a review of drag coefficients over oceans and continents, suggested the following be used for neutral flow over water:

$$C = .51 \times 10^{-3} u^{.46} \qquad (6.19)$$

where u is the 10 m wind speed. This results in a value of .0015 for winds of 10 m s^{-1} and assumes that wave action is fully developed. This is not the case during gap wind events when sea state is fetch limited, so actual drag coefficients over water would be less. Over land, form drag due to uneven topography, as well as frictional drag are important. An average value suggested over land is $C = .01$ which corresponds to a roughness length, z_0 of .2 m (Garratt, 1977). A value of C higher than .01 over land could be appropriate in Howe Sound due to the rugged terrain and aerodynamically rough vegetation.

An appropriate drag coefficient for Howe Sound is likely somewhere between the values for land and water (between .001 and .01), since the sides of the fjord are aerodynamically rough land, while the bottom is relatively smooth water interspersed with frictionally rough islands. Drag coefficients are formulated for 10 m winds, while the wind speed used is a layer average. Thus, drag coefficient values should be less, since layer mean wind speed is greater than the 10 m wind. These estimates result in $h \ / \ C$ values possibly ranging from $5 - 90 \times 10^4$, with a value of 10^5 being chosen as most appropriate.

Figures 6.2 and 6.3 compare observed down channel wind speeds with those calculated from the RAMS simulation, Bernoulli model, and Friction model. In these figures and in subsequent similar figures, the flow is from right to left (north to south) and the horizontal coordinate matches that of RAMS vertical cross section plots. Two lines are plotted for each model, one for output from the pressure gradient between Squamish River (SQR) and Lookout Point (LOO), and the other for output from the pressure gradient between Squamish Town (SQT) and LOO.

The Bernoulli model, which should represent the upper bound of wind speed, is higher than observed everywhere, and much higher than observed in the large pressure gradient scenario. It shows a monotonic increase in speed along the channel. The Friction model, which also shows a monotonic increase and mostly higher than observed wind speeds, is closer to observations than the Bernoulli model due to the inclusion of friction. The lower pressure gradient scenario (based on pressure differences between SQR and LOO), best matches the observations. Neither model is able to represent decreases in wind speed along the channel. Inclusion of variable drag coefficients over land and water would have resulted in slightly flatter curves from the starting point at horizontal coordinate -100 to -126 (over land) in figures 6.2 and 6.3, producing a somewhat better agreement with observations.

a)

b)
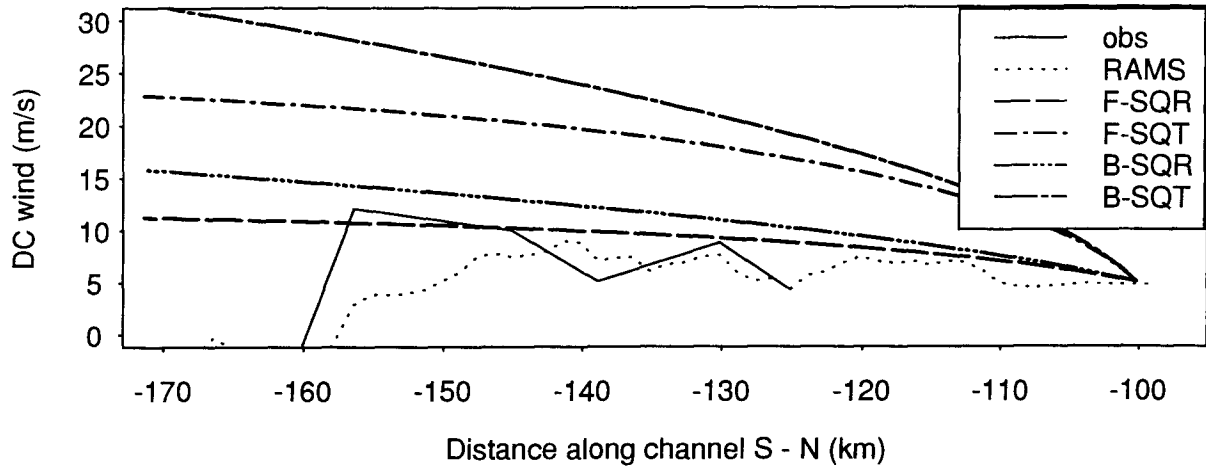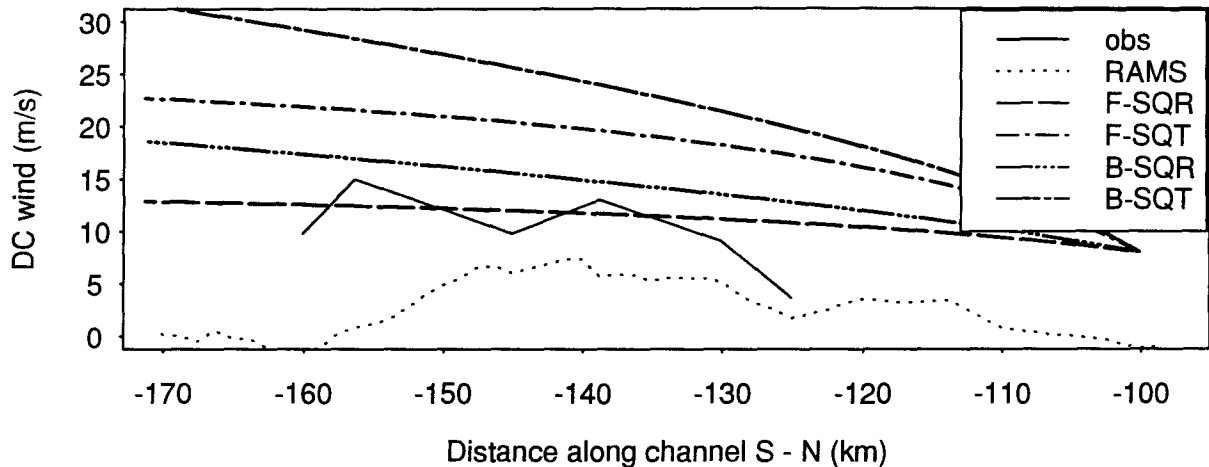
Figure 6.2: Comparison of observed down-channel winds with winds calculated from: RAMS simulation; Friction model; and the Bernoulli equation for January 30 23:00 and January 31 05:00.

The boundary layer height divided by drag coefficient $(h \ / \ C)$ value for the friction calculation is 10^5. The line labelled "obs" is observed data; "RAMS" is RAMS model output; the prefix "F-" is output from the Friction model; the prefix "B-" is output based on the Bernoulli model; the suffix "SQR" means the SQR — LOO pressure gradient was used; and the suffix "SQT" means the SQT — LOO pressure gradient was used.

a)

January 31, 11:00 PST

b)
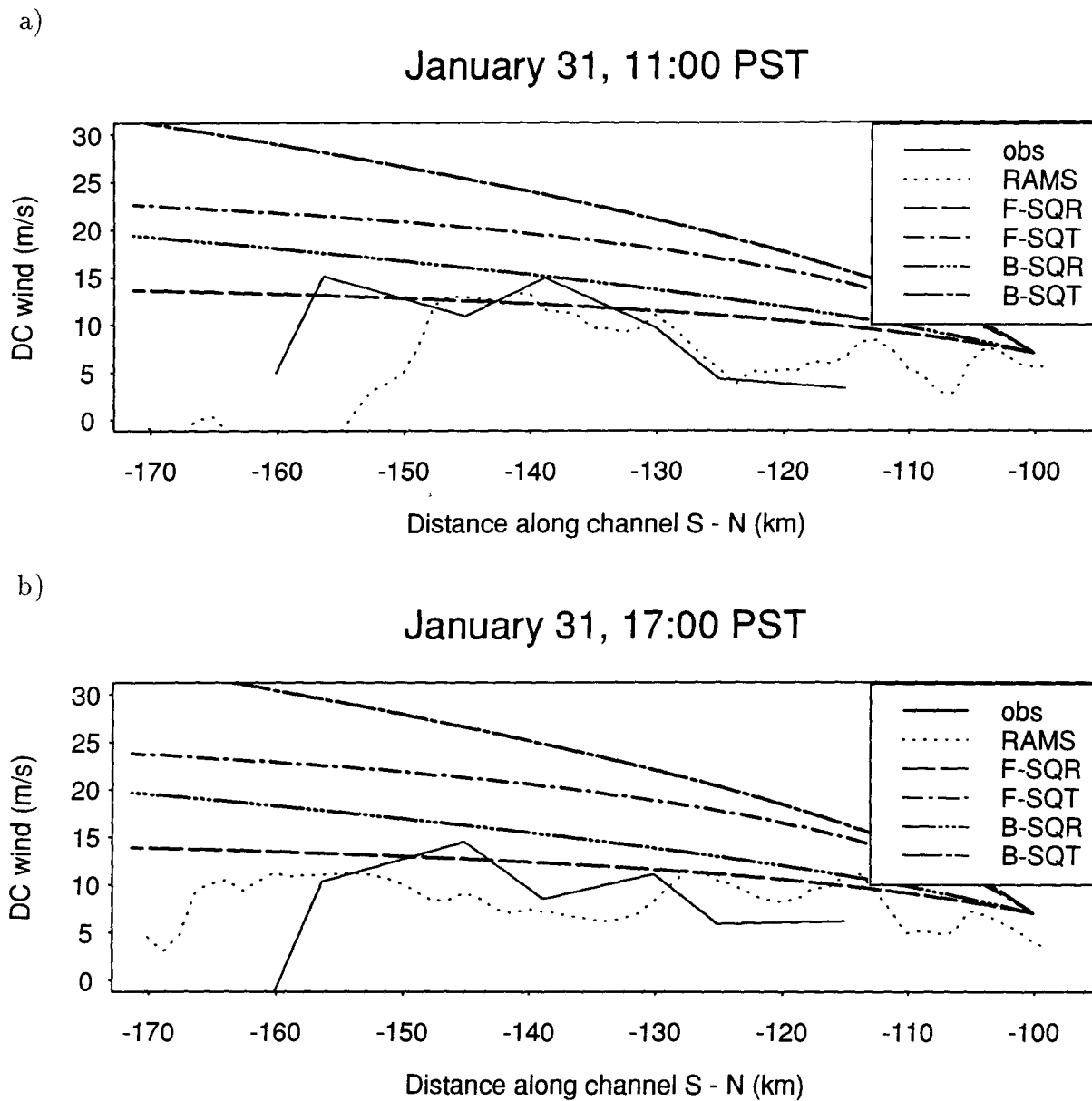
January 31, 17:00 PST

Figure 6.3: Comparison of observed down-channel winds with winds calculated from: RAMS simulation; Friction model; and the Bernoulli equation for January 31 11:00 and January 31 17:00.
Legend as in figure 6.2.

6.3   Discussion

Two simple models of wind flow in a channel have been presented which result from simplifications to the momentum equation. The Bernoulli model is the balance between horizontal pressure gradient and acceleration, while the Friction model also includes friction. Neither model explicitly includes horizontal pressure gradients resulting from variable gap wind depth or channel base elevation, or horizontal variations in channel cross section. Both models show a monotonic increase in wind speed, and winds mostly stronger than observed.

These models would be most applicable in constant elevation channels of relatively uniform cross section, where hydraulic effects, such as transitions between subcritical and supercritical flow, do not occur. The minimal ability of these models to accurately represent gap winds in Howe Sound (with both accelerating and decelerating winds along the channel), implies that they do not fit the traditional gap wind classification. In fact, Howe Sound gap winds violate several assumptions implicit in these models. The model described in chapter 7 will relax the most limiting assumptions to include pressure gradients resulting from changes in channel elevation and gap wind depth, to incorporate variations in channel cross section along the fjord, and therefore to implicitly include the hydraulic effects which were observed in the RAMS simulation.

Chapter 7

Hydraulic channel flow: an analog to gap wind

One goal of this research is to find models of gap wind flow which are both computationally and conceptually simpler than 3-dimensional mesoscale numerical models. Investigations using simple analytic models with fixed boundary layer heights and channel base elevations (chapter 6) point out their inadequacy in representing anything but hydraulically subcritical, monotonically increasing, down-channel flow. Since gap winds are a low level flow of dense air, constrained horizontally by fjord walls, and vertically by an inversion, they would seem to resemble the flow of water in a channel. Moreover, results from numerical modelling show similarities between gap wind flow and hydraulic flow (chapter 5): descending, supercritical flow in zones of strong wind; sharply ascending flow where wind rapidly becomes light and subcritical. For these reasons, it seems that hydraulic channel flow theory is a potentially useful analog to gap wind flow.

This chapter will describe basic hydraulic theory and extend it to include synoptic pressure gradients and friction. The model thus created will then be applied to airflow in rectangular and realistic channels, and compared with observations. Finally, the model will be used to test the sensitivity of gap wind to initial and boundary conditions.

7.1 Hydraulic theory

Hydraulic theory has been used extensively for many years (often in a civil engineering context) to study the flow of water in open channels. The developments described in this section follow closely those which can be found in classical hydraulics textbooks, such

145

as Henderson (1966), except that here gravity (g) is replaced by effective (or reduced) gravity (g') to account for the different densities of water and air; a different formulation for friction is used; and an externally imposed synoptic pressure gradient is included (something which is clearly of minor importance when considering the flow of water).

Simplified atmospheric applications of hydraulics (which only considered inviscid flow through rectangular channels and no synoptic pressure gradient) can be found in the strong katabatic wind theory of Ball (1956) which has been applied by Arakawa (1968), and Pettre (1982) to strong wind flow in valleys. Pettre (1982) studied the "Mistral" — a low level flow similar to gap wind which occurs through the Rhône valley in France. He applied hydraulic theory for a rectangular channel of constant elevation with no external pressure gradient or friction, and used it to interpret wind observations along the valley. He found that observed strong flow occurred downwind of the major horizontal contraction in the valley, which was in agreement with hydraulic theory. A sharp decrease in wind speed near the end of the valley was attributed to a hydraulic jump. Aircraft observations of wind and potential temperature corroborated the hydraulic interpretation of the winds. Pettre (1982) provides a precedent for the application of hydraulic theory to phenomena like gap wind. The assumptions implicit in the extension of hydraulics to gap wind, will be discussed after the theory is developed.

Consider two layer incompressible channel flow with the upper, less dense (ρ_2) fluid at rest, while the lower moving fluid of higher density (ρ_1) is relatively shallow (height h). Assume flow in the lower layer is parallel to the ground and constant in the cross-channel and vertical directions, so it varies only in the down-channel direction. This is meant to be analogous to gap winds' lower, nearly neutral layer of strongest winds surmounted by a stable layer. Further assume the hydrostatic approximation holds, and the time and length scales are sufficiently small that Earth's rotation can be ignored. Let the channel be aligned along the x direction with the configuration and variables shown in figure 7.1,

and assume the flow is steady-state ($\frac{\partial}{\partial t} = 0$). The steady-state assumption is supported by RAMS results in which the total velocity tendency was shown to be small (section 5.4).

With these assumptions, the momentum equation is:

$$\underbrace{u\frac{du}{dx}}_{1} + \underbrace{g'\frac{dh}{dx}}_{2} + \underbrace{g'\frac{de}{dx}}_{3} + \underbrace{\frac{1}{\rho}\frac{dP}{dx}}_{4} - \underbrace{\frac{1}{\rho}\frac{d\tau}{dz}}_{5} = 0 \tag{7.1}$$

where u is down-channel speed; h is thickness of the lower layer; P is large scale pressure at the top of the layer; e is the channel elevation; τ is the eddy stress; $g' = \frac{(\rho_1 - \rho_2)}{\rho_1} \times g = \frac{(\theta_2 - \theta_1)}{\theta_1} \times g$ is reduced gravity; and ρ is air density. In equation 7.1: term 1 is velocity advection; term 2, is a horizontal pressure gradient force due to a gradient in the thickness of the dense air; term 3, is a horizontal pressure gradient force due to changes in valley bottom elevation; term 4, is an external pressure gradient force imposed at the top of the system (alternately referred to as a "synoptic pressure gradient"); and term 5, is friction.

The equation of continuity in the outflowing air is:

$$Q = uA = uh\bar{b} = \text{constant} \tag{7.2}$$

$$\frac{d}{dx}(uA) = \frac{dQ}{dx} = 0 \tag{7.3}$$

where A is channel cross sectional area, $\bar{b}$ is mean width, and Q is total discharge which is conserved along the channel.

If one divides equation 7.1 by g', and uses continuity to replace u by $\frac{Q}{A}$ the resulting equation is:

$$-\frac{Q^2}{g'A^3}\frac{dA}{dx} + \frac{dh}{dx} + \frac{de}{dx} + \frac{1}{g'\rho}\frac{dP}{dx} - \frac{1}{g'\rho}\frac{d\tau}{dz} = 0 \tag{7.4}$$

where, by the chain rule:

$$\frac{dA}{dx} = \frac{d(h\bar{b})}{dx} = \bar{b}\frac{dh}{dx} + h\frac{d\bar{b}}{dx} \tag{7.5}$$
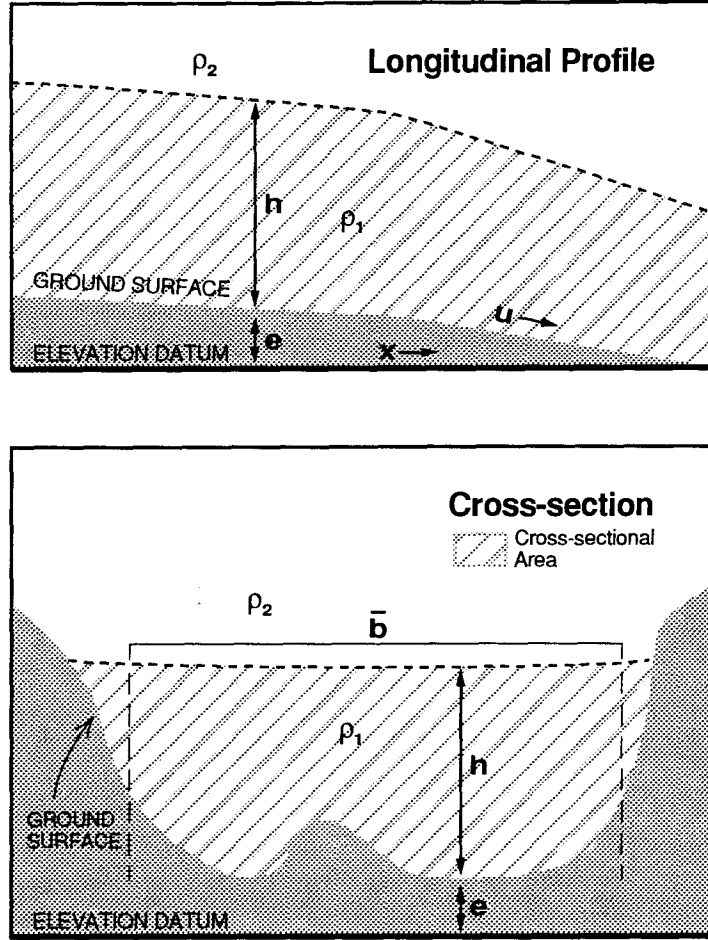
Figure 7.1: Definition sketch for airflow in a channel.

If one defines the channel slope, S_0 as positive "down hill", then $\frac{d\epsilon}{dx} = -S_0$. If the external pressure gradient is defined as a "slope", S_P, and made positive for decreasing pressure along x, then $\frac{1}{g'\rho}\frac{dP}{dx} = -S_P$. The momentum equation can now be written:

$$(1 - \frac{Q^2}{g'A^3}\bar{b})\frac{dh}{dx} = S_P + S_0 + \frac{hQ^2}{g'A^3}\frac{d\bar{b}}{dx} + \frac{1}{g'\rho}\frac{d\tau}{dz} \tag{7.6}$$

The Froude number as before is defined as:

$$F = \frac{u}{\sqrt{g'h}} \tag{7.7}$$

If friction is parameterized as in chapter 6, then the momentum equation can finally be written:

$$(1 - F^2)\frac{dh}{dx} = S_P + S_0 + \frac{F^2 h}{\bar{b}}\frac{d\bar{b}}{dx} - CF^2 \tag{7.8}$$

This equation lies at the heart of the hydraulic model. It is similar to standard hydraulics treatments (for example Henderson (1966)) except that gravity has been replaced by reduced gravity, an external pressure gradient is included, and friction is parameterized as discussed in chapter 6. Despite its apparent simplicity, the equation can describe a variety of complex flow situations. It incorporates pressure gradients which are externally imposed, pressure gradients due to changing channel elevation, and pressure gradients due to changing boundary layer depth. It can incorporate friction, and channels of variable cross section. This equation relaxes many of the most limiting assumptions of the analytic models described in chapter 6. This will be discussed further in section 7.2.

As discussed in chapter 5, Froude number determines the flow regime: if the Froude number is less than 1, flow is subcritical; if the Froude number is greater than 1, flow is supercritical; and if it is equal to 1, flow is critical. Since the Froude number is the ratio of fluid speed to wave speed, supercritical flow means that fluid travels faster than gravity waves on the fluid interface. Therefore, in supercritical flow, fluid disturbances can only propagate downstream — no "information" can propagate upstream, so that it is controlled by upstream conditions. Supercritical flow is directly analogous to supersonic flow in gases with Mach number greater than 1. In subcritical flow which is controlled by downstream conditions, information can propagate both up and downstream.

7.1.1 Hydraulic flow regimes

Equation 7.8 permits solutions of different characteristics depending upon whether the flow is sub- or supercritical, and the sign of the right hand side of the equation (ie.

the steepness of the channel and pressure slope compared to friction and the amount of horizontal contraction). At each location along the fjord, it is possible to find the *critical depth*, h_c, the depth at which the flow at that location would be critical ($F = 1$). This is found by setting the Froude number to 1 in equation 7.7 and solving for h_c. For channels of rectangular cross section, this is simply $h_c = \sqrt[3]{\frac{Q^2}{g'A^2}}$ (after Henderson (1966)). For non-rectangular channels, this will in general have to be found iteratively since A is a non-constant function of h. The critical speed can also be defined as the speed when the flow is critical: $u_c = \sqrt{g'h_c}$, which can be found directly once h_c is known.

If the flow depth is below the critical depth, then the speed will be greater than the critical speed and the flow will be supercritical with a Froude number greater than 1, and vice-versa for subcritical flow. It is the occurrence of supercritical flow which creates the strongest winds in a channel.

In channels of constant slope and cross section it is possible to define a flow state called *uniform flow* (Henderson, 1966), in which state the fluid thickness is constant ($\frac{dh}{dx} = 0$), and the pressure and channel slope terms are exactly balanced by friction (since with constant cross section the contraction term $- \frac{F^2 h}{\bar{b}} \frac{d\bar{b}}{dx}$ in equation 7.8 is zero):

$$S_P + S_0 = CF^2 \qquad (7.9)$$

Uniform flow could really only exist for long channels of uniform slope, roughness and cross section. The flow in such a channel would asymptotically tend toward uniform flow.

It can be seen that if the channel is horizontal ($S_0 = 0$), and since $S_P = \frac{\eta}{g'}$ (with the pressure gradient force, $\eta = -\frac{1}{\rho}\frac{dP}{dx}$ as in chapter 6), the condition of uniform flow reduces to

$$u = \sqrt{\frac{\eta h}{C}} \qquad (7.10)$$

which is the same as equation 6.12 and was the result found in the friction model after the flow had evolved over a long time (as $t \to \infty$). Uniform flow will have a certain

depth, h_0, called the *uniform depth*, that can be determined for a given location by solving equation 7.9, which in general must be solved iteratively. Locations where the total slope, $S_T (= S_P + S_0)$, is zero or negative, have undefined uniform depths. Even though gap wind flow in natural channels is probably never uniform, (the channel cross section varies so the contraction term on the right hand side of equation 7.8 is non-zero) the concept of *uniform flow* along with that of *critical flow*, is useful in understanding possible hydraulic flow regimes in channels where variations in cross section are negligible.

Situations where the total slope, S_T, is greater than the friction term for critical flow, must have supercritical uniform flow and therefore a uniform height, h_0, less than the critical height, h_c. Such slopes are called "steep". Situations where the total slope, S_T, is less than the friction term for critical flow, must have subcritical uniform flow and therefore a uniform height, h_0, greater than the critical height, h_c. Such slopes are called "mild". If the total slope equals the friction term for critical flow, then the flow is critical, and the slope is called "critical". Flows with total slopes that are horizontal, or adverse cannot have uniform flow (since friction and opposing slopes would eventually decrease the wind speed to zero, giving infinite uniform height)(Henderson, 1966).

It is difficult to apply equation 7.8 where the flow crosses transitions between sub- and supercritical, since several of the terms become zero, making $\frac{dh}{dx}$ large or infinite. An additional complication is that equation 7.8 does not incorporate the loss of momentum and energy which occurs in a turbulent hydraulic jump. This will be treated later by considering conservation of momentum.

The concept of *controls* is a very important one in hydraulic theory. A control is a channel feature that fixes the flow in its locality. A control can act to force subcritical flow upstream and supercritical flow downstream, when flow becomes critical at the control. A control is the only location where the flow can transit from subcritical to supercritical. The reverse transition, however, from supercritical to subcritical, which

occurs as a *hydraulic jump* does not in general occur at a control, although its location is determined by a control further downstream (Henderson, 1966).

Whether or not a feature will act as a control, depends on both the boundary conditions (pressure slope, terrain slope, amount of horizontal contraction, and friction), and the flow itself (discharge, speed and depth). Under certain flow conditions a feature may act as a control while under other conditions it will not. If a feature acts as a control, then the right hand side of equation 7.8 will change signs from negative to positive. This can occur when the slope changes from "mild" to "steep", or near the location of maximum horizontal contraction. The reverse change, from positive to negative, may result in a hydraulic jump, although this will usually occur further downstream. A fixed boundary layer height at the channel terminus, like a reservoir, acts as a control on upstream flow. Figure 7.2 shows schematic examples of gap wind through the above features in flow situations where they do and do not act as controls. In river channel hydraulics other features such as weirs, flumes and sluice gates may also act as controls.
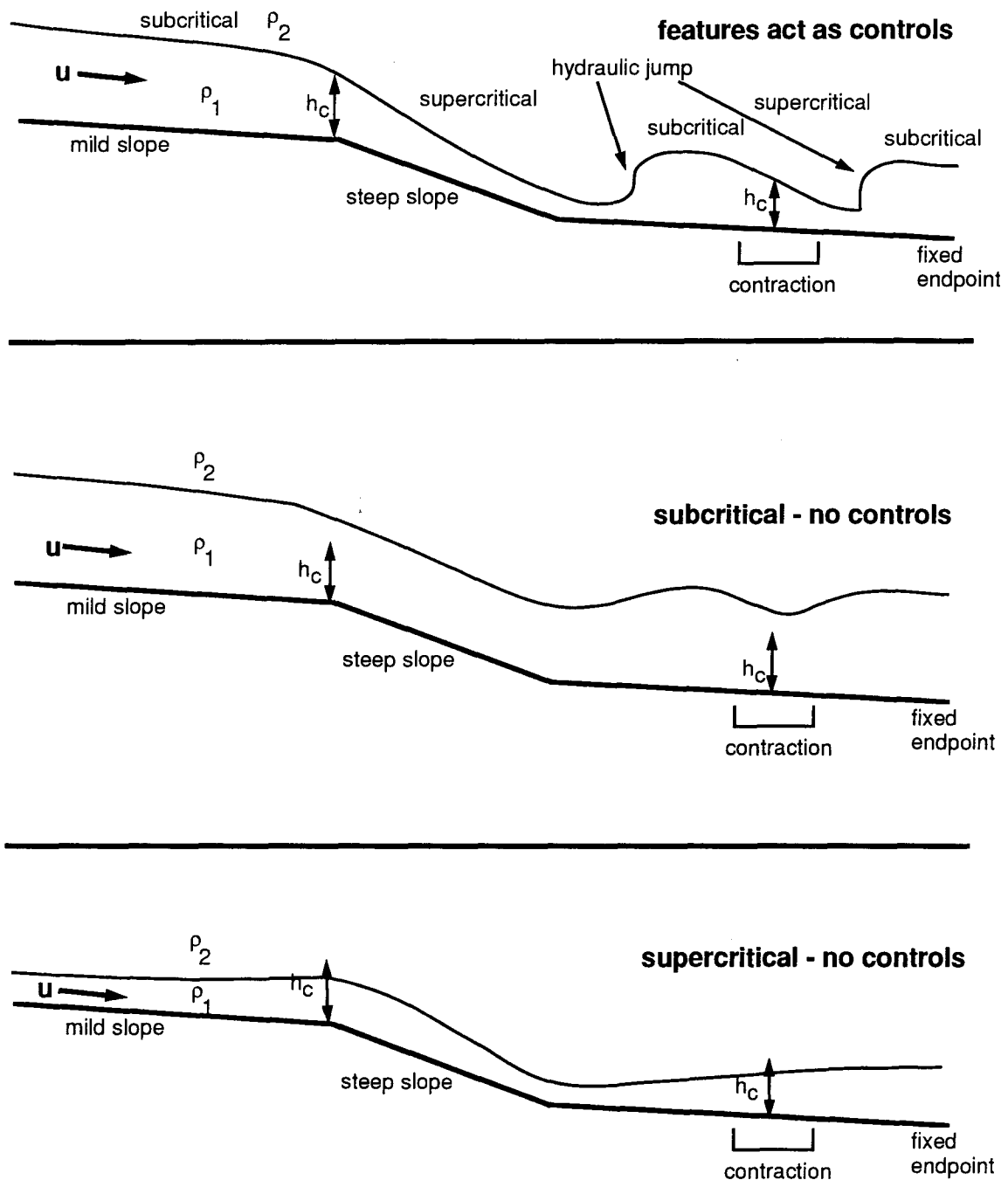
Figure 7.2: Longitudinal profiles of channel flow height through various features that: do act as controls; don't act as controls because the flow is too slow and deep (subcritical); and don't act as controls because the flow is too fast and shallow (supercritical)

7.1.2 The energy equation

The momentum equation gives considerable qualitative channel flow information, and could also be used in a numerical integration to find it quantitatively. The traditional approach in hydraulics however is to use an integrated form of the momentum equation. This is a statement of conservation of energy and a form of the Bernoulli equation. The energy equation can be found by starting with the equation of momentum (equation 7.1), dividing it by g' and making the substitution for the friction term of equation 6.3 and the pressure slope defined before, resulting in:

$$\frac{u}{g'}\frac{du}{dx} + \frac{dh}{dx} + \frac{de}{dx} - S_P + \frac{Cu^2}{g'h} = 0 \tag{7.11}$$

This equation is now integrated along x:

$$\Delta(\frac{u^2}{2g'} + h + e) = \overline{(S_P - CF^2)}\Delta x \tag{7.12}$$

where the left hand side is the change in total energy along x (the change in "head"), and the right hand side contains the factors causing the total energy to change (friction, and external pressure gradient). The over bar denotes an average over the horizontal interval Δx. This equation is the one used in the "step method" to be discussed later to find the flow between control points. The first two terms on the left hand side of equation 7.12 define the flow "specific energy":

$$E = \frac{u^2}{2g'} + h \tag{7.13}$$

That this equation is actually a cubic in h, can be easily seen in the case of a rectangular channel where $Q = uhb$ with b the width. If u^2 is replaced by $\frac{Q^2}{h^2b^2}$, then the result is $h^3 - Eh^2 + \frac{Q^2}{2g'b^2} = 0$. This equation has generally three roots, of which one is negative and can be ignored. The two positive roots represent different values of h at which the flow can have the same specific energy. This can be seen in figure 7.3 which depicts h versus

E for a particular discharge and width. Flows through valleys of varying cross section are represented by a family of such curves. The two heights possible for a given discharge are called "alternate" heights. The smaller h value is for supercritical flow, while the larger is for subcritical flow. At the minimum in E, there is only one positive root, at the critical height, h_c. A similar analysis could be used for non-rectangular channels, except that in general the roots must be found iteratively.
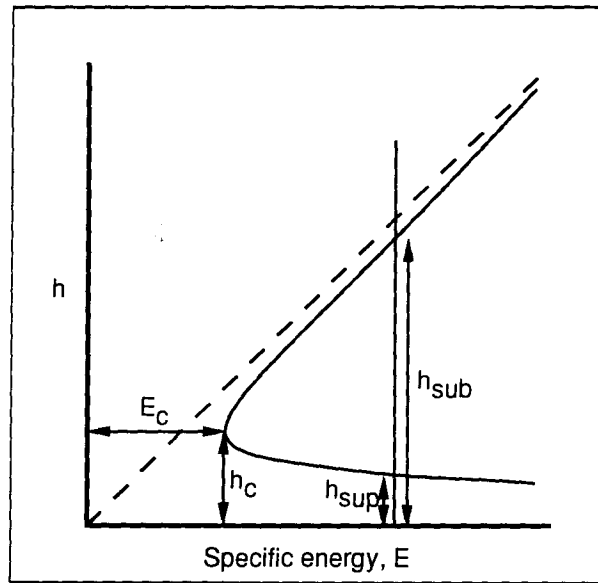
Figure 7.3: Schematic illustration of h versus specific energy for a particular flow condition (after Henderson (1966)).

7.1.3 The hydraulic jump

When flow transits from super- to subcritical in a hydraulic jump, there is considerable energy loss due to turbulence. This energy loss is not represented on the right hand side of equation 7.12, so the equation breaks down and cannot be used to find the flow. Instead, a technique utilizing conservation of momentum principles can be used on either side of a hydraulic jump (Henderson, 1966).

Consider the slab of air containing a hydraulic jump in the channel depicted in figure 7.4. Ignoring the frictional drag of the channel which is a minor term compared to the
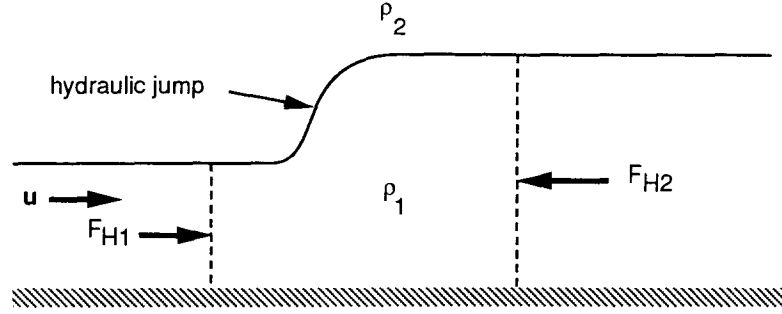
Figure 7.4: Forces acting on a slab of air on either side of a hydraulic jump

energy lost in the hydraulic jump, the change in momentum across the slab must equal the difference in hydrostatic forces acting on each face of the slab:

$$\Delta(Q\rho u) = Q\rho u_2 - Q\rho u_1 \tag{7.14}$$

$$= F_{H1} - F_{H2} \tag{7.15}$$

where F_H is the hydrostatic force acting on the face of each end of the slab. The hydrostatic thrust is equal to the mean pressure due to the weight of air times the cross sectional area:

$$F_H = \rho g' \bar{h} A \tag{7.16}$$

where $\bar{h}$ is the height of the centroid of cross sectional area A. If the slab under consideration was large, we would also need to consider an addition to the hydrostatic thrust by externally imposed pressure gradients and an additional force due to the mass of the slab on a slope. However, we are only interested in the case when the length of the slab is small – just large enough to contain the jump, which in the present treatment is considered to be vertical. Additionally we assume that the pressure on top of the cold air layer is the same on either side of the jump. Equating the change in momentum to

the difference in forces, after some manipulation results in the following:

$$\frac{Q^2}{g'A_2} + A_2\overline{h_2} - (\frac{Q^2}{g'A_1} + A_1\overline{h_1}) = 0 \tag{7.17}$$

This equation can be solved iteratively for the two heights on either side of the jump (h_1 and h_2), which are called "conjugate heights". For rectangular channels it can be solved directly, leading to the well known hydraulic jump equation (Henderson, 1966):

$$\frac{h_2}{h_1} = \frac{1}{2}(\sqrt{1 + 8F_1^2} - 1) \tag{7.18}$$

where F_1 is the upstream Froude number.

7.2 The hydraulic model

With an equation for conservation of energy (equation 7.12) which is applicable on either side of a transition from sub- to supercritical flow, and conservation of momentum (equation 7.17) which is applicable on either side of a transition from super- to subcritical flow, it is possible to construct a model describing the flow of a relatively dense fluid (in this case cold air) underlying less dense fluid (in this case warm air) in a channel. The equations and definitions used are repeated here for clarity.

The energy equation:

$$\Delta(\frac{u^2}{2g'} + h + e) = \overline{(S_P - CF^2)}\Delta x \tag{7.19}$$

The hydraulic jump equation:

$$\frac{Q^2}{g'A_2} + A_2\overline{h_2} - (\frac{Q^2}{g'A_1} + A_1\overline{h_1}) = 0 \tag{7.20}$$

where:

$S_P = -\frac{1}{g'\rho}\frac{dP}{dx} = $ the externally imposed pressure gradient (expressed as a slope)

$C = $ a frictional drag coefficient

$F = \frac{u}{\sqrt{g'h}}$ = the Froude number

h = the height of fluid (gap wind) above ground level

e = the elevation of the valley floor above some datum

$Q = uA = uh\overline{b}$ the total discharge of fluid (gap wind), which is assumed to be conserved along the channel

u = the mean velocity in the fluid (depth averaged gap wind speed)

$g' = \frac{(\rho_1 - \rho_2)}{\rho_1} \times g = \frac{(\theta_2 - \theta_1)}{\theta_1} \times g$ = reduced gravity

ρ = the fluid (air) density

A = the cross sectional area, which is a function of x and h

$\overline{b} = \frac{A}{h}$ = the mean channel width

The input data required to solve the above equations are:

- Q, the discharge of outflowing air.

- a tabulation of cross sectional area, A, for various heights at various horizontal locations along the channel

- e, the elevation of the channel floor at various horizontal locations along the channel

- θ_1, θ_2, the potential temperature of the lower and upper air layers

- $\frac{dP}{dx}$, the externally imposed horizontal pressure gradient along the channel

- C, drag coefficient values at horizontal locations along the channel

- h_f, the height of gap wind at the end of the channel

The model described by the above equations relaxes the most limiting assumptions of the analytic models described in chapter 6 by including parameters such as: varying channel elevation and cross section; externally imposed pressure gradients; friction; and

variations in the height of gap wind. There remain however, a number of assumptions implicit in the hydraulic model itself, as well in its extension to gap winds. The hydraulic model (even as applied to water) is only valid where the flow is steady in time, gradually varying in space, 1-dimensional, and on slopes which are not too steep. Thus transient phenomena such as waves are not incorporated. Flows which are rapidly varied in space such as hydraulic jumps and drops, are constructed by the superposition of gradually varying sections.

The extension of hydraulics to gap wind adds other assumptions. The gap wind should bear some resemblance to water – a clearly marked lower, more dense layer surmounted by a definite inversion. The hydraulic model does not incorporate entrainment of air from above, or any other interactions with overlying air (other than an externally imposed pressure gradient) such as transport of momentum. This could be a problem in cases where lower level air is not clearly of different density than the air above. Velocity in the hydraulic model is a layer mean velocity which is assumed to be constant across the entire channel (1-dimensional). In fact, as observations and RAMS simulations have shown, velocity is not constant across the channel, with certain regions having greatly enhanced flow. This can be the case in river channels as well, and its affect on the height profile incorporated by multiplying the velocity head term ($\frac{u^2}{2g}$) in the energy equation by a velocity coefficient, α, which varies between 1.1 and 2.0, according to Hoggan (1989). This correction was felt to be small and of unknown validity for gap wind, so was not used. In any case the correction only applies to the fluid depth, not its velocity. It is assumed that energy losses due to channel sinuosity are negligible. There are empirical ways to account for this in river hydraulics, but these were not tried.

7.2.1 Method of solution – hydmod

The energy equation is solved over finite steps, in an upstream direction (usually) for subcritical flow, and in a downstream direction (always) for supercritical flow. This is called the "step method" in classical hydraulics. The equation is always solved in reaches *between control points*, with a complete solution for the entire fjord being comprised of the superposition of solutions over individual reaches. For subcritical flow, the influence of downstream control points can extend upstream through other control points as far as necessary. Likewise, supercritical flow resulting from an upstream control point, can extend downstream through other control points if necessary. The hydraulic jump equation is used to determine the location of a hydraulic jump in reaches where there is supercritical flow from an upstream control point, and subcritical flow from a downstream control point. In the model it is possible for subcritical flow from a downstream control point to extend "influence" upstream far enough to "drown" an upstream control point which created supercritical flow, resulting in no supercritical flow, and no hydraulic jump. A flow diagram of the model created as part of this work to solve these equations, called *hydmod*, is shown in figure 7.5.

The terrain data (C, e, and A at 100 m intervals of h from the ground to 2000 m above ground) are input along the valley at regular intervals (every 2500 m in this case). Since the input intervals are too coarse to solve the energy equation accurately, data are interpolated horizontally using cubic splines to the much higher resolution (62.5 m) model spacing. At high resolution horizontal locations, cubic splines are computed for cross sectional area (A) as a function of height, giving A at any height for any horizontal location along the fjord. Once initial data have been input and interpolated to the model resolution, the model: computes critical and uniform flow at all points; finds all potential control points; computes sub- and supercritical flow up and downstream from

each potential control point assuming critical flow at the control point; solves the actual flow (which may or may not become critical at any control point); and finally outputs / plots the results. The model is coded in FORTRAN 77, while the plotting and analysis module is in S+.

It was necessary to make a few somewhat arbitrary assumptions in creating the hydraulic model. *Hydmod* uses the initial height and speed of gap wind only to compute the discharge. Uniform height and speed are used as the actual initial conditions. This is because incorrect specification of height and speed could create initial conditions which are physically unrealistic resulting in an incorrect simulation. For example if the specified initial conditions made the flow subcritical and deeper than the uniform height, then the flow depth would increase in height as though the flow were into a "reservoir". The cross sectional area above 2000 m, or above the highest terrain in each cross section, is assumed to be rectangular. This can be justified by considering that if the gap flow reaches this height, then it is probably flowing over the mountains on either side of the fjord as well, so the air itself provides a kind of lateral boundary. None of the simulations made had flow depths as great as this.
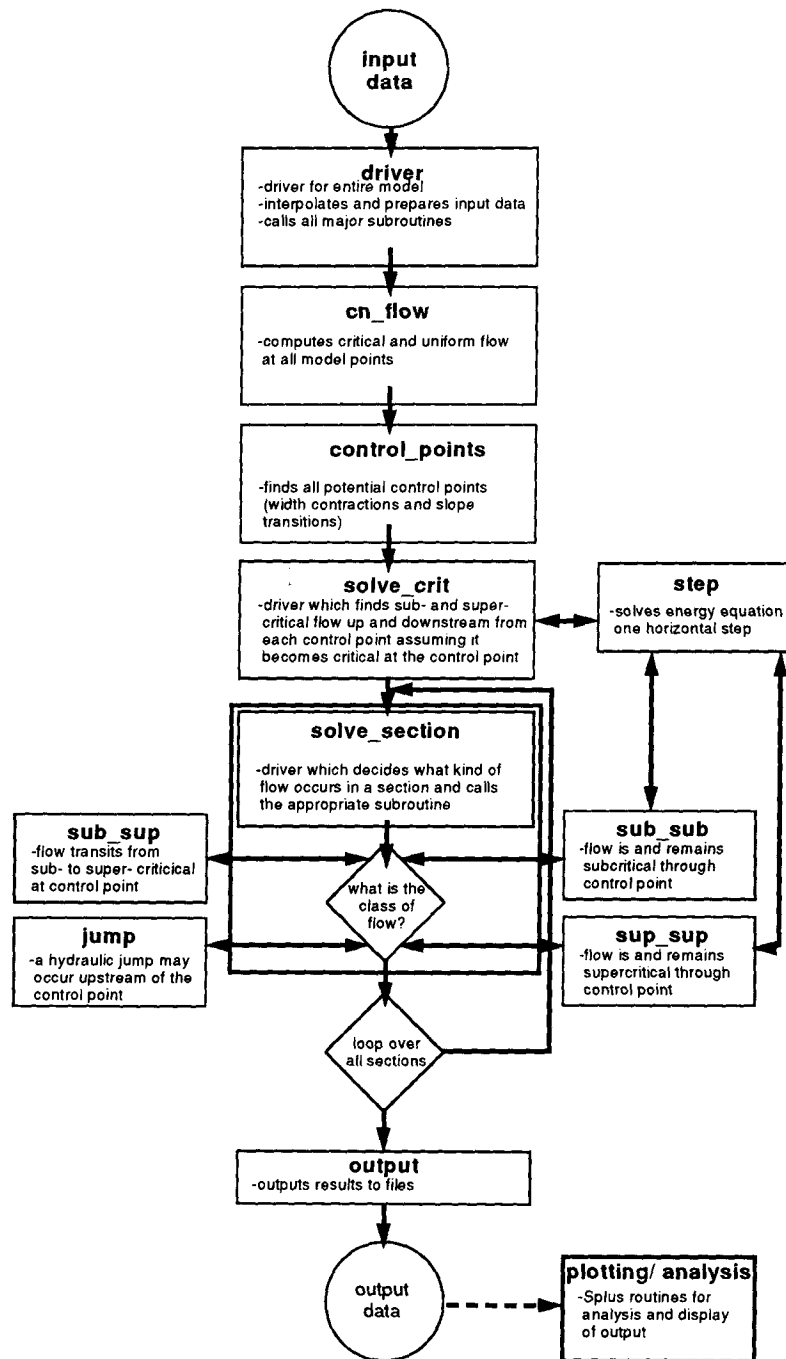
Figure 7.5: Simplified flow chart for *hydmod*.

7.3 Results

Hydmod is used to simulate gap winds in both a "realistic" representation of the Howe Sound fjord, and in an idealized rectangular channel with one horizontal contraction. The purpose of tests using a rectangular channel are to check the model's veracity, and to elucidate the role of various initial and boundary conditions.

Hydmod can test the sensitivity of the flow to various parameters. The external parameters which can be tested are: synoptic pressure gradient; height and speed of gap wind at the start of the channel (ie. variations in discharge); height of gap wind at the channel exit; and effective gravity, which is a function of the difference in potential temperature between the upper and lower layers. In addition the effect of internal parameters can be tested: the frictional roughness of the fjord; and the configuration of the channel itself. In order to test the sensitivity of the flow to various parameters, most probable values, and the likely range of each must be specified. This is straightforward for some parameters, and more difficult for others.

The average observed value of synoptic pressure gradient is 0.004 Pa m^{-1} from the sea level pressure analysis shown in figure 3.10b and will be used as the most probable value, while a likely range would be from 0.0 to 0.02 Pa m^{-1}. The observed average gap wind initial height value of 800 m will be used as the most probable value, while a likely range would be from 150 to 1500 m. These values will also be used for gap wind height at the channel exit. An average observed gap wind speed at the head of the fjord of 5 m s^{-1} will be used as the most probable value, while a range of 1 m s^{-1} to 15 m s^{-1} is chosen as most likely. An estimated drag coefficient value of 0.01 (chapter 6) will be used as most probable, with a range of 0.001 - 0.02 chosen as likely. The average observed potential temperature in the gap wind layer of 267 K will be used as the most probable values. The likely range in potential temperature difference between upper and lower levels is

1 to 20 K. The maximum value of 20 K is from observations of a very severe gap wind event by Jackson (1993). The most probable value chosen for the potential temperature of the upper layer in the rectangular channel tests is in the middle of this range – 277 K. The most probable input values and likely range used for the rectangular channel tests are summarized in table 7.1.

In the plots which follow, a force balance analysis of the hydraulic model output has been carried out. To facilitate comparison with RAMS, the *hydmod* force balance has been made as compatible as possible with that of the RAMS simulation. The forces are defined as follows, by multiplying equation 7.1 by −1:

$$\underbrace{-u\frac{du}{dx}}_{1} \underbrace{-g'\frac{dh}{dx}}_{2} \underbrace{-g'\frac{de}{dx}}_{3} \underbrace{-\frac{1}{\rho}\frac{dP}{dx}}_{4} \underbrace{-\frac{1}{\rho}\frac{d\tau}{dz}}_{5} = 0 \qquad (7.21)$$

where the terms are velocity tendencies caused by: 1 - advection; 2 - pressure gradient due to changing height; 3 - pressure gradient due to changing channel elevation; 4 - external pressure gradient; and 5 - friction. A direct comparison of forces is difficult for several reasons. It is difficult to separate the horizontal pressure gradient term in RAMS into elevation, gap wind height, and external pressure gradient components. The RAMS force balance analysis was a vertical average in the fixed layer below 679 m, whereas the *hydmod* forces pertain to the entire gap wind layer. Also, in *hydmod* the Coriolis force is not represented, and the total tendency is zero by definition.

Sensitivity tests are carried out for both the rectangular and realistic channel in the following way. All input parameters are held constant at the most likely value, except one which is varied through the probable range in ten increments. The results are summarized in plots of maximum and mean gap wind versus the input parameter which was varied so that sensitivity of the wind to that parameter can be assessed.

Input Variable	most likely value	probable range
h_0 initial height	800 m	150 – 1500 m
h_f ending height	800 m	150 – 1500 m
u_0 initial speed	5 m s^{-1}	1 – 15 m s^{-1}
$\frac{dp}{dx}$ pressure gradient	0.004 Pa m^{-1}	0.0 – .02 Pa m^{-1}
θ_1 lower pot. temp.	267 K	267 K
θ_2 upper pot. temp.	277 K	268 – 287 K
C drag coefficient	.01	.001 – .02

Table 7.1: Values used in *hydmod* runs and sensitivity tests for the rectangular channel.

7.3.1   Rectangular channel

The rectangular channel used to test the model and help assess the importance of initial and boundary conditions is 50 km in length and 5 km in width. In the centre of the channel there is a width contraction to 3 km. The channel is horizontal, although the effect of varying external pressure gradients is like "tilting" it. The effect of the horizontal width contraction is similar to that of a terrain elevation maxima which is effectively a vertical contraction.

Figures 7.6 and 7.7 show flow height, speed, Froude number, and force balance components along the channel for a *hydmod* simulation with the most likely input data parameters (flow is from right to left). The incoming subcritical flow speed increases and height decreases as it nears the contraction where the flow transits to supercritical. Downstream of the contraction, the flow is supercritical for a short distance before

transiting to subcritical in a hydraulic jump. The subcritical flow downstream of the contraction is determined and controlled by the gap wind depth at the end of the channel. The peak wind speed is located in the supercritical zone immediately downstream of the contraction. The shape of the Froude number (figure 7.7a) and wind speed plots (7.6b) are similar and opposite in character to the gap wind height plot (7.6a). This follows directly from the definition of Froude number. In this (figure 7.7b) and subsequent force balance analysis plots, lines labelled "advection" and "friction" are components of accelerations due to advection and friction. The lines labelled "pgf elevation", "pgf height", and "pgf external" represent components of acceleration from horizontal pressure gradient forces due to: channel elevation changes, gap wind height changes and externally imposed pressure gradients, respectively. The force balance analysis plot (7.7b) clearly shows the largest forces within the contraction are the pressure gradient force due to horizontal gradient of gap wind height, and advection which opposes it. Friction and the external pressure gradient force are smaller. The main force balance is between height pressure gradient and the external pressure gradient in subcritical flow away from the contraction. This agrees qualitatively with the RAMS force balance analysis presented in chapter 5.4 which showed the main balance was between pressure gradient and advection. The sign and character of the *hydmod* forces near the contraction are qualitatively similar to the RAMS forces shown in figure 5.41 between -120 and -160 km for example. In the RAMS force balance, the zone of increasing wind has positive velocity tendency due to pressure gradient, which is partially balanced by a negative advection velocity tendency, and vice versa in the zone of decreasing wind. This is similar to the force pattern in figure 7.7b near, and downstream of the contraction. The magnitude of the *hydmod* forces are however considerably larger than the RAMS forces.

a)

b)
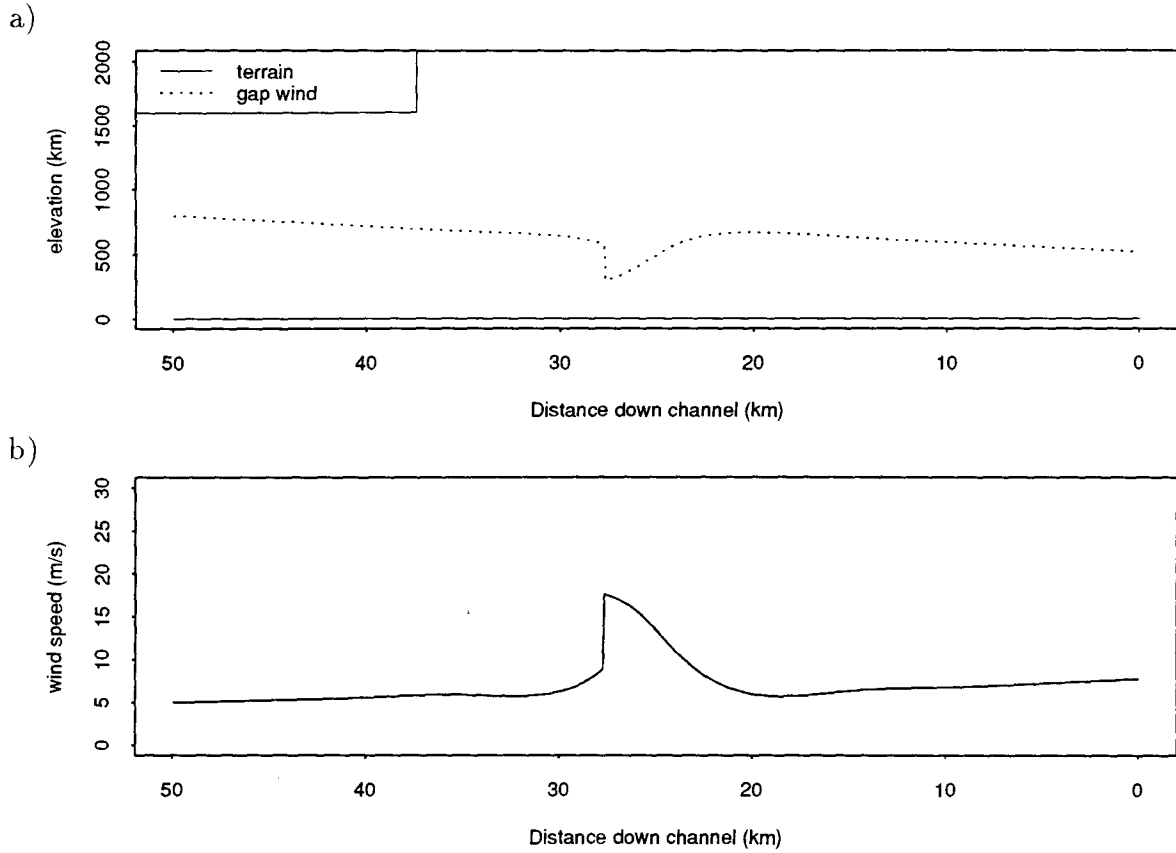
Figure 7.6: Gap wind flow for rectangular channel with "most likely" input parameters. a) Height of gap wind; b) Gap wind speed.

Sensitivity tests

Figures 7.8 to 7.13 show the sensitivity of mean and maximum wind speed to h_0 (initial gap wind height), h_f (gap wind height at end of channel), u_0 (initial wind speed), $\frac{dP}{dx}$ (external pressure gradient), g' (effective gravity - by varying the potential temperature of the upper layer over a 20° range), and C (drag coefficient).

a)

b)
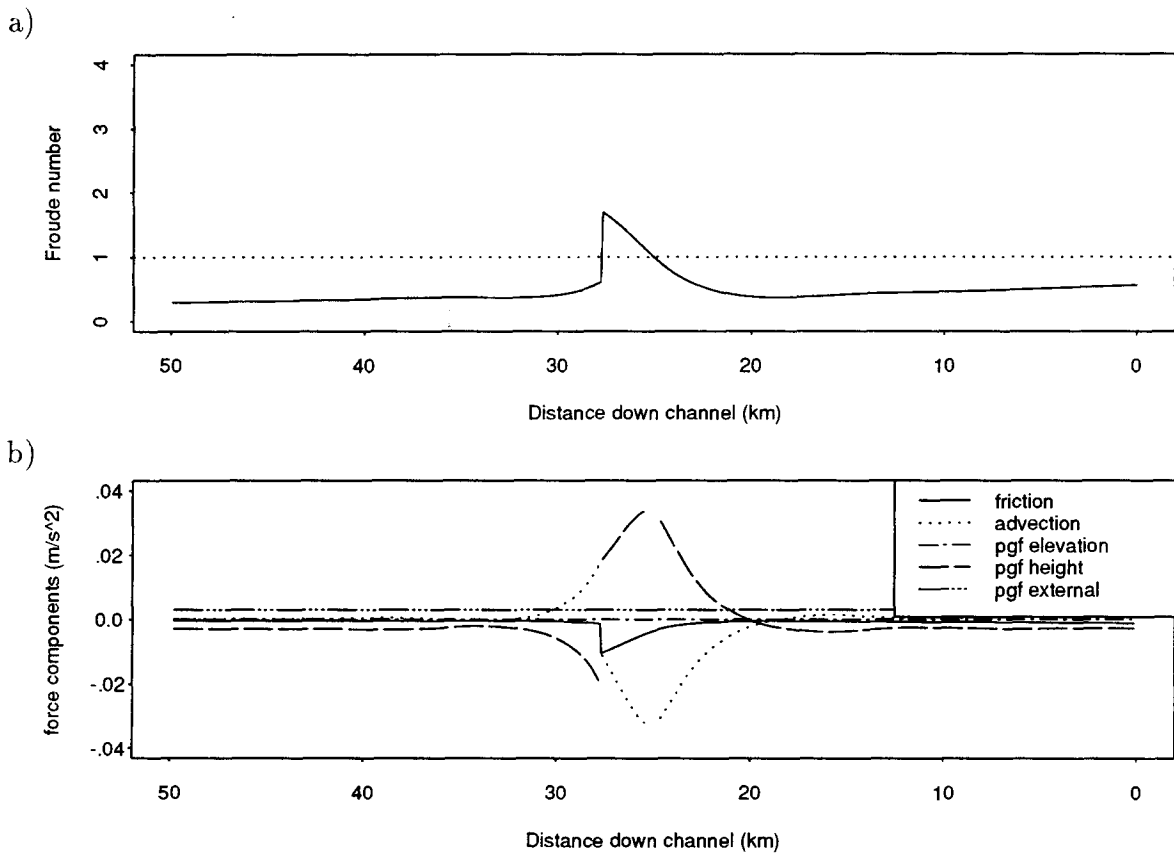
Figure 7.7: Gap wind flow for rectangular channel with "most likely" input parameters. a) Froude number; b) Force balance components.
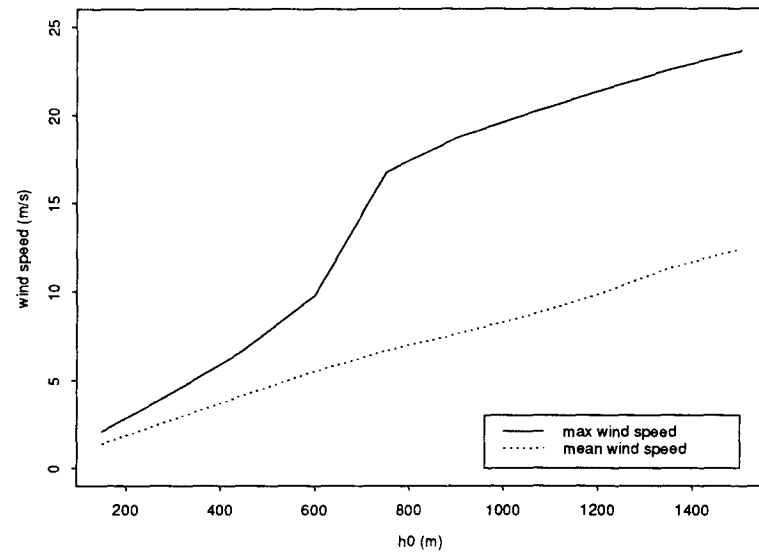
Figure 7.8: Sensitivity of mean and maximum gap wind speed to changes in h_0 (initial gap wind height) for a rectangular channel with one contraction.
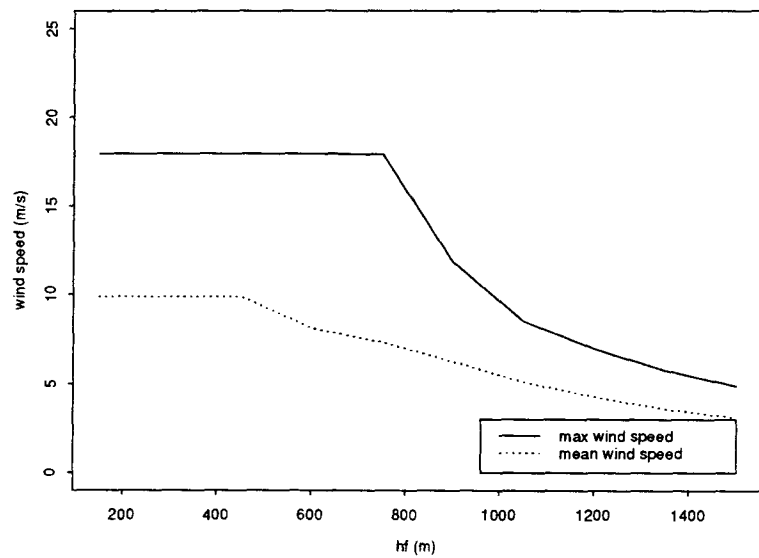
Figure 7.9: Sensitivity of mean and maximum gap wind speed to changes in h_f (gap wind height at end of channel) for a rectangular channel with one contraction.
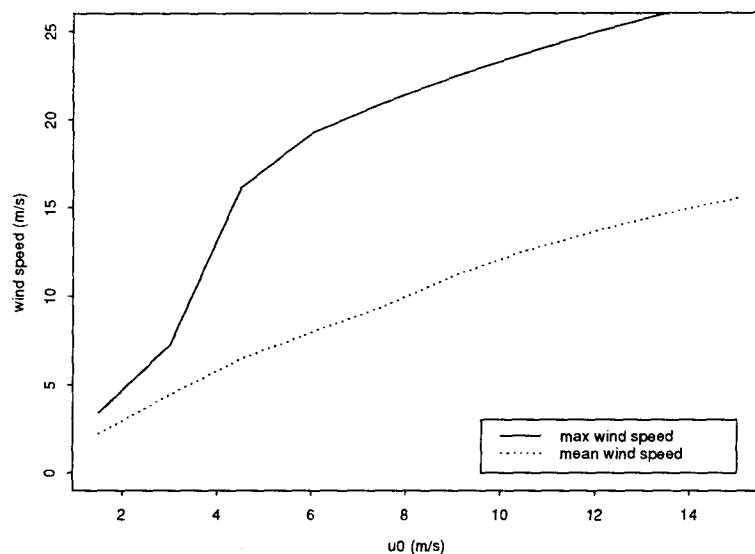
Figure 7.10: Sensitivity of mean and maximum gap wind speed to changes in u_0 (initial wind speed) for a rectangular channel with one contraction.
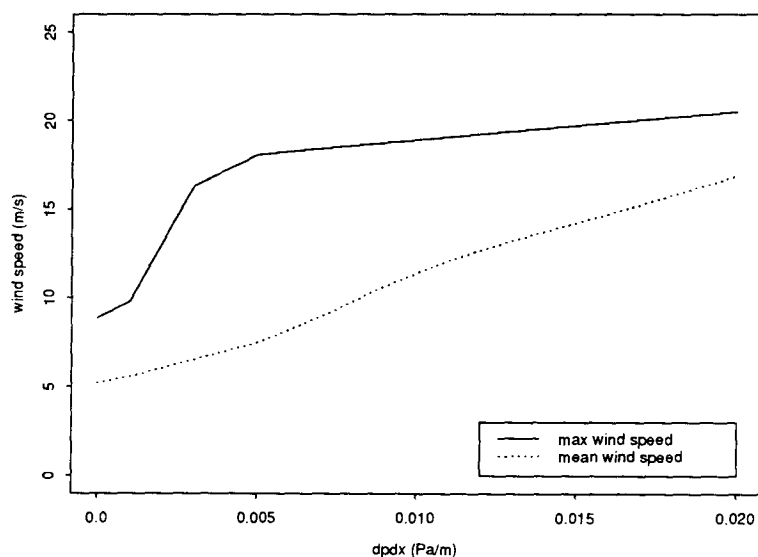
Figure 7.11: Sensitivity of mean and maximum gap wind speed to changes in $\frac{dp}{dx}$ (external pressure gradient) for a rectangular channel with one contraction.
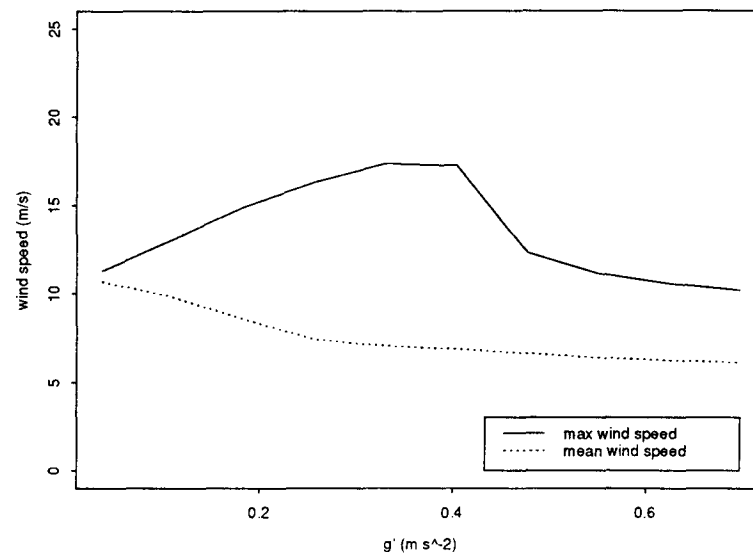
Figure 7.12: Sensitivity of mean and maximum gap wind speed to changes in g' (effective gravity) for a rectangular channel with one contraction.
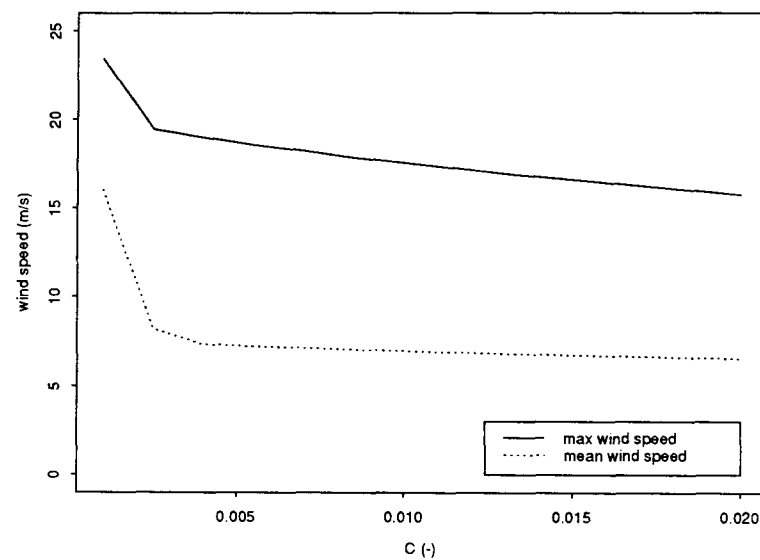
Figure 7.13: Sensitivity of mean and maximum gap wind speed to changes in C (drag coefficient) for a rectangular channel with one contraction.

The results show that increases in u_0, h_0, and $\frac{dP}{dx}$ lead to increased gap wind speed – this will be called *positive sensitivity*. Increases in h_f, and C lead to decreased gap wind speed – this will be called *negative sensitivity*. Increases in g', first increase and then decrease the maximum wind speed (ie. there is an optimum g'), while the mean wind speed shows a slight, but steady decrease.

The sensitivity of flow speed to h_0 (figure 7.8) and u_0 (figure 7.10) shows similar positive sensitivity and will be grouped together for discussion. The maximum flow speed has the greatest sensitivity – the largest increase across the range – to these variables. Three distinct regions of flow can be noted from the maximum wind speed curves in each of figures 7.8 and 7.10. The first zone, at low values of h_0 and u_0, has subcritical flow throughout the channel. Typical flow characteristics from this regime are depicted in figures 7.14 and 7.15 which are for h_0 of 300 m. The flow everywhere is subcritical, with maximum speed at the channel contraction. The force components show a balance, mainly between the external pressure gradient force and the height pressure gradient force. Since the RAMS force balance analysis doesn't differentiate between the various pressure gradient components of the force balance, this would correspond to a small pressure gradient term – between -100 and -120, and -155 and -170 km in figure 5.41. Advection becomes important near the contraction and gap wind height increases along the channel.

The second distinct flow regime in the sensitivity of wind to h_0 and u_0 is when critical flow begins. This is indicated in figures 7.8 and 7.10 by a very rapid increase in maximum wind speed. Figures 7.6 and 7.7, which depict the flow for the "most likely" input parameters, show this mixed flow transition.

The third sensitivity regime occurs with large h_0 and u_0, where the flow speed increases at a rate similar to the subcritical regime. Here, the extent of supercritical flow

is increasing and the various flow features resemble figures 7.6 and 7.7 except the super-critical flow downstream of the contraction is of greater extent.

a)

b)
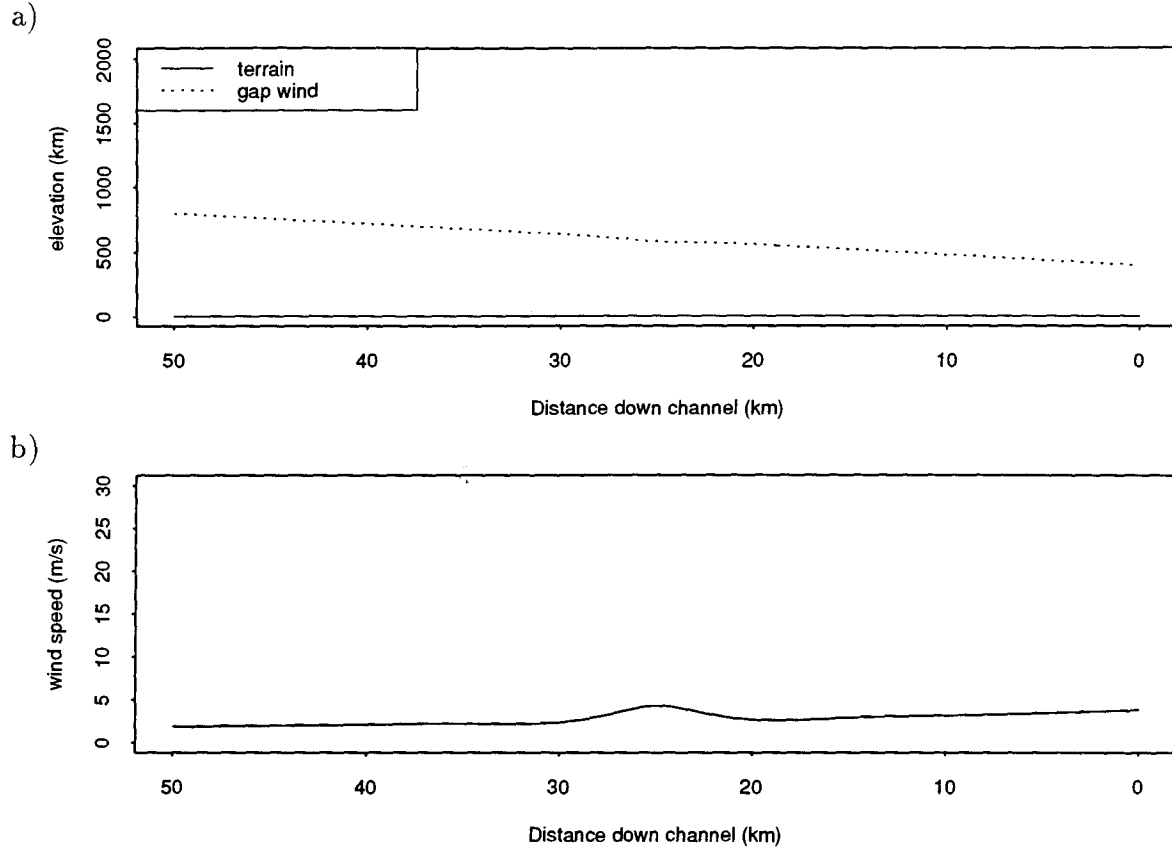
Figure 7.14: Gap wind flow for rectangular channel showing subcritical regime, with $h_0 = 300$ m. a) Height of gap wind; b) Gap wind speed.

The flow speed sensitivity to $\frac{dP}{dx}$ (external pressure gradient, figure 7.11) is positive and similar to that for h_0 and u_0. Again, there are three distinct regimes, the low speed regime where the flow in everywhere subcritical, a middle regime of rapidly increasing maximum flow where the flow is starting to become supercritical near the contraction, and a regime for large values of $\frac{dP}{dx}$, where the extent of supercritical flow is increasing. In the third regime, supercritical flow exists as an initial condition at the start of the channel, transits to subcritical in a hydraulic jump upstream of the contraction, transits

a)

b)
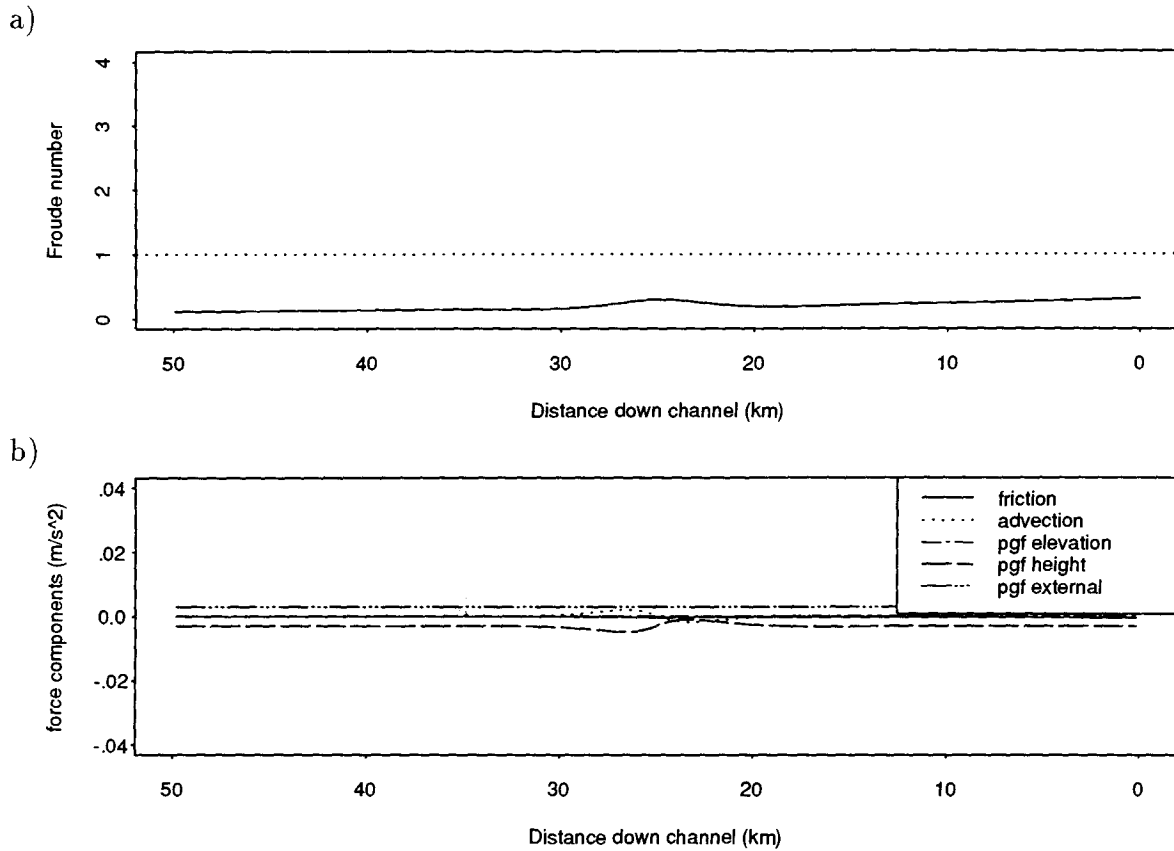
Figure 7.15: Gap wind flow for rectangular channel showing subcritical regime, with $h_0 = 300$ m. a) Froude number; b) Force balance components.

to supercritical at the contraction, and then jumps back to subcritical further downstream under the controlling influence of the fixed gap wind height at the channel end. This can be seen in figures 7.16 and 7.17 which are for $\frac{dP}{dx}$ of 0.013 Pa m^{-1}. In the RAMS force balance, figure 5.41, friction is an important component in the zone of strong supercritical flow (near location -145 km), however it is less than or equal to the advection term. The plots for maximum $\frac{dP}{dx}$ of 0.02 (figures 7.18 and 7.19), show supercritical flow throughout the channel, except near the end where the flow jumps to subcritical due to the end of channel control. In the supercritical flow created by the large externally imposed pressure gradient, the primary force balance (figure 7.19b) is between external pressure gradient

and friction. Advection and height pressure gradients are smaller, but become important near the contraction.

a)

b)
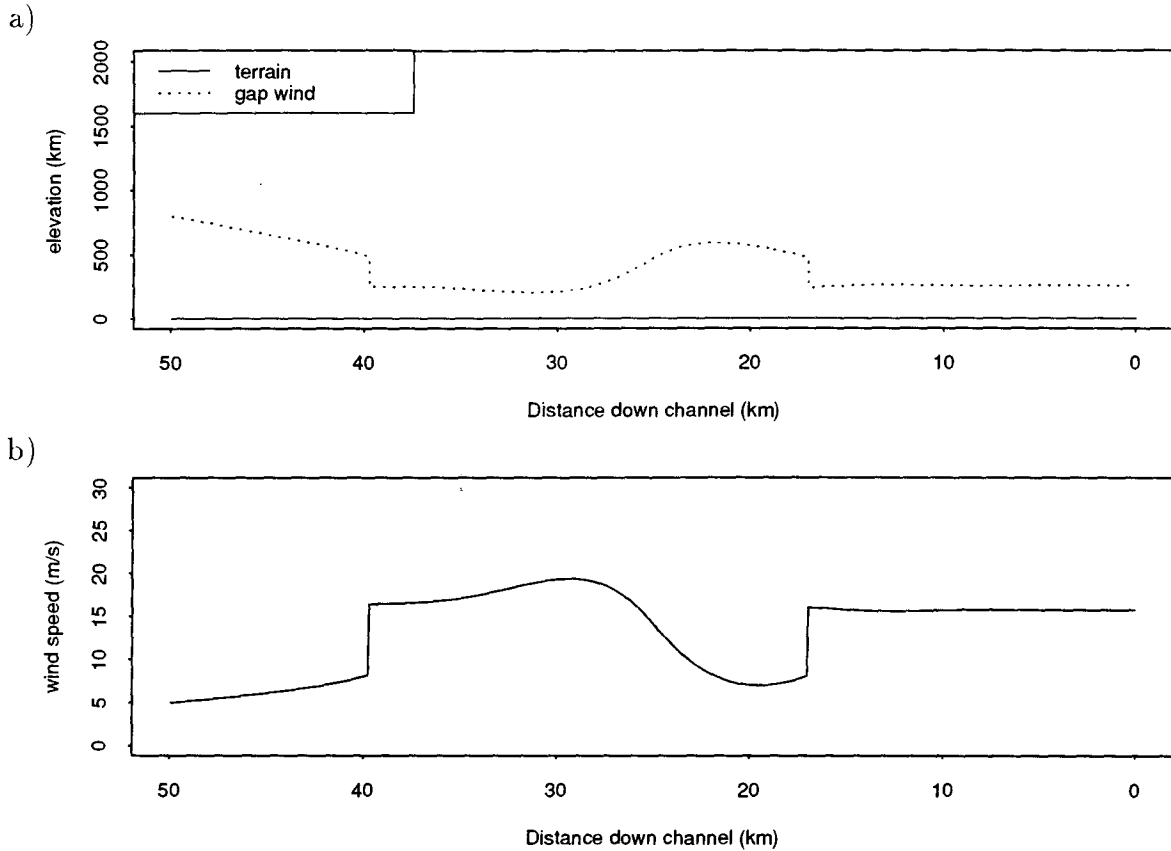
Figure 7.16: Gap wind flow for rectangular channel showing predominantly supercritical regime, with $\frac{dP}{dx} = 0.013$ Pa m^{-1}. a) Height of gap wind; b) Gap wind speed.

The sensitivity of gap wind to h_f is opposite to that of h_0. Increasing values of h_f mean that subcritical flow controlled by the the end point height is able to propagate further upstream, resulting in decreased flow speeds in the channel. Once again, there are three flow regimes apparent in figure 7.9. The first, for low values of h_f have relatively high wind speeds. Here, the height of the gap wind at the channel end is too low to act as a control so that no influence is exerted upstream. The second flow regime with h_f of 450 to 1050 m, is where the end point is able to act as a control on the flow. This is similar

a)

b)
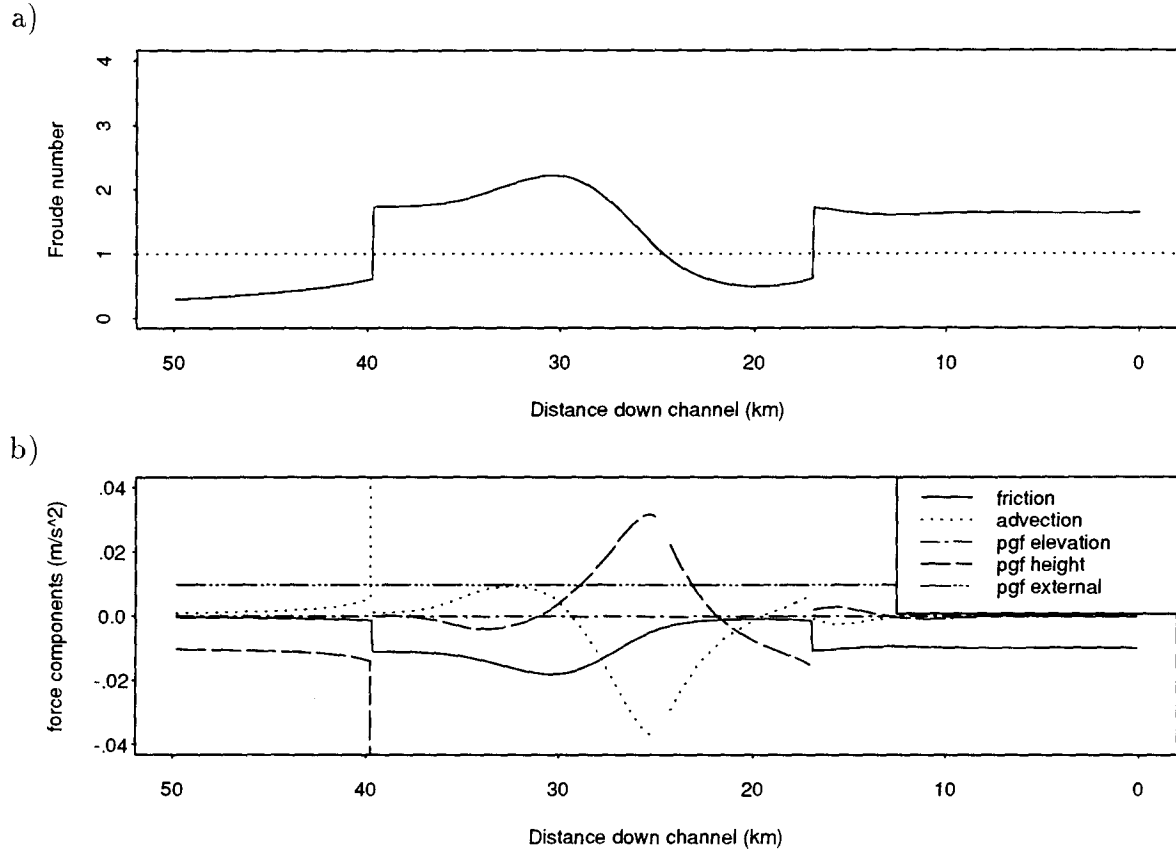
Figure 7.17: Gap wind flow for rectangular channel showing predominantly supercritical regime, with $\frac{dP}{dx} = 0.013$ Pa m^{-1}. a) Froude number; b) Force balance components.

to the simulation with the "most likely" input parameters shown in figures 7.6 and 7.7. The third regime, for large values of h_f, is one in which the downstream control is able to completely "drown" the flow upstream, forcing slow, subcritical flow throughout. This is shown in figures 7.20 and 7.21 which are for h_f of 1050 m.

The sensitivity of the flow speed to increasing C (drag coefficient) is also negative with increasing drag coefficient resulting in decreasing wind speed (figure 7.13) as would be expected. However the sensitivity is not large compared to most of the other parameters. Indeed the curve is quite flat for values of C larger than 0.003. This is because the frictional term in the force balance is typically of minor importance compared with

a)

b)
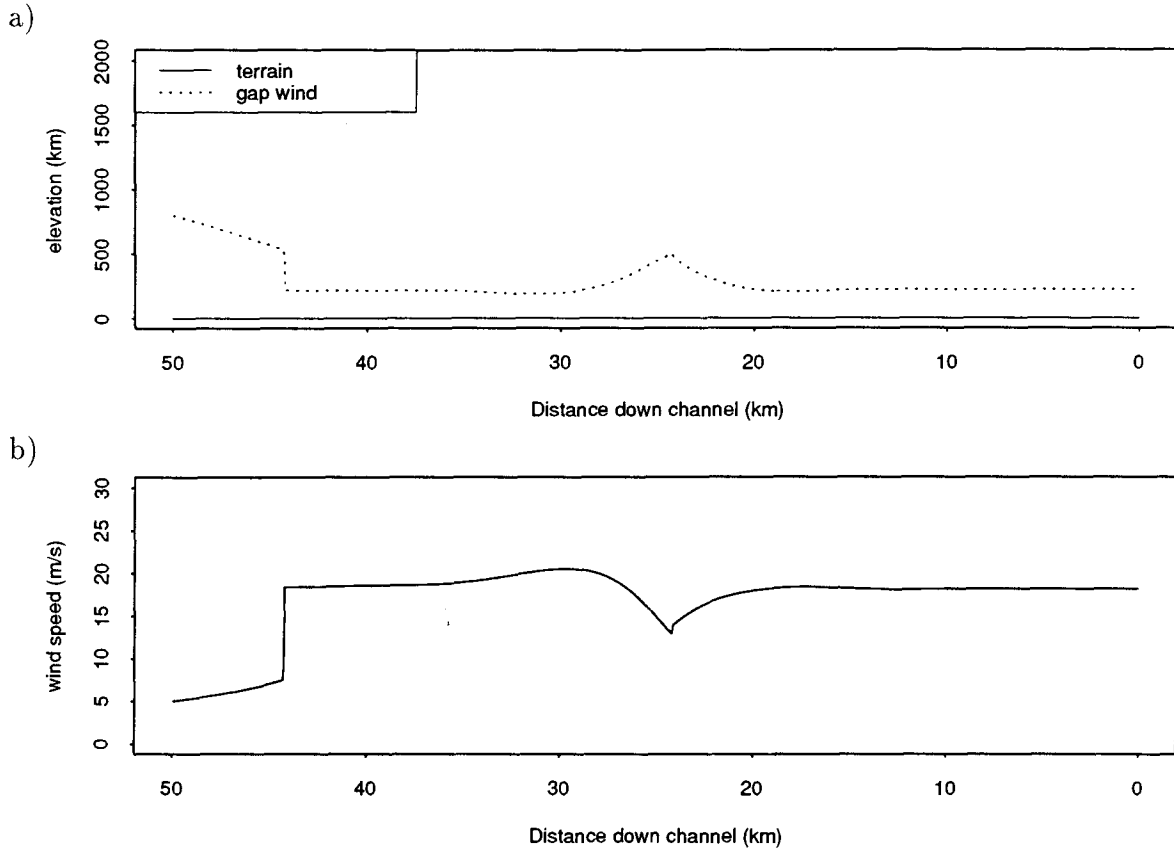
Figure 7.18: Gap wind flow for rectangular channel showing entirely supercritical regime, with $\frac{dP}{dx} = 0.02$ Pa m^{-1}. a) Height of gap wind; b) Gap wind speed.

changes in gap wind height, external pressure gradient, and advection. In the case of predominantly supercritical flow, the sensitivity would be much more negative (as it is for small C values), because the force balance is primarily between friction and external pressure gradient. Initially high flow speeds for low values of C (0.001), are due to propagation of supercritical flow through the contraction which jump to subcritical further downstream in response to the upstream influence of h_f. This is shown in figures 7.22 and 7.23. Larger drag coefficients result in critical flow at the contraction, with subcritical flow extending upstream and supercritical flow downstream.

The sensitivity of gap wind flow to g' (effective gravity) shown in figure 7.12 is mixed.

a)

b)
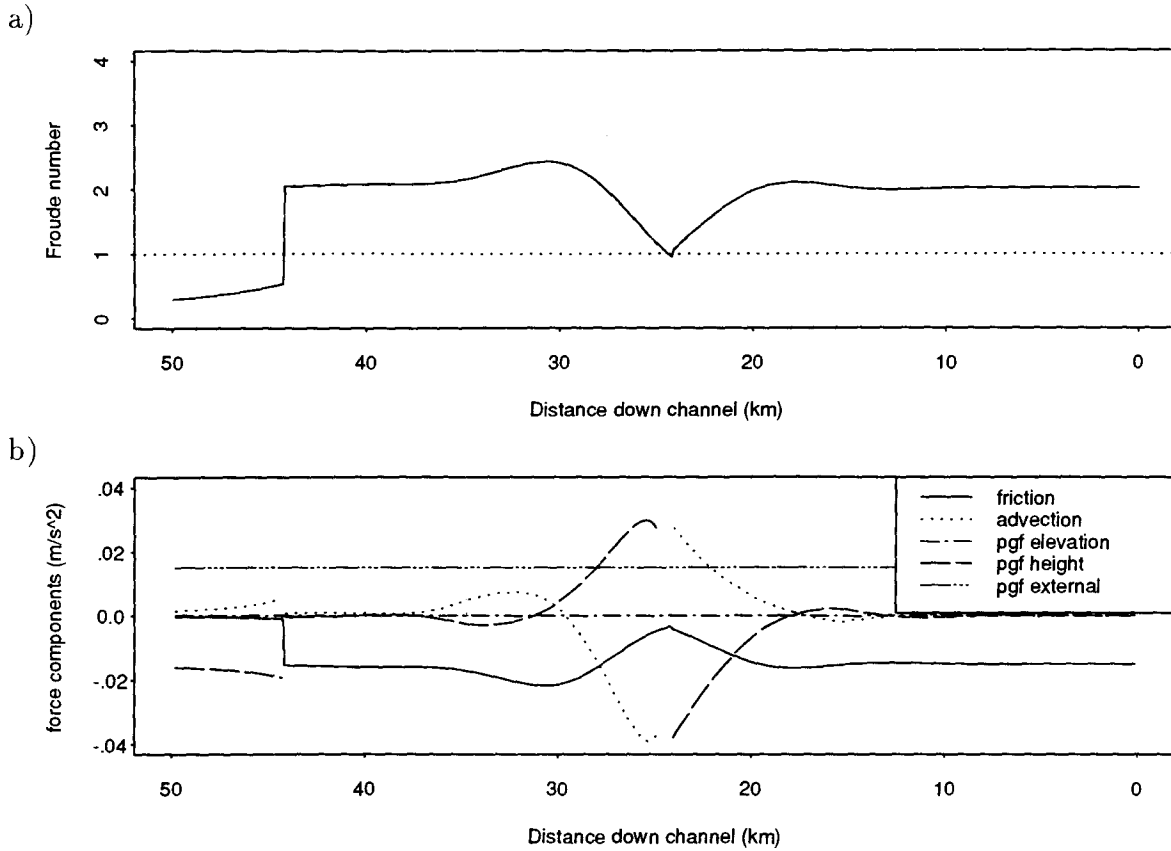
Figure 7.19: Gap wind flow for rectangular channel showing entirely supercritical regime, with $\frac{dP}{dx} = 0.02$ Pa m^{-1}. a) Froude number; b) Force balance components.

The mean flow speed declines as g' increases while the maximum speed first increases and then declines. The initial flow, for low values of g' is nearly everywhere supercritical. This flow state is shown in figures 7.24 and 7.25. Supercritical flow can exist for relatively small wind speeds with low g' because of the inverse relationship between g' and the Froude number. As for the case of supercritical flow with large $\frac{dP}{dx}$, the force analysis (figure 7.25b) shows the main balance is between friction and external pressure gradient, and that changes in height are only important near the contraction. A difference between the two situations (large $\frac{dP}{dx}$, and small g') is the force component magnitudes are much smaller for small g', resembling RAMS force balance component magnitudes. Because

a)

b)
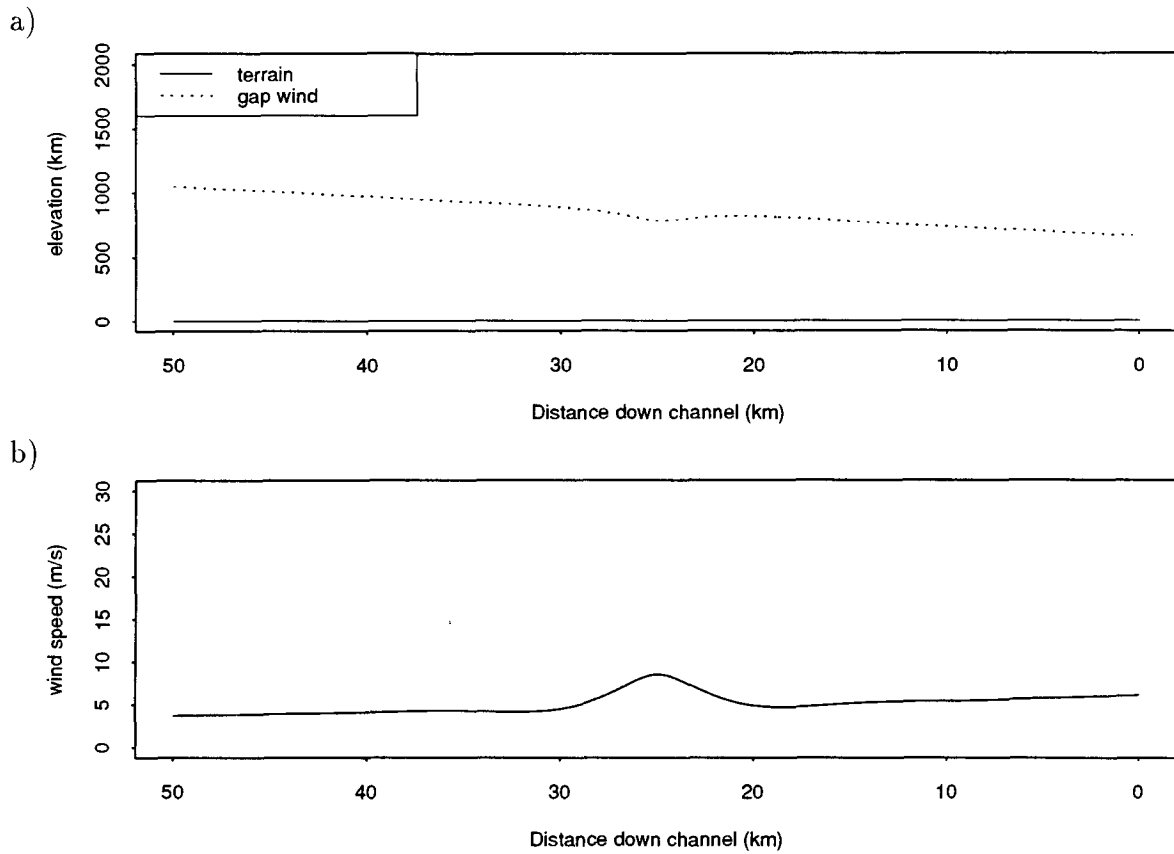
Figure 7.20: Gap wind flow for rectangular channel showing influence of downstream control on flow, with $h_f = 1050$ m. a) Height of gap wind; b) Gap wind speed.

the force balance is between external pressure gradient and friction in these situations, the friction model of chapter 6 would be an appropriate simple model to apply. This is expected since under these conditions, the pressure gradient resulting from variations in gap wind height which is fundamental to hydraulic flow, will be small compared to other forces. Values of g' in the middle of the probable range result in a mixed flow regime similar to the "most likely" flow shown in figures 7.6 and 7.7 with supercritical flow downstream of the contraction and subcritical flow upstream. The effect of this is to increase the peak wind, but decrease the mean wind – the flow becomes more variable. As g' is further increased the flow becomes subcritical everywhere, resulting in decreased

a)

b)
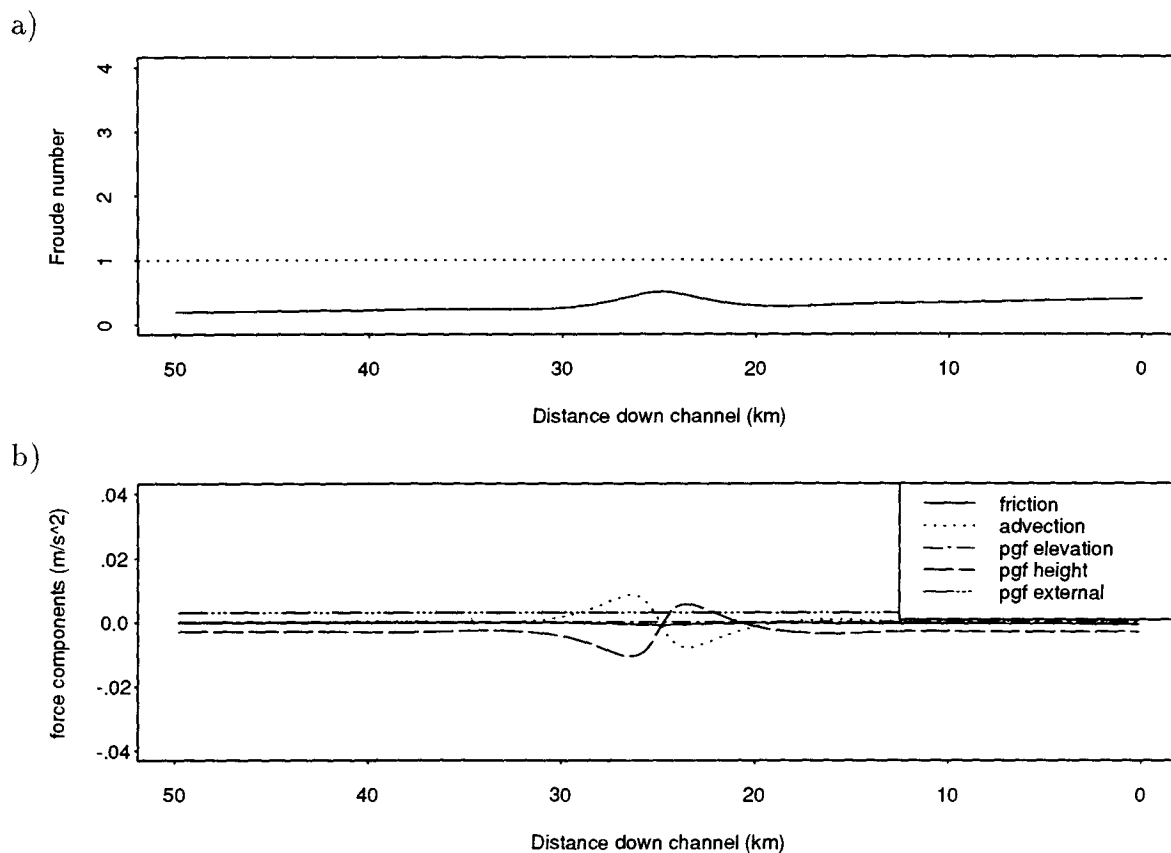
Figure 7.21: Gap wind flow for rectangular channel showing influence of downstream control on flow, with $h_f = 1050$ m. a) Froude number; b) Force balance components.

peak wind speeds and somewhat decreased mean wind speeds. This flow regime is shown in figures 7.26 and 7.27. Simulations for small values of g' may not be valid due to violation of basic assumptions in the extension of hydraulics to gap winds.

a)

b)
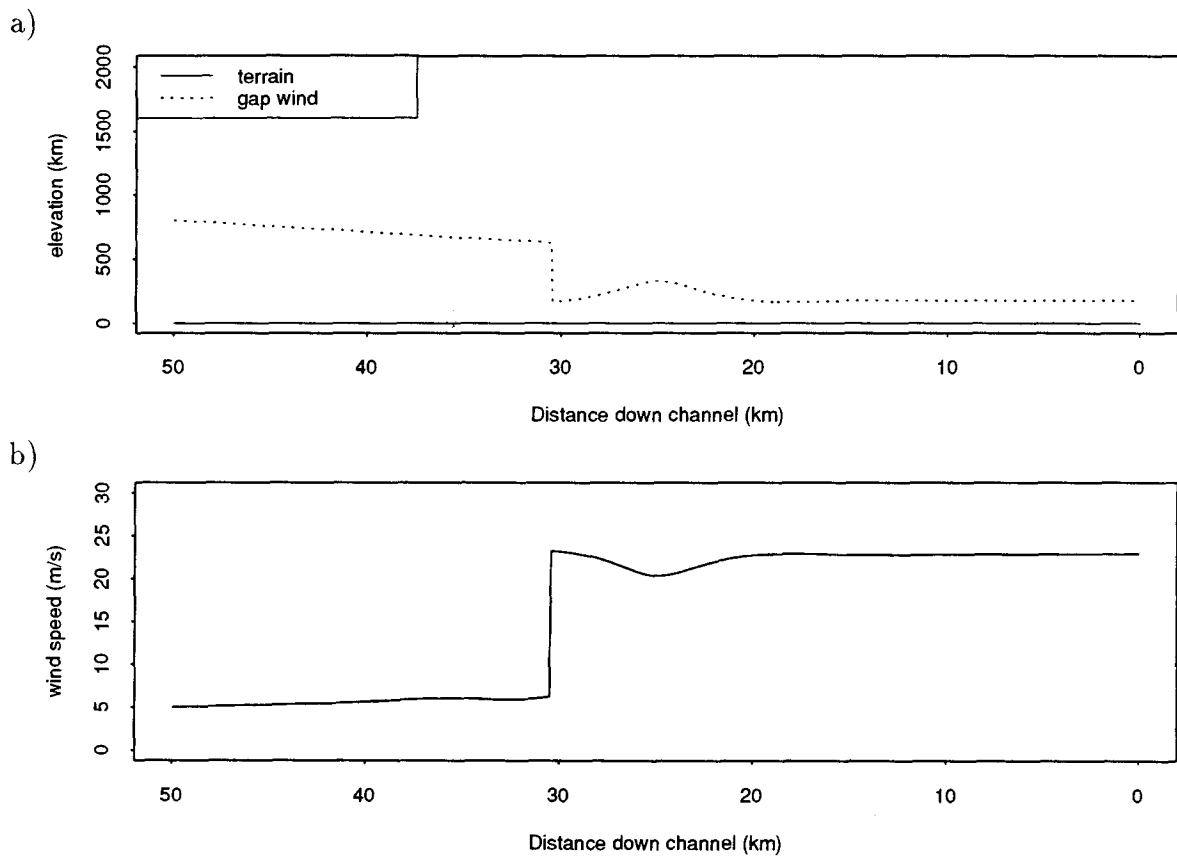
Figure 7.22: Gap wind flow for rectangular channel showing effect of small frictional drag, with $C = 0.001$. a) Height of gap wind; b) Gap wind speed.

a)

b)
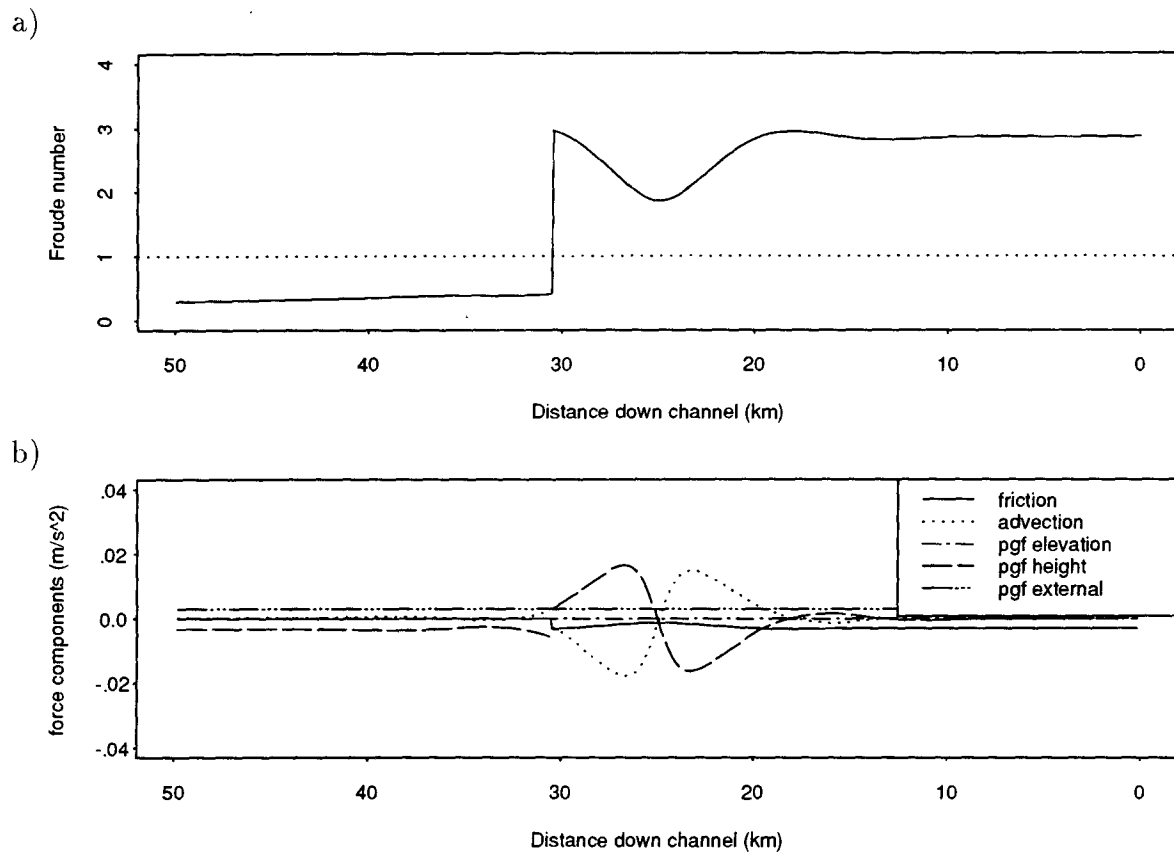
Figure 7.23: Gap wind flow for rectangular channel showing effect of small frictional drag, with $C = 0.001$. a) Froude number; b) Force balance components.

a)

b)
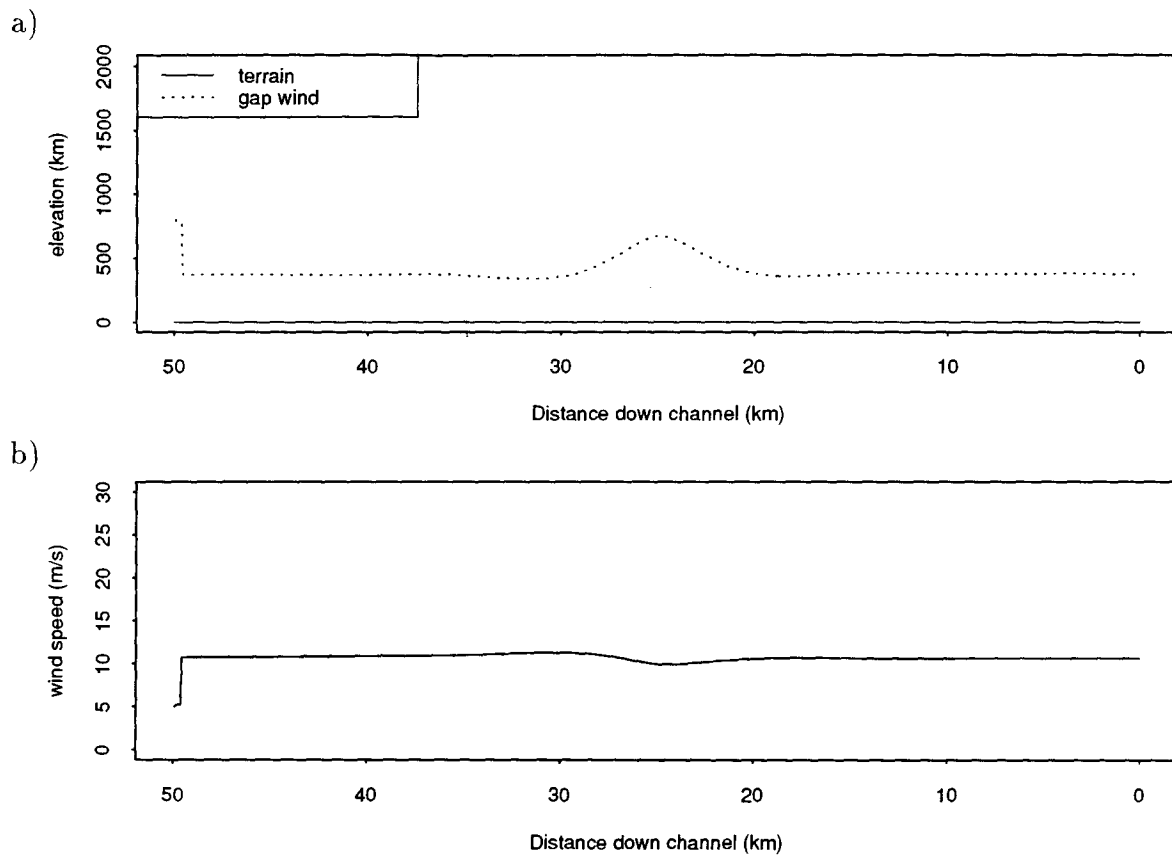
Figure 7.24: Gap wind flow for rectangular channel showing effect of small effective gravity due to a difference in potential temperature between the layers of 1° C. a) Height of gap wind; b) Gap wind speed.

a)

b)
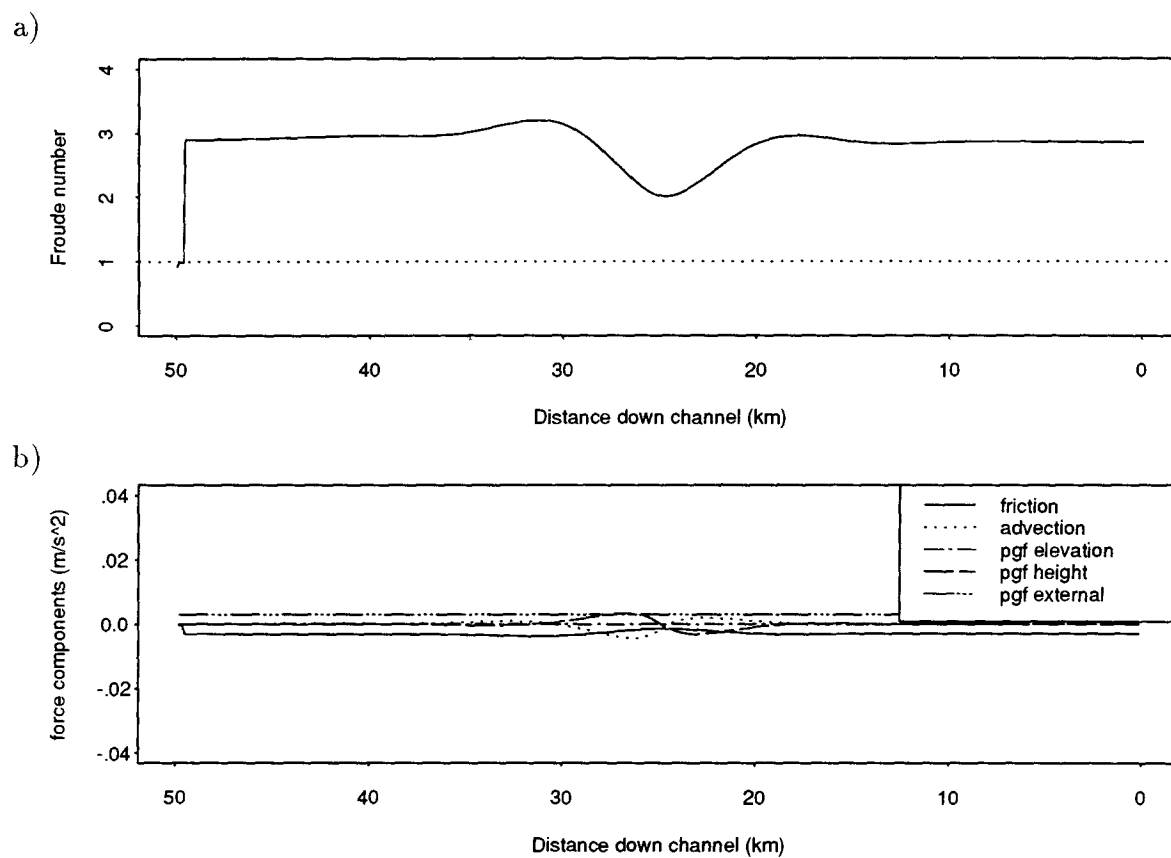
Figure 7.25: Gap wind flow for rectangular channel showing effect of small effective gravity due to a difference in potential temperature between the layers of 1° C. a) Froude number; b) Force balance components.

a)

b)
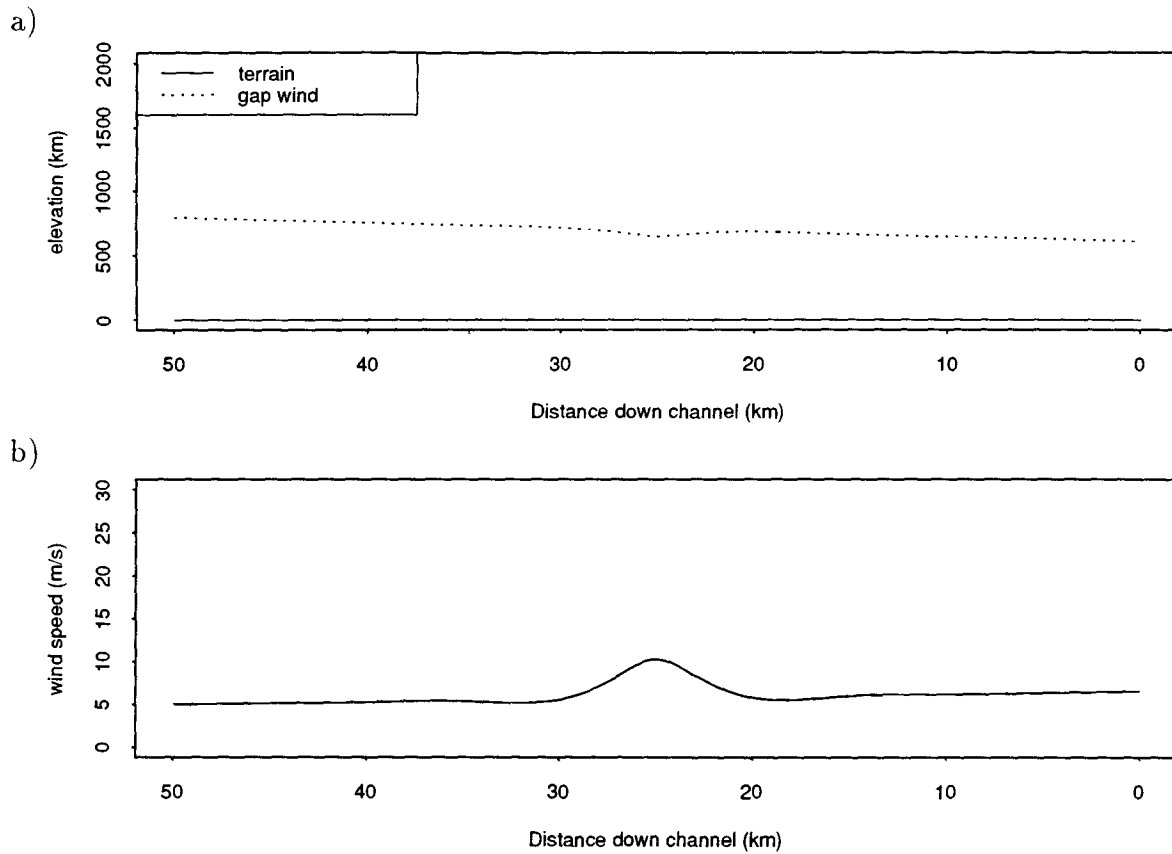
Figure 7.26: Gap wind flow for rectangular channel showing effect of large effective gravity due to a difference in potential temperature between the layers of 19° C. a) Height of gap wind; b) Gap wind speed.

a)

b)
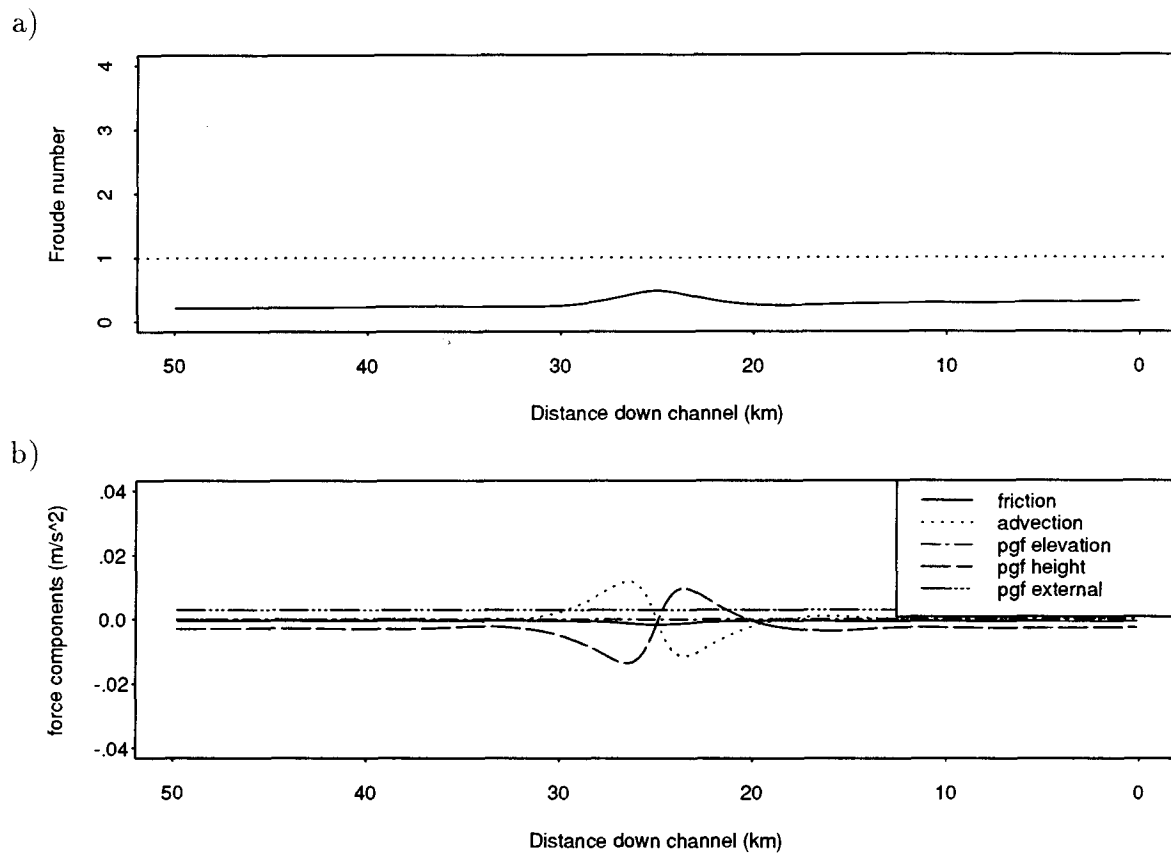
Figure 7.27: Gap wind flow for rectangular channel showing effect of large effective gravity due to a difference in potential temperature between the layers of 19° C. a) Froude number; b) Force balance components.

7.3.2 Howe Sound – realistic and modified channel

Results from rectangular channel simulations are useful to clearly show the effects of varying external parameters, and to better understand atmospheric application of hydraulic theory. They will serve as a benchmark for comparison with the results from channels of more realistic geometry. Such a channel has been constructed, as mentioned previously, by taking cross sections perpendicular to the channel orientation at 2500 m intervals from Squamish Airport (SQA) near the head, to Lookout Point (LOO) at the mouth of Howe Sound. The cross section locations are shown in figure 7.28 and the area data are summarized in tables B.1 and B.2 in appendix B which tabulate the cross sectional area below the given height in 100 m intervals from 0 to 2000 m, at each of the 21 locations (0 km is SQA, 50 km is LOO).

One problem with using actual terrain cross section data without modification stems from limitations inherent in the hydraulic model. *Hydmod* is 1-dimensional. It allows variation in the flow only in the along-channel direction, and presumes that flow in the lower layer is constant in the vertical and cross-channel directions. Observations and RAMS simulation results (figure 5.16) indicate the flow is not constant in the cross-channel direction, especially where the channel widens. Rather, observations suggest the significant flow is constrained by topography to the main channel along the eastern side of Howe Sound, with more stagnant flow elsewhere. Tests using the unmodified terrain cross section data shown in tables B.1 and B.2, which will be presented subsequently, show simulated gap winds too slow and shallow where the channel widens. To circumvent this problem, a modified channel was created by connecting the main ridge lines of Anvil, Gambier, and Bowen Islands with a vertical "wall". The location of this unique numerical "geomorphic formation", as well as the position and orientation of cross sections are shown in figure 7.28. The cross sectional areas at each location and height for the

modified channel, are shown in tables B.3 and B.4.

Hydmod will be compared with actual data and RAMS model output. To simplify comparison with RAMS output, as in chapter 6, plots will be made with horizontal orientation and scale corresponding to that of the RAMS simulation. The numbers along the top of each plot correspond to the cross section number in figure 7.28. *Hydmod* output for the "most likely" values of input parameters for the (unmodified) realistic channel are shown in figures 7.29 - 7.30. The "most likely" input parameters are slightly different than for the rectangular channel simulations and are given in table 7.2. The main difference is the "most likely" value for g' was reduced to correspond to a potential temperature difference of 5° C, h_f was reduced to 600 m, and the drag coefficient, C, was set to 0.02 over land and 0.005 over water. This was so the base configuration for the modified and realistic channels would more closely match observations. The potential temperature difference of 5° C, depending to some extent upon how it is measured, is closer to what is found from the AIRsonde™ profiles than the 10° C difference used in the rectangular channel tests which was chosen because it lay in the middle of the probable range. Drag coefficient values are chosen following arguments outlined in chapter 6. Such a large value of C over land was chosen because the aerodynamically rough coniferous forest is combined with high form drag due to rough terrain. The value of C over water is also large because it must include the effects of aerodynamically rough sidewalls. A value for h_f was difficult to estimate, as there were no data available on which to base this. The RAMS h_f is thought to be too large for reasons discussed in chapter 5 — a factor which contributed to poor RAMS results in the southern part of Howe Sound. For this reason an h_f value of 600 m was chosen as smaller than those estimated from RAMS vertical cross section plots (800 - 1200 m) in figures 5.22 to 5.32. The probable range of these variables, used in sensitivity tests remains the same.

Initially subcritical flow in figures 7.29 and 7.30 becomes supercritical in a hydraulic
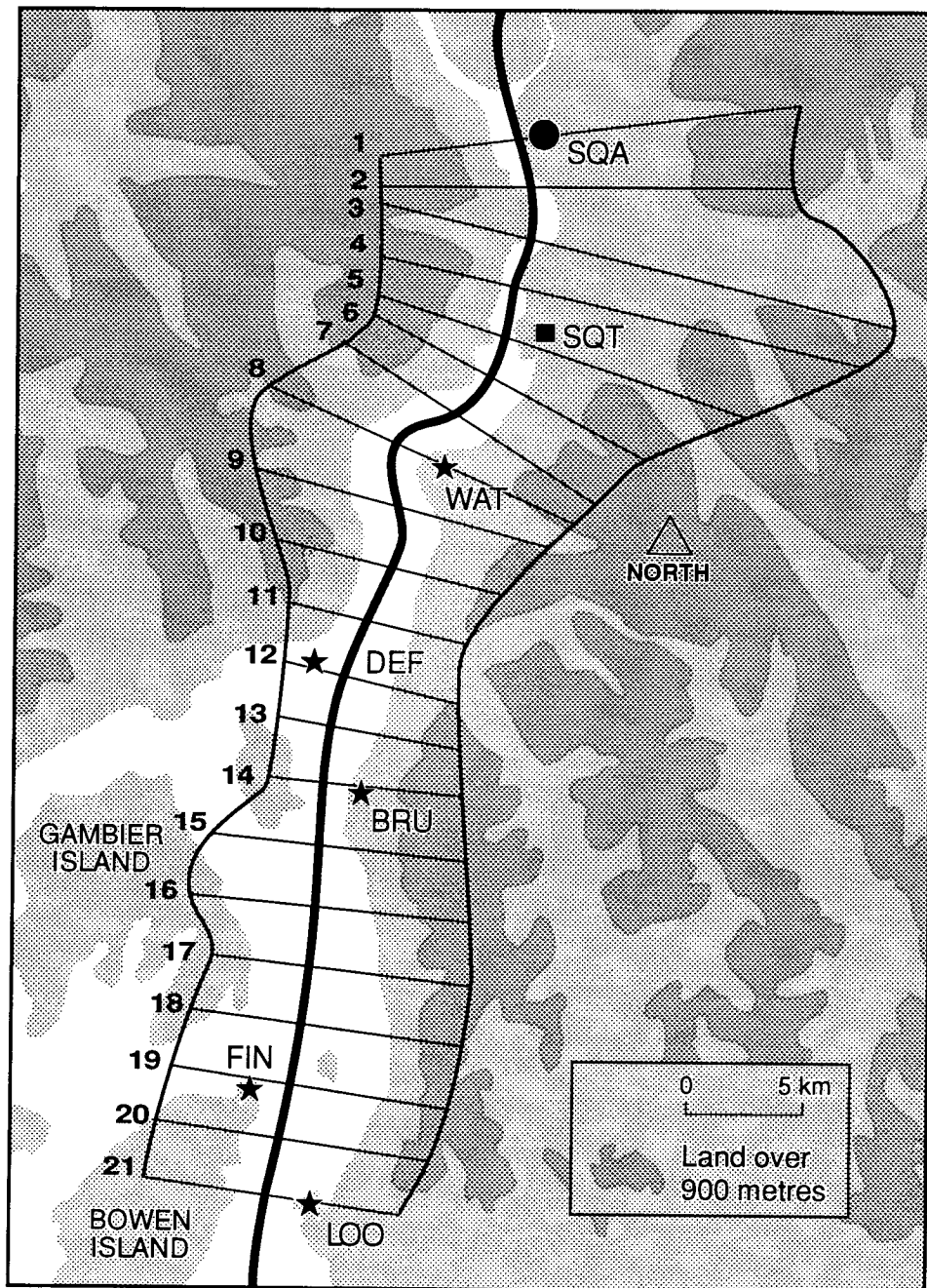
Figure 7.28: Topography of Howe-Sound region, showing locations of cross sections and of artificial "wall" along western side used to reduce channel width.

Input Variable	most likely value	probable range
h_0 initial height	800 m	150 – 1500 m
h_f ending height	600 m	150 – 1500 m
u_0 initial speed	5 m s^{-1}	1.5 – 15 m s^{-1}
$\frac{dp}{dx}$ pressure gradient	0.004 Pa m^{-1}	0.0 – .02 Pa m^{-1}
θ_1 lower pot. temp.	267 K	267 K
θ_2 upper pot. temp.	272 K	268 – 287 K
C drag coefficient	.02 land; .01 water	.001 – .02

Table 7.2: Values used in *hydmod* runs and sensitivity tests for modified channel.

drop near the horizontal coordinate of -126.5 km between SQT and WAT. This location corresponds to the horizontal contraction at 12.5 km in the cross section data of tables B.1 and B.2. The supercritical flow then reverts to subcritical in a hydraulic jump near -147 km as a result of subcritical flow upstream of the fixed gap wind depth at the channel terminus (mouth of Howe Sound). The simulated winds in the wide southern part of the channel are less than usually observed since the flow expands to fill the channel.

Simulation results for the "most likely" parameter values in the "modified channel" are given in figures 7.31 and 7.32. These results, as for the unmodified channel, show flow which is controlled by the contraction at -126.5 km (12.5 km in tables B.3 and B.4). The modified channel, however also has a control point at -142.5 km (32.5 km in the table) which is the contraction between Anvil Island and BRU. This seems closer to observed gap wind patterns which show strong winds downstream of this second contraction. (See for example the down-channel wind time series for Finisterre Island – figure 5.7b.)

During the *hydmod* simulations, between 8 and 16 potential control points were found, however only horizontal contractions at these two points were significant enough to act as controls. A comparison of the *hydmod* force balance for the "most likely" reduced channel conditions (figure 7.32) with the RAMS force balance (figure 5.41) is qualitatively similar to the comparison of the rectangular channel forces with RAMS forces. Zones of increasing winds are marked by large tendencies due to pressure gradients (primarily from horizontal gradients in gap wind height in the hydmod case), which are mostly balanced by advection. Friction becomes an important force in the areas of fast supercritical flow.

a)
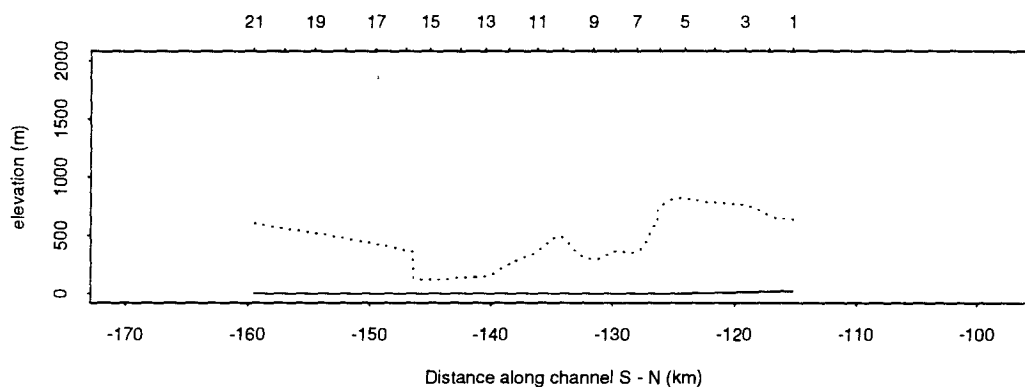
b)
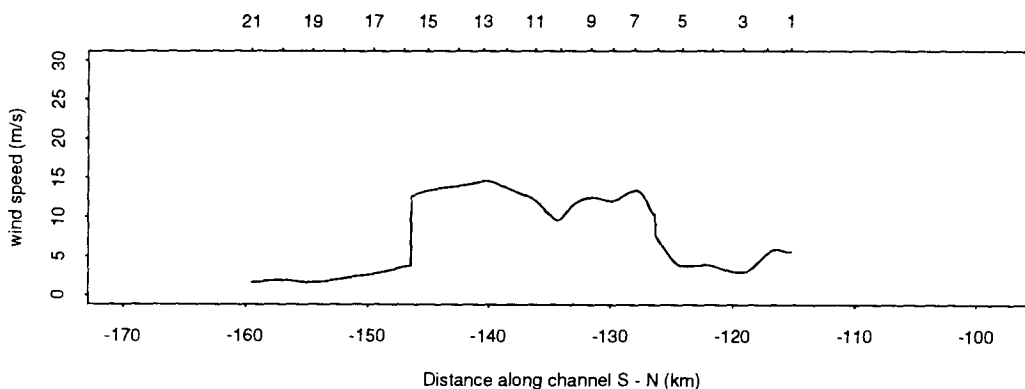
Figure 7.29: Gap wind flow for "realistic channel" using "most likely" input parameters. a) Height of gap wind; b) Gap wind speed.

Hydmod simulations using the modified channel geometry will now be compared with

a)

b)
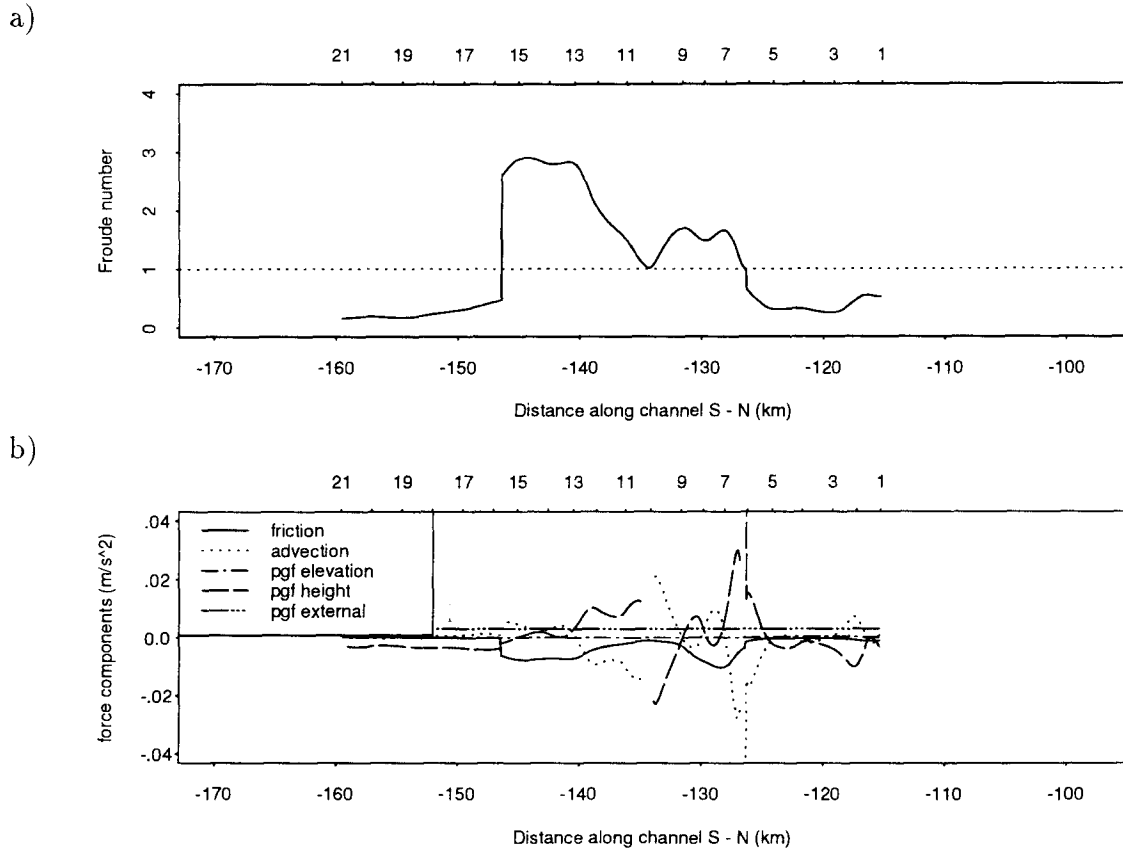
Figure 7.30: Gap wind flow for "realistic channel" using "most likely" input parameters. a) Froude number; b) Force balance components.

observations and RAMS model output at the four times which were used in chapter 6 to test the simple analytic models. In order to do this it is necessary to choose appropriate values of h_0, h_f, u_0, $\frac{dP}{dx}$, g', and the drag coefficient C. C is estimated over land to be .02, and .005 over water (see chapter 6 and the preceeding paragraphs for a discussion of this). As discussed in chapter 6, there was difficulty estimating the external pressure gradient at specific times because of conflicting pressure data. As a consequence, results using two estimates of external pressure gradient at each time are shown. Effective gravity, g' (due to a potential temperature difference between the two air layers), is difficult to estimate because the air, while showing distinct layers, is nevertheless continuously stratified. It

a)

b)
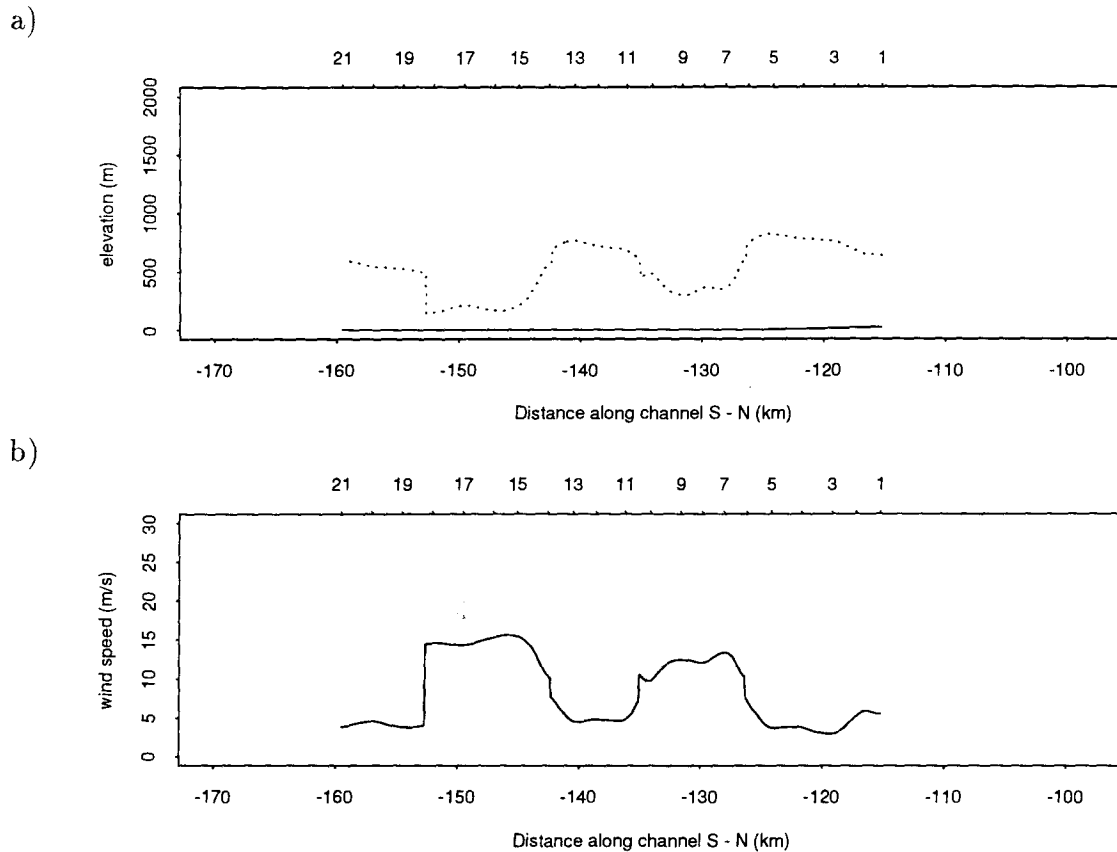
Figure 7.31: Gap wind flow for "modified channel" using "most likely" input parameters. a) Height of gap wind; b) Gap wind speed.

is set at values corresponding to a potential temperature difference of 3 or 4 °C which are estimated from AIRsonde™ profiles. h_0 and u_0 are estimated from AIRsonde™ profiles, leaving only h_f unobserved and unestimated. There is no easy solution to this problem, so h_f has been simply set to 600 m for reasons outlined previously. Higher values of h_f were found to degrade the flow representation near the channel terminus.

Table 7.3 gives the input parameters used as input to hydmod for the four times simulated. Figures 7.33 – 7.36 compare *hydmod* gap winds with observations and RAMS simulation values. The comparison being made is between modelled volume averaged wind (hydmod) and observed 10 m wind at a point so that one would expect *hydmod* winds

a)

b)
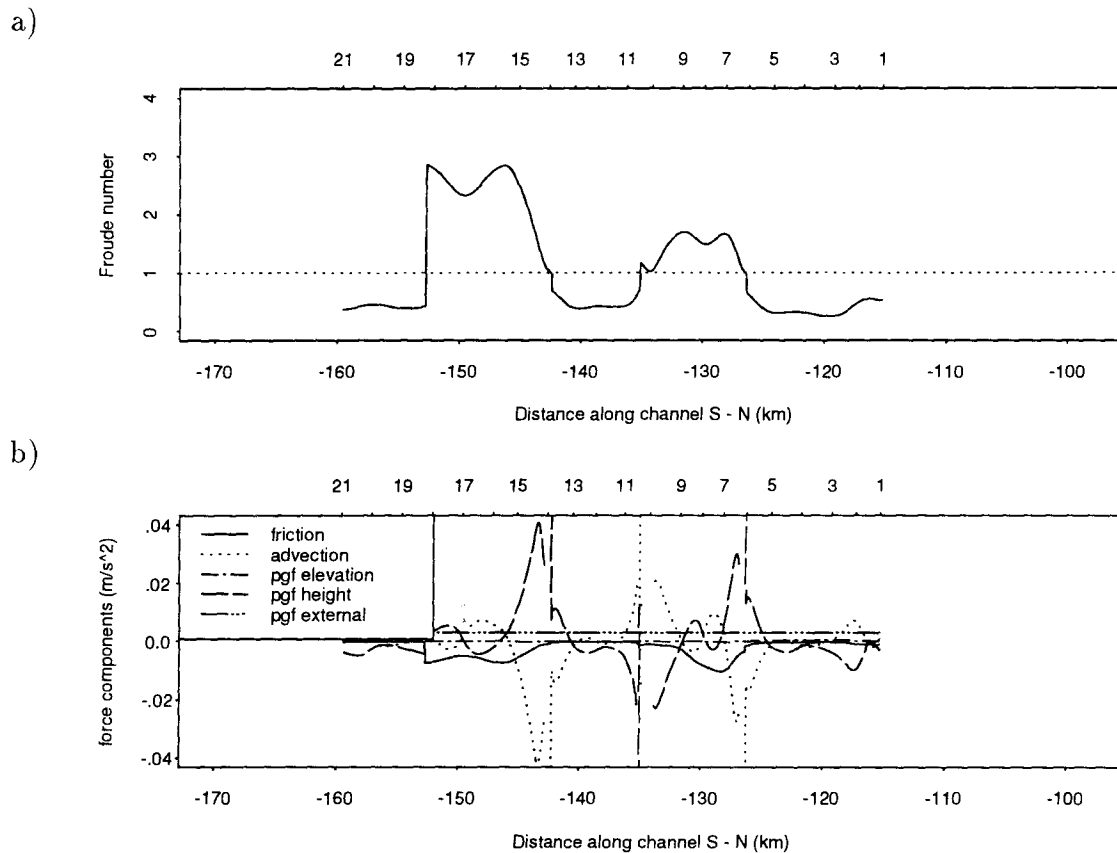
Figure 7.32: Gap wind flow for "modified channel" using "most likely" input parameters. a) Froude number; b) Force balance components.

to be somewhat stronger than observed. *Hydmod* shows some success at replicating the observed gap wind flow at these times. The surface wind observations for the most part lie between the high and low external pressure gradient gap wind curves. In particular, *hydmod* simulates both the lowest wind speeds near the start of the channel (which is expected since this is near where the initial conditions are applied), and the highest wind speeds in supercritical flow near the end of the channel. It is also able to model the observed decrease in wind near the channel exit, which in *hydmod* is due to the "backwater" effect of fixed gap wind height at the exit. The *hydmod* simulation (compared to observations) is qualitatively inferior to the RAMS simulation in the northern half of

the channel, but superior to RAMS in the southern half where the RAMS simulation had difficulties.
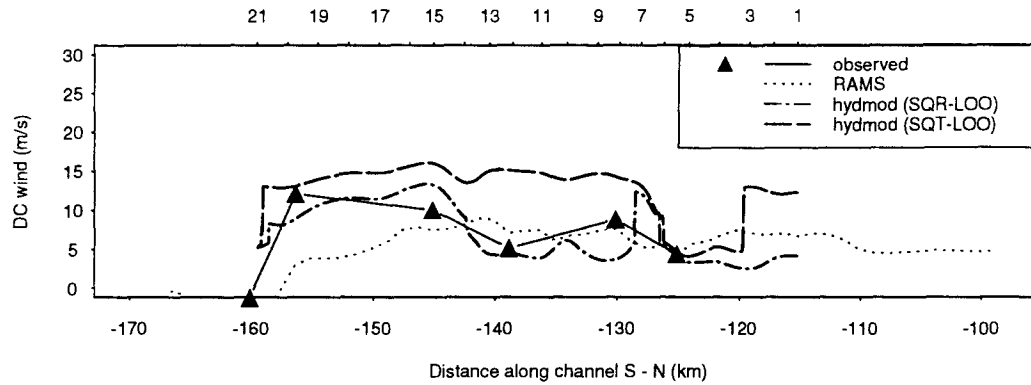
Figure 7.33: Comparison of *hydmod* output for two pressure gradient possibilities with observations and RAMS output for January 30, 23:00 PST.
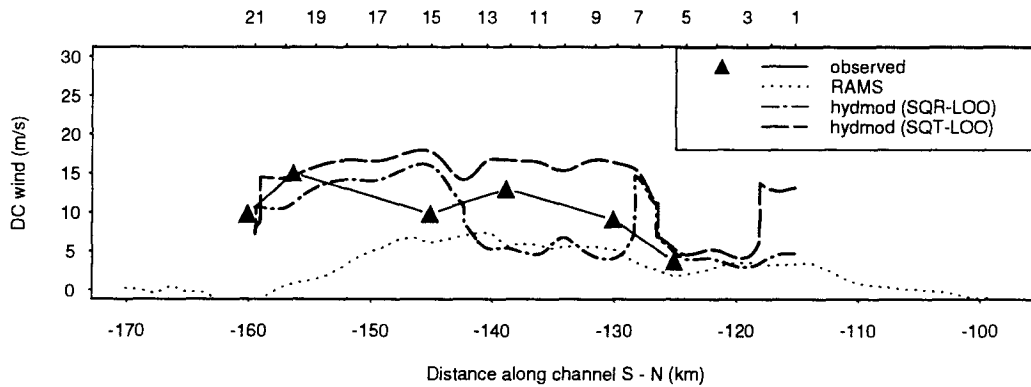
Figure 7.34: Comparison of *hydmod* output for two pressure gradient possibilities with observations and RAMS output for January 31, 05:00 PST.

Sensitivity tests

As for the rectangular channel, sensitivity tests have been carried out on the modified realistic channel. The input data and probable range are summarized in table 7.2. The results for the modified channel, which are qualititatively the same as for the rectangular
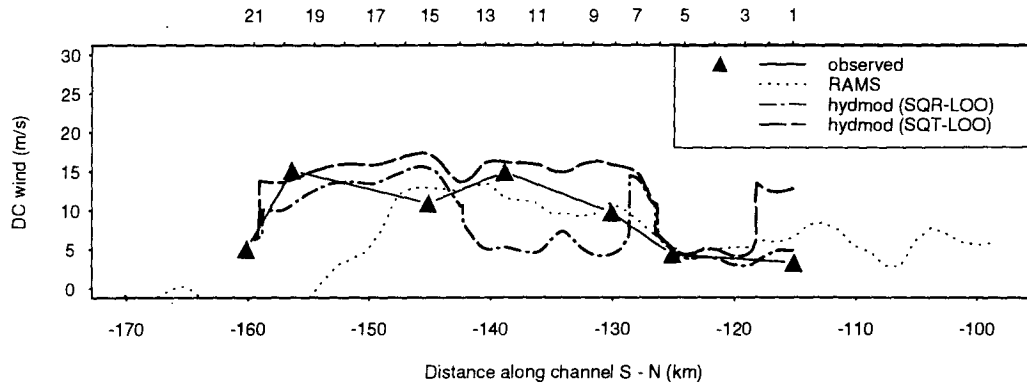
Figure 7.35: Comparison of *hydmod* output for two pressure gradient possibilities with observations and RAMS output for January 31, 11:00 PST.
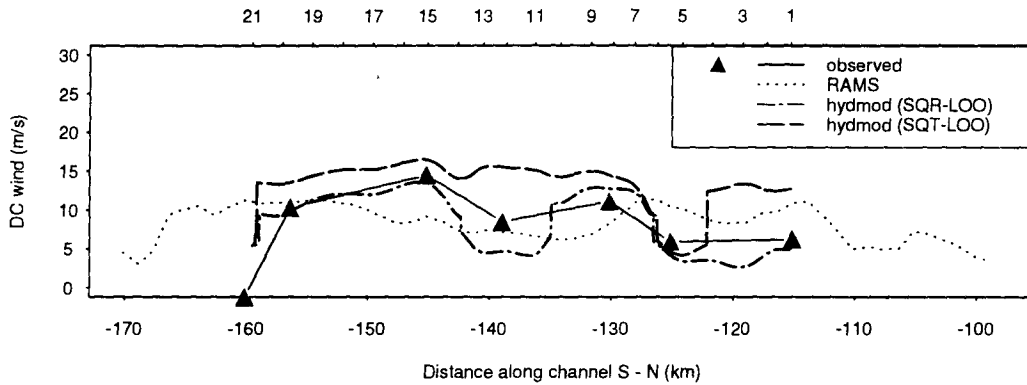
Figure 7.36: Comparison of *hydmod* output for two pressure gradient possibilities with observations and RAMS output for January 31, 17:00 PST.

and realistic channels, are shown in figures 7.37 to 7.42. The main difference between the sensitivities in the modified and rectangular channel tests is in the magnitude of the maximum wind sensitivity (ie. the change in maximum wind over the parameter range) which is greater for the rectangular channel tests. This is mostly due to the smaller potential temperature difference (g') used in the modified channel sensitivity tests which, as noted previously, tends to reduce the variability of the flow.

Parameter	Jan 30, 23:00	Jan 31, 05:00	Jan 31, 11:00	Jan 31, 17:00
initial height - h_0 (m)	1000	900	900	800
ending height - h_f (m)	600	600	600	600
initial speed - u_0 (m s^{-1})	5	8	7	7
pressure gradient - $\frac{dp}{dx}$ SQR-LOO (Pa m^{-1})	0.002	0.0025	0.0029	0.003
pressure gradient - $\frac{dp}{dx}$ SQT-LOO (Pa m^{-1})	0.0086	0.0083	0.0083	0.0092
lower pot. temp. - θ_1 (K)	267	267	267	267
upper pot. temp. - θ_2 (K)	270	271	271	270
drag coefficient - C	.02 over land and .005 over water			

Table 7.3: Values of parameters used in *hydmod* simulations. Times are PST.
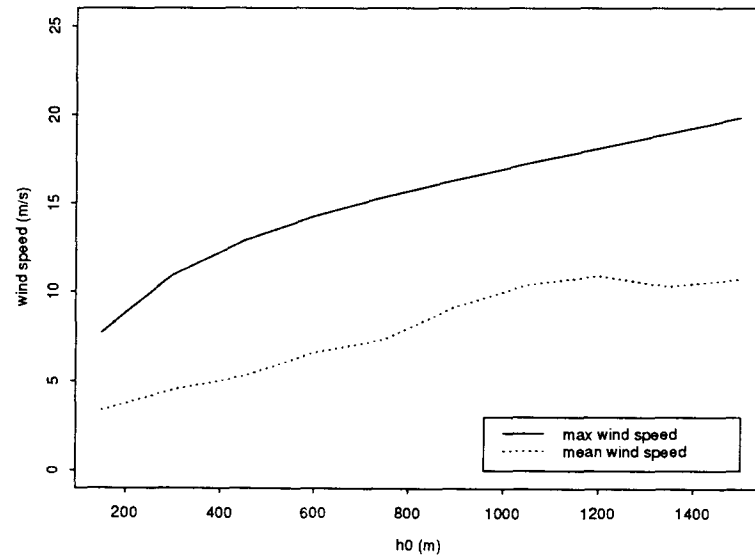
Figure 7.37: Sensitivity of mean and maximum gap wind speed to changes in h_0 (initial gap wind height) for modified channel.
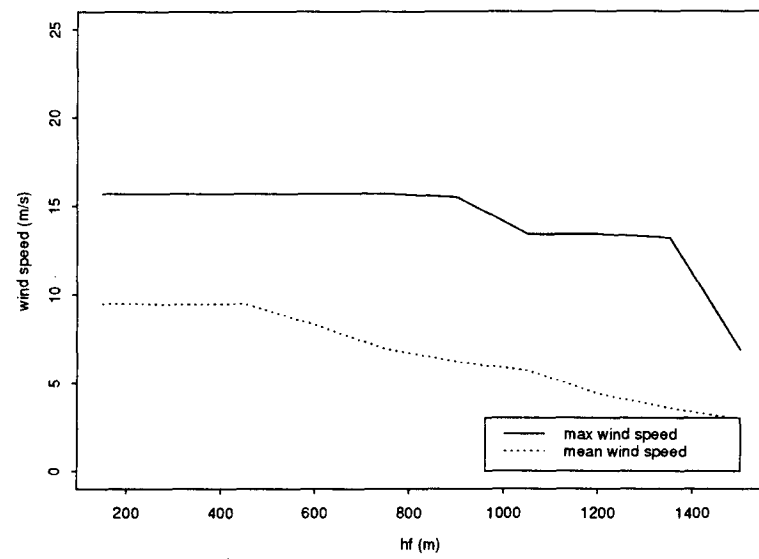
Figure 7.38: Sensitivity of mean and maximum gap wind speed to changes in h_f (gap wind height at end of channel) for modified channel.
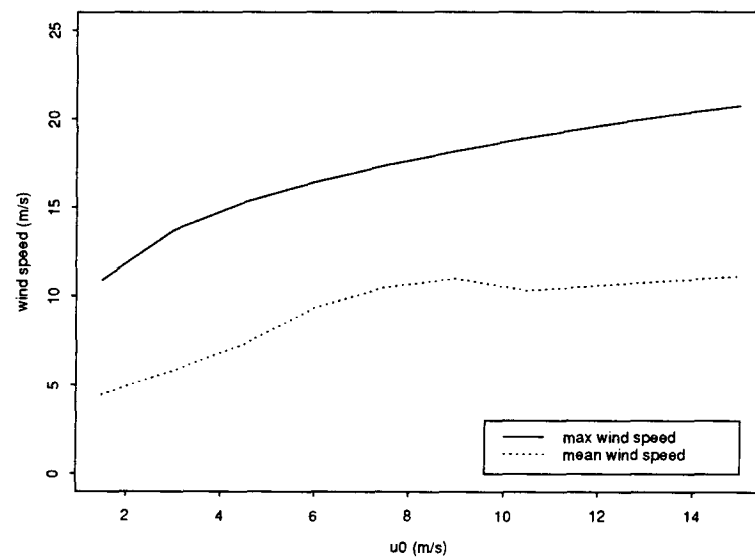
Figure 7.39: Sensitivity of mean and maximum gap wind speed to changes in u_0 (initial wind speed) for modified channel.
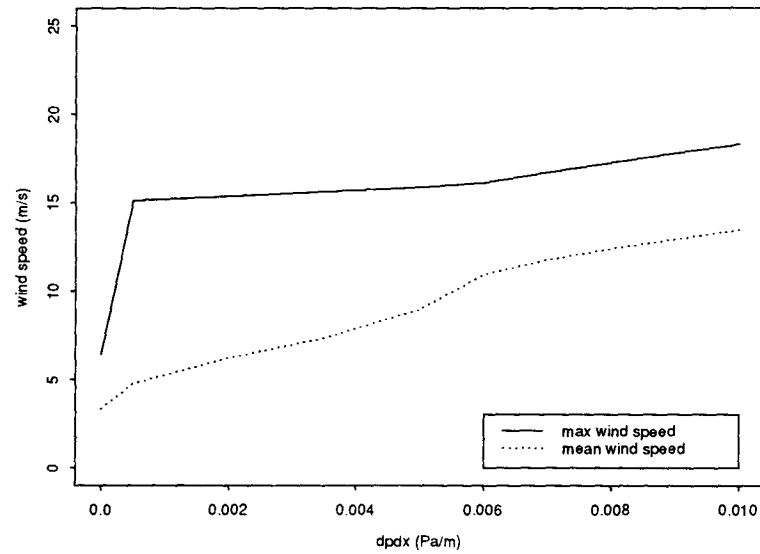
Figure 7.40: Sensitivity of mean and maximum gap wind speed to changes in $\frac{dp}{dx}$ (external pressure gradient) for modified channel.
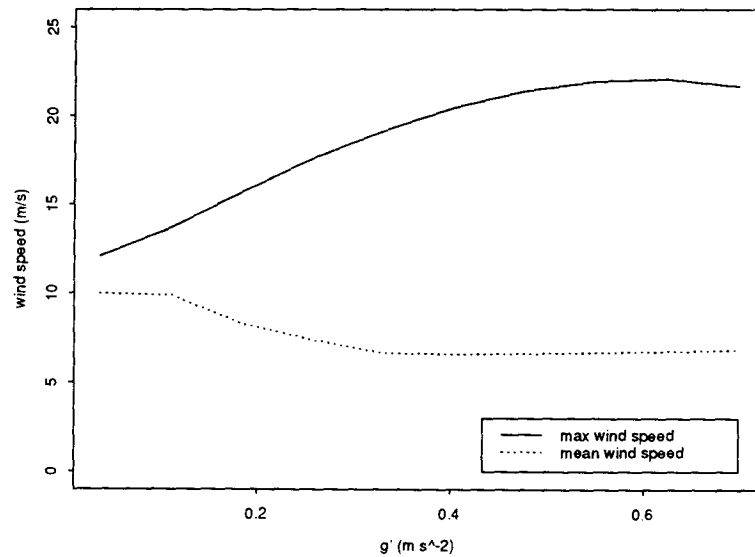
Figure 7.41: Sensitivity of mean and maximum gap wind speed to changes in g' (effective gravity) for modified channel.
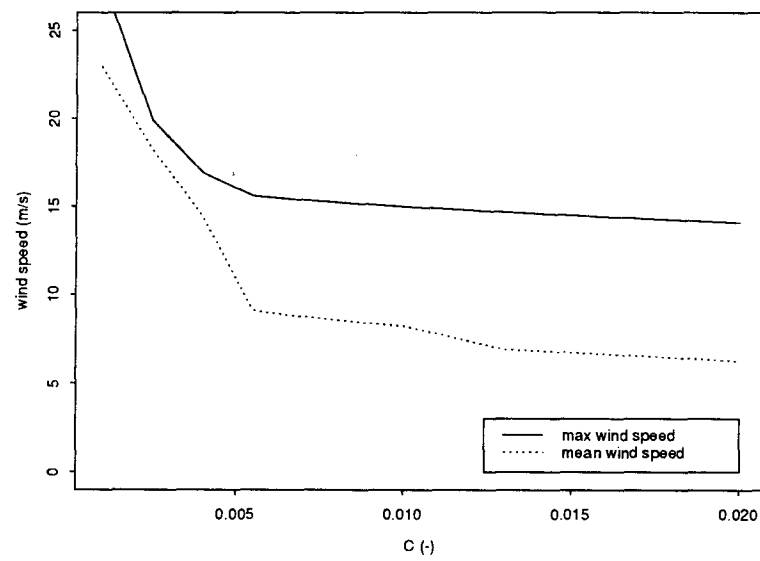
Figure 7.42: Sensitivity of mean and maximum gap wind speed to changes in C (drag coefficient) for modified channel.

7.4 Discussion and summary

Open channel hydraulic flow has been proposed as a possible analog to gap wind. This has been prompted by perceived similarities: gap winds are the flow of cold, dense low-level air horizontally constrained by a channel, which resembles the flow of water in a river, with the density difference across the inversion representing the water surface.

There are, however a number of limitations intrinsic in the hydraulic analog and its extension to gap wind, which may cause problems. Because *hydmod* is 1-dimensional with constant flow in the vertical and cross-channel directions, it is unable to correctly simulate gap wind where the channel widens unless the actual flow widens as well. In such a situation, observations suggest a stagnant zone of air forms, and that gap wind is constrained by smaller topographic features to the eastern channel of Howe Sound. In order to achieve realistic flow results in this part of Howe Sound, it was necessary to reduce the horizontal extent of gap winds by modifying the cross sections to include a vertical "wall" along the topographic ridge lines of Anvil, Gambier, and Bowen Islands.

Gap wind, while showing indications of two layer structure, is nevertheless continuously stratified, and so not completely represented by two dissimilar airmasses with a step density change between them. This results in practical problems in specifying an appropriate effective gravity (g'), as well as potential fundamental problems because the dynamics of the interface are not modelled. In particular, entrainment of air from above (or of air from slopes along the channel) is not included in *hydmod*. This limitation could be circumvented in future work by implementing the theory of Smith and Sun (1987) which allows layers of constant stratification.

Another problem related to the practical application of *hydmod* is that not all the input data required for initialization are directly available from routine data. The most difficult parameters to specify are the gap wind height at the channel start and end (h_0

and h_f). If this model were being used in a routine forecast setting, these would have to be estimated from nearby radiosonde data, or from numerical weather prediction model output.

Despite these limitations, *hydmod* is able to simulate the main features of gap wind and its variation along a channel with some accuracy. This implies the essence of gap wind is contained in the simple physics of hydraulic theory. The qualitative application of hydraulic theory is instructive to understand spatial gap wind patterns indicating where to expect strong gap wind. In situations where the flow is light and everywhere subcritical, the strongest wind can be found at the location of a horizontal contraction. When the flow is very strong and supercritical everywhere, the speed will be a minimum at contractions. The most striking result is when the flow becomes critical at a control point: the gap wind height decreases and wind speed increases in a zone of very fast supercritical flow which forms downstream. The fast supercritical flow transits suddenly to slow subcritical flow in a turbulent hydraulic jump. These zones of strong gap wind can be inferred both from observations of surface wind and RAMS vertical cross section output which depict descending isentropes in zones of accelerating wind, and ascending isentropes in zones of decreasing wind.

The hydraulic model force analysis indicated flow regimes when the simpler analytic models developed and discussed in chapter 6 would be applicable. For subcritical flow, away from contractions, the primary force balance is between the pressure gradient due to gap wind height variations, and the external pressure gradient. For supercritical flow, away from contractions, the primary force balance is between friction and external pressure gradient, implying the "friction" model of chapter 6 is applicable in this situation. For flow near a contraction, the primary balance is between advection and pressure gradient due to height variations.

Sensitivity tests indicated the importance of various initial and boundary conditions

to gap wind speed. Maximum and mean flow speed was positively sensitive to initial gap wind height, initial wind speed, and externally imposed pressure gradient. Maximum and mean wind speeds were negatively sensitive to gap wind height at the channel terminus, and drag coefficient. The response of mean wind speed to increased effective gravity was slightly negative. The response of maximum wind speed to increased effective gravity was positive for small and moderately large values of g', reaching an optimum and becoming slightly negative at large values of g'. Thus the effect of increased effective gravity over most of the likely range was to increase gap wind variability (increase the wind maximum, but decrease the mean).

Hydmod was only tested for one case at four times. To be more certain of the model's applicability, a test involving several cases should be made in the future. This would not only test the model, but allow values of some of the more poorly known parameters to be empirically determined.

Chapter 8

Summary of conclusions

This chapter summarizes and synthesizes findings of observation analysis, and various modelling approaches. The questions and objectives for the thesis given in chapter 1 are restated and resolved as far as possible. The significance of this work, along with recommendations and future work are mentioned.

8.1 Questions answered

Characteristics of gap winds – internal dynamics

horizontal outflow structure:

- Where does the maximum wind speed occur?

Since virtually all biological (including human) activity occurs at the surface, the horizontal distribution of surface wind has important implications, especially when the wind is strong and potentially damaging. Therefore, this question has been of prime concern in all parts of the thesis, from analysis of data to RAMS and hydraulic modelling. The observational network, despite its sparseness was able to give an indication of zones of maximum wind speed. RAMS output had excellent horizontal resolution, but had accuracy problems in the southern part of the domain. Hydraulic modelling gave the simplest realistic representation of gap flow, and clearly indicated where zones of maximum wind would occur, based on the flow regime and topography.

The observations suggest (figures 5.15 to 5.17) the axis of strongest gap wind is along the eastern main channel of Howe Sound. The precise wind maximum location along this axis, cannot be pin-pointed from observations due to station sparseness, however for this case, the strongest winds were observed at Finisterre Island, Defence Island, and Brunswick Point (figures 5.7 and 5.6).

RAMS output which shows the wind field in more detail, also indicates a narrow zone of strong flow, the axis of which however passes through the middle of Howe Sound instead of along the eastern edge for reasons discussed in chapter 5. Within this axis, zones of strongest flow are found around the horizontal coordinate of -150 and -130 km in figures 5.22 to 5.32 which are near Brunswick Point and Watts Point respectively. These locations are also quite close to relative maximum horizontal channel contractions.

Both observations and RAMS output are in accord with hydraulic modelling results which predict that zones of strongest wind should be at locations of horizontal contractions for subcritical flow, and downstream of these contractions for flow which becomes supercritical at them. Froude numbers determined from RAMS output seem to confirm this pattern – in figures 5.35b, c, d, and 5.36a a zone of supercritical flow develops downstream of the horizontal contraction near Watts Point, as well as downstream of Brunswick Point.

- How do changes in internal boundary conditions (topography, valley slope, roughness, and width) affect the flow?

These questions can be best answered by hydraulic modelling and sensitivity tests. The effect of valley slope is like that of external pressure gradient – see equation 7.8 where it is apparent the two have an equivalent effect. Therefore the *hydmod* sensitivity test in which the external pressure gradient varied is also applicable to valley floor slope so that increasing slope will increase gap wind speeds. (The equivalent range in slope shown in

figure 7.40 is 0 to ~ 1.) In the case of fjords such as Howe Sound however, the only location where the valley floor can have a downward slope is over land, where enhanced frictional retardation tends to counteract the effect of slope. *Hydmod* sensitivity tests showed the effect of increasing roughness (drag coefficient) is to decrease gap wind as expected. The force balance analysis of RAMS output has indicated that friction (diffusion) is the third most important force, after pressure gradient and advection. A force analysis of *hydmod* output shows that friction is only a large term when the flow is fast and supercritical. This is confirmed by sensitivity tests which indicate only supercritical flow has strong negative sensitivity (figure 7.42). Valley width determines locations of horizontal constrictions which play a key role in determining the location of wind maxima. If one were to adjust the width of valleys, the hydraulic analog indicates the narrower the contraction, the greater likelihood that it will act as a control resulting in supercritical flow downstream. Therefore one would expect, if all else were equal, a stronger gap wind response in valleys which have a greater degree of contraction.

- What are the effects of obstacles such as islands, on outflow winds?

The effects of islands are three-fold. First, they act to increase surface friction, because they are aerodynamically much rougher than the ocean which surrounds them. Second, hydraulically they can act as controls on the flow in the same way as horizontal channel contractions. If flow is forced over an island, it can become critical at the peak of the island, and supercritical on the downwind side, resulting in decreased wind speeds upwind, and increased winds downwind. This can be seen in the RAMS Froude number plots in figures 5.35 – 5.37, downwind of Gambier Island. Finally, they can deflect air through channels, creating channel contractions and hydraulic control points. This third effect was utilized in hydraulic modelling when the channel horizontal extent was reduced to obtain more accurate simulation results.

- How does flow vary temporally / diurnally? Are there wave-like (periodic in space or time) fluctuations?

Airflow in valleys under light synoptic conditions frequently exhibits thermally driven mountain – valley circulation: during the day there is light up-valley flow (anabatic), while at night there is light down-valley drainage flow (katabatic). While gap winds do not occur under light synoptic conditions, it is possible these thermally driven local flows could modulate, or be superimposed on gap wind flow. Observations show (figures 5.5 to 5.10) that strong gap winds began at most stations in the early evening – at the time when, under light synoptic conditions, an anabatic wind would be ending, and a katabatic wind starting. The wind at the two southern-most stations, Finisterre Island and Lookout Point (figures 5.7b and 5.8a) show an afternoon decrease in gap wind – when one would expect up-valley anabatic flow, under light synoptic conditions. Other stations do not show a speed decrease. The decrease in gap wind speed near the end of the channel, could also be due to increased boundary layer height during the daytime near the channel terminus which, according to hydraulic model results, causes greatly decreased gap wind speed near the end of channel. This follows from the negative sensitivity of gap flow to h_f seen in figures 7.9 and 7.38.

All stations however show diurnal variation in temperature. If the higher daytime temperatures are completely mixed in the gap wind layer, which is reasonable given that this layer is mixed by mechanical turbulence and of neutral stability according to AIRsonde™ data, then this would result in a decrease in effective gravity (g') during the daytime, and an increase at night. According to the *hydmod* sensitivity tests, the maximum wind is usually positively sensitive to g' (the maximum wind decreases for very large values of g'), while the mean wind is slightly negatively sensitive. The result of diurnal temperature variations then, from a hydraulic perspective, would be an increase

in maximum gap winds just before dawn, and a decrease during the day, which is in agreement with qualitative mountain / valley flow considerations.

Gap winds are the flow of stratified air over rough terrain. Therefore, it is reasonable to suppose that gravity waves could be generated. Wave-like fluctuations at time scales less than a few hours, are not observable in the data. Output from RAMS were only saved at 15 minute intervals, so that fluctuations with time scales less that an hour or so are not resolvable at a point in RAMS output. However with horizontal resolution of 1.25 km, gravity wave features with wavelengths larger that 5 km or so should be observable in RAMS fields at a given time. Since airflow closely follows isentropes, it is expected that gravity waves would be visible as wavy features in potential temperature cross sections (figures 5.22 to 5.32). While these cross sections do clearly show larger scale wave like features related to hydraulic transitions from subcritical to supercritical flow, there is no clear indication of smaller scale gravity wave features, either near the surface, or along the density interface marking the top of gap winds. It is however possible that these features exist, but at scales too small to be resolved. A complete treatment of questions concerning internal gravity waves, which will not be done here, could follow the work of Scorer (1949), in which trapped internal gravity wave are explained as resulting from vertical variations in the Brunt-Väisälä frequency.

vertical outflow structure:

- What is the depth of outflowing air, and how does it vary along a fjord?

The gap wind depth at Squamish Town can be found from AIRsonde™ observations at four times during the event. RAMS output, which agrees well with AIRsonde™ data, gives temperature and wind structure at 1.25 km horizontal and approximately 100 m vertical resolution over the entire domain. *Hydmod* output gives an analysis of gap wind depth and layer averaged speed along the main channel axis. The gap wind

depth at Squamish was observed to be 800 to 1000 m (figures 5.11 to 5.14). RAMS vertical cross sections of potential temperature along the main channel (figures 5.22 to 5.32) indicate that gap wind depth varies in a manner consistent with hydraulic theory during the course of the event. In particular, zones of decreasing gap wind height are associated with subcritical flow approaching channel contractions, or possibly with a transition to strong supercritical flow. Zones of increasing height are associated with subcritical channel expansions, and possibly with hydraulic jumps in transitions from fast supercritical to slow subcritical flow. The depth from the *hydmod* "most likely" simulation for the modified channel (figure 7.31) varies between 200 and 1000 m. Typical height variations from RAMS vertical cross section plots of wind and potential temperature (figures 5.22 to 5.32) are between approximately 200 and 1200 m.

- Where is the vertical speed maximum? How does the height of the speed maximum vary along the fjord?

Hydmod, which computes layer mean wind speed, cannot give any information about vertical variations in gap wind speed. AIRsonde™ observations from Squamish Town (figures 5.11 to 5.14) show peak winds usually near the top of the gap wind layer – at 319, 955, 718, 887 m. The peak gap wind for January 30, 16:00 PST (figure 5.11) at 319 m is the exception, being considerably below the top of the boundary layer. RAMS vertical cross sections (figures 5.22 to 5.32) also show an increase in gap wind speed away from the surface and place the peak speed in the center of the boundary layer.

- What is the vertical temperature structure? Does an inversion mark the top of the outflowing air?

Both AIRsonde™ observations and RAMS output show the lower gap wind layer is approximately neutral, presumably due to mechanical turbulent mixing. This layer is

surmounted by a stably stratified layer. The stably stratified layer usually includes an inversion or near isothermal layer which is confirmed by both AIRsonde™ observations and RAMS output.

- Is it possible to extrapolate results from the study of one fjord to others? Is it possible to separate the phenomena from their internal boundary conditions?

In order to completely answer this question, observations of gap wind depth and speed would have to be made in other fjords, and then used to test the findings of this work. If the dynamics of gap flow can be represented by a simple hydraulic analogy, then *hydmod* could be applied to other fjords. The qualitative relationships between topography, gap wind height, and speed which follow from the hydraulic analogy, would also apply in other channels. However, the probable range of input parameters may differ. In particular, for fjords further north, one would expect potentially larger external pressure gradients and effective gravity.

Reaction of flow to external boundary conditions

The major external parameters which, based on previous studies of related wind flows, were thought to control and influence outflow are: direction and magnitude of horizontal surface pressure gradient; temperature contrast between the cold air inland and warmer maritime air on the coast; geostrophic wind velocity at mountain top level; depth of cold air in interior (height of inversion); vertical wind profile – presence of critical layers and regions of wind reversal.

The assessment of these parameters and their importance for gap wind is made by using *hydmod* to perform sensitivity tests.

- Are these the important external parameters for gap winds?

Hydmod sensitivity tests have been made on all of the above parameters except geostrophic wind velocity at mountain top level, which however could be thought of as being related to the external pressure gradient; and the vertical wind profile which cannot be represented in the hydraulic model. The gap wind flow was found to be sensitive to each of the parameters (see the discussion in chapter 7).

- What is the relative importance of each?

It was found the flow was positively sensitive to external pressure gradient, and the depth and speed of gap wind at the channel start. The difference in temperature between the cold air inland and warm coastal air is related to effective gravity, and also to the external pressure gradient. Gap flow was found to become more variable with increasing temperature contrast (effective gravity): the mean speed decreased while the maximum speed increased, until an optimum value of effective gravity was reached after which the maximum speed also decreased.

- Are there other important external parameters?

Hydraulic modelling showed the importance of the boundary layer height at the channel terminus (mouth of Howe Sound) in determining winds near the end of the channel. It was found that increased terminus boundary layer heights resulted in decreased wind speed. This is likened to the rising level of a lake "backing up" a river flowing into it.

- Are there threshold values which these parameters must exceed for the flow to begin or to be maintained?

The hydraulic analog indicates that for the flow to begin, there must be down-channel flow at the channel head (otherwise there would be a negative discharge) which means the external pressure gradient should be directed down-channel. For strong winds, the

flow must become critical at some point in the channel. This will first occur when the right hand side of equation 7.8 is zero, which is near the point of maximum horizontal or vertical contraction. The height and speed of critical flow can be found by iteratively solving equation 7.7, and will depend on the topography at the point of maximum contraction, as well as on the discharge. Whether or not critical flow will be achieved at the maximum contraction point will depend mainly on whether uniform height is below or above critical height. For a given discharge this will depend on external pressure gradient, drag coefficient and topography at the control point. If the channel terminus boundary layer height is large enough, it could extend influence upstream to "drown out" the control point.

- How do external forcing parameters affect flow characteristics?

- Which parameters are most important?

Hydraulic modelling indicates that increasing external pressure gradient and discharge (initial wind speed, and height), result in increased wind speeds. Increasing surface friction and end channel boundary layer height, result in decreased gap wind strength. Increasing effective gravity (difference in potential temperature between the lower and upper layer), results in increased variability in the flow — higher wind speeds for supercritical flow (until an optimum effective gravity is reached), but lower speeds for subcritical flow. The flow is most sensitive to discharge, external pressure gradient, and end channel boundary layer height. Only fast, supercritical flow showed strong sensitivity to surface friction.

8.2 Significance

Several contributions have been made.

- This work provided the first reasonably detailed surface, and vertical sounding data of gap winds in a British Columbia fjord.

- The study used a 3-dimensional numerical model to simulate a real gap wind event. The modelling utilized real topography and input data and was able to provide a plausible simulation. The work highlighted the difficulty in applying a mesoscale model to phenomena which span many topographic and atmospheric scales, and pointed out the importance of resolving major topographic features. The model was very sensitive to the way in which topography was smoothed and represented, with the best simulations resulting when the topography was filtered so that all topographic variations with wavelength less than four times the horizontal spacing were removed. Despite some limitations in the RAMS simulation, the flow was adequately represented over much of the domain. The high resolution of RAMS output in 3-dimensions, indicated a close resemblance between gap wind and open channel hydraulic flow. This prompted the creation and application of a simple model based on river channel hydraulics to simulate gap winds.

- A hydraulic model of gap wind was created in which classical hydraulic theory was extended to include external pressure gradients. The hydraulic model contained the essential features of gap flow when compared to observations and RAMS output. By applying the ideas of hydraulics, qualitative information on the location of zones of maximum wind speed under various flow conditions can be found for any fjord in gap wind conditions.

- As there is starting to be a consensus in the literature that downslope winds are also fundamentally similar to hydraulic flow (Durran, 1986, 1990; Smith 1985), this points out the dynamic similarity between what are traditionally termed "downslope winds", and the Squamish or gap wind described in this thesis. Previous

studies of gap winds in nearby locations (Overland and Walter (1981) for example) have not explicitly found hydraulic effects.

8.3 Recommendations and future work

- A simulation using a 3-dimensional mesoscale model, like RAMS, should be made of a severe gap wind event to confirm the conclusions and inferences drawn from simulations of the present moderate event are applicable to stronger events as well. Such a simulation should include an expanded grid 3 and grid 4, so that topographic channels are better resolved, to improve simulation accuracy in the southern part of the domain.

- *Hydmod* should be tested and implemented as an analysis / forecast tool for meteorologists forecasting winds in channels under gap wind conditions. It could be used with current data to analyze wind conditions at locations between observing stations. It could also be used with forecast data to provide a wind forecast in a channel. The computational requirements of the model are slight, so that it will run quickly on any modern computer. The topographic data needed for the model are easily obtained from a topographic map. The meteorological data required for the model could be obtained from a combination of surface observations and numerical weather prediction model output. With *hydmod* in routine use, some of the more poorly known parameters could be "tuned" to improve simulation results by comparing model output with observations, and the usefulness of the model as a forecast tool evaluated.

- *Hydmod* could be extended to include two layers of constant stratification (rather than two neutral layers separated by a step change in temperature), after the theoretical work of Smith and Sun (1987) for downslope winds. The new model

would then need to be tested and compared both with observations and the present model.

Appendix A

RAMS description

In writing this description, extensive use has been made of notes prepared by Morran (1988) which were based on Tremback et al. (1986). CSU RAMS (Colorado State University Regional Atmospheric Modeling System) represents the merging of three numerical models. These were a non-hydrostatic cloud model (Tripoli and Cotton, 1982), and two hydrostatic mesoscale models (Mahrer and Pielke, 1977a; Tremback, Tripoli and Cotton, 1985). RAMS has been written in a modular fashion with many options possible. The code is written in non-standard FORTRAN 77 which requires the use of a special preprocessor to convert it to standard fortran and enables the use of extended features. Some of the non-standard features that the preprocessor allows are:

- use of more structured loops avoiding statement numbers

- use of activation characters in the first column of a line to activate conditional compilation of that line

- global inclusion of COMMON blocks and PARAMETER statements in chosen modules

A.1 Model formulation

RAMS is non-hydrostatic, elastic, uses the quasi-Boussinesq approximation (Dutton and Fichtl, 1969), a terrain following vertical coordinate, and is integrated using a semi-implicit "time-split" numerical technique.

216

Some of the options and features available in RAMS (**bold face** are those used in this study) are: (from Morran (1988), Tremback et al. (1986))

1. Horizontal coordinate:

   - **Standard Cartesian.**

   - Latitude / longitude.

2. Vertical coordinate:

   - Standard Cartesian.

   - **Sigma-z.** The vertical coordinate is terrain following and transformed according to: (Gal-Chen and Somerville, 1975)

   $$z^* = H(\frac{(z - z_s)}{(H - z_s)})$$
   (A.1)

   where z^* is the height of a particular grid point in the terrain following coordinate system; z_s is terrain elevation at that grid point; z is the untransformed vertical coordinate; and H is the height of the model top at which the z^* coordinate surface becomes horizontal (ie. 18507.493 metres in this case). After Clark (1977), this vertical coordinate transform, leads to the following transformations of derivatives of some quantity A:

   $$\frac{\partial A}{\partial x_i} = (\frac{1}{a})(\frac{\partial ab^{ij}A}{\partial x_j^*})$$
   (A.2)

   where a is given by

   $$a(x, y) = 1 - \frac{z_s(x, y)}{H} = \frac{\partial z}{\partial z^*}$$
   (A.3)

   and the tensor b^{ij} is

   $$b^{ij} = \begin{pmatrix} 1 & 0 & \frac{1}{a}\frac{\partial z_s}{\partial x}(\frac{z^*}{H} - 1) \\ 0 & 1 & \frac{1}{a}\frac{\partial z_s}{\partial y}(\frac{z^*}{H} - 1) \\ 0 & 0 & \frac{1}{a} \end{pmatrix}$$
   (A.4)

which then results in the following transformed velocity components

$$u^* = u \qquad (A.5)$$

$$v^* = v \qquad (A.6)$$

$$w^* = (u \, ab^{13} + v \, ab^{23} + w)\frac{1}{a} \qquad (A.7)$$

3. Basic equations:

- **Non-hydrostatic time-split compressible** (Tripoli and Cotton, 1980) **with a semi-implicit scheme for the small time step.** The non-hydrostatic model was chosen because on grid 4, terrain steepness and small grid spacing violates assumptions implicit in the hydrostatic assumption. A non-hydrostatic model permits fast moving sound waves which normally means that the time step must be small so that the Courant-Friedrichs-Lewy (CFL) stability criterion is not violated. This means that waves or flow features must travel no further than one grid distance per time step (otherwise the model would be numerically unstable). For computational efficiency, the time-split semi-implicit scheme of Klemp and Wilhelmson (1978) is used. This involves stepping the "acoustic terms", (those which contain sound waves) at a smaller time-step than the more slowly varying terms of interest. The quasi-Boussinesq approximation is used to separate the the high frequency variable of density from the Navier-Stokes predictive equations. The quasi-Boussinesq approximation differs from the fully Boussinesq approximation in that elasticity is permitted and the base state varies with height. The result of this is that in the formulation of model equations, when the terms are decomposed into base state plus perturbation quantities plus sub-grid scale perturbations, quantities which are ratios of perturbation to base state are ignored, except

when multiplied by gravity.

The model momentum equation in tensor notation is (Tripoli and Cotton, 1982):

$$
\underbrace{\frac{\partial \rho_0 u_i}{\partial t}}_{1} + \underbrace{\frac{\rho_0 \theta_0}{a} \frac{\partial a b^{ij} \pi'}{\partial x_i^*}}_{2} =
$$

$$
\underbrace{ADV(\rho_0 u_i)}_{3} + \underbrace{\rho_0 TURB(u_i)}_{4} +
$$

$$
\underbrace{g(\frac{\theta'}{\theta_0} + 1.61 r_v - r_T)\delta_{i3}}_{5} + \underbrace{\varepsilon_{ij3} f u_i}_{6} \tag{A.8}
$$

where: quantities subscripted "0" are fixed reference state variables; primed quantities (') are model resolvable perturbations from the reference state; u_i is velocity; x_i^* is the transformed coordinate; ρ is density; θ is potential temperature; π is the Exner function which replaces pressure and is defined as:

$$
\pi = C_P \frac{P}{P_{100}}^{\frac{R}{C_P}} \tag{A.9}
$$

where C_P is the specific heat capacity at constant pressure for dry air, P is total atmospheric pressure; P_{100} is 100 KPa, and R is the gas constant for dry air; ADV is the advection operator; $TURB$ is the turbulence operator described below; r_T and r_v are the total and vapour mixing ratios; δ_{i3} is the Kronecker delta function; and f is the Coriolis parameter. In equation A.8, term 1 is the momentum tendency (acceleration); term 2 the pressure gradient force; term 3 the momentum advection; term 4 the sub-grid scale friction; term 5 the vertical acceleration due to buoyancy; and term 6 the Coriolis acceleration. The advection operator for a variable A is defined as:

$$
ADV(\rho_0 A) = -(\frac{1}{a})[\frac{\partial}{\partial x_k^*}(a b^{jk} \rho_0 u_j A) - A \frac{\partial}{\partial x_k^*}(\rho_0 u_j)] \tag{A.10}
$$

which is the difference between a mass flux divergence term and a momentum divergence term. The turbulence operator is:

$$TURB(A) = -(\frac{1}{a})\frac{\partial}{\partial x_k^*}[ab^{jk}(\overline{A''u_j''})] \tag{A.11}$$

where a double prime ($''$) denotes perturbations at a scale smaller than those which are resolved in the model (ie. sub-grid scale perturbations). In addition to the momentum equations, there are equations for Exner function tendency (Klemp and Wilhelmson, 1978):

$$\frac{\partial \pi'}{\partial t} + \frac{1}{a}\frac{R}{C_v}\frac{\pi_0}{\rho_0\theta_0}\frac{\partial}{\partial x_j^*}(ab^{ij}\rho_0\theta_0 u_j) = 0 \tag{A.12}$$

and a thermodynamic energy equation:

$$\frac{\partial \rho_0\theta_{il}}{\partial t} = ADV(\rho_0\theta_{il}) + \rho_0 TURB(\theta_{il}) + \rho_0 S(\theta_{il}) \tag{A.13}$$

where θ_{il} is the ice-liquid water potential temperature which is conserved over all phase changes (equivalent to potential temperature in this case because phase changes weren't allowed), and S is a source or sink operator for θ_{il} which would be due only to radiational diabatic heating. There is also a mass continuity equation for water substance which will not be shown.

Equations A.8, A.12, A.13, and the mass continuity equation for water are a complete set of time dependent equations.

- Hydrostatic incompressible or compressible (Tremback, Tripoli and Cotton, 1985).

4. Dimensionality: 1, 2 or **3** dimensions.

5. Grid Structure:

- **Arakawa-C grid stagger.** This staggers variables on a grid so that velocity components are defined at different locations than the rest of the variables, and results in increased finite difference accuracy, especially for the pressure field. If T, representing the thermodynamic variables is located at the grid intersections, then U (east-west velocity) is located half a grid distance to the east and west of T; V (north-south velocity) is located half a grid distance to the north and south of T; and W (vertical velocity) is located half a grid point above and below T. This is illustrated in figure A.1.

```
T ———— U ———— T ———— U ———— T
|              |              |
|              |              |
V              V              V
|              |              |
|              |              |
T ———— U ———— T ———— U ———— T
|              |              |
|              |              |
V              V              V
|              |              |
|              |              |
T ———— U ———— T ———— U ———— T
```
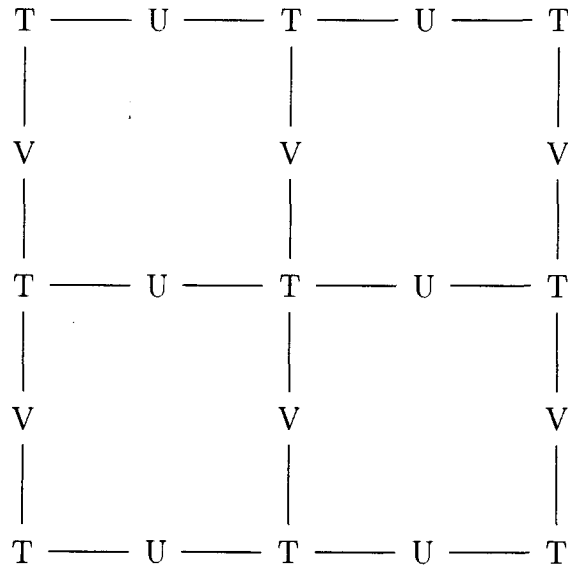
Figure A.1: Arakawa type C grid stagger used in the model.
T represents location of thermodynamic variables; U east-west velocity; V north-south velocity; and W (not shown, but located half a grid distance above and below T) vertical velocity.

- unlimited number of nested grids and levels of nesting (**4 nested grids used**).

6. Finite differencing:

- **time split - leapfrog on long time step (for slowly varying, non-acoustic terms on the right hand side of equations A.8 and A.12), forward-backward on small time-step (for acoustic terms on left hand side of equations A.8 and A.12)** (Tripoli and Cotton, 1980),2nd or 4th order flux conservative advection.

- forward-backward time split, 2nd or 6th order flux conservative (Tremback et al., 1987).

7. Turbulence closure:

- **Smagorinsky-type eddy viscosity** Smagorinsky (1963) **with Ri dependence.** The sub-grid scale dissipation is down gradient with eddy viscosity coefficients dependent upon length scale, deformation, and Brunt-Väisälä frequency. The vertical scale length is buoyancy adjusted according to the Richardson number (Ri).

- Level 2.5 type closure using eddy viscosity as a function of a prognostic turbulent kinetic energy.

- O'Brien profile function in a convective boundary layer (Mahrer and Pielke, 1977a); local exchange coefficient in a stable boundary layer (McNider, 1981).

8. Condensation:

- Grid points fully saturated or unsaturated.

- **No condensation.** The case simulated was dry and cloudless. Water vapour was therefore carried in the model only as a passive tracer.

9. Cloud microphysics:

- Warm rain conversion and accretion of cloud water to raindrops, evaporation and sedimentation (Tripoli and Cotton, 1980).

- In addition to the above: specified nucleation of ice crystals, conversion nucleation and accretion of graupel, growth of ice crystals, evaporation, melting and sedimentation (Cotton et al., 1982).

- In addition to the above: predicted nucleation and sink of crystal concentration, conversion and growth of aggregates, melting, evaporation and sedimentation.

- **No precipitation processes.** The case simulated was observed to be dry and cloudless, hence precipitation processes were not included in order to save computer time.

10. Radiation:

- Shortwave radiation model including molecular scattering, absorption of clear air (Yamamoto, 1962), ozone absorption and reflectance (Lacis and Hansen, 1974), transmittance and absorptance of a cloud layer (Stephens, 1978), clear-cloudy mixed layer approach (Stephens, 1977).

- **Shortwave radiation model described by** Mahrer and Pielke (1977a) **which includes the effects of forward Rayleigh scattering** (Atwater and Brown, 1974), **absorption by water vapour** (McDonald, 1960), **and terrain slope** (Kondrat'yev, 1969).

- Longwave radiation model including emissivity of a clear atmosphere (Rodgers, 1967), emissivity of cloud layer (Stephens, 1978), and emissivity of a "clear and cloudy" mixed layer (Herman and Goody, 1976).

- **Longwave radiation model described by** Mahrer and Pielke (1977a) **including emissivities of water vapour** (Jacobs, Pandolfo and Atwater, 1974) **and carbon dioxide** (Kondrat'yev, 1969) **and the computationally efficient technique of** Sasamori (1972).

- No radiation.

11. Lower Boundary:

    - Specified surface temperature and moisture function or specified surface fluxes coupled with constant flux layer condition based on similarity theory (Manton and Cotton, 1977).

    - Surface layer temperature and moisture fluxes are diagnosed as a function of the ground surface energy balance (Mahrer and Pielke, 1977a). The energy balance includes longwave and shortwave radiative fluxes, latent and sensible heat fluxes, and conduction from below the surface. To include the latter effect, a multilevel prognostic soil temperature model is computed.

    - **As above, but modified to be applied prognostically rather than diagnostically and increase computational efficiency.** (Tremback and Kessler, 1985).

12. Upper boundary conditions:

    - **Rigid lid.** This is the only boundary condition that can be used in this version of RAMS with variable initial conditions. The flow feature of interest is shallow relative to the vertical extent of the model so that problems with top boundary conditions should be minimized.

    - Rayleigh friction layer.

- Prognostic surface pressure (hydrostatic only).

- Material surface top. (hydrostatic only) (Mahrer and Pielke, 1977a)

- Gravity wave radiation condition (Klemp and Durran, 1983).

13. Lateral boundary conditions:

- Klemp and Wilhelmson (1978) radiative boundary condition.

- Orlanski (1976) radiative boundary condition.

- Klemp and Lilly (1978) radiative boundary condition.

- Any of the above coupled with the "mesoscale compensation region" described by Tripoli and Cotton (1982) with fixed conditions at the boundary.

- Sponge boundary condition of Perkey and Kreitzberg (1976) when large scale data are available. This includes a viscous region and the introduction of large scale fields into the model computations near the lateral boundaries.

- **Lateral boundaries which are "nudged" toward specified larger scale fields, following** Davies (1976). **The fields at the boundaries are from a larger scale model run (CMC FEM).**

14. Initialization

- Horizontally homogeneous.

- Horizontally homogeneous but with variations to force cloud initiation.

- **Variable initialization with large scale data obtained from a larger model (CMC FEM),** possibly enhanced by vertical soundings. **The large scale data is objectively analysed on isentropic surfaces and interpolated to the model grid.**

Appendix B

Hydmod data

ht (m) x (km)	100	200	300	400	500	600	700	800	900	1000
0.0	.1375	.5375	1.075	1.713	2.450	3.300	4.175	5.063	6.013	7.050
2.5	.2250	.4875	.8750	1.550	2.300	3.138	4.063	5.050	6.113	7.288
5.0	.3250	.8875	1.550	2.425	3.488	4.675	5.900	7.175	8.525	9.963
7.5	.2750	.7750	1.425	2.088	2.813	3.588	4.413	5.288	6.213	7.188
10.0	.4125	.8625	1.350	1.875	2.463	3.188	4.038	4.963	5.925	6.913
12.5	.2125	.4750	.7750	1.100	1.463	1.888	2.388	2.963	3.613	4.375
15.0	.3500	.7375	1.163	1.638	2.138	2.675	3.250	3.875	4.550	5.275
17.5	.3500	.7375	1.250	1.838	2.650	3.575	4.575	5.625	6.738	7.963
20.0	.4125	.9375	1.563	2.238	2.975	3.763	4.600	5.525	6.575	7.663
22.5	.2750	.6625	1.088	1.550	2.063	2.625	3.225	3.863	4.538	5.325
25.0	.3500	.7625	1.250	1.838	2.563	3.325	4.138	4.988	5.863	6.788
27.5	.4875	1.063	1.788	2.588	3.425	4.300	5.225	6.175	7.175	8.213
20.0	.8500	1.850	2.950	4.100	5.350	6.738	8.150	9.600	11.09	12.65
32.5	1.000	2.075	3.338	4.750	6.363	8.225	10.25	12.34	14.51	16.75
35.0	1.175	2.638	4.163	5.763	7.525	9.488	11.51	13.59	15.71	17.92
37.5	1.100	2.413	4.025	5.850	7.800	9.900	12.07	14.40	16.80	19.25
40.0	1.100	2.700	4.563	6.538	8.625	10.80	13.00	15.24	17.51	19.81
42.5	1.563	3.463	5.413	7.438	9.538	11.71	13.96	16.30	18.72	21.19
45.0	1.900	4.075	6.463	8.863	11.27	13.70	16.14	18.61	21.10	23.60
47.5	1.375	2.975	4.775	6.775	8.825	10.94	13.11	15.41	17.79	20.17
50.0	1.000	2.800	4.838	7.038	9.338	11.71	14.14	16.56	18.99	21.41

Table B.1: Cross sectional areas below the given height, along the "real" channel. Heights are from 100 to 1000 m. Area is $\times 10^6$ m^3.

ht (m) x (km)	1100	1200	1300	1400	1500	1600	1700	1800	1900	2000
0.0	8.288	9.600	10.99	12.51	14.24	16.01	17.84	19.69	21.59	23.49
2.5	8.525	9.800	11.15	12.59	14.06	15.59	17.14	18.70	20.27	21.85
5.0	11.44	12.96	14.54	16.19	17.84	19.49	21.14	22.79	24.44	26.09
7.5	8.275	9.488	10.71	11.94	13.16	14.39	15.61	16.84	18.06	19.29
10.0	7.938	9.038	10.41	11.82	13.29	14.76	16.25	17.75	19.25	20.75
12.5	5.200	6.088	7.075	8.225	9.488	10.80	12.17	13.57	15.00	16.42
15.0	6.050	6.850	7.713	8.688	9.763	10.84	11.91	12.99	14.06	15.14
17.5	9.263	10.64	12.09	13.56	15.04	16.51	17.99	19.46	20.94	22.41
20.0	8.813	9.988	11.16	12.34	13.51	14.69	15.86	17.04	18.21	19.39
22.5	6.225	7.175	8.175	9.238	10.34	11.44	12.54	13.64	14.74	15.84
25.0	7.775	8.813	9.950	11.20	12.55	13.90	15.25	16.60	17.95	19.30
27.5	9.288	10.45	11.66	12.90	14.15	15.40	16.65	17.90	19.15	20.40
20.0	14.27	15.96	17.67	19.40	21.15	22.90	24.65	26.40	28.15	29.90
32.5	19.05	21.42	23.80	26.25	28.80	31.37	33.97	36.57	39.17	41.77
35.0	20.16	22.41	24.72	27.11	29.56	32.04	34.54	37.04	39.54	42.04
37.5	21.75	24.27	26.81	29.37	31.97	34.61	37.26	39.91	42.56	45.21
40.0	22.19	24.62	27.09	29.56	32.05	34.55	37.05	39.55	42.05	44.55
42.5	23.67	26.17	28.69	31.22	33.77	36.32	38.87	41.42	43.97	46.52
45.0	26.12	28.67	31.22	33.77	36.32	38.87	41.42	43.97	46.52	49.07
47.5	22.57	25.00	27.42	29.85	32.27	34.70	37.12	39.55	41.97	44.40
50.0	23.84	26.26	28.69	31.11	33.54	35.96	38.39	40.81	43.24	45.66

Table B.2: Cross sectional areas below the given height, along the "real" channel. Heights are from 1100 to 2000 m. Area is $\times 10^6$ m^3.

ht (m) x (km)	100	200	300	400	500	600	700	800	900	1000
0.0	.1375	.5375	1.075	1.713	2.450	3.300	4.175	5.063	6.013	7.050
2.5	.2250	.4875	.8750	1.550	2.300	3.138	4.063	5.050	6.113	7.288
5.0	.3250	.8875	1.550	2.425	3.488	4.675	5.900	7.175	8.525	9.963
7.5	.2750	.7750	1.425	2.088	2.813	3.588	4.413	5.288	6.213	7.188
10.0	.4125	.8625	1.350	1.875	2.463	3.188	4.038	4.963	5.925	6.913
12.5	.2125	.4750	.7750	1.100	1.463	1.888	2.388	2.963	3.613	4.375
15.0	.3500	.7375	1.163	1.638	2.138	2.675	3.250	3.875	4.550	5.275
17.5	.3500	.7375	1.250	1.838	2.650	3.575	4.575	5.625	6.738	7.963
20.0	.4125	.9375	1.563	2.238	2.975	3.763	4.600	5.525	6.575	7.663
22.5	.2750	.6625	1.088	1.550	2.063	2.625	3.225	3.863	4.538	5.325
25.0	.3500	.7625	1.250	1.838	2.563	3.325	4.138	4.988	5.863	6.788
27.5	.4125	.9125	1.438	2.013	2.600	3.213	3.850	4.513	5.188	5.900
20.0	.4625	.9625	1.488	2.038	2.600	3.175	3.775	4.400	5.050	5.738
32.5	.2500	.5250	.8250	1.150	1.525	2.000	2.500	3.025	3.563	4.138
35.0	.5750	1.175	1.800	2.450	3.113	3.788	4.488	5.213	5.963	6.725
37.5	.7125	1.525	2.425	3.350	4.300	5.275	6.275	7.300	8.350	9.438
40.0	.6000	1.275	2.038	2.863	3.763	4.713	5.688	6.688	7.700	8.738
42.5	.8625	1.775	2.725	3.688	4.663	5.663	6.688	7.725	8.775	9.850
45.0	.9250	1.875	2.838	3.813	4.800	5.800	6.825	7.875	8.950	10.04
47.5	.5500	1.188	1.950	2.850	3.775	4.725	5.688	6.688	7.713	8.750
50.0	.4250	1.125	1.950	2.900	3.938	5.013	6.138	7.263	8.388	9.513

Table B.3: Cross sectional areas below the given height, along the modified channel. Heights are from 100 to 1000 m. Area is $\times 10^6$ m^3.

| ht (m) | 1100 | 1200 | 1300 | 1400 | 1500 | 1600 | 1700 | 1800 | 1900 | 2000 |
x (km)										
0.0	8.288	9.600	10.99	12.51	14.24	16.01	17.84	19.69	21.59	23.49
2.5	8.525	9.800	11.15	12.59	14.06	15.59	17.14	18.70	20.27	21.85
5.0	11.44	12.96	14.54	16.19	17.84	19.49	21.14	22.79	24.44	26.09
7.5	8.275	9.488	10.71	11.94	13.16	14.39	15.61	16.84	18.06	19.29
10.0	7.938	9.038	10.41	11.82	13.29	14.76	16.25	17.75	19.25	20.75
12.5	5.200	6.088	7.075	8.225	9.488	10.80	12.17	13.57	15.00	16.42
15.0	6.050	6.850	7.713	8.688	9.763	10.84	11.91	12.99	14.06	15.14
17.5	9.263	10.64	12.09	13.56	15.04	16.51	17.99	19.46	20.94	22.41
20.0	8.813	9.988	11.16	12.34	13.51	14.69	15.86	17.04	18.21	19.39
22.5	6.225	7.175	8.175	9.238	10.34	11.44	12.54	13.64	14.74	15.84
25.0	7.775	8.813	9.950	11.20	12.55	13.90	15.25	16.60	17.95	19.30
27.5	6.625	7.375	8.125	8.875	9.625	10.38	11.12	11.87	12.62	13.37
20.0	6.438	7.163	7.900	8.650	9.425	10.20	10.97	11.75	12.52	13.30
32.5	4.738	5.363	6.013	6.688	7.463	8.263	9.088	9.913	10.74	11.56
35.0	7.500	8.300	9.175	10.13	11.12	12.15	13.20	14.25	15.30	16.35
37.5	10.59	11.76	12.95	14.17	15.42	16.71	18.01	19.31	20.61	21.91
40.0	9.788	10.85	11.94	13.04	14.14	15.24	16.34	17.44	18.54	19.64
42.5	10.96	12.09	13.22	14.39	15.56	16.74	17.91	19.09	20.26	21.44
45.0	11.14	12.26	13.39	14.51	15.64	16.76	17.89	19.01	20.14	21.26
47.5	9.800	10.87	11.95	13.02	14.10	15.17	16.25	17.32	18.40	19.47
50.0	10.64	11.76	12.89	14.01	15.14	16.26	17.39	18.51	19.64	20.76

Table B.4: Cross sectional areas below the given height, along the modified channel. Heights are from 1100 to 2000 m. Area is $\times 10^6$ m^3.

Glossary

AIRsonde™ instrument package which, when attached to a helium balloon, can give atmospheric vertical sounding information (dry and wet bulb temperature, and pressure)

CMC FEM Canadian Meteorological Centre Finite Element Model — a numerical model of the atmosphere used for weather forcasting

RAMS Colorado State University Regional Atmospheric Modeling System — a state of the art mesoscale numerical model developed by several researchers over several years at Colorado State University.

AES Atmospheric Environment Service — Canadian Government Department responsible for the provision of weather services (among other things)

MOE British Columbia Ministry of the Environment

MTH British Columbia Ministry of Transportation and Highways

UBC University of British Columbia

T Temperature

W Wind

T$_D$ Dew point temperature

P Pressure

ASL Above sea level

RMSD Root mean square difference

UTC Coordinated Universal Time

PST Pacific Standard Time

ATK Point Atkinson lighthouse manned weather station (AES)

ALT Alta Lake (Whistler) manned weather station (AES)

PAM Pam Rocks automatic weather station (AES)

SQA Squamish Airport manned weather station (AES)

SQT Squamish Townsite automatic weather station (MOE)

LAN Langdale automatic weather station (MOE)

DEE Deeks Peak automatic weather station (MTH)

HAR Mount Harvey automatic weather station (MTH)

STR Mount Strachan automatic weather station (MTH)

ALB Alberta Creek automatic weather station (MTH)

DAI Daisy Lake automatic weather station (UBC)

SQR Squamish River automatic weather station (UBC)

WAT Watts Point automatic weather station (UBC)

DEF Defence Island automatic weather station (UBC)

BRU Brunswick Point automatic weather station (UBC)

MEL Port Mellon automatic weather station (UBC)

FIN Finisterre Island automatic weather station (UBC)

LOO Lookout Point automatic weather station (UBC)

RAG Ragged Island automatic weather station (UBC)

Bibliography

Arakawa, S., 1968: A proposed mechanism of fall winds and dashikaze, *Met. Geophys.*, **19**, 69–99.

———, 1969: Climatological and dynamical studies on the local strong winds, mainly in Hokkaido, Japan, *Geophys. Mag.*, **34**, 349–425.

Atkinson, B. W., 1981: *Mesoscale Atmospheric Circulations*, Academic Press, New York.

Atmospheric Research Incorporated, 1986: *Observations of sea spray icing at Green Island, B.C.*, Environment Canada, Atmospheric Environment Service , DSS contract no. 09SB.KM147-6119/1.

Atwater, M. A. and P. S. Brown, 1974: Numerical calculation of the latitudinal variation of solar radiation for an atmosphere of varying opacity, *J. Appl. Met.*, **13**, 289–297.

Ball, F. K., 1956: The theory of strong katabatic winds, *Austral. J. Phys.*, **9**, 373–386.

Bannon, P. R., 1981: Synoptic-scale forcing of coastal lows: forced double Kelvin waves in the atmosphere, *Quart. J. Roy. Meteor. Soc.*, **107**, 313–327.

Beal, H. T., 1985: *Outflow winds from Northern B.C. Mainland inlets*, unpublished manuscript.

Bénévant, E., 1930: Bora et mistral, *Annales de Geographie*, **39**, 286–298.

Cameron, D. C., 1931: Easterly gales in the Columbia River Gorge during the winter of 1930-1931 - Some of their causes and effects, *Mon. Wea. Rev.*, **59**, 411–413.

Cameron, D. C. and A. B. Carpenter, 1936: Destructive easterly gales in the Columbia River Gorge, December 1935, *Mon. Wea. Rev.*, **64** , 264–267.

Clark, T. L., 1977: A small-scale dynamic model using a terrain-following coordinate transformation, *J. Comp. Phys.*, **24**, 186–215.

Clark, T. L. and W. R. Peltier, 1977: On the evolution and stability of finite amplitude mountain waves, *J. Atmos. Sci.* , **34**, 1715–1730.

————, 1984: Critical level reflection and the resonant growth of nonlinear mountain waves, *J. Atmos. Sci.* , **41**, 3122–3134.

Clark, T. L. and R. D. Farley, 1984: Severe downslope windstorm calculations in two and three spatial dimensions using anelastic interactive grid nesting: A possible mechanism for gustiness, *J. Atmos. Sci.* , **41**, 329–350.

Cotton, W. R., M. A. Stephens, T. Nehrkorn and G. J. Tripoli, 1982: The Colorado State University three-dimensional cloud/mesoscale model – 1982. Part II: an ice phase parameterization, *J. de Rech. Atmos.*, **16**, 295–320.

Davies, H. C., 1976: A lateral boundary formulation for multi-level prediction models, *Quart. J. Roy. Meteor. Soc.*, **102**, 405–418.

Deardorff, J. W., 1972: Parameterization of the planetary boundary layer for use in general circulation models, *Mon. Wea. Rev.*, **113**, 89–98.

Durran, D. R., 1986: Another look at downslope windstorms. Part I: The development of analogs to supercritical flow in an infinitely deep, continuously stratified fluid, *J. Atmos. Sci.* , **43**, 2527–2543.

————, 1990: Mountain waves and downslope winds. *Atmospheric Processes over Complex Terrain*, W. Blumen, Ed., American Meteorological Society, Boston, Mass., p. 323.

Durran, D. R. and J. Klemp, 1983: A compressible model for the simulation of moist mountain waves, *Mon. Wea. Rev.*, **111**, 2341–2361.

Durran, D. R. and J. B. Klemp, 1987: Another look at downslope winds. Part II: Nonlinear amplification beneath wave-overturning layers, *J. Atmos. Sci.* , **44**, 3402–3412.

Dutton, J. A. and G. H. Fichtl, 1969: Approximate equations of motion for gases and liquids, *J. Atmos. Sci.* , **26**, 241–249.

Faulkner, D. A., 1980: *Mesoscale observations of an outflow wind over the southern Strait of Georgia*, Environment Canada, Atmospheric Environment Service, Pacific Region Technical Notes, 80-022.

Gal-Chen, T. and R. C. J. Somerville, 1975: On th use of a coordinate transformation for the solution of the Navier-Stokes equations, *J. Comp. Phys.*, **17**, 209–228.

Garratt, J. R., 1977: Review of drag coefficients over oceans and continents, *Mon. Wea. Rev.*, **105**, 915–929.

Henderson, F. M., 1966. *Open Channel Flow*, Macmillan, New York, p. 522.

Herman, G. and R. Goody, 1976: Formation and persistence of summertime arctic stratus clouds, *J. Atmos. Sci.* , **33**, 1537–1553.

Hoggan, D. H., 1989. *Computer-assisted floodplain hydrology and hydraulics*, McGraw-Hill, New York, p. 518.

Houghton, D. D. and E. Isaacson, 1968: Mountain winds, *Stud. Numer. Anal.*, **2**, 21–52.

Houghton, D. D. and A. Kasahara, 1968: Non-linear shallow fluid flow over an isolated ridge, *Commun. Pure Appl. Math.*, **21**, 1–23.

Hurd, W. E., 1929: Northers of the Gulf of Tehuantepec, *Mon. Wea. Rev.*, **57**, 192–194.

Jackson, P. L., 1993: An intense outbreak of arctic air in southwestern British Columbia, in preparation.

Jackson, P. L. and D. G. Steyn, 1992: The Weather and Climates of Howe Sound, *Can. Tech. Rep. Fish. Aquat. Sci.*, **1879**, 1–16.

Jacobs, C. A., J. P. Pandolfo and M. A. Atwater, 1974: *A description of a general three dimensional numerical simulation model of a coupled air-water and/or air-land boundary layer*, IFYGL final report, CEM Report No. 5131-509a.

Jones, R. E., 1985: *Valley Winds*, CMC Information, **4**, **1**, Environment Canada, Atmospheric Environment Service.

Jurčec, V., 1981: On mesoscale characteristics of bora conditions in Yugoslavia. *Weather and Weather Maps*, G. H. Liyequist, Ed., Contributions to Current Research in Geophysics, **10** , Birkhauser Verlag, Basel.

Klemp, J. B. and D. R. Durran, 1983: An upper boundary condition permitting internal gravity wave radiation in numerical mesoscale models, *Mon. Wea. Rev.*, **111**, 430–444.

Klemp, J. B. and D. K. Lilly, 1975: The dynamics of wave induced downslope winds, *J. Atmos. Sci.* , **32**, 78–107.

———, 1978: Numerical simulation of hydrostatic mountain waves, *J. Atmos. Sci.* , **35**, 78–107.

Klemp, J. B. and R. B. Wilhelmson, 1978: The simulation of three-dimensional convective storm dynamics, *J. Atmos. Sci.* , **35**, 1070–1096.

Klemp, J. B. and D. R. Durran, 1987: Numerical Modelling of Bora Winds, *Meteor. Atmos. Phys.*, **36**(1/4), 215–227.

Kondrat'yev, K. Y., 1969: *Radiation in the atmosphere*, Academic Press, New York, 912 pp..

Lacis, A. A. and J. Hansen, 1974: A parameterization for the absorption of solar radiation in earth's atmosphere, *J. Atmos. Sci.* , **31**, 118–133.

Lackmann, G. M. and J. E. Overland, 1989: Atmospheric structure and momentum balance during a gap-wind event in Sheilikof Strait, Alaska, *Mon. Wea. Rev.*, **117**, 1817–1833.

Lilly, D. K. and J. B. Klemp, 1979: The effects of terrain shape on nonlinear hydrostatic mountain waves, *J. Fluid Mech.*, **95**, 241–262.

Long, R. R., 1954: Some aspects of the flow of stratified fluid systems , *Tellus*, **6**, 97–115.

Macklin, S. A., G. M. Lackmann and J. Gray, 1988: Offshore-directed winds in the vicinity of Prince William Sound, Alaska, *Mon. Wea. Rev.*, **116**, 1289–1301.

Macklin, S. A., J. E. Overland and J. P. Walker, 1984: Low-level gap winds in Shelikoff Strait, Preprints, Third Technical conference on Meteorology of the Coastal Zone, Miami.

Macklin, S. A., 1988: Structure of a mountain-gap wind blowing over a coastal inlet, Preprints, Fourth Conference on Meteorology and Oceanography of the Coastal Zone, Anaheim, Calif..

Macklin, S. A., N. A. Bond and J. P. Walker, 1990: Structure of a low-level jet over lower Cook Inlet, Alaska, *Mon. Wea. Rev.*, **118**, 2568–2578.

Mahrer, Y. and R. A. Pielke, 1977a: A numerical study of the airflow over irregular terrain, *Beitrage zur Physik der Atmosphare*, **50**, 98–113.

———, 1977b: The effects of topography on sea and land breezes in a two-dimensional numerical model, *Mon. Wea. Rev.*, **105**, 1151–1162.

———, 1978: A test of an upstream spline interpolation technique for the advective terms in a numerical mesoscale model, *Mon. Wea. Rev.*, **106**, 818–830.

Manton, M. J. and W. R. Cotton, 1977: Parameterization of the atmospheric surface layer, *J. Atmos. Sci.* , **34**, 331–334.

Mass, C. F. and M. D. Albright, 1985: A severe windstorm in the lee of the Cascade mountains of Washington State, *Mon. Wea. Rev.*, **113**, 1261–1281.

Mass, C. F., M. D. Albright and D. J. Brees, 1986: The onshore surge of marine air into the Pacific Northwest: a coastal region of complex terrain, *Mon. Wea. Rev.*, **114**, 2602–2627.

McDonald, J. E., 1960: Direct absorption of solar radiation by atmospheric water vapor, *J. Meteor.*, **17**, 319–328.

McNider, R. T., 1981: *Investigation of the impact of topographic circulations on the transport and dispersion of air pollutants*, University of Virginia, PhD thesis.

McNider, R. T. and R. A. Pielke, 1981: Diurnal boundary-layer development over sloping terrain, *J. Atmos. Sci.* , **38**, 2198–2212.

Mitchell, J. M., 1956: Strong surface winds at Big Delta, Alaska, *Mon. Wea. Rev.*, **84**, 15–24.

Mook, R. H. G., 1962: Zur bora an Einem Nordnorwegischen fjord, *Met. Rundschau*, **15**, 130–133.

Morran, M., 1988: The CSU RAMS.

North Shore News, February 3, 1989: Arctic temperatures cause chills, spills. Homes, boats, cars damaged.

Orlanski, I., 1976: A simple boundary condition for unbounded hyperbolic flows, *J. Comput. Phys.*, **21**, 251–269.

Overland, J. E. and B. A. Walter, 1981: Gap winds in the Strait of Juan de Fuca, *Mon. Wea. Rev.*, **109**, 2221–2233.

Paradiž, B., 1957: Bura u Sloveniji, Hidrometeoroloski Zavod Ir Slovenije 10 Let Hidrometeorolske Sluzke, Ljubljana.

———, 1959: Bura u Sloveniji, Hidrometeoroloski Zavod NR Hvratske, Rasprave i Prikazi, Zagreb.

Patrick, D., 1980: *Outflow winds in mainland inlets*, Environment Canada, Atmospheric Environment Service, Pacific Region Technical Notes, 80-007.

Peltier, W. R. and T. L. Clark, 1979: The evolution and stability of finite amplitude mountain waves. Part II: Surface wave drag and severe downslope windstorms, *J. Atmos. Sci.* , **36**, 1498–1529.

———, 1983: Nonlinear mountain waves in two and three spatial dimensions, *Quart. J. Roy. Meteor. Soc.*, **109**, 527–548.

Perkey, D. J. and C. W. Kreitzberg, 1976: A time-dependent lateral boundary scheme for limited-area primitive equation models, *Mon. Wea. Rev.*, **104**, 744–755.

Pettre, P., 1982: On the problem of violent valley winds, *J. Atmos. Sci.* , **39**, 542–554.

Reed, R. J., 1981: A case of a bora-like windstorm in western Washington, *Mon. Wea. Rev.*, **109**, 2383–2393.

Reed, T. R., 1931: Gap winds in the strait of Juan de Fuca, *Mon. Wea. Rev.*, **59**, 373–376.

Rodgers, C. D., 1967: The use of emissivity in atmospheric radiation calculations, *Quart. J. Roy. Meteor. Soc.*, **93**, 43–54.

Sasamori, T., 1972: A linear harmonic analysis of atmospheric motion with radiative dissipation, *J. Meteor. Soc. of Japan*, **50**, 505–518.

Schaeffer, G., 1975: Climatology. *The Squamish River Estuary Status of Environmental Knowledge to 1974*, L. M. Hoos and C. L. Vold, Eds., Environment Canada.

Schwerdtfeger, W., 1975: Mountain barrier effect on the flow of stable air north of the Brooks range. *Climate of the Arctic*, G. Weller and S. A. Bowling, Eds., Geophysical Institute, University of Alaska, Fairbanks, pp. 204–208.

Scorer, R. S., 1949: Theory of waves in the lee of mountains, *Quart. J. Roy. Meteor. Soc.*, **75**, 41–56.

Smagorinsky, J., 1963: General circulation experiments with primitive equations: Part I: The basic experiment, *Mon. Wea. Rev.*, **91**, 99–165.

Smith, R. B., 1985: On severe downslope winds, *J. Atmos. Sci.* , **42**, 2597–2603.

———, 1987: Aerial observations of the Yugoslavian bora, *J. Atmos. Sci.* , **44**, 269–297.

Smith, R. B. and J. Sun, 1987: Generalized hydraulic solutions pertaining to severe downslope winds, *J. Atmos. Sci.* , **44**, 2934–2939.

Stephens, G. L., 1977: *The transfer of radiation in cloudy atmosphere*, University of Melbourne, PhD thesis. .

———, 1978: Radiation profiles in extended water clouds. Webster Theory., *J. Atmos. Sci.* , **35**, 2111–2122.

Steyn, D. G. and P. L. Jackson, 1990: Gap winds in Howe Sound, British Columbia I: The phenomenon, Preprints, Fifth Conference on Mountain Meteorology, Boulder, Colorado.

Steyn, D. G. and I. G. McKendry, 1988: Quantitative and qualitative evaluation of a three-dimensional mesoscale numerical model simulation of a sea breeze in complex terrain, *Mon. Wea. Rev.*, **119**, 1914–1926.

The Vancouver Sun, February 1, 1989a: Icy blast kills 13 in west, high wind cuts power to 20,000.

———, February 3, 1989b: Fierce winds leave islands without power.

———, February 4, 1989c: B-b-better b-b-by monday, emergency declared over cold.

Thiessen, A. H., 1911: Precipitation averages for large areas, *Mon. Wea. Rev.*, **39**, 1082–1084.

Tremback, C., G. Tripoli, R. Arritt, W. R. Cotton and R. A. Pielke, 1986: The Regional Atmospheric Modeling System, Proc. International Conf. Development and Application of Computer Techniques to Environmental Studies (Envirosoft 86), Los Angeles, U.S.A..

Tremback, C. J. and R. Kessler, 1985: A surface temperature and moisture parameterization for use in mesoscale numerical models, Preprints, 7th Conference on Numerical Weather Prediction, June 17-20, 1985, Montreal, Québec.

Tremback, C. J., J. Powell, W. R. Cotton and R. A. Pielke, 1987: The forward in time upstream advection scheme: Extension to higher orders, *Mon. Wea. Rev.*, **115**, 540–555.

Tremback, C. J., G. J. Tripoli and W. R. Cotton, 1985: A regional scale atmospheric numerical model including explicit moist physics and a hydrostatic time-split scheme, Preprints, 7th Conference on Numerical Weather Prediction, June 17-20, 1985, Montreal, Québec.

Tripoli, G. J. and W. R. Cotton, 1980: A numerical investigation of several factors contributing to the observed variable intensity of deep convection over South Florida, *J. Appl. Met.*, **19**, 1037–1063.

_____, 1982: The Colorado State University three-dimensional cloud/mesoscale model – 1982. Part I: General theoretical framework and sensitivity experiments, *J. de Rech. Atmos.*, **16**, 185–220.

Tyner, R., 1950: *An investigation into the frequency of offshore winds at Green Island B.C. during the period September 1, 1949 to March 31, 1950*, Meteorological Division Technical Circular, 1861.

————, 1951a: *Paths taken by the cold air in polar outbreaks in British Columbia*, Meteorological Division Technical Circular, 2049 .

————, 1951b: *Polar outbreaks into the Okanagan valley and aouthern coast of British Columbia.*, Meteorological Division Technical Circular, 1919.

Ulrickson, B. L. and C. F. Mass, 1990: Numerical investigation of mesoscale circulations over the Los Angeles basin. Part I: A verification study, *Mon. Wea. Rev.*, **118**, 2138–2161.

Vancouver, G., 1798: *A voyage of discovery to the North Pacific Ocean and around the world*, G. G. and J. Robinson, London, 3 Vols. and Atlas.

Walko, R., 1988: pers. comm..

Willmott, C. J., 1981: On the validation of models, *Phys. Geogr.*, **2**(2), 168–194.

————, 1982: Some comments on the evaluation of model performance, *Bull. Amer. Meteor. Soc.*, **63**, 1309–1313.

Willmott, C. J., S. G. Ackleson, R. D. Davis, J. J. Feddema, K. M. Klink, D. R. Legates, J. O'Donnell and C. M. Rowe, 1985: Statistics for the evaluation and comparison of models, *J. Geophys. Res.*, **90**(C5), 8995–9005.

Yamamoto, G., 1962: Direct absorption of solar radiation by atmospheric water vapor carbon dioxide and molecular oxygen, *J. Atmos. Sci.* , **19**, 182–188.

Yoshimura, M., 1976: Synoptic and aerological climatology of the bora day. *Local Wind Bora*, M. M. Yoshino, Ed., University of Tokyo Press, Tokyo, pp. 99–111.

Yoshimura, M., K. Nakamura and M. M. Yoshino, 1976: Local climatological observations of bora in the Senj region on the Croatian coast. *Local Wind Bora*, M. M. Yoshino, Ed., University of Tokyo Press, Tokyo, pp. 21–39.

Yoshino, M. M., 1969: Synoptic and local climatological study on bora in Yugoslavia, *Geogr. Rev. Japan*, **42**, 747–761.

_____, 1972: An annotated bibliography on bora, *Climatol. Notes*, **10**, 1–22.

_____, 1975: *Climate in a Small Area - An Introduction to Local Meteorology*, University of Tokyo Press, Tokyo.

_____, Ed., 1976a: *Local Wind Bora*, Tokyo University Press, Tokyo.

_____, 1976b: Bora studies: A historical review and problems today. *Local Wind Bora*, M. M. Yoshino, Ed., Tokyo University Press, , Tokyo, pp. 3–18.

Yoshino, M. M., M. T. Yoshino, M. Yoshimura, K. Mitsui, K. Urushibara, S. Ueda, M. Owada and K. Nakamura, 1976: Bora regions as revealed by wind-shaped trees on the Adriatic coast. *Local Wind Bora*, M. M. Yoshino, Ed., Tokyo University Press, Tokyo, pp. 59–74.